Single photon generation and manipulation with semiconductor quantum dot devices

Lorenzo de Santis

▸ To cite this version:

Lorenzo de Santis. Single photon generation and manipulation with semiconductor quantum dot devices. Quantum Physics [quant-ph]. Université Paris Saclay (COmUE), 2018. English. NNT : 2018SACLS034 . tel-01783546

HAL Id: tel-01783546
https://theses.hal.science/tel-01783546v1

Submitted on 2 May 2018

universite
PARIS-SACLAY

UNIVERSITÉ
PARIS
SUD
Comprendre le monde,
construire l'avenir

NNT : 2018SACLS034

Single photon generation and manipulation with semiconductor quantum dot devices

Thèse de doctorat de l'Université Paris-Saclay
préparée à l'Université Paris-Sud

École doctorale n°572
École Doctorale Ondes et Matière (EDOM)
Specialité de doctorat: optique et photonique

Thèse présentée et soutenue à Marcoussis, le 7 Mars 2018
par

Lorenzo De Santis

Composition du Jury :

M	Antoine Browaeys Institut d'Optique Graduate School	Président
M	Fabio Sciarrino La Sapienza University	Rapporteur
M	Julien Claudon Institut Nanosciences et Cryogénie	Rapporteur
M	Wolfgang Löffler Leiden University	Examinateur
Mme	Eleni Diamanti Université Pierre et Marie Curie	Examinatrice
Mme	Pascale Senellart Université Paris-Sud	Directrice de thèse

Thèse de doctorat

Résumé

Les phénomènes quantiques les plus fondamentaux comme la cohérence quantique et l'intrication sont aujourd'hui explorés pour réaliser des nouvelles technologies. C'est le domaine des technologies quantiques, qui promettent de révolutionner le calcul, la communication et la métrologie. En encodant l'information dans les systèmes quantiques, il serait possible de résoudre des problèmes inaccessibles aux ordinateurs classiques, de garantir une sécurité absolue dans les communications et de développer des capteurs dépassant les limites classiques de précision. Les photons uniques, en tant que vecteurs d'information quantique, ont acquis un rôle central dans ce domaine, car ils peuvent être manipulés facilement et être utilisés pour mettre en œuvre de nombreux protocoles quantiques. Notamment, ils sont des porteurs idéals pour le transfert de l'information à grandes distances et aussi pour interfacer des systèmes quantiques de nature différents. Pour cela, il est essentiel de développer des interfaces très efficaces entre les photons et les systèmes quantiques matériels, tels les atomes uniques, une fonctionnalité fondamentale à la fois pour la génération et la manipulation des photons. De nombreux travaux de recherche s'intéressent à la réalisation de systèmes atome-cavité très efficaces, afin de transférer de façon déterministe et réversible de l'information entre les photons et la transition optique d'un atome unique. Des expériences pionnières ont été réalisées en utilisant des atomes naturels dans des cavités, où les interactions peuvent être contrôlées au niveau d'un seul photon. Tout en étant un cadre idéal pour réaliser des protocoles quantiques, les atomes uniques nécessitent d'un grand effort expérimental pour être piégé et manipulé dans des cavités optiques. La réalisation de tels systèmes dans l'état solide permettrait de fabriquer des dispositifs quantiques intégrés et à large échelle.

Dans ce travail de thèse, nous étudions l'interface lumière-matière réalisée par une boîte quantique unique, utilisée comme un atome artificiel, couplée de façon déterministe à une cavité de type micropilier. Ce système permet d'obtenir une situation proche du régime atomique unidimensionnel, où la transition atomique interagit avec un seul mode du champ électromagnétique. Toute l'émission de la boite quantique est canalisée dans la microcavité optique et peut être facilement collectée en dehors des miroirs de la cavité, ce qui permet également une injection efficace de la lumière. Un tel dispositif s'avère être un émetteur et un récepteur efficace de photons uniques, et il est utilisé ici pour implémenter des fonctionnalités quantiques de base.

Tout d'abord, nous montrons comment la boite quantique dans la cavité est une source très brillantes de photons uniques, sous une excitation optique non-résonante et aussi résonante. L'accélération de l'émission spontanée de la boîte quantique dans la cavité et le contrôle électrique de la structure permettent de générer des photons très indiscernables avec une très haute brillance. Cela permet de surmonter les performances des sources de photons uniques basées sur des processus paramétriques, qui sont habituellement utilisée pour les expériences d'optique quantique.

Cette nouvelle génération de sources de photons uniques est utilisée dans ce travail pour générer des états de photons intriqués en chemin appelés états NOON. Ces états intriqués sont des ressources importantes pour la détection de phase optique, et ils pourraient permettre d'effectuer des mesures avec une précision au-delà de la limite quantique standard. Cependant, leur caractérisation optique a été peu étudiée jusqu'à présent. Nous présentons une nouvelle méthode de tomographie pour reconstruire la matrice densité des états NOON encodés en chemin et implémentons expérimentalement cette méthode dans le cas de deux photons.

Enfin, nous étudions le comportement de nos composants comme filtres non-linéaires de lumière. L'interface optimale entre la lumière et la boîte quantique permet l'observation d'une réponse optique non-linéaire au niveau d'un seul photon incident. Ce résultat est obtenu dans un régime d'excitation impulsionnel et sans utiliser aucun postselection. Cet effet est utilisé pour démontrer le filtrage des états Fock à un seul photon à partir d'impulsions classiques incidentes. Ceci ouvre la voie à la réalisation efficace d'interactions effectives entre deux photons dans un système à l'état solide, une étape fondamentale pour surmonter les limitations dues au fonctionnement probabilistes des portes optiques linéaires actuellement employées dans les protocoles de calculs et communications quantiques.

Remerciements

La thèse présentée dans ce manuscrit est le résultat de trois années de travail au sein d'une équipe conviviale et stimulante qui m'a permis de grandir tant d'un point de vue scientifique que personnel. Je suis reconnaissant à toutes les personnes que j'ai eu la chance de rencontrer et qui ont rendu cette expérience possible.

Je remercie les membres de mon jury de thèse, d'abord pour avoir pris le temps de lire mon manuscrit, mais aussi pour avoir été à l'origine d'une discussion scientifique extrêmement stimulante, concluant idéalement ces trois dernières années.

Je remercie Pascale d'avoir rendu ce travail de recherche extrêmement intéressant et agréable. Les connaissances scientifiques qu'elle m'a transmises, son soutien continu et son enthousiasme ont été une impulsion fondamentale qui m'as permis de conclure tres positivement cette experience de these. L'encadrement que j'ai reçu c'était une introduction idéale au monde de la recherche scientifique, et m'as données tous les outils necessaires pour en faire partie.

Je remercie Olivier, pour sa disponibilité, nos discussions stimulantes et sa volonté à faire face à de nouveaux défis scientifiques. Je remercie également Loïc et Daniel pour leurs conseils, leurs explications et leur énergie.

Je remercie Valérian et Niccolo qui m'ont introduit au travail expérimental et accompagné pendant une grande partie de mon parcours dans les laboratoires du C2N. Merci à Carlos, Juan et Guillaume, avec qui j'ai partagé mes journées dans le laboratoire, profitant de leur connaissance, énergie et assistance dans une ambiance amicale.

Je remercie Abdu, Aristide et Isabelle, pour les magnifiques dispositifs qu'ils ont réalisés et que j'ai eu la chance d'utiliser pendant ma thèse. Merci aussi aux nos collaborateurs de Grenoble, Bogdan et Alexia, et de Brisbane, Marcelo et Andrew, pour les échanges toujours constructifs. Merci à l'ensemble du C2N de m'avoir accueilli pendant cette période.

Je remercie beaucoup mes copains de bureau et toute l'équipe GOSS, pour tous les moments partagés au sein et en dehors du laboratoire. Ils m'ont permis de passer trois ans dans un ambiance très stimulant et amicale.

Enfin, je remercie infiniment mes parents, Graziella et Mario, pour leur accompagnement permanent, qui m'as donnee la motivation d'arriver jusqu'a ici.

Contents

Introduction

The development of quantum mechanics at the beginning of the 20th century marked a first quantum revolution. New concepts such as the energy quantization, the wave-particle duality and the uncertainty principle shed new light on the fundamental processes of nature and led to new discoveries such as the laser, the transistor or the GPS that have shaped today's technologies. However, the most subtle features of quantum mechanics, such as quantum coherence or entanglement have not yet been exploited in large scale applications. These are the main concepts that would allow for what is now called a "second" quantum revolution [1].

The beginning of the field of quantum technologies is marked by Feynman's conjecture, that the complexity of a quantum system can be efficiently simulated using a device which processes the information using the laws of quantum mechanics [2]. This has led to a wide research field focusing on the manipulation, storage and transfer of the information encoded in a quantum system. The simplest unit of such quantum information is a quantum bit, or qubit, which is a representation of a quantum mechanical two-level system. The fundamental difference with respect to a classical bit of information is in that a qubit can be prepared in a coherent superposition of states. A quantum computer is a system which allows the preparation, manipulation and readout of a large number of qubits to implement algorithms. The specific tasks that can be executed on a quantum computer can then benefit from a classically impossible parallel computation capability [3, 4]. A typical example, and one of the first quantum algorithms that have been introduced, is Shor's algorithm. It allows for the factorization of prime numbers with a time that scales polynomially with the number size, as opposed to the sub-exponential scaling that can be obtained using classical approaches [5].

The continuous developments in quantum information science has led to the evolution of new fields alongside quantum computation. Quantum simulation of complex physical systems do not necessarily require a quantum computer. It can be performed by engineering controllable quantum systems in order to reproduce the evolution of other systems, in problem-specific machines [6]. Quantum metrology aims at using nonclassical correlations of different quantum states to beat the classical limits of precision measurements [7]. Quantum communication is focused on the transfer of the quantum information and opened up new techniques for secure communication. The most important example is Quantum Key Distribution, which has already reached commercial availability, and offers a way to exchange cryptographic keys with absolute protection from eavesdroppers [8, 9].

Many different physical implementations to encode the quantum information are being explored, each having specific advantages to perform some tasks. Photons offers long range undisturbed transmission, atoms and ions long memory times and high gate fidelities, superconducting circuits reconfigurability and speed, defects in solids and semiconductor nanostructures integration and ease of operation, but this list is certainly not exhaustive. Few of them have shown the capability to manipulate more than a few qubits up to now. The best results have been obtained with trapped ions [10], followed by superconducting quantum bits [11] and photonic quantum systems [12]. While the number of entangled quantum bits is similar for the latters (in the 6 to 10 range), optical technologies are much less efficient and require key advancements for further scaling.

It is plausible that a complex quantum device such as a quantum computer will be eventually realized as a hybrid system, composed of multiple physical subsystems [13]. With this prospect, photons have gained a leading role not only for the possibility of all-optical quantum information processing, but also as ideal quantum information carriers to interconnect different physical systems. This idea is exemplified by the architecture for a quantum network, proposed by Kimble, where a grid of distant quantum nodes is interconnected by quantum channels. In each quantum node, the information can be locally processed, while an interface to travelling photons allows to distribute the quantum information across the network [14]. In the pursue of these objectives, a fundamental step is the scaling of photonic quantum technologies, which require efficient sources, detectors and two-photon gates. Commercially available superconducting nanowires detectors already show near unity efficiencies in a wide spectral range [15] and high temporal resolution. However, both quantum light sources and photon-photon gates remain very inefficient: currently available sources have intrinsically limited efficiencies of few percent and probabilistic two-photon gates have success rates below 15% [16].

Photonic quantum technologies would strongly benefit from highly efficient single-photon sources and deterministic photon-photon gates, and both can be obtained using the anharmonicity provided by an atomic transition [17]. A single atom, which can only scatter one photon at a time, can be used to build single-photon sources as well as condition the transmission of a photon upon the absorption of another. To obtain such sources and gates in an efficient way, each photon sent on the system should interact with the atom and symmetrically the atom should radiate in a well-defined optical mode. This situation is called the one-dimensional atom [18], and can be obtained by controlling the spontaneous emission process of the emitter using cavities [19, 20] or one-dimensional waveguides [21, 22]. Such approach is pursued in the optical domain for atoms [23], ions [24] and solid-state emitters [25, 20, 26].

Among the different emitters studied in the solid-state, quantum dots (QDs) behave excellently as artificial atoms [27]. They can be used as quantum light sources [28, 29], they shows single photon sensitivity [30] and the spin of a single charge carrier in the QD can be used as a stationary qubit and can be optically manipulated [31]. They are ideal candidates to implement many quantum functionalities with semiconductor systems, and have already allowed to demonstrate spin-photon [32, 33, 34] or spin-spin distant entanglement [35]. Moreover, they can rely on the well-established III-V semiconductor nano-fabrication techniques, providing a viable way for the scalable fabrication of quantum devices. In particular, it is possible to couple QDs to many different photonic structures, such as microcavities [21], waveguides [25], plasmonic resonators [36] and microlenses [37], etc. This is a crucial step to make all the quantum operations efficient and compatible with large scale applications.

This thesis work has been developed in the group of Prof. Pascale Senellart at Centre for Nanoscience and Nanotechnology (C2N/CNRS). The group activity is centred on the developing of quantum devices based on single QDs in Cavity QED (CQED) systems. The research team has developed a novel technology in 2008, called in-situ optical lithography [38], that allows for the deterministic and scalable fabrication of CQED devices made by a single QD coupled to a micropillar cavity. The technique allows operation both in the weak and in the strong coupling regimes [38, 39]. Using this technique, an ultrabright source of entangled photon pairs has been fabricated in 2010 [40]. In 2013, during the thesis work of O. Gazzano, the QD-micropillar devices have been demonstrated to be bright sources of single photons with indistinguishabilities in the 70 % to 90 % range [41] and were used to implement a first Controlled NOT gate [42]. The quantum interference between photons generated by two distant sources was the first achievement of the thesis of V. Giesz in 2015 [43]. However, while the source performances were state-of-the-art, the indistinguishability was not high enough to allow for advanced optical quantum protocols. In 2014-2015, during the post-doctoral fellowship of Anna Nowak and Niccolo Somaschi, an electrical control was introduced on the device that allowed for strongly suppressing charge noise [20].

I joined the team in 2014, and during my first year, I worked with V. Giesz and N. Somaschi on the study of the new generation of devices as single-photon sources. We were able to demonstrate that the latest generation of sources could combine both high efficiency and near perfect indistinguishability [44]. In a sec-

ond part of my thesis, I used one of these sources to study path entangled NOON states, a special type of entangled states that are key resources for quantum sensing and quantum metrology. However, their full quantum characterization had been scarcely addressed. In a first step, working in collaboration with O. Krebs, I theoretically proposed a new approach to perform the full quantum tomography of path encoded NOON states. In a second step, I experimentally implemented this new protocol for the case of N=2 photons [45].
In the last part of my thesis, I investigated the performances of the quantum dot-cavity devices for the implementation of non-linear photon-photon gate. I could show that the device shows a non-linearity at the single photon level and performs as an efficient single photon filter [46]. These observations are a key step toward the realization of efficient photon-photon gates in the solid-state.

This manuscript is organized as follows:
In Chapter 1, the fundamentals properties of semiconductor quantum dots are presented, discussing the potential and limitations of these artificial atoms, limitations arising from their coupling to the environment. We then briefly present the basics of cavity quantum electrodynamics and discuss how it can be used to mitigate the effect of the environment. We then detail the system under study, namely a quantum dot in a micropillar cavity and derive its figure of merits. After briefly describing the technological process used to fabricate the devices studied during this thesis, we show that these last generation of quantum dot-micropillar devices provide a close-to-ideal light-matter interface.
In Chapter 2, the devices are studied as single-photon sources. After introducing the metrics used to describe a single-photon source and briefly presenting the state of the art at the beginning of this work, we study the sources under various excitation schemes. We show that the sources show a record brightness with an extremely high photon indistinguishability.
In Chapter 3, we study path entangled NOON states, that are key resources for interferometric based metrology applications. After reviewing the state of the art, we theoretically propose a new technique to characterize path encoded NOON states. We then present our experimental implementation of the protocol and use it to measure a two-photon NOON state generated with a quantum dot source. We show how an overcomplete tomography approach allows for an improved state characterization and briefly discuss how to extend our protocol to an arbitrary number of photons N.
In Chapter 4, we study the quantum dot-cavity system as a non-linear device. We perform reflectivity measurements using an attenuated coherent beam and evidence a non-linearity behaviour at the scale of less than one per pulse. We then analyse the photon statistic of the reflected field and show that our device efficiently convert a coherent field into a quantum one, where 2 and 3 photon components are efficiently suppressed.
Finally, in Chapter 5, we briefly conclude and draw perspectives for this work.

Chapter 1

Fundamentals of Quantum Dots in micropillar cavities

Single atoms and single photons are ideally suited to implements quantum bits (qubits). The former can be employed as stationary qubits to store and manipulate the information, while the latter as flying qubits, for the transfer of the information. A long standing goal for the field of quantum information science is the realization of a quantum network, where multiple stationary quantum nodes are interconnected by quantum channels, allowing the distribution of the quantum information among distant partners. A critical issue is then the realization of a quantum interface between an atom and a photon. Such an interface must be efficient and coherent, allowing the transfer of qubits in a deterministic and reversible way [14].

Natural atoms provide ideal qubit systems which can be optically accessed, and have been used to demonstrate different quantum functionalities [14]. However they are also challenging to trap, prepare and manipulate. Solid-state confined systems behaving as artificial atoms, among which are semiconductors Quantum Dots (QDs), have emerged as promising candidates to realize qubit systems which are scalable and can be integrated into micrometer-sized devices [47, 48]. The main challenges are to isolate them from the detrimental effects coming from the solid-state environment and to realize efficient interactions with light. A fundamental tool towards this goal is given by Cavity Quantum Electrodynamics, which allows to control the light-matter interaction at the single photon level using solid-state cavities [49, 21].

This Chapter explains how we can obtain an efficient interface between an individual optical transition of a QD and a photon. In Section 1.1, we discuss the behaviour of a QD as an artificial atom. In Section 1.2, we see how it can be efficiently interfaced to a photon by coupling it into a micopillar cavity. In Section 1.3, we present the deterministic fabrication of a QD-micropillar device, and the quality of the light-matter interface it can provide. These devices are used all along this manuscript to generate and manipulate single photons.

1.1 A single quantum dot as an artificial atoms

A semiconductor Quantum Dot (QD) is a confined island of a lower bandgap material embedded in a higher bandgap material. The spatial confinement in all the three directions of space gives rise to a zero-dimensional structure where the charge carriers are confined. The resulting discrete energy levels and very sharp optical transitions allow to obtain optical and electronic properties analogous to the ones of natural atoms. For these reasons QDs, as other defect centres in the solid-state, are often called artificial atoms [48]. In the following, we analyse the extent and limitations of such similarity.

1.1.1 Fabrication of self-assembled QDs

The QDs used in this work are InGaAs QDs fabricated using the Stranski – Krastanov growth. This method is based on a strain relaxation mechanism in an heterostructure which leads to the formation of islands of material in an otherwise 2-dimensional growth process [50, 51].

The fabrication begins with the layer-by-layer deposition of InAs (having a bandgap of E_g =0.36 eV at 300 K) on a GaAs substrate (having E_g =1.42 eV at 300 K). Since the two materials have different lattice constants (about 7%), noticeable strain builds up during the deposition. At a critical thickness of the InAs (about 1.7 monolayers), the nucleation of InAs aggregates becomes energetically favourable and further growth happens in forms of 3-dimensional lenses. As a result, one obtains a thin layer of InAs over which is found a random distribution, both in size and position, of InAs islands [52, 53]. The fabrication is then completed with a capping layer of GaAs, to enclose the structures. The resulting islands constitute the optically active QDs [27, 54]. In this work, after the growth, the QDs are annealed at high temperature (850–950°) to adjust their energy. The exposure to high temperatures cause an interdiffusion of elements which leads to a variable mixing of GaAs and InAs materials in the QDs. As a result their potential barrier, with respect to the bulk GaAs, is lowered. The annealing step also affects the shape of the QDs, and leads to a more homogeneous shape distribution in the fabricated sample and an overall larger size.

The specific properties of the produced InGaAs QDs strongly depends on the fabrication conditions. In general, they shows a pyramidal shape largely elongated in the lateral direction, with a typical diameter of 10 to 20 nm and an height of about 3 nm [55]. An Atomic Force Microscope image of an uncapped sample is shown in Fig.1.1.a, where the random spatial and size distribution is clearly visible. Their size variation is responsible for a relatively large inhomogeneous broadening of 30–50 meV. Typical QD density can vary from $10\mu\mathrm{m}^{-2}$ to $500\mu\mathrm{m}^{-2}$. The residual layer of InAs is called wetting layer. Here the carriers are confined only along the growth direction, thus it is effectively a 2-dimensional quantum well. The wetting later presents a bandgap around about 1.45 eV,

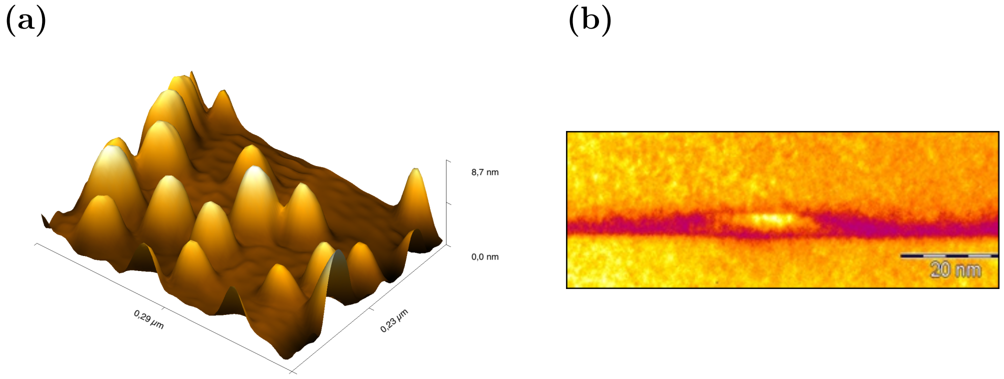

Figure 1.1 – (a) Atomic Force Microscope image of the self-assembled layer of QDs before the deposition of the capping material. (b) Transmission Electron Microscope image of a single InGaAs QD embedded into GaAs material. Image measured by A. Lemaitre and C. Gomez at C2N.

corresponding to a photon wavelength of 855 nm, while the energy levels inside the QDs are typically around 1.34 eV, corresponding to a photon wavelength of 925nm. A Transmission Electron Microscopy of a single QD is shown in Fig.1.1.b, where we can see both the QD and the underlying wetting layer.

1.1.2 Energy levels

The precise calculation of the electronic states of a QD require to consider the specific type and shape of the investigated QDs and is the subject of a wide field of research [56]. Nonetheless, the energy levels of a QD relevant for quantum optics experiments can be roughly estimated using the effective mass approximation and considering a single conduction and a single valence band [21]. Moreover, for the small self-assembled QD, the levels are mainly determined by the confinement, while the carriers interactions can be introduced perturbatively. In the following, we review the different contributions which determine the QD levels.

Quantum confinement A very rough and qualitative understanding of the electronic states in a QD can be obtained considering the ideal situation of a particle in a box. When the dimensions of the system approaches the de Broglie wavelength defined by the effective mass of the charge carriers in the material, quantum confinement effects becomes visible. This mechanism creates discrete states for both the electron and holes inside the InGaAs QDs [57].

In the effective mass approximation, the electron and holes are confined in the QD by the discontinuity in the bandgap between the InAs material and the surrounding GaAs. In a crude approximation, we can consider a 3 dimensional infinite potential well, where the x and y axis define the in-plane section of the

QD while the z axis define the vertical growth direction. The energy of the discrete levels for the carriers are then given roughly by:

$$E_{e/h} = \frac{\hbar^2\pi^2}{2m^*_{e/h}}\left(\frac{n_x^2}{L_x^2} + \frac{n_y^2}{L_y^2} + \frac{n_z^2}{L_z^2}\right) \tag{1.1}$$

As shown in the previous section, the shape of the QD is highly flattened in the in-plane section, with a much smaller height in the growth direction. In reality, the finite barrier height in the z direction leads to a single $n_z = 1$ confined state. The growth direction then is the main quantization axis [58, 59]. This has also the effect of splitting the hole band degeneracy. The lower energy interband optical transitions are between the conduction and the heavy hole band, hence the light hole are neglected in the following [21].

The discrete levels arising from the in-plane confinement have typical spacings of tens of meV. Under non-resonant excitation at 10 K, the thermalization of high energy carriers to the lowest energy state is much faster (<50 ps) than the radiative recombination time ($\approx$ 1 ns). Thus considering only the lowest energy state for the carriers also for the in-plane quantization axis is sufficient to explain most of the observed optical transitions at low excitation power and low temperature.

The resulting levels for the charge carriers in the QD, which can be filled according to the Pauli exclusion principle, are represented in Fig.1.2. Beside the energy of the free particles and the confining potential, the interaction between carriers must also be taken into account to correctly identify the QD states. This is detailed in the rest of the section.

Direct Coulomb interaction Two charge carriers q_i and q_j in the semiconductor, at positions r_i and r_j, will be subject to the Coulomb interaction given by:

$$V_{ij}(\mathbf{r}_i, \mathbf{r}_j) = \frac{1}{4\pi\epsilon_r\epsilon_0}\frac{q_i q_j}{|\mathbf{r}_i - \mathbf{r}_j|} \tag{1.2}$$

When the QD is populated by an electron and a hole, the attractive Coulomb interaction between the two particles lowers the energy of the system. The resulting bound state which is formed is called exciton (X), whose energy E_X is lower than the sum of a confined electron and hole energies alone. As opposite to a bulk crystal however, for the self-assembled InGaAs QDs, the energy levels are mainly defined by the spatial confinement of the carriers, as the QD size is typically smaller than the exciton radius in bulk semiconductor. Considering a particle in a box model, the energy spacing between the discrete levels is proportional to $1/R^2$ with the size R of the potential well, while the Coulomb interaction goes as $1/R$ with the distance R between the charges. For a small QD then the dominant mechanism is the quantum confinement, while the exciton binding energy is a perturbative correction factor [60]. The typical energy shift

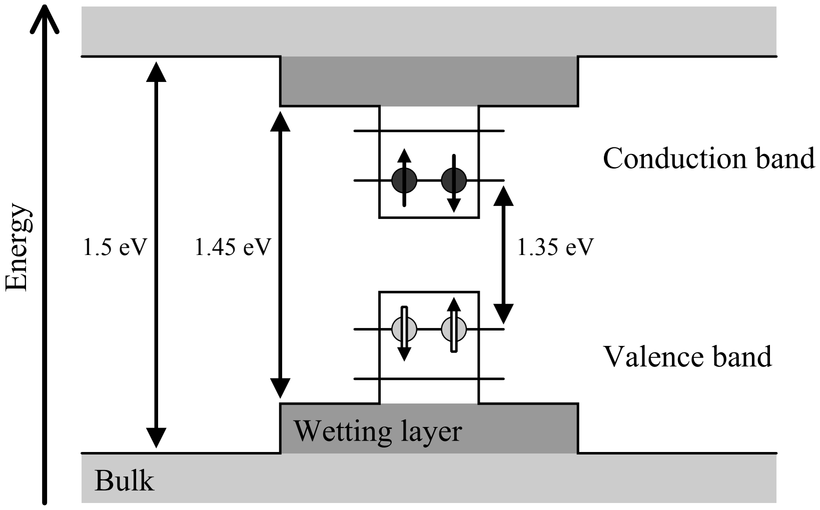

Figure 1.2 – Representation of the energy level structure of non-interacting charges in the InGaAs QD and in the surrounding material (InAs wetting layer and GaAs bulk). The lowest energy state of the QD can be filled by electron and holes according to the Pauli exclusion principle.

from the direct Coulomb interaction for the fundamental electron-hole state is about 20 meV.

Exchange Coulomb interaction The exchange interaction arises from the fermionic statistics of electrons and holes, and effectively couples the spins of the overlapping particles. It is responsible for the fine structure of the exciton levels [61]. We only consider heavy holes and electrons to build the exciton states. Heavy holes have an angular momentum component along the main quantization axis (the growth direction) of $J_{\mathrm{h,z}} = \pm 3/2$, while for the electrons is $S_{\mathrm{e,z}} = \pm 1/2$ [62]. As a result there are four possible exciton states having total angular momentum ±1 or ±2:

$$\begin{aligned}
|{+1}\rangle &= |{\Uparrow\downarrow}\rangle = |{+3/2}, -1/2\rangle \\
|{-1}\rangle &= |{\Downarrow\uparrow}\rangle = |{-3/2}, +1/2\rangle \\
|{+2}\rangle &= |{\Uparrow\uparrow}\rangle = |{+3/2}, +1/2\rangle \\
|{-2}\rangle &= |{\Downarrow\downarrow}\rangle = |{-3/2}, -1/2\rangle
\end{aligned}$$

which, in the absence of the exchange interaction, are degenerate. Only the states having a total angular momentum of ±1 have dipole allowed transition to the ground state of the QD, which has zero angular momentum. These two transitions are coupled to left $|L\rangle$ and right $|R\rangle$ circular photons, having momentum along the propagation direction of -1 and $+1$. On the contrary, the

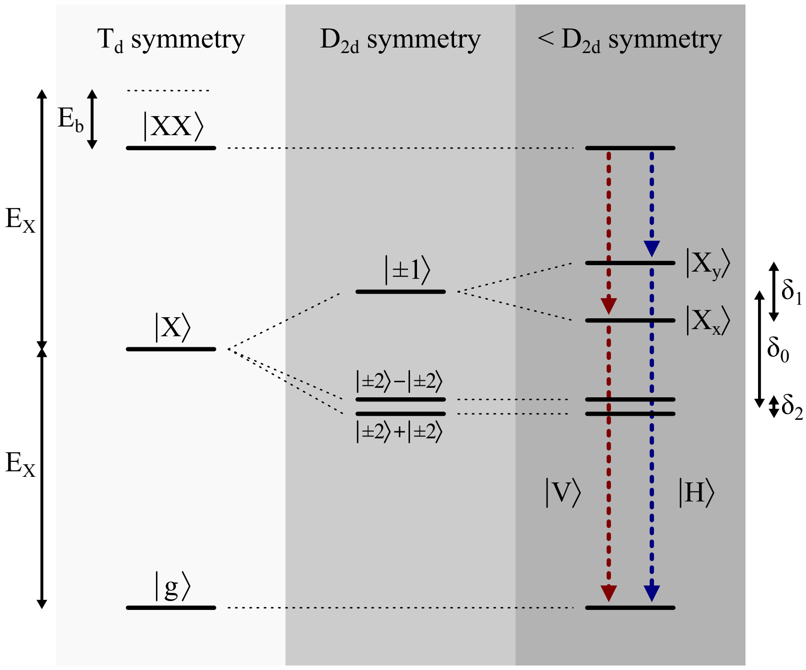

Figure 1.3 – Level structure for the single exciton (X) and biexciton (XX) states in the QD for decreasing degree of point-group symmetry. T_d is the tetrahedral point symmetry of the bulk semiconductor, D_{2d} is the symmetry resulting from the z-confinement only, $< D_{2d}$ is without in-plane symmetry of the QD [58].

states having total angular momentum ±2 are not optically active due to the impossibility of momentum conservation. For this reason $|\pm 1\rangle$ are called bright excitons and $|\pm 2\rangle$ are called dark excitons. The short range part of the exchange interaction between an electron with spin S_e and a hole with spin J_h composing the exciton can be written as [62]:

$$H_{\text{exchange}} = -\sum_{i=\text{x,y,z}} \left(a_i J_{\text{h},i} \cdot S_{\text{e},i} + b_i J^3_{\text{h},i} \cdot S_{\text{e},i} \right) \tag{1.3}$$

where a_i and b_i are the spins coupling constants along each axis, and the z axis corresponds to the growth direction, while x and y corresponds to the in-plane axis of the QD. Using the basis given by the four eigenstate of the total angular momentum of the exciton ($|+1\rangle$,$|-1\rangle$,$|+2\rangle$,$|-2\rangle$), we can write the exchange interaction Hamiltonian for the exciton in the matrix form [62]:

$$H_{\text{exchange}} = \frac{1}{2} \begin{pmatrix} \delta_0 & \delta_1 & 0 & 0 \\ \delta_1 & \delta_0 & 0 & 0 \\ 0 & 0 & -\delta_0 & \delta_2 \\ 0 & 0 & \delta_2 & -\delta_0 \end{pmatrix} \tag{1.4}$$

where $\delta_0 = -3/4(a_z + 9/4b_z)$, $\delta_1 = 3/8(b_x - b_y)$ and $\delta_2 = 3/8(b_x + b_y)$. From the block-diagonal form of this matrix, we can see that the bright and dark exciton states do not mix, but they are split in energy by δ_0, which has a typical value of 500 μeV. On the contrary, state mixing happens in each angular momentum subspace, and the degeneracy of the bright and dark excitons is lifted respectively by δ_1 and δ_2. Typically δ_1 is in the range of 10–100 μeV while δ_2 of 1 μeV [21]. The observed fine structure is represented in Fig.1.3. Focusing on the bright excitons states, the two eigenstates of the exchange hamiltonian become $|\mathrm{X}_x\rangle = (|{+1}\rangle + |{-1}\rangle)/\sqrt{2}$ and $|\mathrm{X}_y\rangle = (|{+1}\rangle - |{-1}\rangle)/\sqrt{2}$, which are split in energy by δ_1, commonly called Fine Structure Splitting (FSS) of the exciton. The two exciton states $|\mathrm{X}_{x/y}\rangle$ are now coupled by two linearly polarized photons $|H\rangle = (|R\rangle + |L\rangle)/\sqrt{2}$ and $|V\rangle = (|R\rangle - |L\rangle)/\sqrt{2}$ to the ground state. This FSS is detrimental for the generation of entangled photon pairs as discussed in the next paragraph. Having $\delta_1 = 3/8(b_x - b_y)$, the splitting vanishes when the x and y axis are equivalent. Thus, if the QD has in-plane rotational symmetry the degeneracy of the bright exciton can be restored. Different techniques have been explored to reduce the exciton Fine Structure Splitting in order to obtain polarization entangled photons, using electric field [63], strain [64] and Purcell broadening of the transitions [40]. In this work we use an annealing step that reduces the anisotropy of the QDs, and we typically have a small but finite FSS around 3–15 μeV.

Multiparticle states Multiple charges can be trapped inside a single QD, leading to more complex contributions to the Coulomb interaction.

When two electron-hole pairs are trapped into a QD, a biexciton state (XX) is formed. The energy of the biexction $E_{\mathrm{XX}} = 2E_{\mathrm{X}} - E_{\mathrm{b}}$ differs from the energy of two uncorrelated excitons $2E_{\mathrm{X}}$ by a binding energy E_{b} due to the Coulomb interaction between the carriers, as represented in Fig.1.3. This binding energy is often found to be positive, implying an attractive interaction between the two pairs, with a magnitude of few meV [56]. The radiative recombination of an electron-hole pair of the biexciton leads to the emission of a photon and leaves the QD in a neutral exciton state. The photon emitted by the biexciton will have an energy different from that of the exciton, by an amount given by the Coulomb energy E_{b}. This allows to spectrally discriminate the two transitions. The polarization of the emitted photon instead is determined by the X state to which the XX state is decaying. In the biexciton state, the s-shell of the QD is fully occupied according to the Pauli exclusion principle. The biexciton thus is in a spin singlet state, which can be written as $|{\Uparrow\Downarrow\uparrow\downarrow}\rangle$. It can radiatively decay into one of the two bright exciton states, which then sequentially decay to the QD ground state (see Fig.1.3). These two transitions are linearly polarized according to the intermediated X state. For a vanishing FSS of the exciton, the biexciton-exciton cascade can be used as a source of entangled photon pairs [65]. In this case the which-path information of the two possible decay sequence is erased, and polarization entangled photons are generated [66, 67, 68, 69].

When a single additional charge is introduced in the QD beside an exciton, a charge exciton state (CX), called trion, is formed. A negative trion is made by two electron and a hole, while a positive trion is made by two holes and one electron. The state of the two carriers of the same species must be antisymmetrized into a singlet state, being fermionic particles [21]. This effectively cancels out the exchange interaction. The CX is a bound state whose energy differs from the sum of the neutral exciton plus the single charge energy. This difference is due to the Coulomb energy whose sign and magnitude depends on the QD size and shape, but has typical values of few meV [56]. As a consequence, the radiative recombination of an electron-hole pair from the CX will produce a photon with different energy from the energy of the neutral exciton one. Once radiatively decayed, the trion leaves the QD in a charged state with a single residual electron or hole [70, 71]. The spin of this residual carrier can be used as a stationary qubit, which can be optically manipulated and measured [72, 73, 74].

1.1.3 Optical properties

In the effective mass approximation, the optical transitions are determined by the creation and the destruction of electron-hole pairs. As in a QD the pair exists in a bound state, the exciton, the optical transitions are defined by the excitonic states. We have seen that the presence of additional pairs introduce additional Coulomb potentials, changing the transition energies for each additional pair. This creates an anharmonic energy spectrum which can be used to isolate and optically address specific transitions. An empty QD can absorb a photon of energy E_{X} which creates an exciton. Once the QD contains an exciton it cannot absorb a second photon of energy E_{X}, but only a photon of energy $E_{\mathrm{XX}} - E_{\mathrm{X}}$. Symmetrically, when the QD is populated with a biexciton and an electron-hole pair radiatively recombine, a photon of energy $E_{\mathrm{XX}} - E_{\mathrm{X}}$ is emitted, and the QD is left with an exciton state. The decay of the exciton leads to the emission of a photon of energy E_{X} [56]. This process is represented in Fig.1.4.a. Multiple electron-hole pairs then recombine in a sequential way giving rise to a radiative cascade [75], where each step produces a photon of different energy. Similarly, the presence of a single additional charge in the QD leads to different energies for the optical transitions of charged excitons.

A typical photoluminescence spectrum from a QD in a planar cavity is shown in Fig.1.4.b. Here the excitation energy of the laser is higher than the bandgap of the GaAs. As a consequence multiple carriers are created in the bulk material and are randomly captured into the QD, filling up various energy levels. The radiative cascade and individual electron or hole capture leads to the appearance of multiple emission lines, which can be attributed to the XX, CX and X states. In an ideal situation, each line emits a single photon arising from an individual electron-hole recombination process. To identify the emission lines different

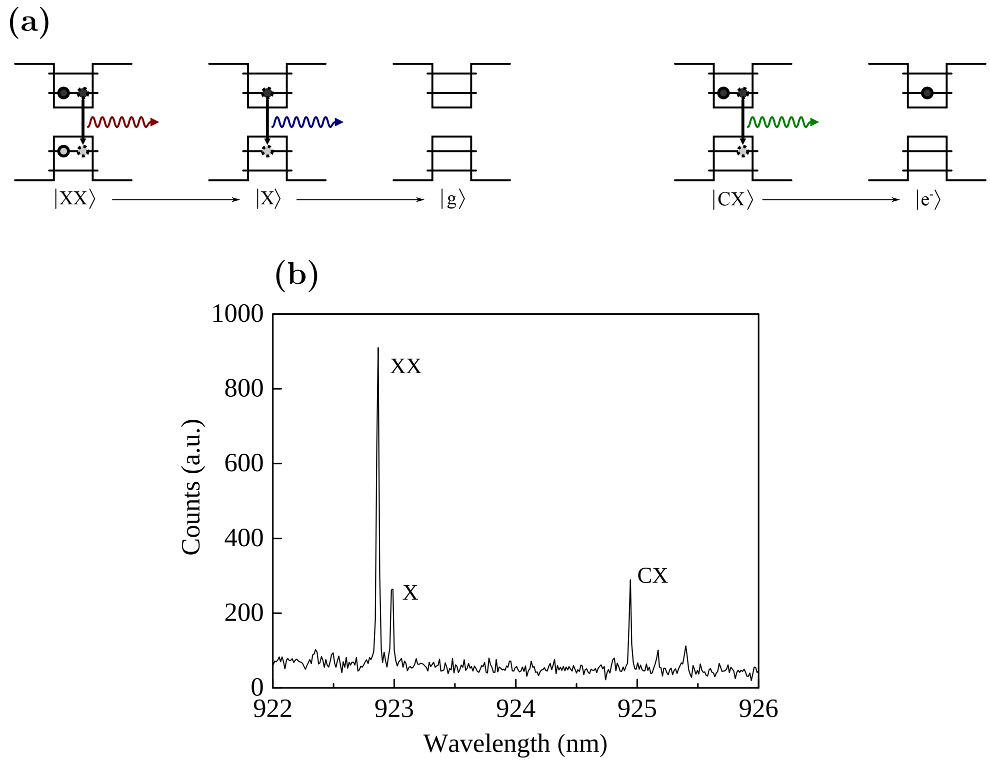

Figure 1.4 – (a) Radiative cascade in the QD. The right part shows the sequential recombination of a biexciton and an exciton state to the QD ground state. The left part shows the recombination of a negative trion, leaving a single resident electron in the QD. Each step generates a photon of different energy. (b) Typical spectra from a QD in a planar cavity. The emission from the recombination of the different states can be spectrally discriminated.

techniques can be used: power dependence of the emission intensity [76], correlations measurements [77] and study of the fine structure of the transitions in magnetic fields [78, 79].

By fixing the energy and the polarization of the excitation laser to correspond to a specific transition, such as the exciton one, is possible to study and manipulate a single two-level system. More details on the different excitation techniques of a QD are given in Section 2.4. In the following we analyse the spontaneous emission process from a QD and how it is affected by the semiconductor environment. In particular, we focus on the neutral exciton transition, which is the one studied in this thesis work.

Spontaneous emission We consider the radiative decay of an exciton state, which can be viewed as a two-level atom, in an homogeneous medium constituted by the GaAs embedding the QD. The full quantum treatment of the spontaneous emission process was first given by Weisskopf and Wigner [80]. With a more general approach, we can consider this problem as the coupling of a discrete state to a quasi-continuum of states by a constant perturbation. Solving this standard quantum mechanics problem, it is found that the occupation probability for the initial state of the system follows an exponential decay [1], whose transition rate can be calculated using the Fermi golden rule [84], given by:

$$\Gamma_{i\to f} = \frac{2\pi}{\hbar} \left|\langle f| H_i |i\rangle\right|^2 \rho(E_f) \tag{1.5}$$

The radiative decay of an exciton is given by the transition of an electron from a conduction band state $|\psi_c\rangle$ to a valence band state $|\psi_v\rangle$. In the dipole approximation, the interaction is given by the dipole hamiltonian $H_i = -\hat{\mathbf{d}} \cdot \hat{\mathbf{E}}$, and the relevant matrix element can be calculated as:

$$| \langle\psi_v| - \hat{\mathbf{d}} \cdot \hat{\mathbf{E}} |\psi_c\rangle | = \sqrt{\frac{\hbar\omega_0}{2\epsilon_0 V}}\mathbf{d}_{\mathrm{ge}} \tag{1.6}$$

where $\mathbf{d}_{\mathrm{ge}} = \langle\psi_v| \mathbf{d}_{\mathrm{ge}} |\psi_c\rangle$ is the dipole moment of the exciton transition. The final density of states in an homogeneous medium having an index of refraction n is given by:

$$\rho(E) = \frac{n\omega_0^2 V}{\pi^2 \hbar c^3} \tag{1.7}$$

Substituting these two into Eq.1.5, we can retrieve the spontaneous emission rate as:

$$\gamma_{\mathrm{sp}} = \frac{n\omega_0^3}{3\pi\epsilon_0\hbar c^3}|\mathbf{d}_{\mathrm{ge}}|^2 \tag{1.8}$$

This defines the radiative lifetime $T_1 = (\gamma_{\mathrm{sp}})^{-1}$ of the exciton. The exponential decay of the population will accordingly generate an exponentially decaying photon wave packet having a time constant T_1. For a large variety of InGaAs QD in bulk GaAs, a decay time of $T_1 = 0.8$–1.3 ns is typically observed. The spectral profile of the emission is a Lorentzian peak having a width γ_{sp} and the generated radiation state, starting from the initial exciton state, can be written as:

$$|\psi\rangle = \sum_{\mathbf{k},\epsilon} g_{\mathbf{k},\epsilon} \frac{e^{-i\omega_{\mathbf{k}} t}}{(\omega_{\mathbf{k}} - \omega_0) + i\gamma_{\mathrm{sp}}/2} \hat{a}^\dagger_{\mathbf{k},\epsilon} |0\rangle \tag{1.9}$$

which identifies a pure single photon state [84]. The spatial distribution of the photon instead is determined by the dipole moment orientation. The spontaneous emission rate γ_{sp} is often expressed in terms of the oscillator strength $f = \frac{2\mathbf{d}_{\mathrm{ge}}}{\hbar\omega_0 m_0}$, a dimensionless quantity describing the strength of the optical transition [21].

---

[1] The constant transition rate obtained with the Fermi golden rule is an approximation valid at intermediate times. The decay of the initial state is slower than exponential at very short and very long timescales, but this small correction can often be neglected [81, 82, 83].

In the following we neglect the possibility for the exciton to recombine non-radiatively. In general however this must be considered as it decreases the efficiency of the transition and influence the decay dynamics. The strength of the radiative decay channel Γ_{rad} to the non-radiative one Γ_{nrad} is quantified by the quantum efficiency $\mathrm{QE} = \Gamma_{\mathrm{rad}}/(\Gamma_{\mathrm{rad}}+\Gamma_{\mathrm{nrad}})$. The quantum efficiency is typically very high in InGaAs QDs, with reported values above 0.9 [85, 86].

However, we consider here two limitations of this spontaneous emission process in the perspective of developing efficient quantum devices, which affect the spatial and spectral profile of the emitted photons. The first fundamental limitation is due to the fact that such emitter is coupled to a final density of state for the electromagnetic field which is almost isotropic. As a consequence, there will be a very small probability of collecting the emitted photons within a given numerical aperture. The efficiency of a source built from a single InGaAs QD in bulk GaAs is lower than 1% [25]. Symmetrically, the probability of interaction between the QD and the photons used to excite is very small, since diffraction effects preclude the focusing the incident light at the nanometre scale of the QD. The interface between such two-level system and a spatially localized optical mode is then highly inefficient.

The second limitation is coming from the fact that, being embedded in a solid-state environment, the excitonic states of a QD are inevitably coupled to the mechanical and electromagnetic degrees of freedom of the host material. Different mechanisms can limit the coherence of the QD state, which also affects the emission properties. In the ideal case, the loss of coherence of the exciton state is due to a decay of the population: the exciton state is destroyed along with the creation of a photon, which happens at a timescale given by the radiative lifetime T_1. In this case T_1 defines both the temporal duration of the photons and their bandwidth. The coherence of the exciton, however, can also be destroyed without loss of population. This process, called dephasing, is due to uncontrolled interactions with the environment, leading to the loss of the information about the phase of the quantum state. When this is faster than the radiative recombination, the photon will not inherit the initial coherence of the exciton, and is described by a statistical mixture. In this case, while the temporal duration of the photons is always given by T_1, their bandwidth is determined by the coherence time T_2 over which the phase coherence is preserved. A simple modelling of this dephasing is a coupling to a Markovian reservoir which projects at random times the optical transition to its excited or ground state [87]. This leads to an exponential decay of the phase coherence with a typical time of T_2^* called pure dephasing time. The total coherence time T_2 of the transition is thus given by [88]:

$$\frac{1}{T_2} = \frac{1}{2T_1} + \frac{1}{T_2^*} \tag{1.10}$$

or equivalently, for a QD in the bulk, the total dephasing rate γ is:

$$\gamma = \frac{\gamma_{\mathrm{sp}}}{2} + \gamma^* \tag{1.11}$$

where the factor of two comes from the fact that γ^* is the damping rate of the phase amplitude, while γ_{sp} is the damping rate of the populations [62]. The bandwidth of the emitted photons is thus determined by γ. If there is a non-negligible pure dephasing γ^*, the observed linewidth of the transitions are larger than what expected from the radiative lifetime of the excited state.

Many sources of decoherence cannot be modeled as the coupling to Markovian reservoir, resulting in the simple model of pure dephasing. In the following paragraphs, we describe the effect of the two main environmental effects affecting the optical transitions of a QD: coupling to phonons and electric and magnetic noise.

Coupling to phonons The states of the charge carriers in the QD are affected by the strain potential in the host material, so that carriers interact with the phonon modes of the structure. In particular, the coupling to acoustic phonons is identified as the main source of decoherence for the QD states [89, 90, 91]. This affects the optical transitions of the QD through two different processes.

The first effect is due to elastic exciton-phonon scattering, producing an incoherent broadening of the Lorentzian spectrum of the isolated exciton transition, called Zero Phonon Line (ZPL). It can be explained by virtual transitions to higher excited states of the exciton, assisted by phonons, which returns to the same initial exciton state [92, 93]. This introduce a loss of phase coherence without any damping of the exciton population. In this condition, the observed width of the ZPL is no longer determined solely by the radiative lifetime of the exciton, but is broadened by this pure dephasing effect.

The second effect is due to inelastic exciton-phonon scattering, which leads to the radiative decay of the exciton assisted by phonons [94, 95, 96]. As a result the exciton recombination can be associated with the absorption (anti-Stokes process) or emission (Stokes process) of an integer number of phonons, thus the energy of the emitted photon is lowered or increased to conserve the total energy of the system. The spectrum of the isolated exciton transition is then modified as shown in Fig.1.5. The sharp ZPL is surrounded by two broadband incoherent phonon sidebands (PSBs). The PSBs represents the photon emitted altogether with the emission of phonons (low energy side of the ZPL) or absorption of phonons (high energy side of the ZPL). At low temperature, this happens on a timescale of tens of picoseconds [97, 98]. At high temperature, the process is more efficient and most of the emission happens in the PSB. By lowering the temperature it is possible to decrease the contribution from the PSB, thus increase the strength of the ZPL, thanks to the lowered phonon population in the material. However, as we can see from Fig.1.5, even at zero temperature the low energy side of the PSB is present because phonon emission is still possible.

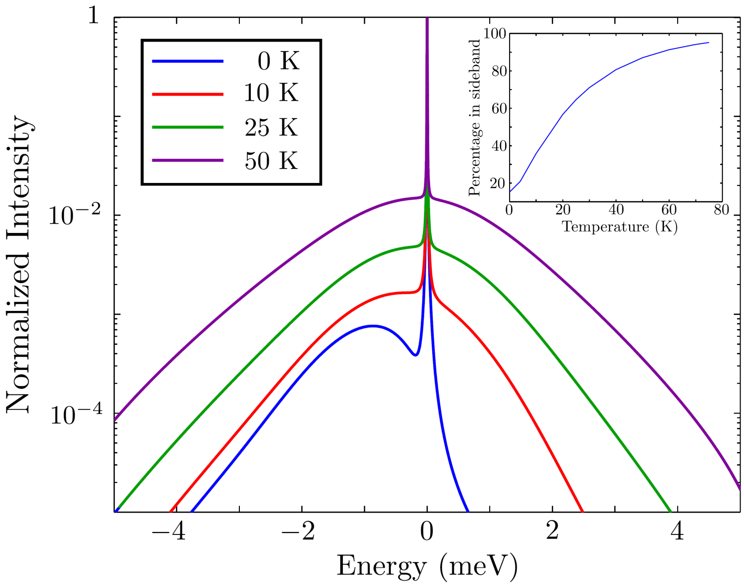

Figure 1.5 – Figure from [21]. Normalized emission spectrum from a QD coupled to a longitudinal acoustic phonon reservoir at different temperatures. The inset shows the fraction of emission into the phonon sidebands.

We see that the coupling of excitons to the phonon bath reduces the coherence of the QD states [99]. This draws a limitation on the similarity with the atom-like behaviour of this solid-state system. To partially overcome the effects described above, low temperature operation as well as spectral filtering of the ZPL is required [100, 101, 102].

Charge and spin noise The carriers in the QD are also coupled to static electric and magnetic fields [56]. In controlled conditions, these fields are important tools to manipulate the QD states. An external electrical field $\mathbf{F}$ introduce an additional potential $V_{\mathrm{F}} = -q\mathbf{F} \cdot \mathbf{r}$, which shifts the electron and hole states respectively to lower and higher energies. This leads to the quantum confined Stark effect, where the transition energies of all the QD states are lowered [103, 104]. In this work, the Stark shift is used to adjust the spectral position of the exciton state to be in exact resonance with the optical mode of the surrounding micropillar cavity, as will be detailed later. The same effect has also been used to control the FSS of the exciton [63]. An external magnetic field $\mathbf{B}$, instead, introduces an additional potential $V_{\mathrm{B}} = -\mu \cdot \mathbf{B}$ which couples to the magnetic moment of each charge carrier and thus depends on the total angular momentum of the electrons and holes. The resulting Zeeman effect allows lifting the degeneracy of the QD states and control their splitting. It is useful not only to study the symmetries of the QD states, but also to exploit spin-selective transitions to interface an external photon with the spin of a charge carrier [73].

The semiconducting environment in which the QD is built however, introduces an uncontrolled electrical and magnetic noise, which can affect the optical transitions through both spectral wandering and dephasing phenomena. Electrical noise arises from fluctuations in the charge carriers distribution, which result in a fluctuating electric field at the QD location. This produces a random Stark shift, with typical times of μs. The wave packets emitted at different times have different central energies, which broadens the transition linewidth observed at above μs time scale [105]. Magnetic noise is due to fluctuations in the nuclear spins of the semiconductor material. This also causes fluctuation of the exciton and trion spectral position that takes place at μs time scale as well [105].

Gated structures has been shown to be effective in suppressing the charge noise. Radiatively limited linewidth have been reported in doped structure, where the residual noise is happening at long timescale with respect to typical radiative recombination times of the excitons [106, 107].

From the above discussion, we can see that the presence of phonons and noise in the environment limits the performances of QDs as artificial atoms. Using the Eq.1.10, we can quantify the coherence of the optical transition through the ratio $\frac{T_2}{2T_1}$. In the ideal situation T_2 is given by $2T_1$ and this ratio is unity. The presence of a fast pure dephasing time T_2^* reduces this ratio. To restore the coherence of the optical transitions, two strategies can be employed. Controlling the semiconductor environment so as to reduce the dephasing effects allows to increase T_2^*, making its contribution to T_2 negligible. The complementary approach is to increase the spontaneous emission rate: if $T_1 \ll T_2^*$ then T_1 will be the dominant contribution to the total coherence time T_2. As mentioned above, the first strategy implies low temperature operation, spectral filtering of the emission, the design of gated structures [108]. The second strategy instead implies the modification of the photonic density of states in the location of the QD, to achieve an enhanced spontaneous emission rate in specific optical modes. This can be achieved by coupling the QD to photonic structures like cavities. It is especially effective to suppress the detrimental effects of phonons, by strongly suppressing the rate of phonon assisted processes as recently demonstrated in our group [100]. Such approach has also the important consequence of allowing to control the emission pattern, making it possible to realize an efficient interface between the QD transitions and specific modes of the electromagnetic field. In this work, we employ both approaches by exploiting the Purcell effect in a gated optical microcavity. In the following we discuss the effect of coupling the emitter to an optical cavity.

1.2 Cavity QED with solid-state microcavities

In the previous section, we have considered the artificial atom in an homogeneous environment, where no specific boundary conditions are imposed to the vacuum electromagnetic field interacting with the atomic transition. However, when the electromagnetic environment of an emitter is modified, its radiative properties can be altered. This has been first noted by Purcell in 1946 [109], who described the enhancement of the spontaneous emission from nuclear magnetic transitions coupled to a microwave resonator, which was later experimentally demonstrated in 1983 [110]. The opposite effect, the possibility to inhibit the spontaneous emission has been proposed by Kleppner [111] in 1981 and observed shortly after [112]. Since then, the study of the interaction between atoms and light confined in cavities has been the subject of an intense field of research, Cavity Quantum Electrodynamics (CQED). The technological advancements allowed reaching unprecedented levels of control over single atoms and single photons, opening new possibilities for fundamental studies of the light-matter interaction as well as applications for quantum information processing [113, 114]. In this work, a micropillar cavity is used to control the spatial distribution of the photons emitted by the spontaneous emission process from the QD as well as to reduce the effect of pure dephasing.

In the following, we review the ideal CQED system, described by the Jaynes-Cummings model, and then a real atom-cavity system which includes dissipative effects. We will then discuss the micropillar cavity used in this work.

1.2.1 The Jaynes-Cummings model

We summarize here the standard derivation of the Jaynes-Cummings model, which can be found in many quantum optics textbooks, such as [84, 83]. We consider an ideal cavity supporting a single quantized mode of the electromagnetic field at a frequency ω_c, interacting with a two-level atom having a transition frequency ω_0 between its excited state $|e\rangle$ and ground state $|g\rangle$. The total hamiltonian of the system is given by:

$$H = H_{\mathrm{a}} + H_{\mathrm{f}} + H_{\mathrm{i}} \tag{1.12}$$

where H_a and H_f describes respectively the total energy of the atom and of the field and H_i describe the interaction energy between the two. Assuming the vacuum energy $\frac{1}{2}\hbar\omega_{\mathrm{c}}$ to be the origin of the electromagnetic field energy, the two hamiltonian terms $H_{\mathrm{a}} + H_{\mathrm{f}}$ can be written as:

$$H_{\mathrm{a}} + H_{\mathrm{f}} = \hbar\omega_0\hat{\sigma}^\dagger\hat{\sigma} + \hbar\omega_{\mathrm{c}}\hat{a}^\dagger\hat{a} \tag{1.13}$$

where we have introduced the atomic rising $\hat{\sigma}^\dagger = |e\rangle\langle g|$ and lowering $\hat{\sigma} = |g\rangle\langle e|$ operators. The interaction terms is given by the electric dipole Hamiltonian

$H_\mathrm{i} = -\hat{\mathbf{d}}\cdot\hat{\mathbf{E}}$ where $\hat{\mathbf{d}} = q\hat{\mathbf{r}}$ is the electric dipole operator and $\hat{\mathbf{E}}(\mathbf{r}, t)$ is the electric field operator. For simplicity, we assume the atom to be fixed at the maximum of the cavity field, and with a dipole moment aligned to its polarization. We can then define the atom-field coupling constant as:

$$g = -\sqrt{\frac{\hbar\omega_c}{2\epsilon_0 V}}\mathbf{d}_\mathrm{ge} \tag{1.14}$$

where $V = \int u(\mathbf{r})d^3\mathbf{r}$ is the mode volume of the field, expanded in terms of the normal modes $u(\mathbf{r})$, and $\mathbf{d}_\mathrm{ge} = \langle g|\,\hat{\mathbf{d}}\,|e\rangle$ is the matrix element for the dipole moment transition between the two atomic states. In the rotating wave approximation, valid when the atomic transition and the field mode are close to resonance ($\omega_0 \approx \omega_\mathrm{c}$), the dipole interaction Hamiltonian can be written as:

$$H_\mathrm{i} = \hbar g(\hat{\sigma}\hat{a}^\dagger + \hat{\sigma}^\dagger\hat{a}) \tag{1.15}$$

It contains two terms describing opposite processes: the de-excitation of the atom combined with the creation of a photon, and the excitation of the atom with the destruction of a photon. The total Hamiltonian describing the Jaynes-Cummings model becomes now:

$$H = H_\mathrm{a} + H_\mathrm{f} + H_\mathrm{i} = \hbar\omega_0\hat{\sigma}^\dagger\hat{\sigma} + \hbar\omega_\mathrm{c}\hat{a}^\dagger\hat{a} + \hbar g(\hat{\sigma}\hat{a}^\dagger + \hat{\sigma}^\dagger\hat{a}) \tag{1.16}$$

We consider here the case of exact resonance ($\omega_0 = \omega_c$). Eq.1.16 can be divided into two commuting parts. The first one is $H_\mathrm{a} + H_\mathrm{c}$, whose eigenstates are the uncoupled atom-field states $|e, n\rangle$ and $|g, n\rangle$ which in absence of interaction are degenerate. The second part is given by the interaction term H_i, that couples only states in the form $|e, n-1\rangle$ and $|g, n\rangle$, resulting in a total hamiltonian in a block diagonal form. The only exception is the ground state of the system $|g, 0\rangle$, which is not coupled to any other state. In each 2×2 subspace, it takes the form:

$$H = \hbar\begin{pmatrix} n\omega_0 & g\sqrt{n} \\ g\sqrt{n} & n\omega_0 \end{pmatrix} \tag{1.17}$$

and is analogous to the Rabi model. It can be diagonalized to give the eigenvalues:

$$E_\pm = \hbar\left(n\omega_0 \pm g\sqrt{n}\right) \tag{1.18}$$

which corresponds to the eigenstates:

$$|\pm, n\rangle = \frac{1}{\sqrt{2}}(|g, n\rangle \pm |e, n-1\rangle) \tag{1.19}$$

The new eigenstates of the system are entangled states of the atom and the photons in the cavity, often called dressed states of the atom. They give rise to the anharmonic energy spectrum shown in Fig.1.6.a. The degeneracy of every

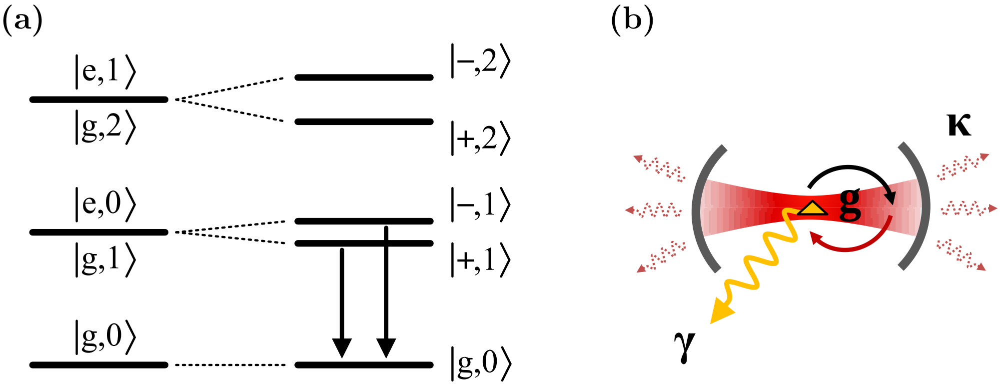

Figure 1.6 – (a) Ground state and first two excited states manifolds for a two-level atom resonant to a cavity, without (left column) and with (right column) dipole interaction. (b) Representation of the atom-cavity system.

excited state of the system is lifted, creating a ladder of doublets separated in energy by $2g\sqrt{n}$. In general, there are four possible transitions between two adjacent ladders. In the classical limit of a high number of photons ($n \gg 1$), when the spacing between levels is almost equal, this leads to the Mollow triplet [83]. On the contrary, only two transitions to the ground state $|g, 0\rangle$ are possible.

To understand the dynamical behaviour of the system, we consider an atom initially excited placed inside the empty cavity. It is not an eigenstate of the system, but can be expressed in terms of Eq.1.19 as:

$$|\psi(t=0)\rangle = |e, 0\rangle = \frac{1}{\sqrt{2}}(|+, 1\rangle - |-, 1\rangle) \tag{1.20}$$

and evolves in time according to:

$$\begin{aligned} |\psi(t)\rangle = \frac{1}{\sqrt{2}} &\left(e^{-iE_+t/\hbar} |+, 1\rangle - e^{-iE_-t/\hbar} |-, 1\rangle\right) \\ &= e^{-i\omega_0 t} \left(i \sin(gt) |g, 1\rangle + \cos(gt) |e, 0\rangle\right) \end{aligned} \tag{1.21}$$

From this last equation, we see that the probability of finding the atom in the excited state oscillates in time as $P_e(t) = \cos^2(gt)$ and, symmetrically, the probability of finding a photon in the cavity oscillates in time as $P_e(t) = \sin^2(gt)$. The single energy quantum in the system oscillate coherently between the atom and the cavity. These are called vacuum Rabi oscillations, to which corresponds a vacuum Rabi doublet in the spectral domain, given by the two transitions to the ground state represented in Fig.1.6.a. However, any realistic atom-cavity system present dissipations that must be considered.

1.2.2 Incoherent processes

The situation described by the Jaynes-Cummings model is completely coherent and gives rise to a fully reversible behaviour. However, in a real situation both the atom and the cavity are subject to irreversible interactions with the environment. There are three important dissipative processes which must be taken into account, represented in Fig.1.6.b:

- The cavity damping rate κ: describes the irreversible optical losses from the cavity field to external electromagnetic modes, and it leads to the finite spectral width of the optical mode of the cavity.

- The QD spontaneous decay rate γ_{sp}: describes the spontaneous emission of the atom into modes other than the cavity one.

- The QD dephasing rate γ^*: describes the damping rate of the coherence of the transition caused by pure dephasing effects.

The state of the system in this case must be described by a density matrix ρ, whose evolution can be computed through a master equation. Each dissipative process is described by a non-hermitian collapse operators $\hat{\mathbf{C}}_{if} = \sqrt{\gamma_{i\to f}}\,|f\rangle\,\langle i|$ representing a random collapse of the system from the state $|i\rangle$ to the state $|f\rangle$ at a rate $\gamma_{i\to f}$. For each collapse operator, a normalized Lindlabad superoperator acting on the density matrix is defined as $\hat{L}[\rho] = \frac{1}{2}\left(2\hat{C}_{\text{if}}\rho\hat{C}_{\text{if}}^{\dagger} - \hat{C}_{\text{if}}^{\dagger}\hat{C}_{\text{if}}\rho - \rho\hat{C}_{\text{if}}^{\dagger}\hat{C}_{\text{if}}\right)$. The master equation for the evolution of the system can then be computed as [115]:

$$\dot{\rho} = -i[H,\rho] + \sum_{if}\hat{L}[\rho] \tag{1.22}$$

where the first part describes the coherent temporal evolution, while the second part the incoherent one. The Hamiltonian operator $H = H_{\text{a}} + H_{\text{f}} + H_{\text{i}}$ for the system is given by the Jaynes-Cummings one of Eq.1.16. The dissipative processes listed above are instead described by the three collapse operators $\hat{\mathbf{C}}_{cav} = \sqrt{\kappa}\hat{a}$, $\hat{\mathbf{C}}_{sp} = \sqrt{\gamma_{\text{sp}}}\hat{\sigma}$ and $\hat{\mathbf{C}}_{deph} = \sqrt{2\gamma^*}\hat{\sigma}^{\dagger}\hat{\sigma}$. The expectation values of the operators describing the system evolution can be derived from the master equation as $\langle\dot{O}\rangle = \text{Tr}[O\dot{\rho}]$. In particular, the populations and the coherences of the atom and cavity fields are described by the equations of motion [116, 117]:

$$\frac{d}{dt}\langle\hat{a}^{\dagger}\hat{a}\rangle = -\kappa\langle\hat{a}^{\dagger}\hat{a}\rangle + g\langle\hat{\sigma}^{\dagger}\hat{a}\rangle + g\langle\hat{a}^{\dagger}\hat{\sigma}\rangle \tag{1.23a}$$

$$\frac{d}{dt}\langle\hat{\sigma}^{\dagger}\hat{\sigma}\rangle = -\gamma\langle\hat{\sigma}^{\dagger}\hat{\sigma}\rangle - g\langle\hat{\sigma}^{\dagger}\hat{a}\rangle - g\langle\hat{a}^{\dagger}\hat{\sigma}\rangle \tag{1.23b}$$

$$\frac{d}{dt}\langle\hat{\sigma}^{\dagger}\hat{a}\rangle = i\delta\langle\hat{\sigma}^{\dagger}\hat{a}\rangle - \frac{\gamma+\gamma^*+\kappa}{2}\langle\hat{\sigma}^{\dagger}\hat{a}\rangle + g(\langle\hat{\sigma}^{\dagger}\hat{\sigma}\rangle - \langle\hat{a}^{\dagger}\hat{a}\rangle) \tag{1.23c}$$

In the low power limit, with a single excitation in the system, we can consider the evolution to be restricted to the subspace spanned by the states $|e,0\rangle$, $|g,1\rangle$ and $|g,0\rangle$. Assuming the absence of pure dephasing ($\gamma^* = 0$), the eigenfrequences of

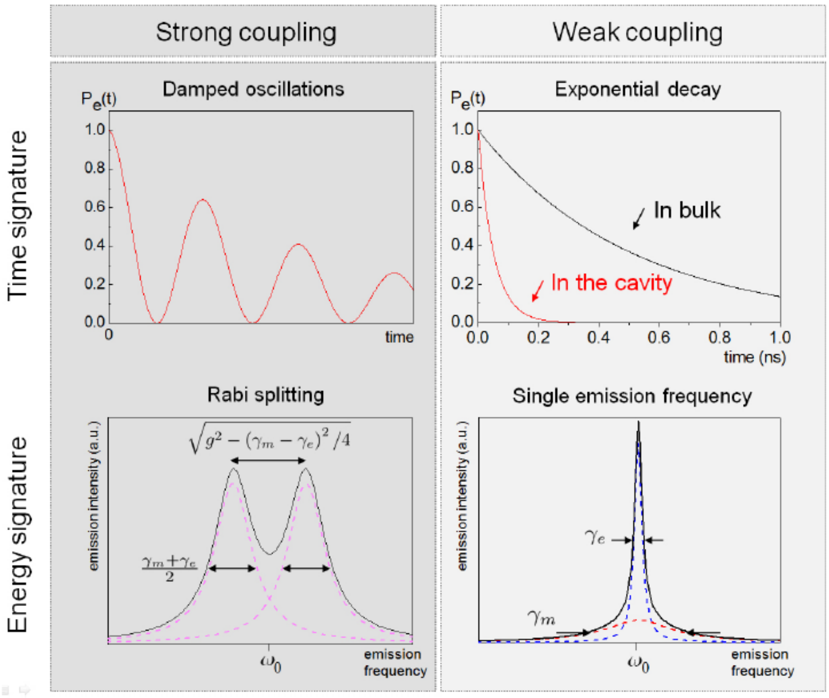

Figure 1.7 – Figure reproduced from [121]. The two regimes of the CQED system. Both the temporal and the spectral characteristics are shown for the strong coupling (left) and weak coupling (right) regime.

this coupled system of equations are [118]:

$$\lambda_0 = -\frac{\kappa}{2} \qquad \lambda_\pm = -\frac{(\kappa+\gamma)}{2} \pm \sqrt{\left(\frac{\kappa-\gamma}{4}\right)^2 - g^2} \tag{1.24}$$

Depending on the value of the argument of the square root we obtain two regimes presenting very different behaviours, as shown in Fig.1.7 [119, 120].

Strong coupling regime When $g > |\kappa - \gamma|/4$, the two solutions $\lambda_\pm$ are complex, thus the evolution of the atom and cavity populations is described by two damped oscillations.

The system is in a strong coupling regime, where the coherent exchange of energy between the atom and the cavity dominates over the dissipative processes (left part of Fig.1.7). Here, an initially excited atom which emits a photon into the cavity can reabsorb it to return to the initial excited state. This cycle can happen several times before the photon is lost to the environment. The strong coupling situation is close to the one described by the Jaynes-Cummings model, and Rabi oscillations, damped in time due to the presence of losses, can be observed. Spectrally, this regime is characterized by the resolution of a doublet in emission spectroscopy due to the mixed atom-photon nature of the states.

Weak coupling regime When $g < |\kappa - \gamma|/4$, the two solutions $\lambda_\pm$ are real, describing an exponential damping.

The system is in the weak coupling regime, where the dissipative processes dominates over the coherent exchange between the atom and the cavity (right part of Fig.1.7). As for the spontaneous emission in free space, the radiative decay of an initially excited atom is irreversible. In this case however, the exponential decay of the excited state population happens at a rate given by $\Gamma = \frac{4g^2}{\kappa}$. It is possible thus to obtain a cavity-enhanced spontaneous emission from the atom, whose transition rate will be strongly accelerated by the presence of the cavity. This is the essence of the Purcell effect, that is detailed in the next section. A single Lorentzian peak is observed in the emission spectrum at the atom transition frequency, having a width enhanced by the decay rate in the cavity.

1.2.3 The Purcell effect

The weak coupling regime described above can also be treated perturbatively. In particular, if $\kappa \gg \gamma/2, g$ the cavity mode can be adiabatically eliminated, which consists in modelling the cavity as a reservoir, whose dynamics is much faster than the evolution of the two-level atom. This is equivalent to consider the cavity bandwidth much larger than the linewidth of the transition [115]. Under this assumption, we can use the Fermi golden rule, as in the original approach by Purcell. Looking at Eq.1.5, we can understand how the spontaneous emission rate is modified. By placing the emitter in an optical cavity, it will be coupled to a field having a different amplitude and polarization, as well as a different possible density of final states for the process. This situation can be modeled as the coupling of the emitter to a quasi-mode density of states ρ_{qm}, built from the cavity mode and the free space continuum [122, 123, 124]. Considering a single cavity mode centred on ω_c having a width κ, the emitter is effectively coupled to a Lorentzian mode density [125]:

$$\rho_{\mathrm{qm}}(\omega) = \frac{2}{\pi\kappa}\frac{\kappa^2}{4(\omega-\omega_c)^2+\kappa^2} \tag{1.25}$$

We assume here the emitter to be spectrally in resonance with the cavity mode, at the maximum of its electric field and having its dipole moment aligned to the field polarization. In such ideal condition, using the Fermi golden rule (Eq.1.5), we find the spontaneous emission rate to be:

$$\Gamma = \frac{2\mathbf{d}_{\mathrm{ge}}Q}{\hbar n^2 V} \tag{1.26}$$

where $\mathbf{d}_{\mathrm{ge}}$ is the electric dipole moment of the transition, n is the refractive index of the material at the emitter location, $Q = \omega_c/\kappa$ is the quality factor of the cavity and V is the effective volume of the optical mode of the cavity. To quantify the enhancement of the spontaneous emission into the confined mode of the cavity, we can relate the decay rate in the cavity Γ to the decay rate of the same emitter in an homogeneous medium γ_{sp}, which we have already calculated in Eq.1.8. This ratio is defined as the Purcell Factor [109]:

$$F_{\mathrm{P}} = \frac{\Gamma}{\gamma_{\mathrm{sp}}} = \frac{3}{4\pi^2}\frac{Q(\lambda/n)^3}{V} = \frac{4g^2}{\kappa\gamma_{\mathrm{sp}}} \tag{1.27}$$

The spontaneous emission rate into the cavity mode is proportional to Q/V, thus high quality factor and low mode volume are required to reach a strong emission rate in the cavity mode. This constitutes an important figure of merit to determine the potential Purcell factor achievable with a specific cavity [126].

In general the enhancement of the emission into the cavity mode does not inhibit the spontaneous emission into the continuum of modes outside the cavity, to which the emitter decay at a rate γ_{sp}. The total lifetime of the emitter is thus $(T_1)^{-1} = \Gamma + \gamma_{\mathrm{sp}}$. However, with a very strong Purcell factor $F_{\mathrm{P}} \gg 1$, $(T_1)^{-1}$ is mostly determined by the emission into the cavity, much faster than the emission in the free space continuum. We can calculate the fraction of photons emitted into the cavity mode, called the mode coupling, as:

$$\beta = \frac{\Gamma}{\Gamma + \gamma_{\mathrm{sp}}} = \frac{F_{\mathrm{P}}}{F_{\mathrm{P}} + 1} \tag{1.28}$$

It is clear from this equation that for $F_{\mathrm{P}} \gg 1$, $\beta \to 1$. A high Purcell factor allows to funnel most of the radiative emission from the atomic transition into the optical mode of the cavity.

A second important consequence is the mitigation of pure dephasing effects. We have seen before that the total coherence time of the optical transition is $(T_2)^{-1} = (2T_1)^{-1} + (T_2^*)^{-1}$, which including the Purcell-enhanced coupling to a cavity mode can be written as $\gamma = \frac{\Gamma+\gamma_{\mathrm{sp}}}{2} + \gamma^*$. With a high Purcell factor we can achieve $\frac{\Gamma}{2} \gg \gamma^*$, thus the dephasing rate γ is dominated by the radiative decay rate Γ. Equivalently, the shortening of the radiative lifetime will cause a radiative broadening of the transition linewidth beyond the one caused by pure dephasing. In this condition, the emitted wavepackets are Fourier transform limited.

From the above discussion, we see how a strong Purcell effect ensures that the transition primarily interacts with the optical mode of the cavity, thus it gets effectively isolated from other dissipative processes. Moreover, the cavity can be engineered to be easily interfaced with external optical modes, used as input and output ports to realize an efficient interface between the propagating photons and the QD transition.

Note that other approaches based on suppressing the QD emission in all optical modes but one can also be used to interface a QD and propagating photons. This is achieved by coupling the QD to 1-dimensional waveguide such as nanowires [25], nanotrumpets [127] or photonic crystal waveguides [128, 129]. In this case, while efficient coupling between the QD and the photons is achieved, the absence of Purcell effect does not allow for mitigating the pure dephasing effects.

1.2.4 CQED with a QD in a micropillar

To confine light in solid-state cavities, the three structures most commonly used are microdisks, photonic crystals and micropillars, which allows to achieve both the weak and the strong coupling regimes with a single QD emitter [130, 131]. A microdisk is a semiconductor disk much flattened in one dimension which confines a whispering gallery mode. Using GaAs based microdisks, quality factors up to few 10^4 and a Purcell factor up to 42 have been reported [125, 132, 133]. Photonic crystals are structures where a periodic modulation of the reflective index can be used to create a photonic bandgap. This, associated to artificial defects placed in the structure, allows the realization of confined optical modes. Two-dimensional photonic crystal are widely used in conjunction with QDs and allows to reach very small mode volume for the cavity field, of the order of $0.1\lambda^3$, with quality factor of the order of 5×10^4 and Purcell factors up to 28 [134, 135, 136]. However, coupling the light from the photonic crystal cavities to external fibre or waveguides is challenging, and extraction efficiencies have been reported up to 44% [137]. A micropillar cavity is constituted by two mirrors creating a Fabry-Perot resonator, where additional lateral confinement is created by shaping the structure in a cylindrical shape. The first demonstration of the Purcell effect in a micropillar has been reported in 1998 by Gerard et al. [126]. Mircopillar cavities allows to obtain mode volumes of the order of λ^3, with typical reported quality factors in the weak coupling regime of few 10^4 and Purcell factors up to 30 [138, 139, 140, 141].

The device used in this work is based on a micropillar cavity, at the center of which is placed a single QD, whose structure is modified to allows for the realization of electrical contacts, and is detailed in the rest of the section.

The micropillar cavity A schematics of the QD-micropillar device is shown in Fig.1.8.a. The InGaAs QD is located at the centre of a λ-cavity having a cylindrical shape. The cavity is constituted by a GaAs spacer sandwiched between a top and a bottom AlGaAs/GaAs Distributed Bragg Reflector (DBR). The two DBRs induce a vertical confinement of the light in the micropillar, while the lateral confinement is given by total internal reflection. The resulting three dimensional confinement of the light allows reaching a strong Purcell effect altogether with an optical mode profile well suited for the external interfacing. The micropillar is guiding the photons, which are emitted upwards with a field distribution having a high overlap with a Gaussian mode. An efficient collimation or coupling to optical fibres can be obtained.

The parameters g, γ and κ governing the physics of a CQED device, already introduced before, are shown in Fig.1.8.a for the specific case of a micropillar. The coupling strength g describes the ratio at which the energy can be coherently exchanged between an exciton and a cavity photon. The bare QD dephasing rate $\gamma = \frac{\gamma_{\text{sp}}}{2} + \gamma^*$ describe the rate at which the coherence of the exciton transition is lost. It is given by the sum of unwanted spontaneous emission γ_{sp} in modes other than the cavity mode plus the pure dephasing rate γ^*. The total cavity damping rate $\kappa = \kappa_{\text{top}} + \kappa_{\text{bottom}} + \kappa_{\text{loss}}$ describe the photon losses from the cavity. It is given by the sum of three contributions: κ_{top} and κ_{bottom} which account for photons escaping from the top or bottom mirror, and κ_{loss} which accounts for unwanted leakage through the sidewalls of the cavity. The objective of this QD-micropillar device is to efficiently interface the propagating photons with the QD inside the cavity. With a high Purcell effect, the coherent exchange g overcomes the dephasing rate γ and most of the emission from the QD will happen in the confined mode of the cavity. When accessing the micropillar from the top, the total cavity damping rate should be dominated by the losses κ_{top} through the top mirror. In this way, most of the emission from the QD can be collected from the top port and symmetrically, if the excitation mode is well overlapped to the cavity mode, most of the incident light will interact with the QD.

The performances of the QD-micropillar device as a light-matter interface can be described using three fundamental parameters:

- The cooperativity $C = \frac{g^2}{\kappa\gamma}$: quantifies the strength of the coherent processes to the incoherent ones. It can be related to the Purcell factor as $F_P = \frac{4\gamma}{\gamma_{\text{sp}}} C$.

- The output coupling efficiency $\eta_{\text{out}} = \frac{\kappa_{\text{top}}}{\kappa}$: quantifies fraction of photons escaping the cavity across the top mirror, from which they can be efficiently collected.

- The input coupling efficiency η_{in}: quantifies the spatial overlap between the free-space optical beam used to excite the device and the confined mode of the cavity.

A very high cooperativity ensure that the QD primarily interacts with the optical mode of the cavity and the information can be reversibly transferred between the light and the matter field. In order to use the device as an emitter, a high output coupling efficiency is required to be able to collect all the photons emitted from the cavity. Symmetrically, to use the device as a receiver, a high input coupling efficiency is needed to be able to couple all the incident photons to the cavity.

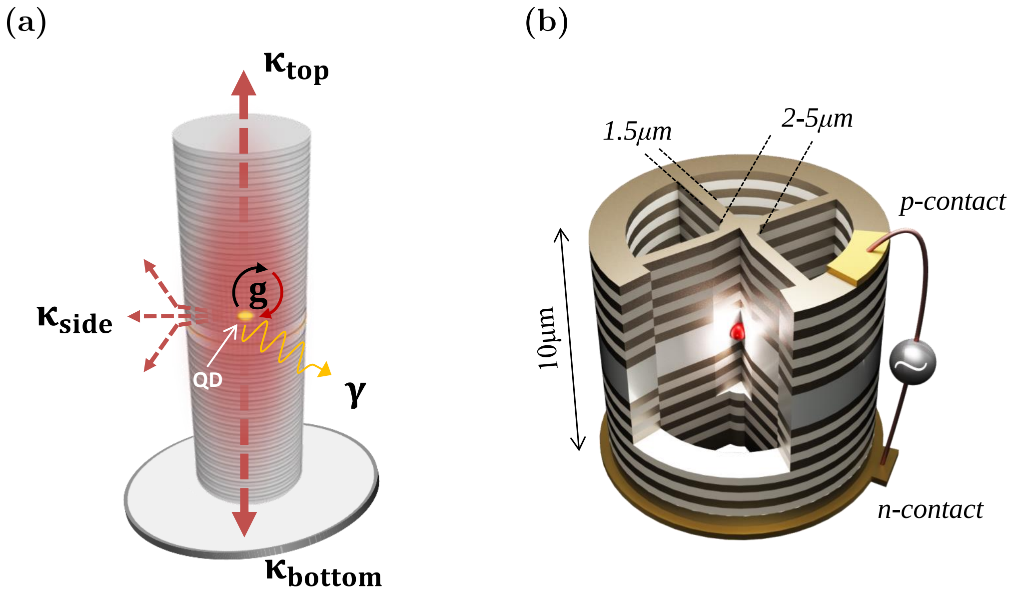

Figure 1.8 – (a) Figures of merit of the physics of the QD-micropillar device. g is the coupling strength between the QD and the cavity. γ is the total dephasing rate of the QD. κ_{top} and κ_{bottom} describe photon escaping rates through the top or bottom mirror, while κ_{loss} the unwanted sidewall losses rate. (b) Schematics of an electrically contacted micropillar.

Gated micropillars As mentioned before, the fabrication of QDs embedded in diode structures allowed to demonstrate the controlled shift of the optical transition energies though the confined Stark effect, the control of the exciton fine structure splitting and the reduction of dephasing due to charge noise. While the realization of bulk contacted structures has been extensively studied [142, 143, 106, 104, 63], the fabrication of electrically controlled QDs coupled to cavities is very challenging, and few works have been reported.

The first realization of a QD coupled to an electrically contacted microcavity has been reported in 2007 by Strauf et al. [144], providing a Purcell factor between 2 and 4 and an extraction efficiency from the cavity of 0.38. The following year, Bockler et al. [145] reported the electrical control of a QD in a micropillar, showing a Purcell factor of 10. An analogous device has been used in 2010 by Heindel et al. [146] to demonstrate an electrically driven QD-micropillar single-photon source, later fabricated also using site controlled QDs [147]. The performances of these devices however were still not at the level of uncontacted QD-cavity systems as charge noise was still high. Moreover, a deterministic fabrication technology for electrically controlled cavity devices were still lacking.

The electrically contacted QD-micropillar cavities used in the present work, represented in Fig.1.8.b, have been first developed in 2013 by Anna Nowak [148] and then by Niccolo Somaschi in the current design [44]. The fabrication is based on a deterministic in-situ lithography technique, presented in the next section, which allows the spatial and spectral matching of the QD and the micropillar cavity as well as the design of electrical contacts. In this device, the QD is coupled to a micropillar cavity which is fabricated with a p-i-n doping profile allowing to define a diode structure, used to apply the external bias. The micropillar cavity is at the center of Fig.1.8.b, and is connected by four 1 dimensional ridges to a circular frame surrounding it. This frame allows to define ohmic gates for electrical connections. As demonstrated in [148], the presence of the 1-dimensional ridges results in a slightly increased mode volume as compared to the case of isolated pillars with the same diameter. Moreover, it contributes to slightly increase the side losses through lateral coupling to the waveguides so that a lower κ_{top} is necessary to obtain a high η_{out}. In the following section, we detail the fabrication procedure for the electrically controlled QD-micropillar device.

1.3 Realization of an optimal light-matter interface

To achieve a high Purcell effect, a high quality factor and a small mode volume are needed. Beside the design of an appropriate cavity, a fundamental challenge is also the spatial and spectral matching of the QD transition to the optical mode of the cavity. The best coupling is indeed achieved only when the QD is positioned at the maximum of the cavity electric field and its transition energy matches the central energy of the cavity mode. Both the spectral and spatial random distribution of the self-assembled QDs are a major challenge for their coupling to photonic nanostructures such as a microcavities.

Using complex growth techniques, it is possible to control the spatial position of the fabricated QDs. Recently, this technique allowed also the coupling of single QDs to cavities and waveguides [149, 147]. However the optical quality of these site-controlled QDs is still limited with respect to the self-assembled ones [150]. The first technique to deterministically couple a photonic crystal to a self-assembled QD was developed in 2005 [151, 152], and was based on a SEM or AFM imaging system to locate the QD position and aligning an electronic lithography to define the cavity around it. With a different approach, it has been possible to couple a QD to an external cavity realized using the termination of an optical fibre [153, 154]. This also allows to directly couple the emission to the fibre. The devices used in this work are fabricated using a cryogenic photolithography technique first developed in our group in 2008 by Dousse et al [38]. This technique, now adopted by different groups, allowed to reach both the weak [38] and strong coupling regimes [39] in a micropillar cavity with a single self-assembled QD. In the following we detail this fabrication method and the performances that we can expect from a typical device.

1.3.1 Deterministic fabrication using in-situ lithography

The fabrication of the QD-micropillar devices, performed in our team, can be decomposed into three main steps: the growth of the QDs in a planar cavity, the in-situ optical lithography defining a cavity centred on each QD, and the etching of the structures. The deterministic spatial and spectral coupling is possible thanks to the low-temperature far-field optical lithography technique which is performed in-situ, while characterizing the QD emission.

Growth The first part of the fabrication consists in the growth of a planar cavity made of two GaAs/$\mathrm{Al_{0.9}Ga_{0.1}As}$ $\lambda/4$ Bragg mirrors containing a GaAs λ-cavity. At the centre of this, is placed a low-density layer of self-assembled InGaAs QDs. The growth is done by Aristide Lemaître by Molecular Beam Epitaxy (MBE), a technique which allows the epitaxial growth of atomically flat semiconductor heterostructures, with a thickness control at the level of single monolayers. The Bragg mirrors are made by alternating layers of GaAs and $\mathrm{Al_{0.9}Ga_{0.1}As}$, with 30 pairs for the higher reflective bottom mirror, and 20 pairs for the top one. After the deposition of the bottom mirror and half of the λ-cavity, the layer of QDs is grown using the Stranski–Krastanov method, as explained in Section 1.1.1. The QD layer is then covered with the second half of the λ-cavity and the top mirror. The bottom mirror has a gradual n-doping profile, while the top mirror a p-doping profile, allowing the realization of ohmic contacts at the top and the bottom of the structure.

Lithography The second step is the low temperature in-situ lithography, performed by Niccolo Somaschi using the technique developed in the team in 2008 [38]. This part consists in selecting a specific QD from the randomly distributed ensemble, and to deterministically couple it to the optical mode of a micropillar cavity, using the setup sketched in Fig.1.9.a. The planar cavity obtained from the previous step is spin coated with a layer of positive photoresist and placed in a closed-cycle He cryostat, at a temperature of 8K. The positioning of the sample is controlled with a 3-axis piezo-controlled stages, while three confocal optical lines are aligned and focused on the sample with a same microscope objective. A first line is used for an above-band excitation of the QDs in the sample using a red laser, having a wavelength between 780nm and 850nm. The Photoluminescence Signal, spectrally filtered by a dichroic mirror to remove the excitation laser light, is collected using a second line and detected with a spectrometer. A specific transition of the QD, which for this work corresponds to a neutral exciton state, can be identified by studying the power dependence of its emission intensity. This allows also to determine the energy at which the cavity mode must be defined The total intensity of the signal from a specific QD transition can then be monitored, for a fixed excitation power, as a function of the spatial position of the sample, controlled by the piezo actuators. The precise location

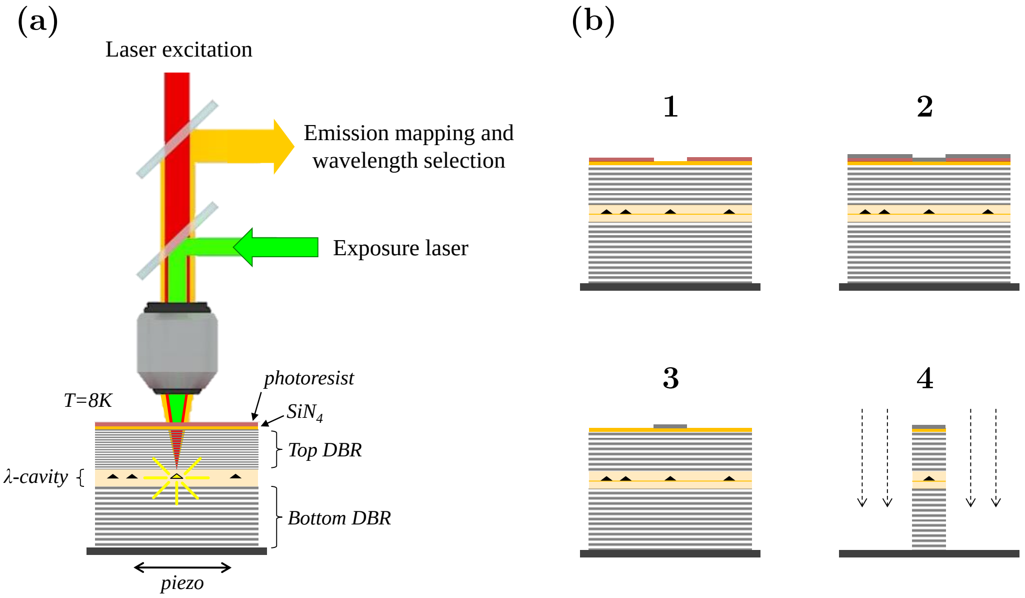

Figure 1.9 – (a) Schematic of the in-situ lithography (see details in the text) (b) Ex-situ etching of the structure defined by the optical lithography. Step 1: development of the positive photoresist. Step 2: deposition of a 40nm layer of Ni and hard mask. Step 3: lift-off of the residual photoresist. Step 4: dry etching of the micropillars, as defined by the Ni layer.

of the selected QD can be obtained with a 50nm accuracy by maximizing the collected intensity.

Having both the position and the emission energy of a specific QD, the third optical line is used to expose the photoresist in order to define the shape of the micropillar cavity. The spatial matching is achieved by positioning the sample on the exact location of the chosen QD, while the spectral matching is achieved by adjusting the diameter of the micropillar. Indeed, the energy of the fundamental optical mode of the micropillar cavity decreases for increasing diameters. In the first generation of the technology [38] the pillar size was adjusted by changing the exposure time. Indeed, the focused spot size of a green laser, having a wavelength of 532nm, define a circular area with a typical size of 0.8 μm. However, since the resist exposure is a non-linear process, the size of the exposed area increases with the exposure time or the incident laser power. A calibration of the procedure allowed to identify the exposure conditions to obtain a specific diameter for the micropillar, which, in turns, identify the energy of its optical mode. This procedure can be repeated for multiple QDs in a same sample, in order to obtain multiple QD-micropillar device from each planar cavity.

This technique has later been upgraded to define more complex structures [148]. By exposing the photoresist while moving the sample, it is possible to draw arbitrary shapes in the resist, including the 1 dimensional ridges and the

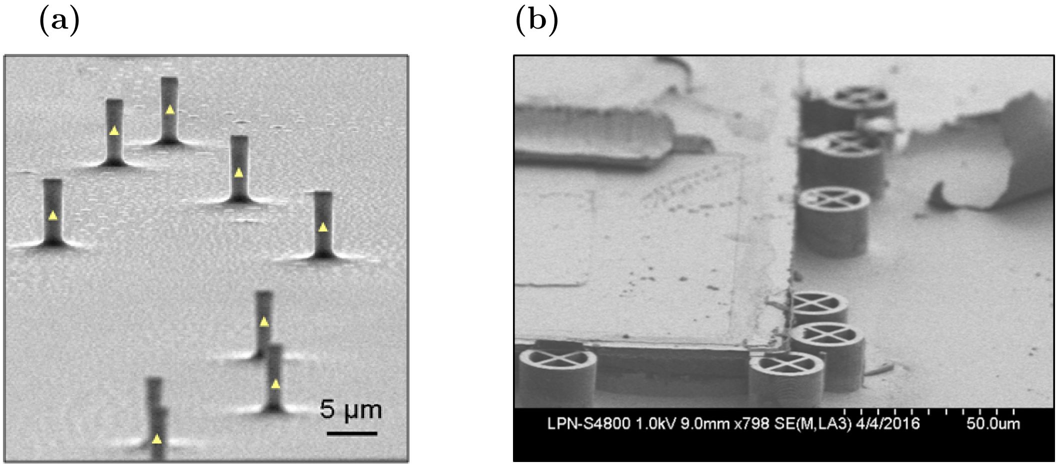

Figure 1.10 – Scanning Electron Microscope images. (a) First generation of deterministically coupled QD-micropillar sample. (b) Second generation of devices, including electrical control.

surrounding frame used to realize the electrically contacted micropillar cavities [148, 44].

Etching The last part of the fabrication, performed by Isabelle Sagnes, is the etching of the structure previously defined using the in-situ lithography. The processing of the sample during the etching is shown in Fig.1.9.b. This part begins with the development of the positive photoresist, dissolving the exposed areas directly above the QD of interest (step 1). A layer of Ni is deposited on the whole planar structure (step 2). This is followed by a lift-off step to remove the residual photoresist, allowing to obtain circular Ni shapes of the right diameter centred on the QD (step 3). Finally a dry etching process is used to remove all the surrounding material (step 4). The result is a sample with multiple micropillar cavities, each coupled to a single QD.

Two SEM image of samples obtained with the in-situ lithography technique are shown in Fig.1.10. Fig.1.10.a shows several single micropillar cavities obtained with the first generation of the technique [38]. Fig.1.10.b instead shows the most advanced devices, i.e. the electrically contacted micropillars, where the cavity is placed at the centre of a circular frame. In the same image a bigger structure to which all the devices are connected can be seen. The bigger planar area is used to deposit metallic contacts, thanks to which an electrical bias can be applied. The complex shapes of all the visible structures has been defined using the same lithographic step, where the sample is moved using computer-controlled piezoelectric transducers, while keeping the green exposure laser on. We will see in the following that this last generation of devices achieve a very high Purcell effect and input and output coupling efficiencies.

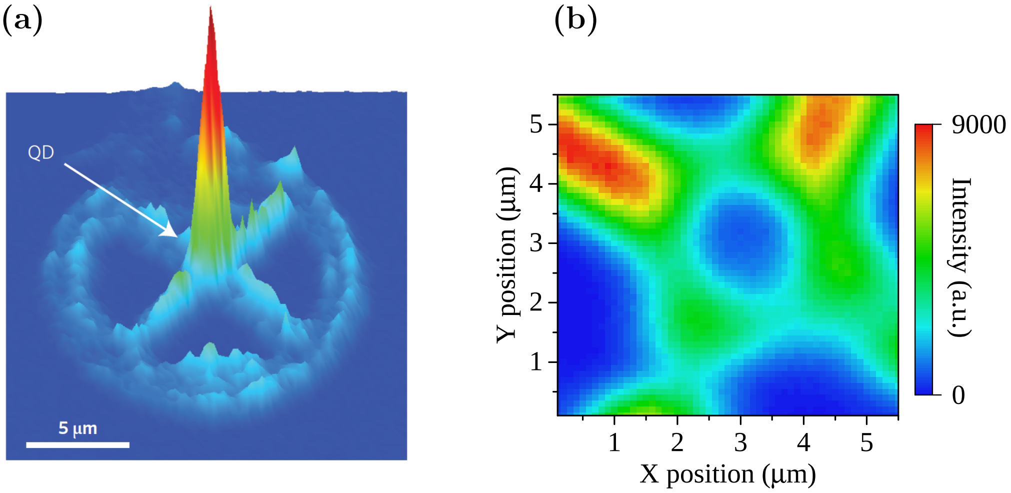

Figure 1.11 – (a) Photoluminescence emission map from the electrically contacted micropillar, highlighting the strong QD emission precisely localized at the center of the structure. (b) Reflectivity map from the same device, highlighting the reflectivity dip due to the cavity mode, at the center of the structure.

After the fabrication is complete, the positioning of the QD at the centre of the micropillar cavity can be verified by collecting a PL emission map, as shown in Fig.1.11.a. Here an 850nm laser is used to excite the device, and the PL intensity at the QD emission energy (≈925nm) is collected as a function of the sample position. We can clearly identify the cross-shaped structure of the device. At its centre, the strong peak is due to the signal from the QD, deterministically positioned to be spatially matched with the cavity.

A similar map of a smaller area at the centre of the device is shows in Fig.1.11.b. Here we excite with a resonant laser (≈925nm) and we collect the total reflected intensity, as a function of the sample position. The QD transition is tuned far from the micropillar mode energy using the external bias, so to observe the empty cavity. Again the four ridges can be identified, going from the centre towards the four corners of the figure. The reflected intensity, as opposite to the previous case, drops at the centre due to the presence of the micropillar mode. This allows to directly observe the spatial positioning of the optical cavity, which is also spectrally matched to the QD energy.

1.3.2 Optimal light matter interface

To fully characterize our CQED device, we determine the values of the g, κ and γ parameters, as presented in Section 1.2.4. This can be done with a theoretical adjustment to a reflectivity spectrum of the device. We first very briefly

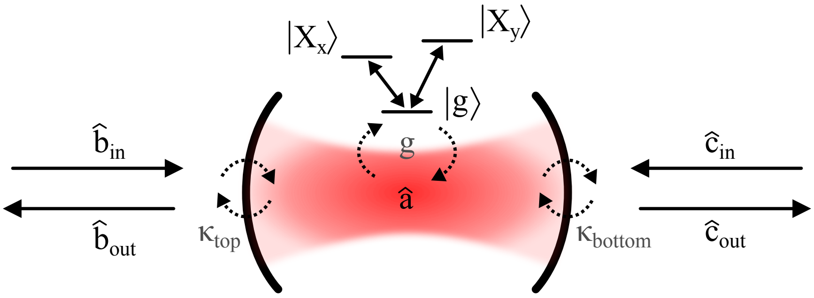

Figure 1.12 – Scheme of a two-sided cavity coupled to a three level system, described with the input-output formalism.

introduce the theoretical model and then shows the results of the fit.

Theoretical model for the QD-micropillar device The theoretical model for the device and the simulation that are shown in the following chapters have been realized in the group of A. Auffeves, by B. Reznychenko and T. Grange, and is represented in Fig. 1.12. The evolution of the QD-cavity system is calculated using the master equation presented in Section 1.2.2. To account for the finite Fine Structure Splitting of the neutral exciton, the QD is modelled as a three level system in a V configuration, with a single ground state and two linearly polarized transitions having an energy difference Δ_{FSS}. To account for the polarization splitting of the micropillar, the cavity as well is modelled with two linearly polarized optical modes H and V, whose axis are at an angle θ from the QD axis.

The behaviour of the QD-cavity system both as an emitter and a receiver of photons, can be described using the input-output formalism. The cavity field $\hat{a}$ communicates with two ports, acting as inputs and outputs interfaces, described by the mode operators $\hat{b}_{\mathrm{out}} = b_{\mathrm{in}}\hat{I} + \sqrt{\kappa_{\mathrm{top}}}\hat{a}$ and $\hat{c}_{\mathrm{out}} = \sqrt{\kappa_{\mathrm{bottom}}}\hat{a}$ where $\hat{I}$ is the identity operator. The excitation laser is modelled as a classical field injected along the H cavity mode through the input mode $\hat{b}_{\mathrm{in}}$. The measured quantities, such as the reflectivity, the fluorescence and the second order correlation function can be calculated using the output field $\hat{b}_{\mathrm{out}}$, which is the optical mode exiting from the top mirror of the micropillar.

Extraction of the CQED parameters of the device To experimentally perform a reflectivity measurement, we scan the energy of a CW laser across the cavity resonance, with the QD transition tuned at the cavity central energy, and we collect the total reflected intensity. The result is shown in Fig.1.13 for a typical device, while a more detailed explanation of the experimental procedure and the extraction of the parameters can be found in Section 4.3.2. We can interpret the observed spectrum as the superposition of the Lorentzian re-

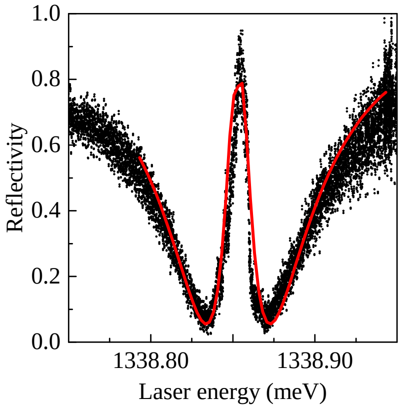

Figure 1.13 – (a) Low power reflectivity spectrum of the QD-micropillar device labelled QD3. From the simulation (red line) is possible to extract the values of $g = 19\mu$eV, $\kappa = 90\mu$eV and $\gamma = 0.35\mu$eV.

flectivity dip due to the cavity and the Lorentzian emission line from the QD transition. The red solid line shows an adjustment of the theoretical model for the device, presented in the paragraph below. It allows to retrieve a value of coupling strength $g = 19 \pm 0.2$ μeV, cavity damping rate $\kappa = 90 \pm 10$ μeV and QD dephasing rate $\gamma = 0.35 \pm 0.1$ μeV. From these three values we can see that, while close to the limit of strong coupling, we operate here in the weak coupling regime since $g < |\gamma - \kappa|/4$. Having $\gamma = \frac{\gamma_{\mathrm{sp}}}{2} + \gamma^*$, we can also observe that the measured dephasing rate is almost fully accounted for by the spontaneous emission rate. Recalling that the spontaneous emission lifetime in bulk is about 1 to 1.3 ns, the corresponding decay rate γ_{sp} is between 0.5 and 0.6 μeV, thus the contribution from the pure dephasing rate γ^* is negligible.

Now, we can retrieve the figures of merit describing the efficiency of our device as a light-matter interface. We obtain a state of the art value of cooperativity $C = \frac{g^2}{\kappa\gamma} = 14 \pm 7$. This cooperativity is much higher than the previous record value of 2.5 obtained with micropillar cavities [155, 156, 157, 158], and even surpassing some of the best results obtained with natural atoms, where reported values of single atoms cooperativities vary between 0.07 and 6 [159, 22, 160, 23]. Neglecting the pure dephasing ($\gamma^* \approx 0$) the measured cooperativity corresponds to a Purcell Factor of $F_{\mathrm{P}} = 2C = 28 \pm 14$. From such a high Purcell factor, we can also calculate a mode coupling $\beta = F_{\mathrm{P}}/(F_{\mathrm{P}} + 1)$ in the range $0.93 - 0.98$. The cavity spectrum allows also to retrieve the output coupling efficiency, which results $\eta_{\mathrm{out}} = 0.64$. The input coupling efficiency can be optimized by adjusting the focused spot size of the excitation laser to closely match the micropillar diameter. By measuring the mode diameter of the incident and of the emitted beams, we have obtained values of η_{in} in the 0.90 to 0.95 range.

From these numbers, we can expect our devices to act both as efficient emitters of single photons and as an efficient receivers of single photons. An incident photon will couple 95% of the times to the optical mode of the cavity, and will interact with the QD with 98% probability before being lost. Symmetrically, the QD will emit a photon with 98% probability in the cavity mode, and such photon will be collected from the top 64% of the times. In the following chapters we will use such near ideal light-matter interface to explore different applications of the QD-micropillar devices in the field of quantum information science.

Chapter 2

Near optimal sources of single indistinguishable photons

The availability of a deterministic single-photon emitter is a milestone for the scaling of most photonic quantum technologies. Fundamentally new applications in computation, communication and metrology can be realized by encoding the information on single photons. Although an on-demand generation of nonclassical states of light is required to realize large scale applications, it has been for long an elusive goal. We study here the emission from the QD-micropillar devices under different excitation regimes. We shows that our device act as a very efficient emitter of single photons, with a state of the art brightness and indistinguishably, opening up new possibilities for the study of large photonic quantum systems.

In section 2.1, we review the interests and the requirements for single photon sources in the field of quantum information science, and in section 2.2, we introduce the metrics to describe them. The different single-photon sources available today are described in section 2.3. In section 2.4, we describe the optical excitation of our QD-micropillar device, and its emission properties are analysed under non-resonant excitation in section 2.5 and under resonant excitation in section 2.6. A comparison with the state of the art for single photon sources and perspectives for this work are given in section 2.7.

2.1 Single photons for quantum technologies

Single photons have early emerged as interesting qubits to encode the quantum information. They have different degrees of freedom, such as polarization, spatial or frequency modes, into which the information can be encoded. Single photons can be easily manipulated and detected and are also highly immune to external disturbances, thus currently appearing as the only viable option as flying qubits for long distance quantum information transfer. These advantages gave them a leading role in many schemes for quantum computation, communications and metrology. The development of these photonic quantum technologies relies on the advances into three key areas [108]: sources, linear and nonlinear gates and detectors. While linear gates [161] and detectors [162] have shown impressive advances, the lack of deterministic and scalable sources of single photons has been an important limitation.

An ideal source of single photons is a device which, each time it is triggered, provides a pure single photon Fock state in a well-defined mode of the electromagnetic field:

$$|\psi\rangle = |1\rangle \tag{2.1}$$

In the simplest case, this equation describes a monochromatic, hence continuous wave, single photon. Typical applications in the field of quantum information science require the photons to be spatially and temporally localized, in order to be processed and detected. This imply both a finite bandwidth as well as the knowledge of the generation time of the photon, which shouldn't be random. For this reasons, continuous wave production of single photons is not analysed here, and we consider only a pulsed generation regime. To describe a single photon wave packet, one needs to write the single photon state as a superposition of different frequencies. Decomposing it in terms of plane waves, having wave vector $\mathbf{k}$, angular frequency $\omega = c|\mathbf{k}|$ and polarization ϵ, we can write it as [84]:

$$|\psi\rangle = \sum_{\mathbf{k},\epsilon} c_{\mathbf{k},\epsilon} |1\rangle_{\mathbf{k},\epsilon} \tag{2.2}$$

with $\sum_{\mathbf{k},\epsilon} |c_{\mathbf{k},\epsilon}|^2 = 1$. The fact that such a wave packet is composed of only Fock states $|n\rangle$ with $n = 1$ defines the single photon character of the state. Indeed, it is an eigenstate of the total photon number operator $\hat{n} = \sum_{\mathbf{k},\epsilon} \hat{n}_{\mathbf{k},\epsilon}$ with eigenvalue of 1. The coefficients $c_{\mathbf{k},\epsilon}$ define the distribution of the field in the wave packet, thus both the spatial and spectral profile of the photon. The capability of a device to produce a state in the form of Eq.2.2 can be translated into three different properties that can be used to characterize its performances as a source: brightness, single photon purity and indistinguishability. The brightness describes the efficiency of generating a photon, the single photon purity describes how well the multi-photon probability has been suppressed and finally the indistinguishability reveals if all the photons are emitted in a same quantum state.

2.2 Characterization of a single-photon source

In this section we describe the metrics used to characterize a single photon source, later on employed to experimentally determine the performances the QD-micropillar devices.

2.2.1 Brightness

The brightness B can be defined as the probability $P(1)$ with which, once triggered, the source provides a single photon Fock state. If the efficiency of the source is limited, it will generate a state composed of vacuum and single photons, in the form [163]:

$$|\psi\rangle = \alpha\,|0\rangle + \beta\,|1\rangle \tag{2.3}$$

where $|\alpha|^2 = P(0)$, $|\beta|^2 = P(1)$ and $P(0) + P(1) = 1$. Here we consider a pure state but the same is valid also for a mixture of vacuum and single photons. The experimental value of the brightness $\overline{B}$ can be measured at any position of the setup using a single photon detector. The detection probability will be determined by $P(1)$, and the detected count rate can be written as $R_{\text{photons}} = \Gamma_{\text{laser}} P(1)$. By normalising the detected photon rate R_{photons} to the rate at which the source is triggered, considering that the maximum single photon rate is limited by the repetition rate of the laser Γ_{laser}, we can estimate the average number of photons per excitation pulse at the detector. Correcting for any experimental losses of the setup η_{setup}, including the detector efficiency, we can retrieve the experimental value of the brightness at any location on the optical setup as:

$$\overline{B} = \frac{R_{\text{photons}}}{\Gamma_{\text{laser}}\eta_{\text{setup}}} \tag{2.4}$$

We see here that this equation for the brightness corresponds to the probability that the source generate a single photon Fock state, $P(1)$, which is also the average photon number $\langle n\rangle = \sum_n nP(n)$ of the state.

When the source generates also Fock states contributions with $n > 1$, the relation between the count rate on a detector and $P(1)$ is more complex. The Single Photon Avalanche Diodes (SPADs) that we use are "click" detectors, incapable of resolving the photon number of the incident state, but only differentiating the presence or absence of photons. For such detector, having an efficiency η, the probability to have a click at the output is [163]:

$$P(\text{click}) = \sum_{n=1}^{\infty} [1 - (1-\eta)^n] P(n) \tag{2.5}$$

and by writing out the first few terms of the summation, we obtain:

$$P(\text{click}) = \eta P(1) + 2\eta\left(1 - \frac{1}{2}\eta\right)P(2) + 3\eta\left(1 - \eta + \frac{1}{3}\eta^2\right)P(3) + ... \tag{2.6}$$

For unit efficiency ($\eta = 1$), this equation gives $P(\text{click}) = \sum_{n=1}^{\infty} P(n)$, implying that the presence of any non-vacuum state will be equally detected, independently of its photon number. On the contrary, for $\eta \to 0$ we can rewrite Eq.2.6

to the leading term in η as:

$$\lim_{\eta\to 0} P(\text{click}) \approx \eta \sum_n nP(n) = \eta\langle n\rangle \tag{2.7}$$

thus in the limit of low detection efficiency the detection probability is proportional to the average photon number of the incident state. For higher efficiencies, the contribution from higher photon number components will be underestimated. The count rate on the detector is given by $R_{\text{photons}} = \Gamma_{\text{laser}} P(\text{click})$. If we include the detector efficiency η, assumed to be low, into the overall setup efficiency η_{setup} we can experimentally retrieve the average photon number emitted by the source as:

$$\overline{\langle n\rangle} = \frac{R_{\text{photons}}}{\Gamma_{\text{laser}}\eta_{\text{setup}}} \tag{2.8}$$

This assumption of low detection efficiency will be valid in our experiments despite the use of SPADs having typically $\eta \approx 0.28$ because of the use of an optical setup of overall low efficiency (some percent). Additionally, in the case of the single-photon sources studied in this manuscript, where $P(n > 1) \ll P(1)$ by at least one order of magnitude, we can consider $\langle n\rangle \approx P(1)$. Both Eq.2.4 and Eq.2.8 then give a faithful estimation of the average photon number, thus the brightness $B = P(1)$ of the source.

2.2.2 Single photon purity

The single photon purity describes the probability that no more than one photon is emitted by the source in each wave packet. In general, for a non ideal photon source, the state of Eq.2.2 is:

$$|\psi\rangle = \sum_{\mathbf{k},\epsilon,n} P_{\mathbf{k},\epsilon}(n)\, |n\rangle_{\mathbf{k},\epsilon} \tag{2.9}$$

where n is not restricted to be 1. The presence of multiple photons, independently of their origin and of the mode profile of the wave packet, will degrade the performances of a device as a single-photon source.

Second order coherence The standard metric to access information about the photon statistics of the electromagnetic field is the second order correlations function, introduced by Glauber [164], which can be accessed with photon counting experiments. In term of photon creation and destruction operators the normalized second order correlation function for a stationary electromagnetic field can be written as:

$$g^{(2)}(\tau) = \frac{\langle \hat{a}^\dagger(0)\hat{a}^\dagger(\tau)\hat{a}(0)\hat{a}(\tau)\rangle}{\langle \hat{a}^\dagger(0)\hat{a}(0)\rangle\langle \hat{a}^\dagger(\tau)\hat{a}(\tau)\rangle} \tag{2.10}$$

This function describes the conditional probability of detecting a second photon after a time τ given a first photon detection event, normalized to the independent probabilities of detecting two photons. At zero time delay ($\tau = 0$) the above equation corresponds to the autocorrelation of the signal intensity, thus the normalized probability of detecting two photons at the same time. It becomes:

$$g^{(2)}(0) = \frac{\langle \hat{n}(\hat{n}-1) \rangle}{\langle \hat{n} \rangle^2} = 1 + \frac{\langle (\Delta \hat{n})^2 \rangle - \langle \hat{n} \rangle}{\langle \hat{n} \rangle^2} \tag{2.11}$$

where the variance of the photon number $\hat{n}$ in the field is $\langle (\Delta \hat{n})^2 \rangle = \langle \hat{n}^2 \rangle - \langle \hat{n} \rangle^2$. We see from the above equation that the value of the $g^{(2)}(0)$ is directly linked to the variance of the photon number in the analysed state, and can be used to classify the nature of the light based on its photon statistics.

Coherent light A coherent state of light $|\alpha\rangle$ shows a normalized correlation function of any order equal to 1. For such state indeed is possible to factorize the expectation values for the photon operators [165], which also imply the fact that each photon detection event is independent to any other. In particular we have $g^{(2)}(0) = 1$, thus the probability of detecting two photons at the same time is the same as for different times.

A coherent state $|\alpha\rangle$ is the eigenstate of the photon annihilation operator, and in the Fock state basis it is given by a Poisson distribution of photon number states:

$$|\alpha\rangle = e^{-\alpha^2/2} \sum_{n=0}^{\infty} \frac{\alpha^n}{\sqrt{n!}} |n\rangle \tag{2.12}$$

The Poissonian statistics reflect the random distribution of the detection events from a coherent state. It has an average number of photons $\langle \hat{n} \rangle = |\alpha|^2$ and a squared variance of $(\Delta n)^2 = |\alpha|^2 = \langle \hat{n} \rangle$. It is often referred to as classical state, because its expectation value for the electric field operator shows the oscillatory dependence expected from a classical electromagnetic wave, and its electric field fluctuations have the same magnitude as for the vacuum [166]. A laser operated above threshold generates coherent states of light.

Thermal light A thermal state of light describes the radiation generated by matter at thermal equilibrium with the environment (the blackbody radiation). The photon distribution follows the Bose-Einstein statistics, and the photon numbers probabilities can be calculated as [165]:

$$P(n) = \frac{\langle n \rangle^n}{(1 + \langle n \rangle)^{1+n}} \tag{2.13}$$

where $\langle n \rangle$ is the average photon number for the state and the square of the variance is given by $(\Delta n)^2 = \langle n \rangle^2 + \langle n \rangle$. The photon number variance is higher

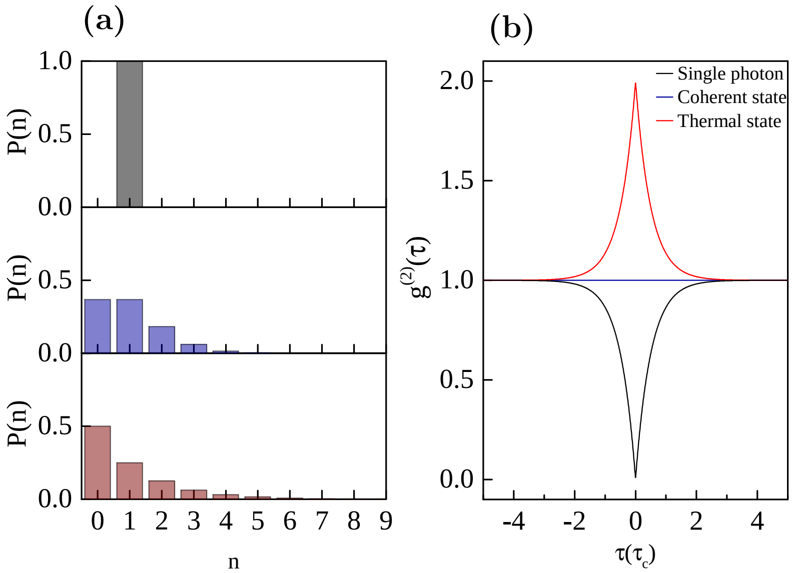

Figure 2.1 – (a) Photon number distribution for a single photon state (top), a coherent state (middle) and a thermal state (bottom), each having an average photon number $\langle n \rangle = 1$. (b) Second order correlation function $g^{(2)}(\tau)$ for the same three states as a function of delay τ in units of coherence time τ_c.

than the one of a coherent state, and the corresponding statistics is defined as super-Poissonian. Indeed, using Eq.2.11 we can obtain $g^{(2)}(0) = 2$, implying that the conditional probability of detecting two photons is higher than the product of two independent photon detection probabilities. This effect is called photon bunching.

Antibunched light Photon number states $|n\rangle$ are eigenvalues of the photon number operator, thus they show a zero variance $(\Delta n)^2 = 0$. While for the vacuum state $|0\rangle$ the second order correlation is zero, for a state with $n \geq 1$ we can obtain from Eq.2.11 that $g^{(2)}(0) = 1 - \frac{1}{n}$. This violates the classical limit for the second order correlation function, determined by the Cauchy–Schwarz inequality. Considering Eq.2.10 as the statistical average of real quantities, we must have $\langle n(0)\rangle^2 \leq \langle n(0)^2 \rangle$, which imply $g^{(2)}(0) \geq 1$ [165]. For this reason photon number states, among others, are defined as nonclassical states of light. For a single photon $|1\rangle$ we have $g^{(2)}(0) = 0$, which means that two coincident photons cannot be detected, and is reflecting the particle nature of the light. This effect is called photon antibunching.

A general superposition of photon number states can gives rise to any value of $g^{(2)}(0)$, both below and above 1. By calculating its expectation value on a generic wave packet ρ we obtain:

$$g^{(2)}(0) = \frac{\mathrm{Tr}[\rho\hat{n}(\hat{n}-1)]}{\mathrm{Tr}[\rho\hat{n}]^2} = \frac{\sum_{n=0}^{\infty} n(n-1)P(n)}{\left(\sum_{n=0}^{\infty} nP(n)\right)^2} = \\ = \frac{2P(2)+6P(3)+12P(4)+...}{(P(1)+2P(2)+3P(3)+...)^2} \tag{2.14}$$

We can see that the $g^{(2)}(0)$ relates the probability of observing multi-photon Fock components $P(n > 1)$ to the average photon number $\langle n\rangle = \sum_n nP(n)$ of the state. This quantity can then be used to find an upper bound for the multi-photon probability. We can write [167]:

$$P(n > 1) = \sum_{n=2}^{\infty} P(n) \leq \frac{1}{2}\sum_{n=0}^{\infty} n(n-1)P(n) \tag{2.15}$$

where we have used the fact that $n(n-1) \geq 2$ for every $n \geq 2$. Rewriting the last equation in terms of the $g^{(2)}(0)$ we obtain:

$$P(n > 1) \leq \frac{1}{2}\langle n\rangle^2 g^{(2)}(0) \tag{2.16}$$

We see that a $g^{(2)}(0) = 0$ can be obtained with a state made by vacuum and single photons only.

Measurement of the second order correlation function In a pulsed regime, it is convenient to consider a discrete version of the second order correlation function, where each pulse is treated as a whole. Each instant of time t then corresponds to the signal triggered by a different excitation pulse. Assuming that the initial condition of the source is the same at each excitation cycle, only the relative temporal delay between two pulses is relevant. In this condition, we can consider the operators $\hat{a}(0)$ and $\hat{a}(\tau)$ of Eq.2.10 as the pulse-integrated destruction operators separated by an integer number of pulses.

To experimentally access the value of the second order correlation function, a Hanbury-Brown and Twiss (HBT) configuration is used [168]. In such an intensity interferometer, the signal is sent to a beam splitter and a correlation measurement is performed on the two outputs using single photon detectors, as represented in Fig.2.2. An autocorrelation measurement can be turned into a cross correlation between the two optical modes into which the original signal has been split. The field operators at the inputs ($\hat{a}_0$, $\hat{a}_1$) and at the outputs ($\hat{b}_0$, $\hat{b}_1$) of the beam splitter are related by the beam splitter transformation as [166]:

$$\begin{pmatrix}\hat{b}_0\\ \hat{b}_1\end{pmatrix} = \begin{pmatrix}\sqrt{T} & \sqrt{R}\\ \sqrt{R} & -\sqrt{T}\end{pmatrix}\begin{pmatrix}\hat{a}_0\\ \hat{a}_1\end{pmatrix} \tag{2.17}$$

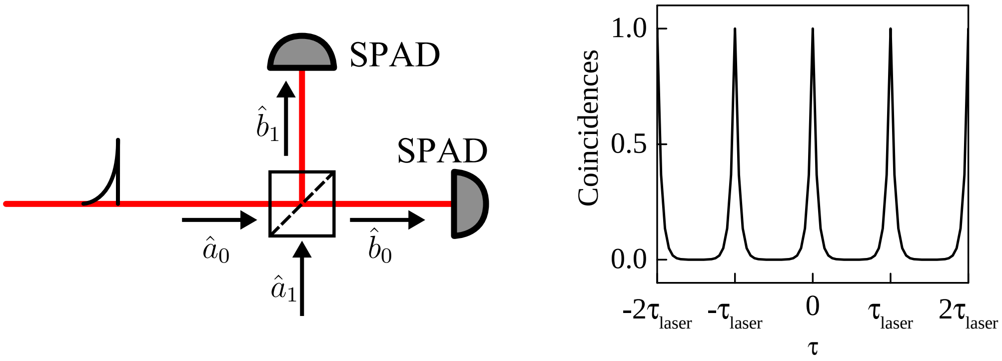

Figure 2.2 – Hanbury-Brown and Twiss interferometer for the measurement of the $g^{(2)}(\tau)$. The signal is sent to a beam splitter, whose second input is the vacuum. A correlation measurement is performed on the two outputs. The right curve shows a typical correlation curve where an histogram of the coincidences event between the two detectors is plotted as a function of time delay

Using these relations we can express a measurement on the outputs as a function of the input modes. Considering that we have the signal at the input port $\hat{a}_0$ and the vacuum at the input port $\hat{a}_1$, we find that:

$$g_{in}^{(2)}(\tau) = \frac{\langle \hat{a}_0^\dagger(0)\hat{a}_0^\dagger(\tau)\hat{a}_0(\tau)\hat{a}_0(0)\rangle}{\langle \hat{a}_0^\dagger(0)\hat{a}_0(0)\rangle\langle \hat{a}_0^\dagger(\tau)\hat{a}_0(\tau)\rangle} = \frac{TR\langle \hat{b}_0^\dagger(0)\hat{b}_1^\dagger(\tau)\hat{b}_1(\tau)\hat{b}_0(0)\rangle}{T\langle \hat{b}_0^\dagger(0)\hat{b}_0(0)\rangle R\langle \hat{b}_1^\dagger(\tau)\hat{b}_1(\tau)\rangle} \tag{2.18}$$

This means that the $g^{(2)}(0)$ of the input signal can be measured on the two outputs of the beam splitter and is insensitive to imperfections in the R and T coefficients. The experimental value of the second order correlation function at zero time delay $\overline{g^{(2)}(0)}$, is retrieved by normalizing the number of detected coincidences from a same excitation pulse, to the number of coincidences triggered by different pulses, thus uncorrelated events. Using two SPADs detectors, this corresponds to the conditional probability that both detectors click, divided by the product of the individual probabilities that each detector click:

$$\overline{g^{(2)}(0)} = \frac{P_{01}(\text{click, click})}{P_0(\text{click})P_1(\text{click})} \tag{2.19}$$

As shown by Stevens et al. [169], this can be calculated to be:

$$\begin{aligned}\overline{g^{(2)}(0)} &= \frac{\sum_{n=2}^{\infty}\left[1-(1-\eta_0 T)^n-(1-\eta_1 R)^n+(1-\eta_0 T-\eta_1 R)^n\right]P(n)}{\left[\sum_{n=1}^{\infty}[1-(1-\eta_0 T)^n]P(n)\right]\left[\sum_{n=1}^{\infty}[1-(1-\eta_1 R)^n]P(n)\right]} \\ &= \frac{2P(2)+6P(3)(1-\frac{1}{2}\eta_0 T-\frac{1}{2}\eta_1 R)+\ldots}{\left[P(1)+2P(2)(1-\frac{1}{2}\eta_0 T)+\ldots\right]\left[P(1)+2P(2)(1-\frac{1}{2}\eta_1 R)+\ldots\right]}\end{aligned} \tag{2.20}$$

where η_0 and η_1 are the efficiencies of the two detectors measuring the modes $\hat{b}_0$ and $\hat{b}_1$. In the limit of low detection efficiency we see that Eq.2.20 reduces to the form of Eq.2.14, thus gives the correct value of the second order correlation function:

$$\lim_{\eta_0,\eta_1\to 0}\overline{g^{(2)}(0)} = \frac{2P(2)+6P(3)+...}{(P(1)+2P(2)+...)^2} = g^{(2)}(0) \tag{2.21}$$

Moreover, for a typical single-photon source, we have that $P(n>2) \ll P(2) \ll P(1)$, and independently of the efficiencies of the detectors we can approximate Eq.2.20 to:

$$\overline{g^{(2)}(0)} \approx \frac{2P(2)}{P(1)^2} \approx g^{(2)}(0) \tag{2.22}$$

As already mentioned for the case of the brightness, we work here in a regime where both these approximations are valid.

2.2.3 Indistinguishability

Applications in quantum information science require to perform conditional operations depending on the state of two photons. These operations are typically implemented by linear optical quantum gates, where an effective photon-photon interaction is achieved by means of quantum interference effects. For these interferences to happens, the single photons must be indistinguishable. In the ideal case then all photons emitted by the source are in a same pure quantum state as in Eq.2.2. For a real source however, coupling to the environment can cause a fast decay of the coherence of the transition, as explained in Section 1.1.3 for the specific case of QDs. The emission must then be described by a statistical mixture of pure photon wave packets $|\psi_i\rangle$:

$$\rho = \sum_i c_i |\psi_i\rangle\langle\psi_i| \tag{2.23}$$

The indistinguishability is reduced due to the fact that different emission processes from a same source generates different photon wave packets. The degree of indistinguishability of the emitted photons is given by the degree of purity $\mathrm{Tr}[\rho^2]$ of the state of Eq.2.23 generated by the source.

Interference of single photons The indistinguishability between two photons can experimentally be measured through a quantum interference experiment first demonstrated by Hong, Ou and Mandel in 1987 [170]. This effect, at the hearth of many quantum information processing schemes, is depicted in Fig.2.3. When impinging on a beam splitter, the wave packet of a single photon is split into a transmitted and a reflected part, which differs by a $\pm\pi/2$ phase difference [171]. If a single photon is sent on each entrance, out of the four possible outcomes of the process, the two probability amplitudes for the two photons to exit

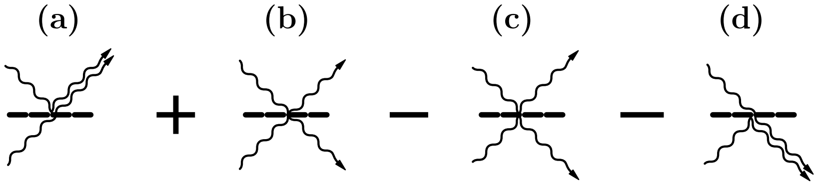

Figure 2.3 – Hong-Ou-Mandel interference between two single photons. The four figures represents the four possible outcomes of two photons impinging of a beam splitter: (a) the first reflected and the second transmitted, (b) both transmitted, (c) both reflected, (d) the first transmitted and the second reflected. When the two photons are indsitinguishable the cases (b) and (c) destructively interfere.

from different ports will destructively interfere. As a result both photons will always exits from the same port. If the two interfering photons are described by a same quantum state, we can write the state at the input and at the output of the beam splitter as:

$$|1,1\rangle \xrightarrow{BS} \left(|2,0\rangle - |0,2\rangle\right)/\sqrt{2} \tag{2.24}$$

In this case no coincidences can be measured at the two outputs. If the two photon are distinguishable in some degrees of freedom, such as a different spectral profile and coherence length, the interference will not be complete. For two distinguishable photons labelled a and b, we can write the input and output states as:

$$|1_a, 1_b\rangle \xrightarrow{\text{BS}} \frac{1}{\sqrt{2}} \left(|2_{ab}, 0\rangle - |0, 2_{ab}\rangle\right) + |1_a, 1_b\rangle - |1_b, 1_a\rangle \tag{2.25}$$

In this case there will be the possibility for the two photons to exit from different outputs and coincidences can be detected. The visibility of this quantum interference effect is proportional to the mean wave packet overlap M between the two incident photon states. For two mixed states, we have $M = \text{Tr}[\rho_i\rho_j]$, which becomes $M = |\langle\psi_i|\psi_j\rangle|^2$ if the two photon states are pure [172]. Studying the Hong-Ou-Mandel (HOM) interference we can then estimate the indistinguishability of the photons.

Experimental measurement of the indistinguishability In this work, we study the HOM interference of two photons emitted at different times by the same device. This allows us to access the indistinguishability of the emission from the source as $M = \text{Tr}[\rho^2]$. The experimental configuration used to do this is shown in Fig.2.4.a. Each excitation pulse is split using an unbalanced Mach-Zender into two pulses separated by a controlled temporal delay δt. The source is then excited twice every τ_{laser}, which is the period determined by the repetition rate of the laser $\Gamma_{\text{laser}} = 1/\tau_{\text{laser}}$. The signal coming from the source, triggered by

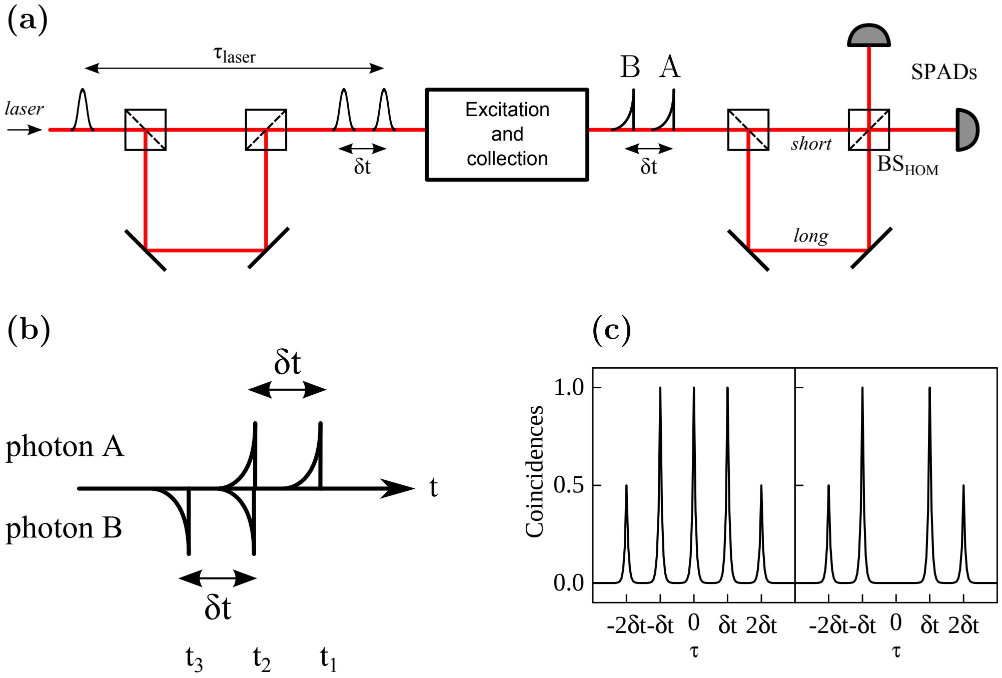

Figure 2.4 – Hong-Ou-Mandel interferometer for the measurement of the indistinguishability. (a) Experimental setup. Each laser pulse is split to excite twice the sample. The emitted photons (A and B) are sent to a Mach-Zender where they can interfere on the last beam splitter ($\mathrm{BS}_{\mathrm{HOM}}$). A correlation measurement is performed using two SPADs. (b) The two photons (A and B) are probabilistically distributed into three time bins (t_1, t_2 and t_3). (c) Expected correlation histograms for the case M=0 (left) and M=1 (right).

each pulse, is then directed towards a second Mach-Zender interferometer whose delay is adjusted to match the temporal separation δt between two subsequent excitations. In this way two emitted photons (A and B) can be temporally overlapped on the last beam splitter ($\mathrm{BS}_{\mathrm{HOM}}$), where they can interfere according to the HOM effect. A correlation measurement on the two outputs of this last beam splitter produces the five peaks structure shown in Fig.2.4.c, repeated every τ_{laser}.

To understand such correlations histogram, we can analyse in more details what happens to the emitted photons going through the second Mach-Zender (right part of Fig.2.4.a). Upon arrival on the first beam splitter (considered to be ideal, with $R = T = 0.5$), each photon wave packet is split into two parts, one of which acquires a relative delay of δt by the time they reach the second beam splitter. Since the delay δt is much larger than the coherence time of a photon, which is dictated by the radiative lifetime of the emitter, no interference can be observed between the two parts of a single photon wave packet. We can effectively consider them as routed between either the short or the long arm of the interferometer. The two photons (A and B) directed towards the detectors can thus be distributed into 3 time bins (t_1, t_2 and t_3) equally spaced by δt, as shown in Fig.2.4.b. Coincidences can be detected at relative delays τ of 0, δt and $2\delta t$ with relative probabilities of 1:2:1. The HOM interference can take place when the photon A is sent through the long arm and the photon B through the short arm (leading to a relative delay of $\tau = 0$), which happens with 25% probability. The other events, ruled by classical probabilities, happens when both photons take the same arm (giving $\tau = \delta t$) or when A takes the short and B the long one (giving $\tau = 2\delta t$), and can be used as a reference. In the classical case of fully distinguishable photons, when no quantum interference can take place ($M = 0$), the symmetry of the correlation measurement with respect to the zero delay events leads to the histogram of Fig.2.4.c (left), with relative peak areas of 1:2:2:2:1. In case of perfect interference ($M = 1$) between the two photons, the peak at zero delay vanishes, leading an histogram with relative peak areas of 1:2:0:2:1 as in Fig.2.4.c (right). The visibility of the two-photon interference can be extracted by comparing these two situations as:

$$V_{\mathrm{HOM}} = \frac{C_{\perp} - C_{\parallel}}{C_{\perp}} \tag{2.26}$$

and by considering an non-ideal beam splitter BS_{HOM} with reflectivity and transmission coefficients R and T, the experimental value of the mean wave packet overlap can be obtained as [108]:

$$\overline{M} = V_{\mathrm{HOM}} \frac{(R^2 + T^2)}{2RT} \tag{2.27}$$

Alternatively, the side peaks can be used as a reference to extract the value of the mean wave packet overlap from a single measurement. Including the effect of a non-zero $g^{(2)}(0)$, the expected areas for the peaks, normalized to the total number of excitation cycles, are [173]:

$$\begin{aligned}
A_{-2\delta t} &= R^2 \\
A_{-\delta t} &= 2RT + 2R^2 g^{(2)}(0) \\
A_0 &= T^2 + R^2 - 2RT\overline{M}(1-\epsilon)^2 + 4RTg^{(2)}(0) \\
A_{+\delta t} &= 2RT + 2T^2 g^{(2)}(0) \\
A_{+2\delta t} &= T^2
\end{aligned} \tag{2.28}$$

where R and T are the reflection and transmission coefficients of $\mathrm{BS}_{\mathrm{HOM}}$ and $(1 - \epsilon)$ is the classical interference visibility of the last Mach-Zender, accounting for imperfect mode overlap between the two interfering arms of the interferometer. Relating the zero-delay peak area (A_0) to the lateral ones ($A_{\pm\delta t}$), the experimental value of the mean wave packet overlap $\overline{M}$ is [44, 174]:

$$\overline{M} = \frac{1}{(1-\epsilon)}\left[2g^{(2)}(0) + \frac{R^2+T^2}{2RT} - \frac{A_0}{A_{-\delta t}+A_{+\delta t}}\left(2+g^{(2)}(0)\frac{(R^2+T^2)}{RT}\right)\right] \tag{2.29}$$

In the following experimental work, we will use this second relation to extract the mean wave packet overlap.

2.3 Available single-photon sources

In the following we discuss the two classes of sources currently used, compatible with the above requirements: nonlinear crystals, which can behave as heralded single-photon sources and single quantum emitters, which can behave as on-demand single-photon sources [163].

2.3.1 Spontaneous Parametric Down Conversion sources

For a long time, Spontaneous Parametric Down Conversion (SPDC) sources have been the most commonly used for quantum optics experiments. These sources are typically based on the $\chi^{(2)}$ nonlinear optical susceptibility of some materials, where the nonlinear interaction with an incident pump beam creates two frequency down-converted beams, called signal and idler, as represented in Fig.2.5.a. This down-conversion process, stimulated by vacuum fluctuations, leads to the decay of a pump photon (from a mode $\hat{a}_p$) into a correlated photon pair (in two modes $\hat{a}_s$ and $\hat{a}_i$). The two produced photons must satisfy the phase-maching conditions to conserve the energy and momentum of the original photon, which altogether define the joint spectral amplitude of the pair. This first requirement for SPDC sources implies a spatial and spectral filtering to control the shape of the output state, limiting the effective useful conversion efficiency. We assume here that the joint spectral amplitude of the produced pair can be engineered to be in a single spatial and spectral mode [175], without noticeable loss of performances. In the parametric approximation of a classical pump beam, the interaction Hamiltonian corresponds to a two-mode squeezing Hamiltonian [176]:

$$\hat{H}_{\mathrm{PDC}} = \hbar(\lambda^* \hat{a}_s^\dagger \hat{a}_i^\dagger + \lambda \hat{a}_s \hat{a}_i) \tag{2.30}$$

where $\lambda \propto \chi^{(2)}\mathcal{E}_p$ is a parameter proportional to the nonlinear susceptibility $\chi^{(2)}$ of the crystal and the field amplitude of the pump $\mathcal{E}_p$. The output state of the SPDC process can be calculated by applying the evolution operator associated to Eq.2.30 to the initial vacuum state as [166]:

$$|\psi_{\mathrm{SPDC}}\rangle = \exp[-i\hat{H}_{\mathrm{PDC}}t/\hbar]\,|0,0\rangle = \mathrm{sech}(\lambda)\sum_{n=0}^{\infty}\tanh^n(\lambda)\,|n,n\rangle_{s,i} \tag{2.31}$$

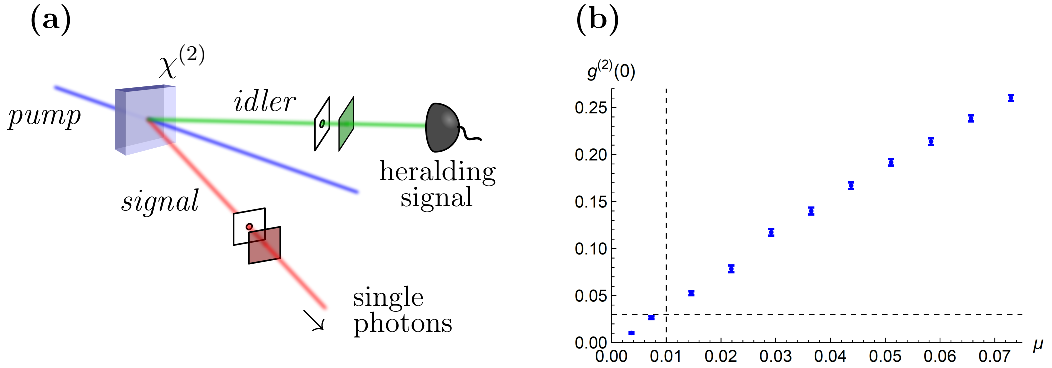

Figure 2.5 – (a) Schematic of a SPDC source. A pump laser is sent through a $\chi^{(2)}$ nonlinear crystal. The pump photons are downconverted into the signal and idler beams. Spatial and spectral filtering is applied to the downconverted beams, and one of the two is used to herald the presence of a photon in the twin beam. (b) Figure reproduced from [44]. Measured heralded second order correlation function $g^{(2)}(0)$ as a function of the source brightness, defined as the average photon number in the signal mode.

where $|n,n\rangle$ represents the product of two n-photon Fock state in the signal and idler modes. It corresponds to a two-mode squeezed vacuum state. If we measure the photon statistics at only one of the two output modes, it shows a thermal distribution of photon number states, where the probability of observing n photons is $P = \langle n\rangle^n/(\langle n\rangle+1)^{n+1}$. For small λ however it can be rewritten as [163, 177]:

$$\begin{aligned}|\psi_{\text{SPDC}}\rangle &= \sqrt{1-|\lambda|^2}\sum_{n=0}^{\infty}\lambda^n\,|n,n\rangle \\ &= \sqrt{1-|\lambda|^2}\left(|0,0\rangle + \lambda\,|1,1\rangle + \lambda^2\,|2,2\rangle + \ldots\right) \qquad (2.32)\end{aligned}$$

The probability of generating a pair of n-photon Fock state is $P(n) = (1-|\lambda|^2)|\lambda|^{2n}$, and the ratio $P(n+1)/P(n) = |\lambda|^2$ is linearly dependent on the pump power. For small incident power $|\lambda| \ll 1$ then the probability of creating multi-photon pairs is very small, thus it is possible to probabilistically generate single photon states by collecting one of the two output modes and using the other mode as an heralding signal. While SPDC devices cannot be on-demand, they are employed as heralded sources. Due to the fact that there is a perfect correlation between the photon number in the idler and in the signal modes, the detection of a single photon in one of the two can be used to herald the presence of the twin photon. The performances of such source depends both on the pump power and the efficiency of the detectors.

The measurement operation performed by a detector is described by its Positive-Operator-Valued Measure elements. For a detector having no Photon Number Resolving (PNR) capability and an efficiency η, the probability of detecting a signal is [163]:

$$P(\text{click}) = \sum_{n=1}^{\infty}[1-(1-\eta)^n]P(n) \tag{2.33}$$

For $\eta = 1$, a successful detection on the idler mode will herald on the signal mode the state:

$$|\psi_{\text{SPDC}}^{\text{herald}}\rangle \approx \frac{1}{|\lambda|}\left(\lambda\,|1,1\rangle + \lambda^2\,|2,2\rangle + ...\right) \tag{2.34}$$

Neglecting higher photon-number contributions, the second order correlation function can be calculated from $g^{(2)}(0) = 2P(2)/P(1)^2$, as detailed in Section 2.2.2. For the state of Eq.2.34, this gives $g^{(2)}(0) = 2|\lambda|^2$, thus a small $g^{(2)}(0)$ can be obtained for a low incident power. In this condition however, most of the time the output of the SPDC process will be the vacuum state $|0\rangle$ and the heralding is not successful. Typically to obtain a $g^{(2)}(0) \leq 0.05$, thus a photodetection signal dominated by single photons, the brightness is limited to 1% [44], as shown in Fig.2.5.b.

To overcome the limitations imposed by the presence of multi-photon components a PNR detector can be used, which can discriminate the detection events due to single photons. In this case the probability of detecting n photons from the incident distribution is given by [163]:

$$P(n) = \sum_{m=n}^{\infty}\binom{m}{n}(1-\eta)^{m-n}\eta^n\,|m\rangle\langle m| \tag{2.35}$$

which for $\eta = 1$ corresponds to a perfect n-photon projection $P(n) = |n\rangle\langle n|$ and can thus be used to filter only the events where a single photon has been emitted. As shown by A. Christ and C. Silberhorn [175], in the ideal case of perfect PNR detection, the heralding of a single photon with unit fidelity can be achieved. In this case, the pump power can be increased to decrease the vacuum contribution, but the heralding efficiency is fundamentally limited to 25% due to the thermal photon statistics of the state generated by the SPDC source. The realization of a pure deterministic single-photon source, having efficiency > 99%, would require a multiplexed setup of at least 17 SPDC sources [175], thus is demanding from the experimental point of view.

2.3.2 Single Quantum Emitters

Single quantum emitters can be used as on-demand sources of single photon Fock states. They are based on the spontaneous emission process, triggered by vacuum fluctuations, of an electronic transition between two discrete energy levels, which can only generate a single photon state. Let's consider an atomic two-level system, having an excited state $|e\rangle$ and a ground state $|g\rangle$. The spontaneous emission process cause an exponential decay of the excited state population, whose rate can be calculated using the Fermi golden rule:

$$\Gamma_{i \to f} = \frac{2\pi}{\hbar} |\langle f|\hat{H}_i|i\rangle|^2 \rho(E_f) \tag{2.36}$$

where $|i\rangle$ and $|f\rangle$ are the initial and final state of the system and $\rho(E_f)$ the available density of final states. In the rotating wave approximation, the electric dipole Hamiltonian describing the interaction between such transition and the electromagnetic field can be written as [84, 83, 178]:

$$\hat{H}_i = \hbar \sum_{\mathbf{k},\epsilon} g_{\mathbf{k},\epsilon} (\sigma a^{\dagger}_{\mathbf{k},\epsilon} + \sigma^{\dagger} a_{\mathbf{k},\epsilon}) \tag{2.37}$$

where $\sigma = |g\rangle \langle e|$ and $\sigma^{\dagger} = |e\rangle \langle g|$ are the atomic lowering and raising operators, $\hat{a}^{\dagger}_{\mathbf{k},\epsilon}$ and $\hat{a}_{\mathbf{k},\epsilon}$ are the field creation and destruction operators (for a specific mode $\mathbf{k}, \epsilon$) and $g_{\mathbf{k},\epsilon}$ is the atom-field coupling factor. Assuming the initial state of the system to be $|i\rangle = |e, 0\rangle$, where we have the atom in the excited state $|e\rangle$ and the field in the vacuum state $|0\rangle$, the perturbation described by Eq.2.37 only couples final states in the form $|f\rangle = |g, 1_{\mathbf{k},\epsilon}\rangle$. The radiation part of the final state is thus always is the form of a single photon state [1], whose specific mode profile will be determined by the accessible density of final states $\rho(E_f)$ and their coupling to the initial state $g_{\mathbf{k},\epsilon}$:

$$|\psi_{\text{sp}}(t \to \infty)\rangle = \sum_{\mathbf{k},\epsilon} c_{\mathbf{k},\epsilon} |g, 1_{\mathbf{k},\epsilon}\rangle = |g\rangle \otimes \sum_{\mathbf{k},\epsilon} c_{\mathbf{k},\epsilon} |1_{\mathbf{k},\epsilon}\rangle \tag{2.38}$$

Once the electron has decayed to the ground state $|g\rangle$, no other emission can take place, until it is excited again to $|e\rangle$.

Different types of quantum emitters are explored: natural atoms [182] and ions [183], molecules [184] and solid-state emitters [48]. Atoms and ions may appears as ideal candidates. They have many transitions which can be isolated and used for the production of single photons. Moreover any particle of a same species generates identical photons, thus multiple sources of indistinguishable photons can be realized [185]. An important limitation though is that atoms require very complex experimental setups in order to be isolated and trapped, and cannot be stored for long times. This makes it challenging to realize scalable devices. Solid-state sources instead are easier to manipulate and can be miniaturized and integrated. On the contrary, they are inevitably coupled to

---

[1] The result obtained with the Fermi golden rule corresponds to the first order of a perturbation expansion in the atom-field coupling. Considering higher orders will include contributions from multi-photon spontaneous emissions, which are typically negligible. Two-photon spontaneous emission has been studied in situation where the first-order transition is forbidden by selection rules or suppressed by a cavity [179, 180, 181].

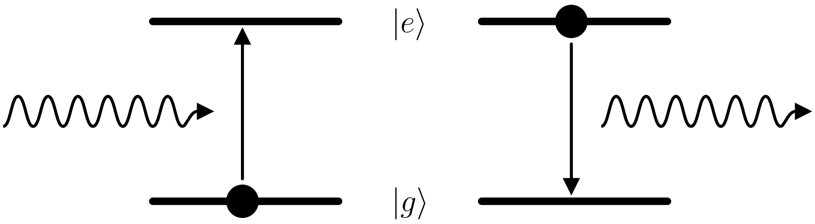

Figure 2.6 – Single quantum emitter. A two-level system is prepared to its excited state and the spontaneous emission process is used to generate a single photon. No photon can be emitted until the system is reinitialized to the excited state.

their environment, which can strongly affect the source properties. Quantum dots [108], colour centres in diamonds [186], carbon nanotubes [187] and localized states in 2D materials [188] are examples of different systems being studied as single-photon sources. Currently InGaAs QDs, such as the one of this work, shows the best performances.

A fundamental obstacle for any single quantum emitter is the difficulty of collecting the emitted photons. The common strategy is to couple their transitions to cavities or waveguides. By doing so it is not only possible to collect the emission more efficiently, but also to shape the spatial and spectral profile of the emitted photons. An important advantage of InGaAs QDs is in that III-V semiconductor fabrication techniques allows realizing high quality photonic structures, which can be used to produce efficient optical interfaces. As shown in Section 1.3, the fabrication used for the devices analysed here allows obtaining a single QD deterministically coupled to a micropillar cavity and a strong Purcell effect [38]. The high mode coupling achieved, on one side strongly reduce the effect of the environment, on the other side allows to funnel the emission into the confined mode defined by the optical cavity (see Section 1.2.4). We thus expect it to behave as a very efficient source of single and indistinguishable photons. Beside micropillars, also microdisks and photonic crystals cavities are explored to efficiently collect the emission from a QD. Microdisk cavities can be evanescently coupled to fibres [189] and photonic crystals can be engineered to provide out-of-plane directional emission to be coupled to a fibre [190]. An alternative approach is to couple the QD emission to the propagating modes defined by a waveguide. This has been experimentally demonstrated using photonic crystal waveguides by Lund-Hansen et al. [128] and using photonic nanowires by Claudon et al. [25]. The waveguide modes realize a broadband 1 dimensional continuum whose spatial and spectral matching to the QD transition is not as stringent as for a cavity, and in addition a very high mode coupling up to β =0.95 to a single propagating mode of the waveguide can be achieved [25]. An appropriate design of the waveguide allows a very high extraction efficiency, above 0.9 for off-chip approaches [191].

In the rest of this chapter we experimentally characterize the performances of our QD-micropillar device as a single-photon source, using the metric presented in section 2.2, under different optical excitation regimes.

2.4 Excitation regimes of the QD-micropillar device

The excitation of the QD with an optical field can be done using different schemes, represented in Fig.2.7. Electron-hole pair can be created either in the bulk continuum outside the QD, with an above band excitation, or directly into the QD. In the following we define as non-resonant excitation the direct excitation of a higher excited state of the QD, while resonant excitation the direct pumping of the fundamental exciton state.

Above-band excitation For above-band excitations, the energy of the incident laser is tuned to be higher than the GaAs bandgap (about 1.5 eV), creating electron-hole pairs in the bulk material (see scheme in Fig. 2.7). The charge carriers from the continuum will be trapped at random times in the wetting layer, from which they will eventually fall inside the QD. The captured electrons and holes first populate higher excited states of the QD and then rapidly relax through a non-radiative processes towards the fundamental exciton state [192]. This non-radiative relaxation is assisted by optical phonon scattering and happens on a typical timescale of 30 to 50 ns [193, 194, 195].

While easy to implement, this excitation scheme has multiple drawbacks. First of all, it doesn't give a direct control over the number of carriers created. By increasing the excitation power, multiple electron-hole pair can be formed in the bulk, which by relaxing into the QD will fill up the available energy levels before a radiative recombination can happen (which is typically at the timescale of 1 ns for the spontaneous emission of a QD). Moreover, electrons and holes are independently captured from the bulk GaAs, and the QD can be easily loaded with single charges. Thus any exciton complexes can be obtained: single exciton (X) and biexciton (XX) when one or two electron-hole pairs are present in the QD as well as charged excitons (CX) with an odd number of carriers. This process is also sensitive to the quality of the wetting layer, where defects at the interfaces can create trapping centres for the carriers. In the explanation above, we have assumed that the radiative recombination in the QD is the slowest process. However, if the typical time for the capture process is comparable or longer than the radiative lifetime of the exciton in the QD, an additional electron-hole pair can be recaptured after a first one has radiatively recombined [196, 197, 198]. This will lead to the emission of multiple single photons at the neutral exciton energy, which is strongly detrimental for the realization of a

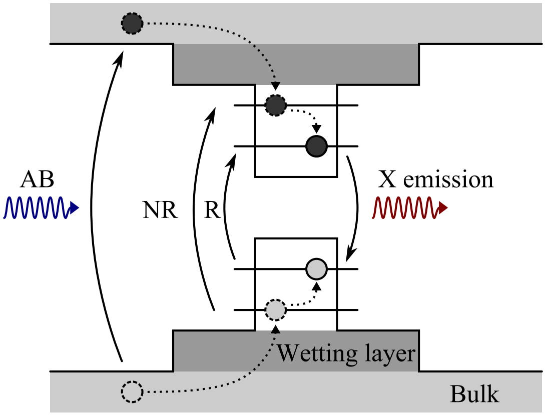

Figure 2.7 – Optical pumping of a QD. For an above band (AB) excitation electron-hole pairs are created in the bulk GaAs and then non-radiatively decay to the fundamental exciton state. For non-resonant (NR) and resonant (R) excitations, the excitonic states are created directly inside the QD.

single-photon source. This excitation technique then is not suited to obtain an efficient single photon emission from a QD.

Non-resonant excitation For a non-resonant excitation, the laser energy is lower than the wetting layer bandgap, and a discrete resonance inside the QD is directly pumped. The presence of these sharp resonances can be due either to higher excited states of an exciton in the QD or to phonon assisted absorption processes [199, 200]. In the first case, the laser directly creates an excited state of the exciton, when then energies of the two matches [201, 202]. Alternatively, if the distance between the pump laser and the energy of a lower-lying electronic level in the QD corresponds to an integer number of optical phonons, such discrete level of the QD can be efficiently populated thanks to a multi-phonon emission process [193, 203, 195]. In both cases, the excitation is followed by a fast non-radiative relaxation towards the fundamental exciton state, as explained for the above-band excitation. The first excitation mechanism allowed to observe Rabi oscillations of the excited exciton state in the QD [201, 202]. However, the coherent manipulation of an excited exciton state is limited to a very short timescale. The non-radiative relaxation, happening on a 50 ps timescale, causes an incoherent population transfer to the fundamental exciton state. In general then, with a non-resonant excitation, the fundamental exciton state cannot be coherently manipulated.

Using this pumping scheme, charges are created by pairs directly inside the QD, avoiding the addition of a single electron or a single hole. This excitation method is independent of the wetting layer quality. Since no recapture process can happen, the fundamental exciton state cannot be excited multiple times. Moreover, the total number of pair created is limited by the number of available discrete states below the excitation energy. By controlling the excitation power, it is then possible to create one or two electron-hole pair, and their sequential recombination will lead to the emission of a single photon at the energy of the fundamental exciton state [75]. To calculate the power dependence of the emission from the exciton state, we assume each incident photon to independently create an electron-hole pair. Following from this simple assumption, the probability of generating n pairs using a laser pulse having an average photon number $\langle n \rangle$ is given by:

$$P(n) = \frac{\langle n \rangle^n}{n!} e^{-\langle n \rangle} = \frac{1}{n!} \left(\frac{P}{P_0} \right)^n e^{-\frac{P}{P_0}} \tag{2.39}$$

where P and P_0 are respectively the incident power and the saturation power for the transition. Considering the radiative cascade in the QD, the emission intensity from the single exciton state is proportional to the probability of creating at least one electron-hole pair and can be simply calculated as $I_\mathrm{X} = I_0(1 - P(0)) = I_0(1 - e^{-P/P_0})$. It clearly shows a saturation behaviour: when the incident power is high enough, every excitation will create at least one electron-hole pair. The probability of obtaining a single photon will then be determined by the quantum efficiency of the X transition. This technique allows also to easily isolate the QD emission from the laser light, as they have different energy and spectral filtering can be used to remove the scattered laser. This non-resonant excitation is used in section 2.5 to study the emission from the QD-micropillar device.

Resonant excitation For a strictly resonant excitation, the laser energy is fixed at the energy of the fundamental exciton state. When exciting resonantly a two-level system with a coherent light field, the state of the system undergoes the well-known Rabi oscillations. In the ideal case of a closed system, under continuous wave driving, the occupation probability for the excited state is evolving in time according to:

$$P_e(t) = \sin^2 \left(\frac{\Omega\, t}{2} \right) \tag{2.40}$$

where $\Omega = 2g$ is the Rabi frequency of the driving field. The first maximum of this function is achieved after a time $t = \pi/\Omega$, when all the population is transferred to the excited state. By tailoring laser pulses so as to met this condition, we can deterministically bring the QD into the excited state and with a minimum amount of pump power. Such transfer is called π pulse excitation.

The resonant excitation of neutral and charged excitons has been used to observe Rabi oscillations in QDs both outside [204, 205, 206] and inside a cavity [207, 208]. This technique do not suffer from any incoherent relaxation process to populate the exciton state. However it is more difficult to isolate the QD emission, as it is at the same energy as for the excitation laser. The emission properties of the QD-micropillar device under resonant excitation are presented in section 2.6.

2.5 Performances for non-resonant excitation

2.5.1 Experimental setup

The experimental setup used for the characterization of the QD-micropillar devices under non-resonant excitation is represented in Fig.2.8. The sample is kept at 8 K in a gas exchange closed-cycle helium cryostat. A pulsed titanium-sapphire laser of tunable energy, providing 3 ps pulses with a repetition rate of 82 MHz is used to optically excite the QD. The laser can be sent through a pulse multiplication stage, used only for the indistinguishability measurements as explained later on, where each pulse is split into two pulses with a controlled delay δt between them. The laser pulses are then coupled to a single mode optical fibre, in order to be transferred to a confocal setup mounted on top of the cryostat. Once collimated again in free space, the excitation pulses are directed towards the sample where a microscope objective (with NA of 0.75) is used both to focus the laser on top of the micropillar cavity and also to collect the photoluminescence from the QD. A non-polarizing beam splitter cube (BS) is used to split and collect the signal coming from the sample. The collected signal (Signal) is then coupled to a second single mode fiber and transferred to the analysis stage. To precisely control the polarization of the incident and collected light and correct for any birefringence of the optical setup, a half wave plate (HWP) and a quarter wave plate (QWP) are inserted into the common path between the BS and the sample.

Depending on the analysis to be performed, the signal from the sample can be directed towards three different stages, as shown in the right part of Fig.2.8.b, each used to study one of the previously described property of a single-photon source. A measurement of the emission spectrum and the total intensity emitted from the source, thus the brightness, can be done using a spectrometer and a CCD. To study the single photon purity and the indistinguishability we use respectively a Hanbury-Brown and Twiss interferometer and an Hong-Ou-Mandel interferometer.

2.5.2 Spectroscopy of a single QD

To measure the emission spectrum from the sample, we send the collected signal into a spectrometer, where it is spectrally dispersed by a grating and detected using a CCD camera placed at one spectrometer output (see Fig.2.8).

By collecting emission spectra while sweeping the voltage, we can observe the

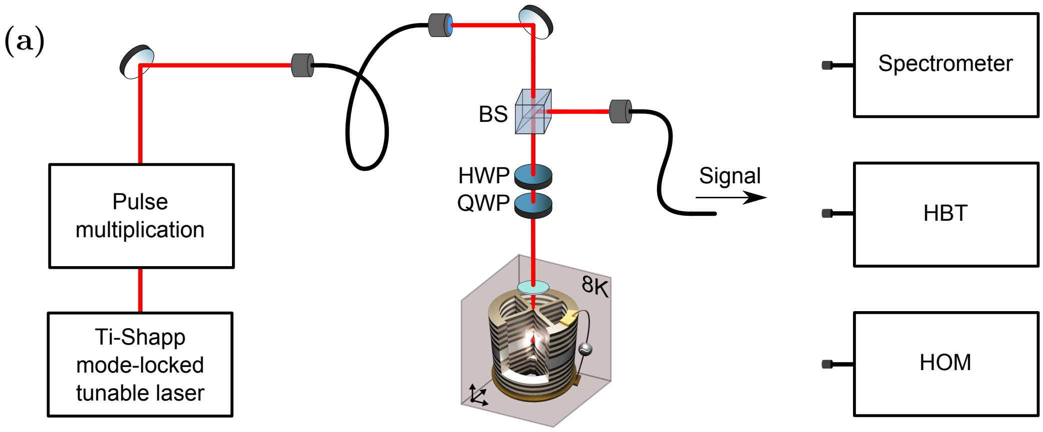

Figure 2.8 – Experimental setup for non-resonant excitation. A pulsed laser is used to excite the sample. The collected signal can be directed towards different analysis stages.

effect of the external bias on the QD states. A typical measurement, performed with an above-band laser excitation at 840 nm, is shown in Fig.2.9, where we observe several emission lines. A very strong signal is coming from the neutral exciton transition, the one targeted during the in-situ lithography, being in close resonance with the cavity mode. All other transitions instead are very dim, being far detuned from the fundamental cavity mode. By increasing the applied bias we can decrease all the emission energies, as expected from the quantum confined Stark effect. The energy shift ΔE of each transition indeed follows the behaviour of an electric dipole under an external electric field [63]:

$$\Delta E = -pF - \alpha F^2 \tag{2.41}$$

where p is the permanent electric dipole moment in the vertical direction, α is the polarizability and F the applied electric field. The quadratic behaviour is clearly visible for all transitions. A small but non-zero permanent electric dipole is also expected as the pyramidal shape of the self-assembled QDs normally leads to a different centre of mass position of the electron and hole wavefunctions along the growth direction [209, 210], corresponding to the direction along which the bias is applied. The right part of Fig.2.9 shows a close-up of the neutral exciton transition being shifted across the cavity resonance. The Purcell effect can be observed as a strong increase of the emission intensity from the QD, when its energy matches the one of the cavity. The voltage required to achieve this resonance condition will also depends on the incident excitation power, but in general we can rely on the observation of the strongest signal, thus the highest Purcell Factor, to adjust the external bias.

A polarization-dependent spectroscopic analysis can also be used to study the polarization splitting for the cavity and for the QD states. We expect both

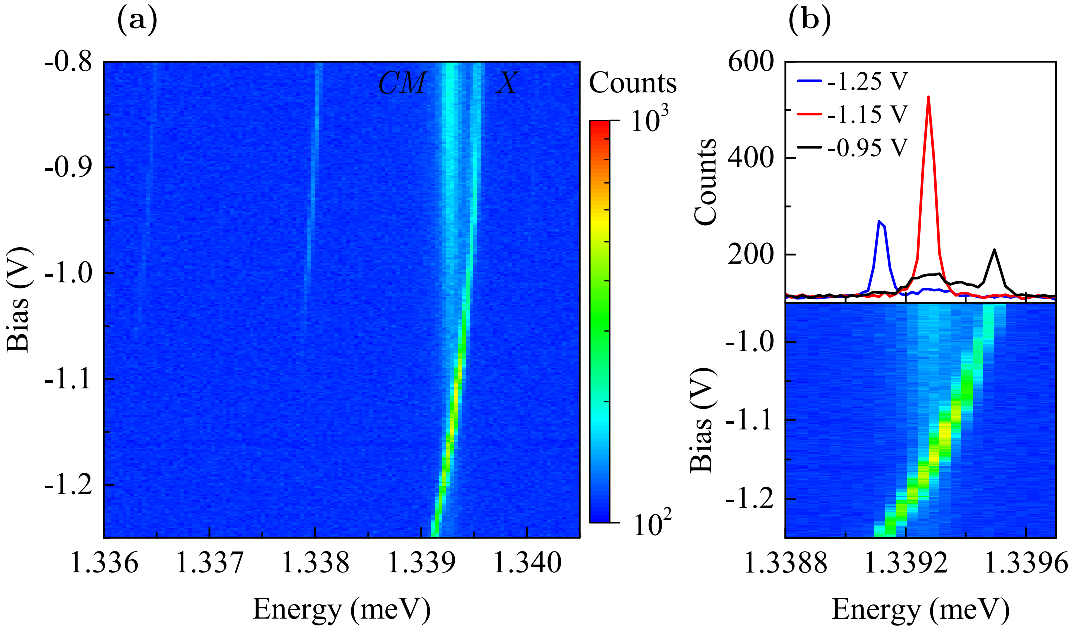

Figure 2.9 – Voltage dependence of the emission spectrum under above-band excitation (840 nm) for the device labelled QD3. (a) Collected intensity as a function of the emission energy and applied bias. (b) Bottom panel: close-up of the same data around the resonance condition. The top panel shows the emission spectrum at -0.95 V (black), -1.15 V (red) and -1.25 V (blue).

the micropillar cavity and the QD to have a slight ellipticity in their in-plane section. The fundamental mode of the micropillar can then be decomposed into two linearly polarized modes slightly split in energy, and similarly the neutral exciton will shows a finite Fine Structure Splitting (FSS) between the energy of the two linearly polarized exciton eigenstates, as explained in Section 1.1.2. This is reflected into the polarization dependence of the emission from the sample. To measure the orientation of both the cavity and exciton eigenstates, the bias is now adjusted in order to detune the QD line away from the cavity so as to clearly distinguish the different contributions to the spectrum. As shown in Fig.2.10.a for the device named QD1, the shift in the cavity mode emission for two orthogonal polarizations is clearly visible, while the shift of the exciton is much smaller. Rotating the half wave plate on top of the sample (HWP) we can collect the emission spectra as a function of the polarization. A fit of multiple Lorentzian peaks to these spectra allows us to retrieve the energies and the axis of the cavity and exciton eigenstates. As it is shown in Fig.2.10.b, both shows a non-zero splitting. Additionally, we can observe that the exciton eigenstates are not aligned to the cavity polarization axis, but they are rotated of about 35° with respect to each other. This condition is required to observe the reso-

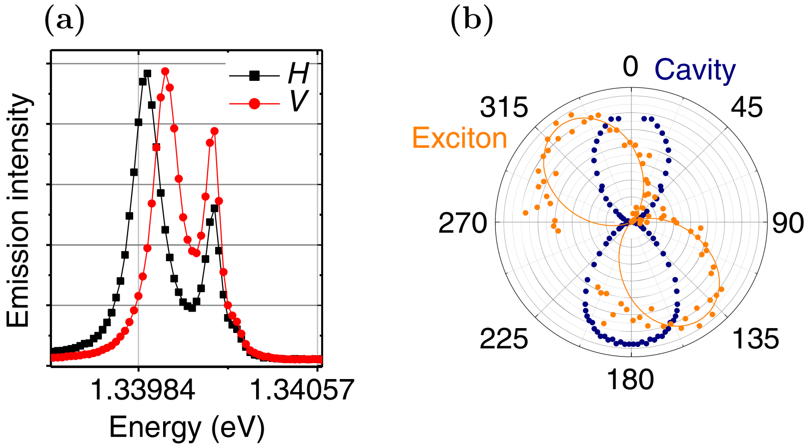

Figure 2.10 – Figure reproduced from [20]. Polarization dependence of the emission spectra measured from device labelled QD1. (a) Emission spectra for linear polarization aligned along the H and V cavity modes. (b) Polarization dependence of the emission from of the cavity and of the exciton. From this measurement a relative angle of about 35° between the two.

nance fluorescence from the neutral exciton state, as explained later in Section 2.6.3. The axis orientation is resulting from the fabrication of the lateral ridges connecting the micropillar cavity to the surrounding circular frame at 45° from the crystallographic orientation of the sample. The exciton FSS is preferentially aligned along the [110] and [1 -1 0] crystal axis of the GaAs substrate, as previously reported in literature [63, 211], while the cavity polarization splitting is determined by the elongation along the lateral ridges. As a result this configuration turns out to be useful to resonantly excite the QD, as will be explained later in Section 2.6.3.

2.5.3 Brightness of the source

Brightness of a QD in a micropillar For a QD coupled to a micropillar, the intrinsic brightness can be calculated from the characteristics of the device as:

$$B = p_X \beta \eta_{out} \tag{2.42}$$

For our devices p_X is the occupation probability for the exciton state (as in this case we consider the emission from the exciton state) at the end of each excitation cycle, β is the mode coupling between the exciton and the micropillar and η_{out} is the output coupling efficiency from the top mirror, as explained in section 1.2.4. Generally p_X describe the efficiency in the preparation of the radiating state of the atomic system, β the probability that the emission is collected by the photonic structure and η_{out} the efficiency in extracting the photons from it. When each of the three terms is equal to 1, we obtain a deterministic source,

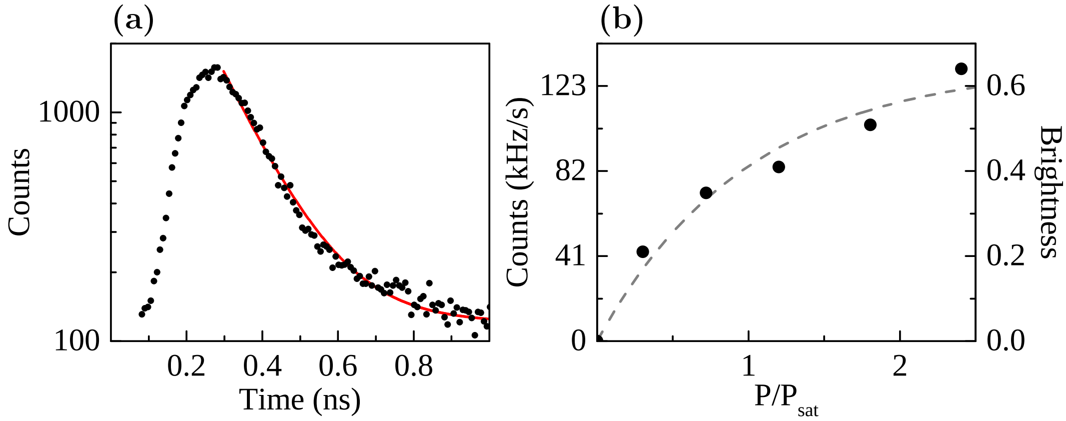

Figure 2.11 – (a) Time dependence of the emission at the energy of the neutral exciton state. (b) Saturation curve of the emission from the same transition, for the device labelled QD1 under non-resonant excitation.

providing a single photon at every excitation cycle, a situation never reached so far.

The definition of Eq.2.42 corresponds to the brightness at the first lens, just outside the source. As such it does not take into account additional signal processing which could be required in order to actually use the emitted photons, like spectral, spatial or polarization filtering, the coupling to an optical fibre or any losses introduced by optical elements. The specific implementation of an experimental setup can further reduce the effective brightness of the source, and it often needs to be taken into account for a useful estimation of B. This will be the case in Sec.2.6, where a cross-polarization configuration is used, limiting the amount of photons which can be collected thus reducing the effective brightness.

Measured brightness The same configuration used in the previous section can also be used to spectrally filter only the emission at the energy of the neutral exciton transition, observed at 925 nm when on resonance with the optical mode of the cavity. To do so the signal is directed to the second output of the spectrometer, where is being spatially filtered in the Fourier plane by the mechanical slits at the output. The resulting signal, in a narrow spectral range around 925 nm, is then detected by a Single Photon Avalanche Diode (SPAD).

The time dependence of the emission can be measured by collecting the detection events from the SPAD as a function of the delay with respect to the excitation laser pulses. The resulting histogram is shown in Fig.2.11.a, obtained using an *ID Quantique* detector having a time resolution of about 30 ps. A fit to a single exponential decay function gives a radiative lifetime of 150 ps for the exciton state. Considering a typical lifetime of 1.3 ns for an InGaAs QD in bulk, from the shortening of the radiative lifetime we can calculate a Purcell factor $F_P = 8.6$.

Such a Purcell factor corresponds to a mode coupling $\beta = 0.90$, implying a dominant fraction of emission from the QD being funnelled into the cavity mode. Considering an output coupling efficiency of $\eta_{out} = 0.7$, which is determined from the reflectivity spectrum as explained in Chapter 4.3.2, we have a photon extraction efficiency from the QD-cavity device of $\beta\eta_{out} = 0.63$. The maximum possible brightness is then $B = \beta\eta_{out}p_X = 0.63$ and can be achieved for a unit occupation probability of the exciton state $p_X = 1$. This condition can be met at saturation, as explained in Section 2.4, if no state other than the neutral exciton can be populated following the excitation pulse.

To experimentally measure the brightness, we monitor the number of detected counts per second by the SPAD as a function of the excitation power. By carefully characterising every elements of the optical setup used for non-resonant excitation, the overall efficiency was estimated to be 0.25%, including the detector efficiency. Using this value we can relate the count rate measured at the detector to the count rate expected on the first lens (here the objective used to collect the photoluminescence). Dividing such number by the laser repetition rate $\Gamma_{laser} = 82$ MHz, we obtain the experimental value of the brightness as $\overline{B} = \frac{R_{\text{photons}}}{\eta_{\text{setup}}\Gamma_{\text{laser}}}$. The result is plotted in Fig.2.11.b, where we see that the signal from the exciton clearly shows a saturation behaviour. At the maximum tested power, we detect 0.125 MHz on the SPAD, which corresponds to a 50MHz count rate at the fist lens, giving a brightness of 0.61. The dashed line in Fig.2.11.b shows a fit to the saturation equation $\overline{B}\left(1 - e^{-P/P_{sat}}\right)$ which gives a brightness at saturation of $\overline{B} = 0.65 \pm 0.07$. This is compatible with the theoretical maximum value of 0.63 estimated before. As such, it is also consistent with $p_X = 1$, suggesting the absence of blinking effects which could limit the brightness by reducing the probability of being in an exciton state due to single charges randomly loaded into the QD.

The very high brightness achieved here is close to the record values of 80% obtained with isolated micropillars cavities [41], showing that the use of connected devices do not significantly alter the optical mode of the cavity.

2.5.4 Single photon purity

To study the single photon purity from the neutral exciton line, we use the external bias to keep the selected transition in resonance with the cavity mode energy, where the highest Purcell effect is observed. The signal from the sample is then sent towards a free space beam splitter cube, and the two outputs from this cube to two different spectrometers, which are used to spectrally filter only the emission from the neutral exciton transition. Each spectrometer output is then detected by a *PerkinElmer* SPAD (having 350 ps resolution and 30% efficiency at 925 nm), and a correlation measurement performed between the two SPADs signals using a *PicoQuant* correlator. A typical measurement, obtained for a high excitation power of 2.5 times the saturation power P_{sat}, where the device

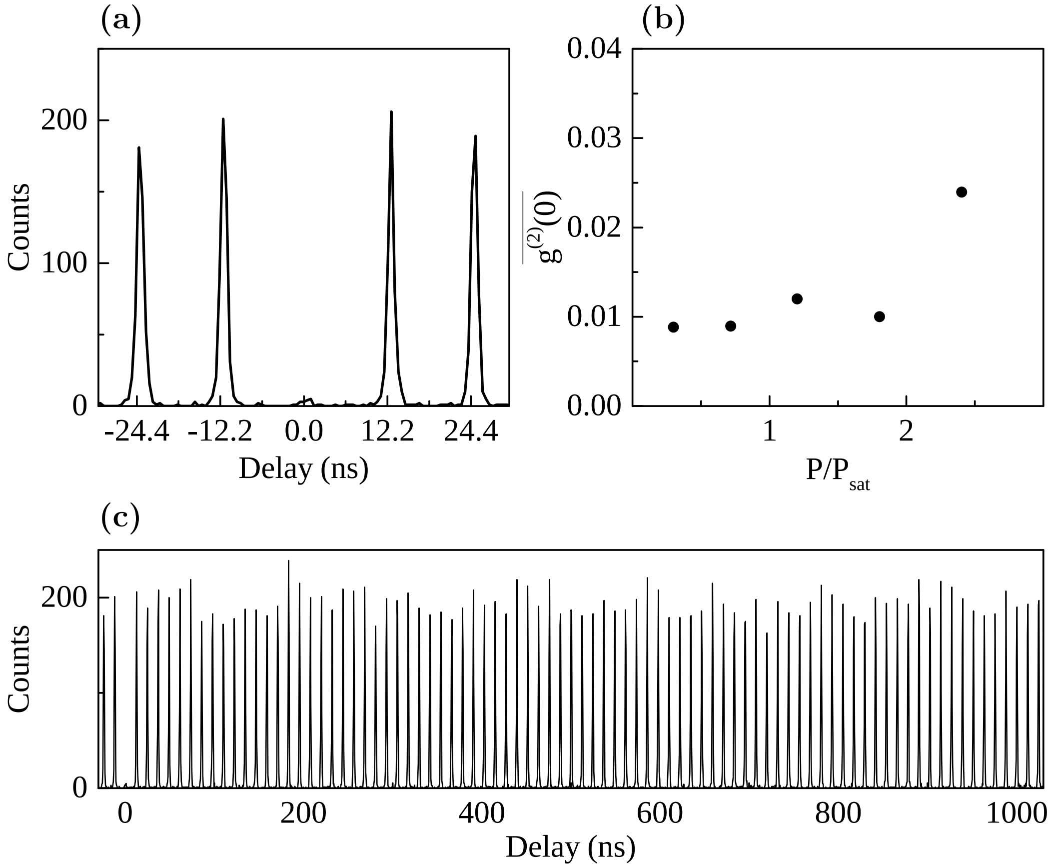

Figure 2.12 – Second order correlation of the emission from the device QD1. (a) Correlation histogram of the $\overline{g^{(2)}(\tau)}$ for an excitation power $P_{\text{in}} = 2P_{\text{sat}}$. (b) Measured $\overline{g^{(2)}(0)}$ as a function of the excitation power. (c) Temporal dependence of the $\overline{g^{(2)}(\tau)}$ for long delays.

has the maximum brightness, is shown in Fig.2.12.a and c. The plots shows the histogram of the detected coincidences, binned with a 128 ps time resolution, as a function of the time delay between the detection events. The series of peaks spaced by 12.2 ns represents the QD emission triggered by different excitation pulses of the laser, while between adjacent peaks we can observe a negligible background. At zero time delay, where we observe the detection events on both SPADs arising from a same excitation pulse, the plot shows a very small area for the peak. The total number of counts in each peak is integrated in a 1 ns range. As explained in Section 2.2.2, by normalizing the area of the central peak to the average area of the peaks at non-zero delay, we can retrieve the value of the second order correlation function at zero time delay, which for Fig.2.12.a is $\overline{g^{(2)}(0)} = 0.024 \pm 0.007$. Such a strong antibunching demonstrate the single photon character of the emission from the QD transition. The $\overline{g^{(2)}(0)}$ has been measured for different values of the excitation power, and the results are plotted in Fig.2.12.b. It shows an almost constant $\overline{g^{(2)}(0)} = 0.013$, with a slight increase only well beyond the saturation.

Fig.2.12.c shows the measurement of Fig.2.12.a for a longer delay, evidencing the absence of any dependence at long time scale. This confirms that no blinking effect is observed in the QD. Such a stability for the long time scale of $\overline{g^{(2)}(\tau)}$ is a first indication of the charge noise suppression obtained with the gated device.

2.5.5 Indistinguishable photon emission

In order to measure the indistinguishability of the photons emitted by the device, we perform here a Hong-Ou-Mandel (HOM) experiment with free space optics on the collected signal, where two photons, emitted one after the other, are temporally overlapped and can interfere on a beam splitter, as explained in Section 2.2.3.

Each laser excitation pulse is now split into two pulses of equal intensity 3 ns apart, using a free space delay line. As a result the sample is excited twice every 12.2 ns. The collected signal is then sent to one entrance of a Mach-Zender interferometer, where the delay between the two arms is set to 3 ns, in order to match the delay between two subsequent excitations. The detection is performed as for the HBT experiment. The two outputs of the last beam splitter of this interferometer are spectrally filtered using two different spectrometers, and detected by two SPADs, as was done in the previous section for the $\overline{g^{(2)}(0)}$. The resulting histogram of a correlation measurement between these two SPADs is shown in Fig.2.13.a.

As described in Section 2.2.3, the measurement shows a structure of five peaks, here spaced by 3 ns, repeated every 12.2 ns, the period dictated by the laser repetition rate. The reduced number of coincidences detected at zero time delay reflects the quantum interference between single photons. The experimental value of the mean wave packet overlap between two subsequent photons can be extracted using Eq.2.29, which relates the area of the zero delay peak to the lateral ones (at a relative delay of ±3 ns). Due to the specific delay chosen here, the outmost peaks of each group are superimposed to the adjacent ones. Since the overlap between different signals is not negligible, to extract the area of the individual peaks we fit a double-sided exponential decay to each of them, shown by the grey lines in Fig.2.13.a. We also measure a reflectance and transmittance coefficients of $R = 0.45$ and $R = 0.50$ for the beam splitter cube where the two photons interfere, and a classical interference visibility in the HOM setup of $(1 - \epsilon) = 0.95$ using a CW laser. From the measurement here presented, we retrieve a value of mean wave packet overlap of $\overline{M} = 0.78$, when corrected using the previously measured $\overline{g^{(2)}(0)} = 0.024$. The photons emitted by the source are thus significantly indistinguishable even at saturation, where the device shows a very high brightness of 0.65.

The measurement of $\overline{M}$ is repeated for different excitation powers and the

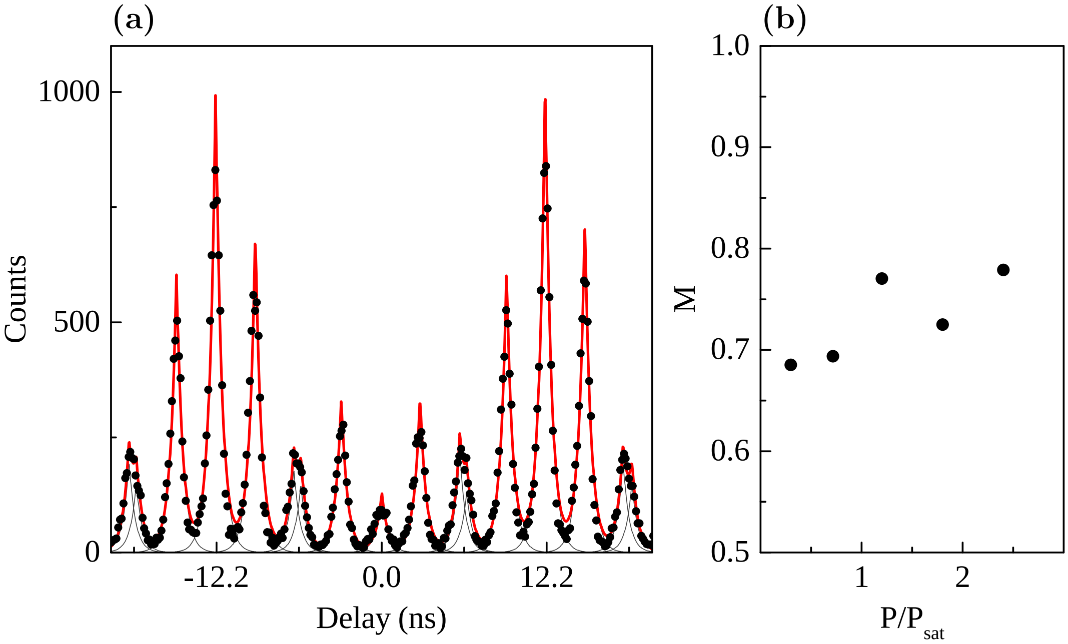

Figure 2.13 – Indistinguishability of the photons emitted by the device QD1 under non-resonant excitation. (a) Correlation histogram obtained from the HOM experiment for $P_{\rm in} = 2P_{\rm sat}$. (b) Measured mean wave packet overlap as a function of the excitation power.

resulting values are plotted in Fig.2.13.b. Here we see that the indistinguishability does not depend on the saturation of the transition, and we always observe a mean wave packet overlap in the range from 0.7 to 0.8, even well beyond the saturation value of the QD transition, where the device shows the maximum brightness.

This is a strong indication that the electrical noise is effectively cancelled through the application of an external bias. Gazzano et al. [41] have previously showed that highly indistinguishable photons (with $M \approx 0.8$) from micropillar cavities can be obtained under non-resonant excitation by introducing a second weak CW pump at 850 nm. This was attributed to a stabilization of the charge environment operated by the second laser. The use of an electrically contacted structure lifts the requirement for a two colour excitation scheme, which still is not effective at high excitation power. By tilting the band of the p-i-n structure, it is possible to sweep away uncontrolled charges from the intrinsic region, where the QD is located, so as to suppress the main source of spectral diffusion. This is consistent with previous studies of gated devices, which already allowed to observe transform-limited linewidth [106, 212]. In particular, it has been demonstrated using spectroscopy measurements that in bulk samples the charge noise takes place mainly at low frequency, below 50 kHz [105], having a negligible effect at the ns timescale separating the two photons that we are probing with this experiment.

In these conditions, one could reasonably expect that the effect of the environment becomes negligible on the indistinguishability of the emitted photons. The high Purcell effect obtained with the micropillar cavity efficiently suppress the phonon-assisted single photon emissions at 8 K [100], while the gated structure suppress the charge noise at high frequency. Still, all the measurements we have performed did not allowed to observe a mean wave packet overlap above 0.8 under non-resonant excitation.

The maximum value of indistinguishability that we observe is indeed limited by the non-resonant excitation scheme. While a transform limited linewidth assure the same decay profile for the emitted photon wave packets, the rise time cannot be coherently controlled. By creating charges in a higher excited state of the QD, a fast non-radiative carrier relaxation to the fundamental exciton state, assisted by phonons, takes place with a typical timescale of tens of picoseconds [195]. This process, required to populate the fundamental QD level, introduces an uncontrolled time-jitter in the emission time of the photons. In the high Purcell regime, this uncertainty in the creation of the fundamental exciton state becomes comparable to the radiative lifetime of the exciton state itself. As a consequence the HOM interference of two photons is limited by the random variations in their arrival time, which makes the two photons distinguishable. This effect has been theoretically studied by Kiraz et al. [87], which have shown that the incoherent excitation of a QD is a fundamental limitation to the obtention of highly indistinguishable photons with high brightness for a QD in an optical cavity. For the high Purcell effect measured here, they predict a maximum indistinguishability around 80%, which is consistent with the limit we observe under non-resonant excitation.

Following this discussion, we expect to be able to observe fully indistinguishable photons using a coherent excitation scheme, by directly exciting the fundamental exciton state.

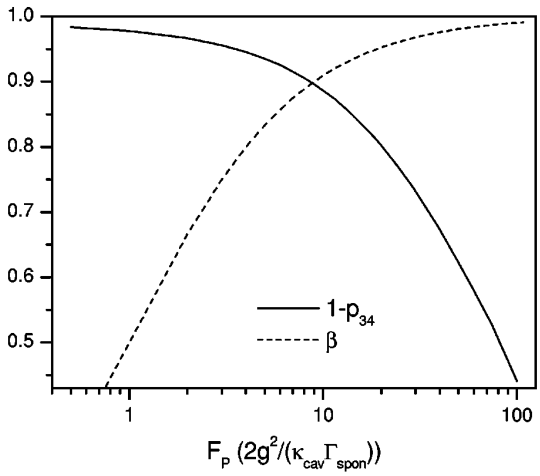

Figure 2.14 – Figure from [87]. Expected indistinguishability $(1 - p_{34})$ and mode coupling (β) as a function of the Purcell effect (F_P) for a QD coupled to a cavity under non-resonant excitation.

2.6 Resonant fluorescence

While embedding the QD in a gated microcavity allows to strongly suppress all dephasing effects due to the coupling with the solid-state environment, a full control of the photon wave packet requires also a resonant excitation scheme. Here we presents the excitation technique and the emission properties of the device under resonant pumping.

2.6.1 Experimental setup

For the resonant excitation scheme a spectral filtering to separate the excitation laser from the signal cannot be used, since they both have the same energy. In a previous work by Ates et al. [207], the resonant fluorescence under continuous wave excitation from a QD in a micropillar cavity has been isolated using a lateral excitation geometry, where the pump laser was focused on the sidewall of the micropillar, while the emission was collected from the top. Since we are working in a reflectivity configuration, where both the excitation and collection are performed through the same top mirror, this spatial filtering of the laser cannot be used either. To suppress the scattered laser light we employ here a cross-polarization configuration, as used by He et al. [208], where excitation and collection are performed along orthogonal polarizations.

The new setup is shown in Fig.2.15, and consists in the same confocal layout as the one of Fig.2.8, where the beam splitter is now replaced by a polarizing beam splitter (PBS). The 3 ps pulses of the titanium-sapphire tunable laser are first spectrally shaped using a monochromator and an optional etalon filter, and then directed towards the sample using the excitation fibre. The incident light is

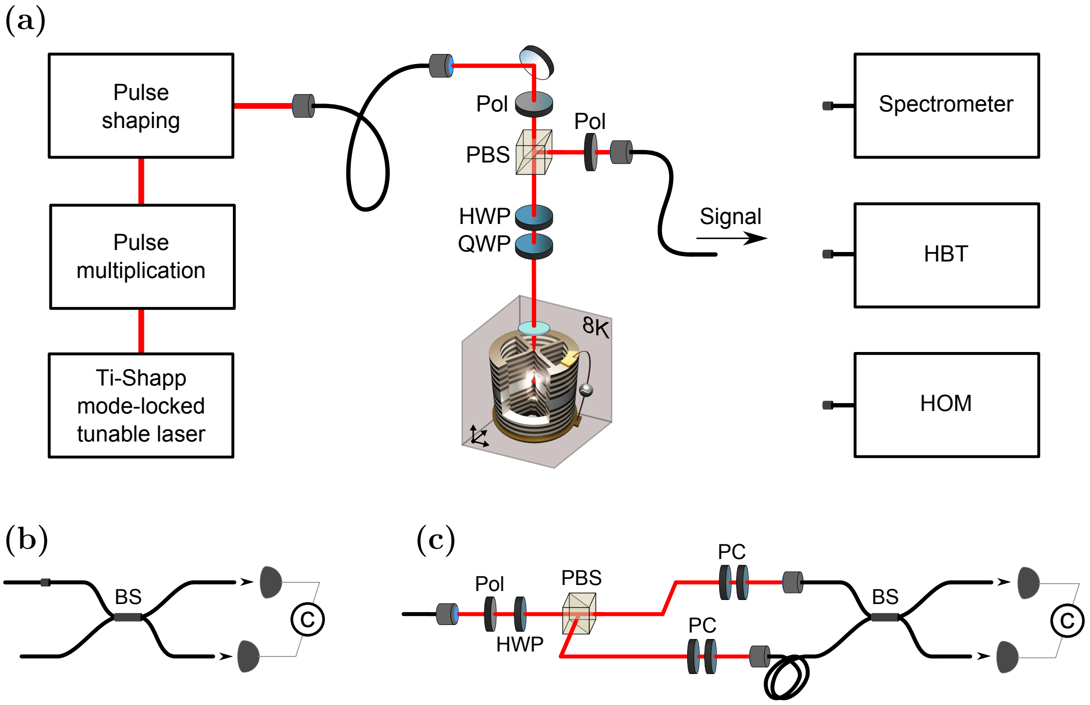

Figure 2.15 – (a) Experimental setup for resonant excitation experiments. (b) Fibered Hanbury-Brown and Twiss interferometer. (c) Fibered Hong-Ou-Mandel interferometer.

linearly polarized using a polariser (Pol) and the PBS. The signal coming from the sample along the orthogonal polarization is then diverted by the PBS and filtered with an additional polariser (Pol), before being coupled to the collection fibre. This configuration allowed to achieve a maximum laser extinction ratio of about 1×10^5 under pulsed excitation. Like for the non-resonant case, the polarization of the incident light (always orthogonal to the collected one) can be chosen by finely adjusting a half wave plate (HWP) and a quarter wave plate (QWP) placed between the PBS and the sample. The signal can be directed to the same analysis stages as before, but now their implementation is slightly different as no additional spectral filtering is required, and will be detailed later on.

2.6.2 Resonant spectroscopy

A careful adjustment of the excitation condition is fundamental in order to efficiently suppress the background of the collected signal, coming from the excitation laser. As the QD must be excited through the optical mode of the cavity, the incident pulses must be matched to the constraints imposed by the cavity.

First of all, the excitation spectrum must be narrow enough to be contained within the Lorentzian cavity linewidth, here of about 120 μeV. For this reason a spectral filtering is applied to the Gaussian pulses provided by the laser, in order to achieve a controlled temporal profile of 15 ps or longer. This allows to minimize the amount of laser light directly reflected back by the cavity.

Secondly, we have seen that the fundamental optical mode of the micropillar is split in energy by 70 μeV into two linearly polarized modes. If the polarization of the incident laser does not match one of the two linear cavity axes, a polarization rotation induced by the cavity splitting will lead to a high amount of laser light being coupled back into the orthogonal polarization. To avoid this effect, the angles of the wave plates must be finely adjusted so that the linear polarization of the laser corresponds to that of the cavity modes and is maintained upon reflection from the cavity.

We define here the H and V polarizations to correspond respectively to the higher and lower energy modes of the cavity. In the following the laser energy is fixed at the higher cavity mode energy and its polarization to H. A measurement of the photoluminescence emission in the V polarization, under resonant continuous-wave excitation, is shown in Fig.2.16, as a function of the emission energy and applied bias. When the QD transition is detuned from the cavity mode energy, if the wave plates are optimally aligned, the background from the scattered laser light is negligible. By tuning the exciton transition in resonance with the cavity mode energy and laser, an increase of more than two orders of magnitude is observed in the collected signal. This is the signature of the resonance fluorescence, emitted by the QD into the polarization orthogonal to the excitation one. The polarization rotation, thanks to which we can excite along H and collect a signal along V, is possible owing to the fact that the exciton has a finite Fine Structure Splitting (FSS), and our excitation does not match any of the two QD axis. To understand how this scheme allows the coherent excitation of the QD we analyse in more details the emission mechanism in cross polarization in the next section.

2.6.3 Coherent manipulation of the exciton transition

When exciting resonantly a two-level system with a coherent light field, the state of the system undergoes the well known Rabi oscillations, where the occupation probability for the excited state is oscillating in time. By tailoring the laser pulses such that at the end of an excitation pulse all the population is transferred to the excited state, we can deterministically excite the QD with a minimum amount of pump power. Such transfer is called π pulse excitation.

In our case, as we are exciting along the H cavity mode, the Rabi rotation will happen between the ground state $|G\rangle$ of the QD and an exciton state $|H\rangle$ linearly polarized along the H cavity axis. As shown in Fig.2.10 both the micropillar cavity and the QD present a slight ellipticity in their in-plane section, which results for device QD1 in a polarization splitting of 70 μeV for the former and a FSS of $\Delta_{FSS} = 15\ \mu eV$ for the latter. The two linearly polarized exciton

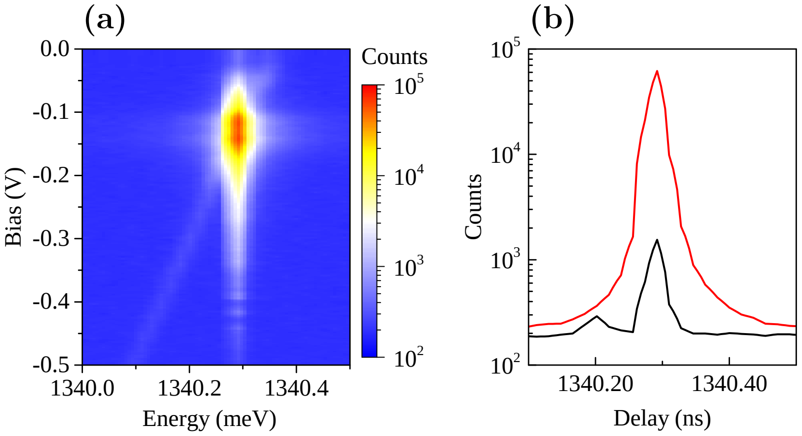

Figure 2.16 – Voltage dependence of the emission spectrum under resonant excitation, for the device QD1. (a) Collected intensity as a function of the emission energy and applied bias. (b) Emission spectrum at -0.35 V (black) and -0.15 V (red), showing the broadening of the transition and the strong increase in the collected intensity.

eigenstates, here called $|X\rangle$ and $|Y\rangle$, are not aligned to the H and V cavity axis, but at an angle $\theta = 35^\circ$ for the device under consideration. The two exciton states $|H\rangle$ and $|V\rangle$, linearly polarized along the H and V cavity axis, can then be written as a superposition of the exciton eigenstates as:

$$|H\rangle = \cos\theta\,|X\rangle + \sin\theta\,|Y\rangle \tag{2.43}$$

$$|V\rangle = -\sin\theta\,|X\rangle + \cos\theta\,|Y\rangle \tag{2.44}$$

To simplify the discussion we consider here $\theta = 45^\circ$. In this case, by exciting along the H cavity mode with a spectrum broader than Δ_{FSS}, we create a superposition of the exciton eigenstates given by $|H\rangle = (|X\rangle + |Y\rangle)/\sqrt{2}$. The free temporal evolution of such state gives $|\psi(t)\rangle = \left(|X\rangle + e^{i\Delta_{FSS}t/\hbar}|Y\rangle\right)/\sqrt{2}$. After a characteristic time given by $\frac{\pi\hbar}{\Delta_{FSS}}$, we see that $|\psi(t)\rangle$ present a maximal overlap with the state $|V\rangle = (|X\rangle - |Y\rangle)/\sqrt{2}$. In this condition the exciton state can efficiently decay by emitting a photon in the V mode of the cavity, which is the one being collected. In absence of other dephasing processes, the loss of coherence only comes from the radiative decay of the exciton into the H and V cavity modes. We thus expect the emitted photons to have a transform limited linewidth and no uncertainty in their emission time, as the population of the exciton state is coherently controlled.

The amount of light emitted with the V polarization, thus the brightness that we observe, will be determined by an interplay between the polarization rotation process and the spontaneous emission rate. As soon as the $|H\rangle$ state is populated, spontaneous emission into the H cavity mode can take place, while the emission into the V mode is delayed by the exciton precession. The higher the value of Δ_{FSS}, the faster the process of polarization rotation will be, hence the population transfer from the $|H\rangle$ to $|V\rangle$. On the contrary, in absence of FSS, no signal will be emitted in the V cavity mode. When $\Delta_{FSS} = 0$ the two linear exciton eigenstates are degenerate, and no polarization rotation takes place.

The device QD1 shows a $\Delta_{FSS} = 15\ \mu eV$ which corresponds to a precession semi-period of about 140 ps. This time is comparable to the radiative lifetime of the exciton, assumed to be the same for the emission into both H and V polarizations. As a consequence we expect that the emitted photons will have a higher probability of being emitted into the H mode than into the V mode of the cavity. Considering that we have an output coupling efficiency $\eta_{out} = 0.7$ and a mode coupling $\beta = 0.96$, supposing a unit occupation probability of the exciton $p_x = 1$ at the π pulse, by collecting both polarization we would achieve a theoretical maximum brightness of $B = \beta\eta_{out}p_X = 0.67$. Using the cross polarization setup here described, where we collect only one polarization, the brightness is limited to 33%. In the best case indeed the QD will emit the same amount of light in both polarizations. This would be the case for a charged exciton, whose transitions are circularly polarized, thus equally coupled to both H and V cavity modes. For a neutral exciton as measured here, this condition cannot be met because of the finite time delay to go from the H to the V polarized state. The exciton precession process as well as a non-unity flip probability for the exciton at the π pulse, are additional limiting factors which reduces the brightness below 33%.

2.6.4 Pulsed resonance fluorescence

To experimentally study the coherent excitation process presented in the previous section, we now probe the sample using spectrally shaped pulses sent through the H cavity mode, and collect the Resonance Fluorescence (RF) emitted along the V cavity mode.

The presence of the polarization precession process can be experimentally tested by measuring the time dependence of the incident pulses and of the emitted signal. Using a SPAD with 30 ps resolution, we cannot access the Rabi oscillations in time, but we can observe the 140 ps delay expected in the V polarized emission. The result is shown in Fig.2.17.a for another device QD3, excited with laser pulses of about 50 ps. The red line shows the time dependence of the wave packet emitted by the QD in the V cavity mode. By tuning the QD out of resonance, we can collect the residual scattered laser light, which highlights the time dependence of the incident pulse (black line). We clearly observe a time delay between the excitation and the emission, consistent with what is predicted from the value of Δ_{FSS}.

The presence of Rabi oscillation is investigated indirectly through power dependent measurements, since the oscillatory behaviour is too fast to be resolved by our detectors. We want to access the evolution of the occupation probability,

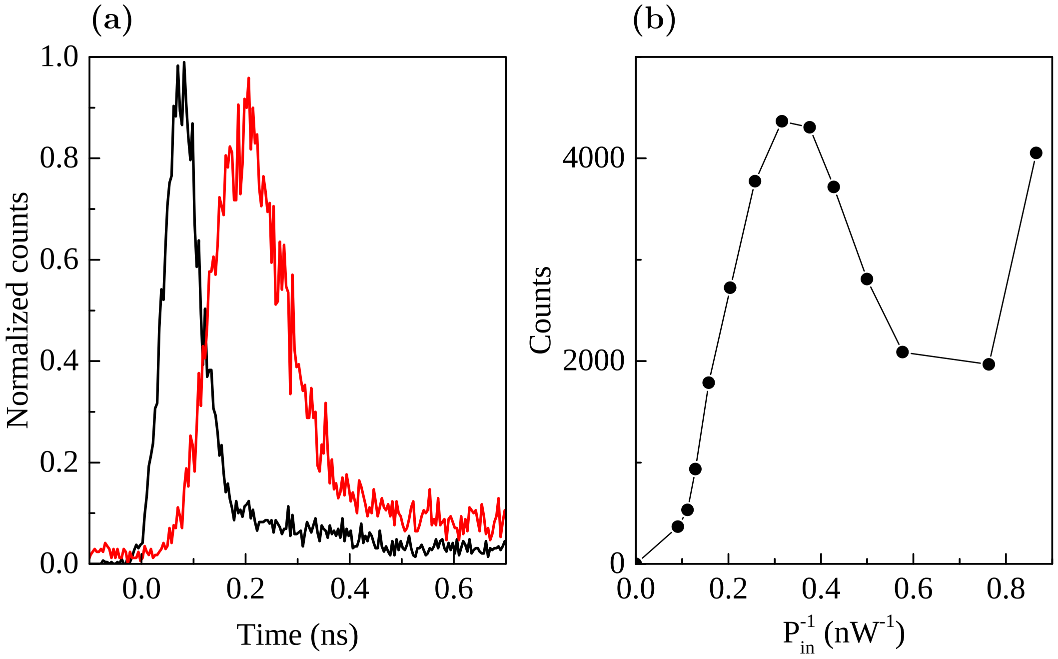

Figure 2.17 – Temporal and power dependence of the resonance fluorescence, for the device QD3, excited with 50 ps laser pulses. (a) Temporal profile of the incident laser (black) and emitted wavepacket (red). (b) Plot the total emission intensity as a function of the square root of the excitation power, revealing the presence of Rabi oscillations.

which is oscillating during the laser pulses. The interaction time t between the exciton and the laser is fixed by the temporal duration of the laser pulses. By changing the excitation power, we can vary the Rabi frequency Ω in such a way to control the occupation probability for the exciton state at the end of the pulse. The coherent drive is followed by the polarization precession process described in the previous section, which eventually leads to the spontaneous emission of a photon into the V polarized mode of the cavity. In a first approximation, the probability of detecting a photon emitted by the QD will be proportional to the probability of finding the exciton in the V exciton state at the end of the excitation pulse. By monitoring the total emission intensity as a function of the excitation power, we can monitor the Rabi oscillation between the exciton and the ground state of the QD due to the laser field.

The time-integrated RF intensity, as a function of the square root of the excitation power, is shown in Fig.2.17.b for a different device, called QD3. We observe the signature of the Rabi oscillations in the collected signal. A full 2π oscillation is present, where the signal follows an harmonic evolution across a maximum to a minimum value again. We have experimental deviations from the ideal Rabi oscillations due to multiple factors. First of all, for higher excitation power the signal to background ratio rapidly degrades. The RF from the QD

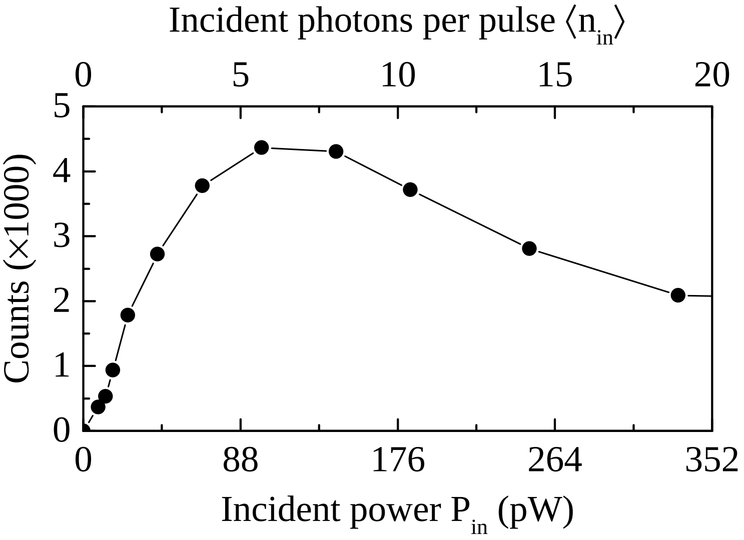

Figure 2.18 – Rabi oscillations as a function of the average incident photon number (top scale) and incident power (bottom scale), for the same data shown in Fig.2.17.b. The π pulse is obtained for only 6 average incident photons per pulse.

cannot exceed the value reached at the π pulse, while the amount of scattered laser leaking through the polarization filtering scheme keeps increasing, and eventually dominates the signal. Secondly, the short radiative lifetime of the transition, of about 150 ps, is responsible for the damping of the oscillations through spontaneous emission. Using a very short pulse ($\ll$150 ps) allows to achieve a reasonably good visibility in the Rabi oscillations. On the contrary, by increasing the pulses duration the decay of coherence due to radiative emission becomes important on the timescale of the excitation pulse itself, leading to a saturation behaviour for longer pulses. Finally, the shape of the oscillations is determined by the laser pulses used to drive the transition, which do not corresponds to an ideal single frequency perturbation suddenly switched on. As the laser pulses have a close to Gaussian shape, they will cause a temporal modulation of the Rabi frequency during the excitation.

The measurement of the Rabi oscillations is reported in Fig.2.18 as a function of the power incident on the device P_{in} (bottom scale). The value of P_{in} can be converted into the average number of photons per excitation pulse as $\langle n_{\text{in}} \rangle = \frac{P_{\text{in}}}{\Gamma_{\text{laser}} \hbar \omega_{\text{laser}}}$, where Γ_{laser} and ω_{laser} are respectively the laser repetition rate and frequency. The result is shown in the upper scale. The π pulse excitation is obtained for only about 6 incident photons per pulse, measured outside the micropillar cavity. The count rate detected on a SPAD from the RF at π pulse excitation is 0.38 MHz. Correcting for the total efficiency of the resonant excitation setup of 2.9%, we expect a 13 MHz count rate on the first lens, which gives a brightness of $\overline{B} = 0.16 \pm 0.02$.

As previously demonstrated in the thesis work of Valerian Giesz [174], the extremely low photon number required to flip the exciton state together with the high brightness is possible owing to the ideal light-matter interface provided by the QD-micropillar device. The very high input coupling efficiency ($\eta_{\text{in}} \approx 1$) and cooperativity ($C = 13$) ensure that every photon sent on the cavity has a high probability of interacting with the QD transition. Symmetrically, a high output coupling efficiency ($\eta_{\text{out}} = 0.7$) allows to collect most of the emitted photons [20]. The lowest number of photon required to have a π pulse excitation is obtained for a longer pulse, having a better spectral matching with the optical transition of the QD. However, in the following we use an excitation pulse duration of about 15 ps, to minimize the possibility of having multiple excitation of the QD during a same pulse (the effect of the excitation pulse duration is analysed in more details in section 4.4.3).

2.6.5 Emission of highly indistinguishable single photons

To study the single photon emission from the signal collected in cross polarization, the second order correlation function is now measured using a fibre-based HBT experiment. As shown in Fig.2.15.b, it consists in a fiber beam splitter whose exits are directly detected by two fiber-coupled SPADs, and a correlation measurement is performed between the two outputs as before. A typical result, obtained from the device QD1 at an excitation power corresponding to 75% of the π pulse, is shown in Fig.2.19.a, from which we can retrieve a value $g^{(2)}(0) = 0.125$. This values changes from pillar to pillar, and by optimizing the setup alignment is normally in the range between 0.03 to 0.10. The significant amount of coincidences detected at zero time delay can be attributed to an imperfect polarization filtering of the excitation laser. The incident pulses have a spectrum larger than the exciton linewidth, thus there will be a certain component of the incident laser directly reflected back by the cavity, which has a noticeable effect even for the low incident power used at the π pulse. To get rid of the unwanted scattered laser and further improve the signal to background ratio, we have introduced an etalon filter having a bandwidth of 15 μeV and a transmission of 70% in the collected signal. By carefully adjusting its tilt angle with respect to the optical beam, is possible to centre its transmission windows to the emission energy of the QD. Repeating the previous measurement with the spectral filtering centred on the ZPL of the exciton, we obtain the result shown in Fig.2.19.b. From such measurement we can calculate now a vanishing value of $g^{(2)}(0) = 0.003 \pm 0.001$, demonstrating an extremely high purity for the single photon emission.

I have developed a new fibre-based HOM experiment to substitute the previous free space one, which was showing some limitations due to the imperfect spatial overlap of the incident photons. To measure the indistinguishability of the single photons emitted in cross polarization then, the signal is directed

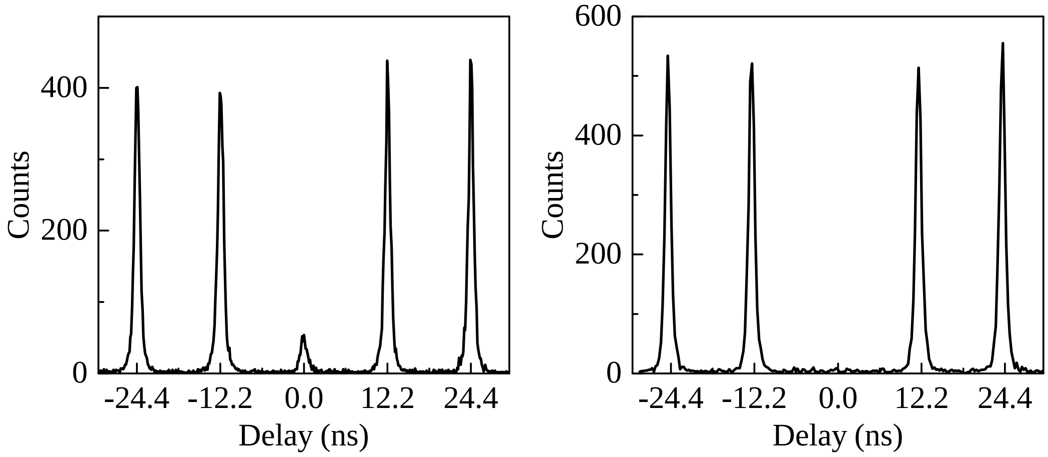

Figure 2.19 – Measurement of the $\overline{g^{(2)}(\tau)}$ under resonant excitation without (left) and with (right) spectral filtering to remove the residual laser, for the signal emitted by the device QD1.

towards the fibre-based HOM setup shown in Fig.2.15.c. The single photons emitted by the sample are passing through a polariser (Pol) and an half wave plate (HWP) in order to fix their polarization to be diagonal. A polarising beam splitter (PBS) is then used to project the photons with equal probability into one of the two outputs, either with an H or a V polarization. The polarization of two photons exiting from different outputs is then restored using polarization controllers (PC) composed of a quarter wave plate and a half wave plate. One of the two photons is passing through a fibre delay line of 2.2 ns, adjusted to the delay of the double excitation. Finally, the two photons are coupled to a fibre beam splitter (BS) where they can interfere. The output are detected by fibre-coupled SPADs, and a correlation measurement is performed between them. This configuration produce the same 5 peaks structure explained before, this time with no overlapping peaks, and can be analysed using the same formulas. The fibre beam splitter used here in the HOM allows to overcome any possible limitation due to an imperfect spatial overlap of the two interfering photons. The experimental challenge is to ensure a precise control of the polarization of each photon, which can be achieved by precisely tuning the wave plates and making sure that the optical fibre are well attached to the optical table. Thanks to this fibred HOM interferometer we measure a classical interference visibility $(1-\epsilon) = 0.998$, with reflectance and transmittance coefficients of $R = 0.508$ and $T = 0.492$.

The correlation histogram obtained from the HOM interference of two successively emitted photons is shown in Fig.2.20.a, for the device QD2. We observe a vanishing peak at zero time delay, reflecting the strong quantum interference effect between the photons. As before, we fit a double-sided exponential decay to each peak in order to retrieve each area. Using Eq.2.29 we obtain mean wave

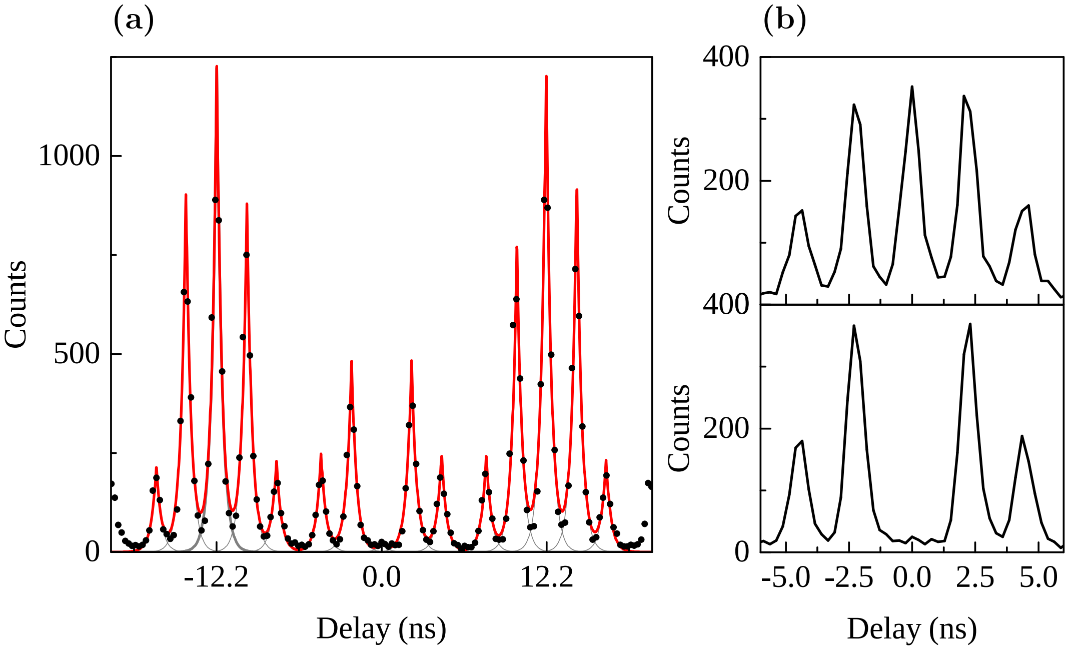

Figure 2.20 – (a) Indistinguishability measurement under resonant excitation for the emission from the device QD1, for an incident power corresponding to 0.75π. (b) HOM interference between two photons having perpendicular (top) and parallel (bottom) polarization.

packet overlap $\overline{M} = 0.995$, corrected for the previously measured $\overline{g^{(2)}(0)} = 0.003$.

To highlight the strength of the quantum interference effect between the photons, the same experiment is repeated after making them distinguishable, by acting on the wave plates in the HOM interferometer. The result is shown in Fig.2.20.b, where in the top panel the two photons have orthogonal polarizations, while in the bottom panel they have parallel polarizations. When the two photons are fully distinguishable, we obtain the same number of zero-delay coincidences as for the side peaks. Calculating the mean wave packet overlap for the case of the top panel, we obtain $\overline{M} = 0.006$. On the contrary, the coincidences at zero time delay completely vanishes when the two photons are fully indistinguishable.

The measurements of $\overline{M}$ and $\overline{g^{(2)}(0)}$ have been repeated for different values of the input power, as presented in Fig.2.21. The results shows a very high single photon purity and mean wave packet overlap up to a π pulse excitation, where the device has the maximum brightness of 16%. Over the whole range we obtain $\overline{M} > 0.97$ (corrected for the $g^{(2)}(0)$) and $\overline{g^{(2)}(0)} < 0.04$. This result demonstrates that under resonant excitation the QD-micropillar gated device is acting as a bright source of fully indistinguishable single photons.

Note that using an etalon to filter out the laser, we also filter out the phonon sidebands. In a following work to which I have participated, we could actually

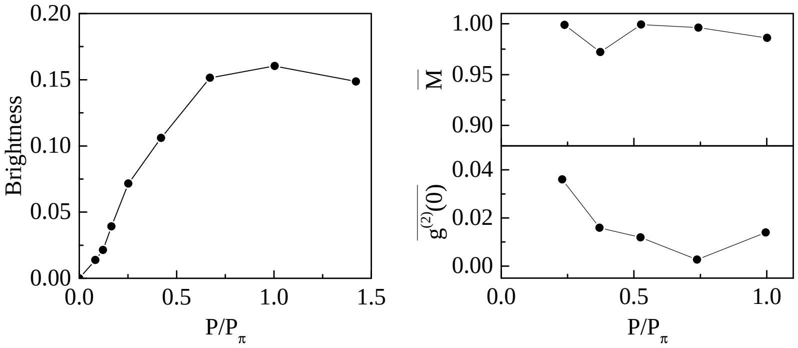

Figure 2.21 – Summary of the properties of the QD-micropillar device QD2 as a single-photon source under resonant excitation, as a function of the excitation power.

show that $\overline{M}$ remains very high even without using such etalon. This is because the very high Purcell effect allows to funnel the QD emission into the ZPL, and largely suppress phonon sidebands [100].

2.7 Conclusion and perspectives

In this chapter we have shown that the QD-micropillar device, under resonant excitation, behave as a very bright source of fully indistinguishable single photons. The performances achievable with our devices are at the state of the art with respect to both single quantum emitter and parametric sources. Combining these sources with efficient gates and detectors, makes it possible to scale up quantum photonic schemes.

Comparison with state of the art sources To compare the results obtained using our QD-micropillar device with other sources, we use the graph of Fig.2.22, where we plot the measured brightness as a function of the indistinguishability, for different single-photon sources showing a $g^{(2)}(0) < 0.05$. In this plot is reported the polarized brightness, i.e. we consider only the emission in a single polarization mode, since for many applications the photons must have a definite polarization. The ideal device is on the top right corner, providing a deterministic production of fully indistringuishable photons [44].

The results from SPDC sources are shown by the grey symbols. These devices, presented in Section 2.3.1, allows to reach very high indistinguishability between the photons emitted within the same pair. However, they are limited by a very low brightness due to the rapid increase of multi-photon generation event for higher pump power. To maintain $g^{(2)}(0) < 0.05$, the brightness is limited to 0.02 (see Fig.2.5.b). The results from the QD-micropillar devices presented here are shown by the red symbols. As opposite to the SPDC devices, QD in micropillars under non-resonant excitation shows a limited indistinguishability, between 0.7 and 0.8 at best. However, they allow to reach a very high brightness owing to the high output coupling efficiency achieved by the micropillar cavities and a low $g^{(2)}(0)$ at saturation. We observe a polarized brightness in the range between 0.3 and 0.4, corresponding to an uncorrected brightness (considering both polarization, as reported in Section 2.5.3) between 0.6 and 0.8. The implementation of a strictly resonant excitation for the QD-micropillar devices allows to achieve the same indistinguishability values as for SPDC source but for a brightness at least one order of magnitude higher. In our case, for an indistinguishability above 0.98, we achieved a brightness of 0.16 which is 20 times higher than that of an SPDC source.

Additional results from other groups using QD-based single-photon sources are reported with blue symbols, confirming and extending the measurements presented in this chapter. We can see that under non-resonant excitation different works have reported indistinguishability values in the 0.8 range [41, 37, 141] and a record polarized brightness of 0.4 has been achieved using a micropillar cavity [141]. Under resonant excitation, an indistinguishability above 0.95 has been obtained with a state of the art brightness above 0.3, using a charged exciton for a QD in a micropillar cavity, still without using a deterministic fabrication [140].

Improvement of the device performances For our devices, the brightness is still limited to 0.16 under resonant excitation, which is the combined result of the extraction efficiency from the cavity, the cross polarization configuration and the polarization rotation process operated by a neutral exciton state.

The brightness can be readily improved using a charged exciton state instead of a neutral exciton. The former indeed is equally coupled to both H and V linear polarization, and emit the same amount of light in both cavity modes [208]. A second improvement to the brightness can be obtained by decoupling the spatial mode of the pump and the collection. This allows to substitute the cross polarization configuration used under resonant excitation with a spatial filtering of the excitation, in such a way to collect the emission in both polarization modes. Such technique has been already demonstrated both in planar cavities [213, 214] and micropillars [207], and offers a way to reach a brightness as high as the one observed under non-resonant excitation.

Scaling up quantum photonics experiments The improvement of the brightness of the source is especially important to scale up the size of quantum optics experiments in terms of number of photons. The probability to successfully collect n photons critically depends on the brighness B, as the n-photon rate scale as B^n. It is clear that the improvement of the source brightness gives an exponential advantage. To realize a multi-photon experiment, multiple single-photon sources can be combined. Such approach is still very challenging since it

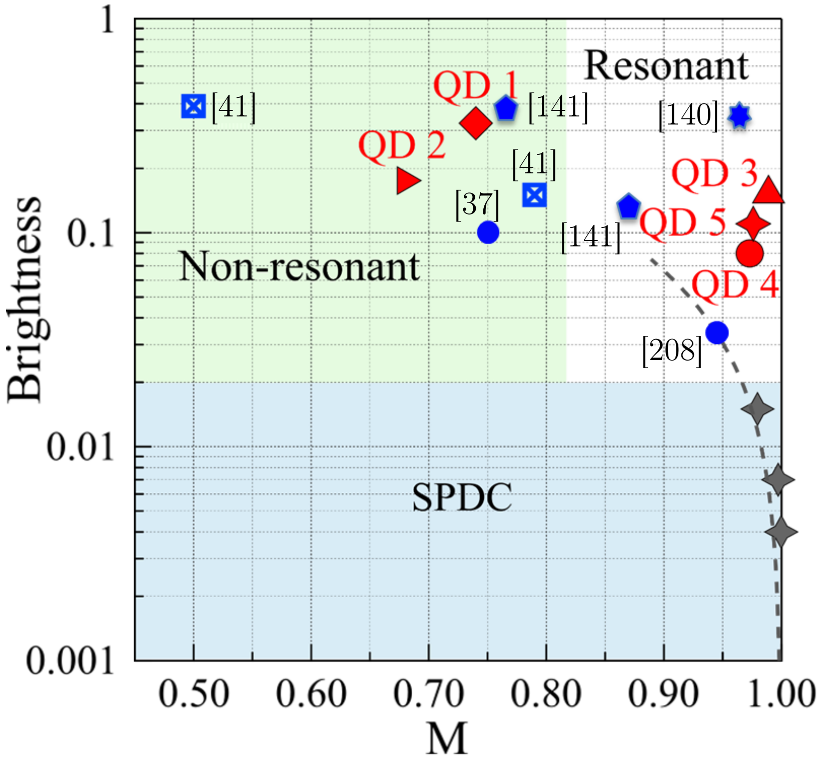

Figure 2.22 – Comparison of different single-photon sources providing a $g^{(2)}(0) < 0.05$. Grey symbols are SPDC source measured in the group of A. White [44], red symbols are the results obtained with the QD-micropillar devices presented in this chapter and blue symbols are results from other QD-cavity sources reported in literature.

requires the controlled fabrication and operation of multiple devices which are able to provide identical photons. Alternatively, the stream of indistinguishable single photons emitted by a single source can be demultiplexed using active optical elements. Moreover, a high degree of indistinguishability must be obtained for photons emitted at longer timescales, as multiple emission cycle have to be combined. As shown by Loredo et al. [215], using a QD-micropillar devices it is possible to measure indistinguishability values above 0.88 for single photons separated by 463 ns. Fig.2.23 reports the indistinguishability measured under resonant excitation as a function of the time delay between the emission of the two interfering photons. We see that it is possible to collect as much as 39 indistinguishable photons, using an excitation rate of 82 MHz. Combined with the high brightness provided by the micropillar cavities, these devices represents a viable way to implement large scale photonic protocols.

A demonstration has been given by recent boson sampling experiments implemented with single photons from QD sources. The boson sampling problem consists in the prediction of the output distribution of a multimode bosonic interferometer, which is computationally hard on a classical computer as it requires

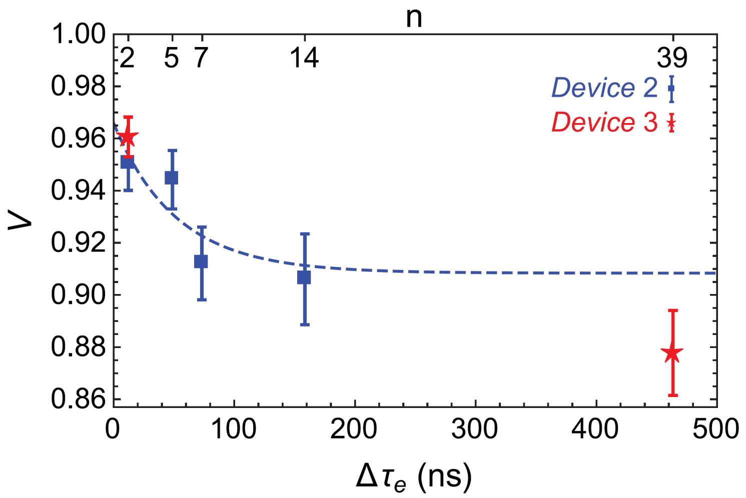

Figure 2.23 – Figure reproduced from [215]. Measured indistinguishability under resonant excitation as a function of the delay between the emitted photons, measured using the devices QD2 and QD3.

the calculation of permanents [216]. A boson sampling experiment implemented with single photons and linear optical elements, allows to efficiently simulate the output distribution of n indistinguishable photons interfering in a photonic circuit with m modes. Such realization has the potential to be the first experimental demonstration of the quantum advantage of a quantum computer, by performing a specific computational task more efficiently that a classical computer. The firsts experimental realisations of boson sampling experiments have been realized with parametric sources and integrated optical circuits [217, 218, 219, 220]. These implementations are however limited to few photons by the low sampling rate achievable with a parametric source. A fundamental improvement, beside high efficiency circuits and detectors, is in the use of bright solid-state single-photon emitters, such as the QD-micropillar devices presented in this chapter. A first demonstration has been given by Loredo et al. [221], using a QD-micropillar sources provided by our group at C2N, showing a 10 to 100 times speedup for a 3-photon boson sampling experiment. The following work of Wang et al. [222] then, always using a QD in a micropillar cavity, demonstrated a 10^5 speedup for a 5-photon experiment.

Many more experiments aiming at manipulating N photons are on their way in the group, using the QD-micropillar sources, in collaboration with F. Sciarrino, R. Osellame and H. Eisenberg, progressively increasing the number of photons. Moreover, this new generation of source has led to the creation of Quandela, spin off company confounded by Niccolo Somaschi, Valerian Giesz and Pascale Senellart, with whom I conducted this study. The objective is to make these sources available to a large community of quantum optics scientists.

Chapter 3

Quantum State Tomography of path-encoded NOON states

Path entangled N-photon states find applications in different fields of quantum information science, most notably quantum metrology. They gives the possibility to perform measurement beyond what allowed by the classical limits of precision. However, both the generation and the characterization of multiparticle states is experimentally difficult. The tomography of path-entangled particles is still in its infancy and the reconstruction of spatially entangled indistinguishable photons hasn't been addressed yet. In this chapter, we develop a method to perform a full Quantum State Tomography (QST) of path-entangled NOON states. The single photons emitted by a QD-micropillar device, presented in the previous chapter, are used to generate a two-photon path entangled state, and QST is used to fully reconstruct its density matrix in the spatial mode basis.

In Section 3.1 we summarize the interest for NOON states in the field of quantum metrology and in Section 3.2 we review the current state of the art. Then in Section 3.3 we present the method we use to generate the two-photon NOON state and introduce a new technique to perform the QST. In Section 3.4 we detail the experimental setup we have realized. This setup in analysed theoretically in Section 3.5 and the experimental results are presented in Section 3.6. We complete the tomographic procedure in 3.7 and the conclusions are presented in Section 3.8.

3.1 Quantum metrology with NOON states

Quantum entanglement, a central concept in the foundation of quantum mechanics, is now used as a tool in a more applied research, which is boosting all the fields related to quantum information, among which is quantum metrology. This field has strongly benefited from the advances in the production and manipulation of quantum states of light, and has already led to important applications in many different areas, where the quantum entanglement can be used to beat the classical limits of precision measurements. These areas include microscopy [223, 224, 225], lithography [226, 227], biology sensing [228, 229] and gravitational wave detection [230, 231], but are not limited to the optical domains. The same ideas have also been used for entangled states of matter, using trapped atoms and ions, to achieve quantum enhanced spectroscopy and atomic interferometry [232, 233, 234, 235, 236].

A central problem in the field of metrology, of fundamental importance for physics, is parameter estimation. The prototypical case is an interferometric measurement, where the parameter of interest is the optical phase. Phase estimation is indeed a commonly found problem in many areas of physics, and extensively treated in literature [232, 237, 238, 239, 240, 241]. As a typical example we can consider a Mach-Zender interferometer, as shown in Fig.3.1, where a classical beam of light is first divided by a beam splitter into two components, which follow different paths. These two components acquire a relative phase difference ϕ and then recombine on a second beam splitter. The value of the phase ϕ can be estimated by measuring the intensity at the output ports of the interferometer, with a precision $\Delta\phi$ scaling at best as $1/\sqrt{n}$, where n is the average number of photons in the beam. This limitation is due to the Poissonian statistics of the photons in the classical beam, implying the absence of correlations in the detection events. Equivalently, the same precision $\Delta\phi$ can be obtained with n repetitions of the same experiment, where a single photon is propagating and being detected at one output: from the central limit theorem, we know that by averaging n independent measurements the statistical error scale as $1/\sqrt{n}$ [232, 237].

This limitation is called Standard Quantum Limit (SQL), or Shot Noise Limit, and has no fundamental origin, but emerges when no quantum correlations are taken into account. The ultimate bound given by quantum mechanics is stated by the Heisenberg number-phase uncertainty relation [242]:

$$\Delta n \Delta\phi \geq 1 \tag{3.1}$$

Using the expected photon number uncertainty for a classical state of light, $\Delta n = \sqrt{n}$, the above relation leads to $\Delta\phi \geq 1/\sqrt{n}$, which saturates to the SQL. However, no limitation is imposed to the individual terms of Eq.3.1, thus we can improve the precision on the phase by increasing the photon number indetermination. Going back to our interferometer, we can reasonably assume that the energy fluctuation cannot be bigger than the total energy in the beam, thus the best situation we can envisage is where $\Delta n = n$ [238]. This leads to the so called Heisenberg Limit of $\Delta\phi = 1/n$, considered to be the fundamental limit for the phase estimation problem [243, 244] [1].

---

[1] Both the validity of Eq.3.1 and the assumption of the upper bound $\Delta n = n$ are not general. However, the Heisenberg Limit can be considered an absolute limit for precision measurements. [243, 245, 246]

Following the above explanation, it is clear how the engineering of quantum states of light showing different forms of Eq.3.1 allows to overcome the SQL by a factor of up to $1/\sqrt{n}$. This has been first proposed by Caves [247] using squeezed states, where the fluctuations in the phase quadrature are reduced, at the expense to higher fluctuations in the amplitude quadrature. Squeezed states have been extensively studied, not only for proof of principles demonstrations but also for interferometric applications, but the Heisenberg Limit has not been achieved yet, as it requires a high degree of squeezing.

An alternative "digital" approach, as called by Dowling [238], is the use of photon number entangled states, a method rapidly advancing thanks to its close connection with optical quantum computing. Indeed, a Mach-Zender interferometer or a Ramsey spectroscope are formally equivalent to a general quantum logic circuit [248]. Among photon number entangled states, the most promising are the NOON states [248], which allows to reach a measurement precision at the Heisenberg Limit with a phase resolution beyond the diffraction limit [249, 250], independently of the number of photons used. A NOON state is a multi-particle state defined over two orthogonal modes, given by the superposition of N particles in one mode A with zero particle in the other mode B, and N particle in mode B with zero particle in mode A:

$$|\psi_{\text{NOON}}\rangle_{\text{A,B}} = \frac{1}{\sqrt{2}}\Big(|N,0\rangle_{\text{A,B}} + |0,N\rangle_{\text{A,B}}\Big) \tag{3.2}$$

Such a state represents a possible implementation of a Schrödinger cat state, where the particles, altogether, are in a coherent superposition of two orthogonal modes, being with the same probability amplitude all in mode A and all in mode B. In a more technical way, a NOON state is a a maximally entangled state, and it can be indeed traced back to one of the four Bell states (by using the vacuum state $|0\rangle$ and N particle states $|N\rangle$ as basis kets of each subsystem). Mathematically, a maximally entangled state of a bipartite system $\rho \in (\mathcal{H}_A \otimes \mathcal{H}_B)$ is a pure state such that the reduced density matrix of either of the two subsystem is maximally mixed, i.e., a multiple of the identity matrix: $\rho_A = \rho_B = \frac{1}{2}\mathbb{1}$ [251]. This means that a measurement in one of the two subspaces will produce a completely random outcome, while there is a perfect correlation in the results obtained by a collective measurement on both. Other notable examples of these states are the Bell states and the GHZ states, whose entanglement properties are fundamental to the fields of quantum communication and computation [5].

3.1.1 Emergence of super-precision and super-resolution

We recall here what we mean by precision and resolution. All optical measurements here are repeated measurements, where at each iteration a state is generated and detected, and the result is obtained by averaging over many iterations. With the ergodic hypothesis, we can assume that this temporal average

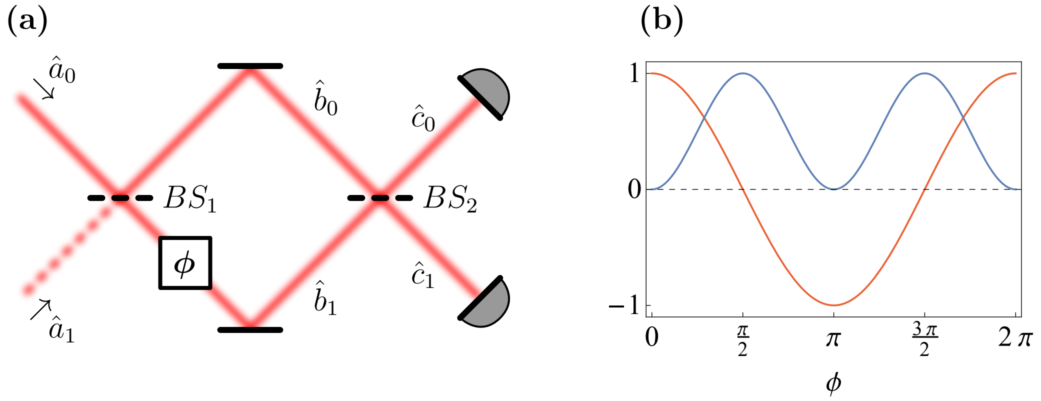

Figure 3.1 – (a) Schematics of a Mach-Zender interferometer. (b) Observed interference fringes for a coherent state (red line) and a 2-photon NOON state (blue line).

corresponds to the outcome of a measurement on the statistical ensemble ρ describing our state. The precision of a measurement is defined as its statistical error. Each iteration will lead to a slightly different outcome. Depending on the state being measured and the chosen measurement operator, the observed variance in the measurement outcomes can be different. The resolution of a measurement instead is the smallest resolvable feature. For an optical system is defined by the Rayleigh diffraction limit, which is of the order of the wavelength λ of the photons.

Considering a photonic implementation of a NOON state, the N photons with which the state is realized can be entangled over different degrees of freedom, such as their polarization, frequency or spatial modes. In order to use the quantum advantage in an interferometric protocol as described above, such a state needs to be spatially entangled, where the two modes A and B of Eq.3.2 correspond to the two arms inside a Mach-Zender interferometer. To understand how the enhanced resolution and precision emerges, we can observe how different states of light evolve in the Mach-Zender of Fig.3.1.a. The beam splitter M_{BS} and phase shift M_ϕ matrix transformations for the photon modes operators can be written as [166]:

$$M_{\mathrm{BS}} = \frac{1}{\sqrt{2}}\begin{pmatrix} 1 & 1 \\ 1 & -1 \end{pmatrix} \qquad M_\phi = \begin{pmatrix} 1 & 0 \\ 0 & e^{i\phi} \end{pmatrix} \tag{3.3}$$

The modes $\hat{a}$, $\hat{b}$ and $\hat{c}$ of Fig.3.1.a can then be linked by the following transformations:

$$\begin{pmatrix} \hat{b}_0 \\ \hat{b}_1 \end{pmatrix} = M_\phi M_{\mathrm{BS}} \begin{pmatrix} \hat{a}_0 \\ \hat{a}_1 \end{pmatrix} \qquad \begin{pmatrix} \hat{c}_0 \\ \hat{c}_1 \end{pmatrix} = M_{\mathrm{BS}} \begin{pmatrix} \hat{b}_0 \\ \hat{b}_1 \end{pmatrix} \tag{3.4}$$

Using these relations, we can calculate the evolution of the input state to the one inside the Mach-Zender, just before the last beam splitter, and at the exit, just after the last beam splitter.

For a classical light beam entering from the top input port, represented by a coherent state $|\alpha\rangle$ with average photon number $n = |\alpha|^2$, and the vacuum on the other input port, we have:

$$|\alpha, 0\rangle \xrightarrow{M_\phi M_{\mathrm{BS}}} \left|\frac{\alpha}{\sqrt{2}}, \frac{e^{i\phi}\alpha}{\sqrt{2}}\right\rangle \xrightarrow{M_{\mathrm{BS}}} \left|\frac{\alpha(e^{i\phi}+1)}{2}, \frac{\alpha(e^{i\phi}-1)}{2}\right\rangle \tag{3.5}$$

where we have used the fact that $|\alpha\rangle$ is generated by applying the displacement operator $\hat{D}(\alpha) = \exp(\alpha\hat{a}^\dagger + \alpha^*\hat{a})$ on the vacuum $|0\rangle$. The interferometer phase is typically estimated through the difference of the intensities detected at the two output ports, $\hat{I}_0 = \hat{a}_0^\dagger\hat{a}_0$ and $\hat{I}_1 = \hat{a}_1^\dagger\hat{a}_1$, thus by measuring the expectation value of the operator:

$$\hat{O} = \hat{a}_0^\dagger\hat{a}_0 - \hat{a}_1^\dagger\hat{a}_1 \tag{3.6}$$

Applying this operator on the final state of Eq.3.5, we obtain for a coherent state that $\langle\hat{O}\rangle = |\alpha|^2\cos(\phi)$. As expected for a classical beam, the intensity at the output ports shows sinusoidal oscillations with ϕ, and is plotted in Fig.3.1.b for $|\alpha|^2 = 1$ (red line). From estimation theory, we can retrieve the uncertainty on the phase value calculated using such operator as:

$$\Delta\phi = \frac{\Delta O}{|\partial\langle\hat{O}\rangle/\partial\phi|} \tag{3.7}$$

where the variance of the observable is given by $(\Delta O)^2 = \langle\hat{O}^2\rangle - \langle\hat{O}\rangle^2$. For the coherent state here considered, we can calculate $(\Delta O)^2 = |\alpha|^2$ and $|\partial\langle\hat{O}\rangle/\partial\phi| = |\alpha|^2|\sin(\phi)|$, thus Eq.3.7 gives $\Delta\phi = 1/|\alpha\sin(\phi)|$. The error reaches a minimum value when ϕ is an odd multiples of $\pi/2$, corresponding to the maximum slope observed in the plot of Fig.3.1.b. In such case we have $\Delta\phi = 1/|\alpha| = 1/\sqrt{n}$, which corresponds to the Standard Quantum Limit. To compare with the case of a two-photon NOON state, presented in the following, we can consider an average photon number of $|\alpha|^2 = 2$. For the coherent state this leads to a minimum uncertainty of $\Delta\phi = 1/\sqrt{2}$.

Replacing the coherent state by a single photon $|1\rangle = \hat{a}^\dagger|0\rangle$, the evolution of the state is now the following:

$$\begin{aligned} |1,0\rangle &\xrightarrow{M_\phi M_{\mathrm{BS}}} \frac{1}{\sqrt{2}}(|1,0\rangle + e^{i\phi}|0,1\rangle) \\ &\xrightarrow{M_{\mathrm{BS}}} \frac{1}{2}(1+e^{i\phi})|1,0\rangle + (1-e^{i\phi})|0,1\rangle \end{aligned} \tag{3.8}$$

The main difference is in that the state of the two interferometer arms is entangled: the single photon is interfering with itself according to the phase shift acquired. We can use again Eq.3.6 and 3.7 to estimate the phase and its variance, obtaining $\langle\hat{O}\rangle = \cos(\phi)$ and a minimum error of $\Delta\phi = 1$. No advantage is obtained with respect to the classical case, as we have a single particle, not correlated to any other. Improving the precision would imply repeating the measurement multiple times, giving no improvement over the SQL.

Finally, we consider the situation where a single photon is entering on each input of the interferometer. This will lead to the Hong-Ou-Mandel interference on the first beam splitter, and the state evolves as:

$$\begin{aligned} |1,1\rangle &\xrightarrow{M_\phi M_{\text{BS}}} \frac{1}{\sqrt{2}}(|2,0\rangle + e^{2i\phi}|0,2\rangle) \\ &\xrightarrow{M_{\text{BS}}} \frac{1}{2\sqrt{2}}(1+e^{2i\phi})(|2,0\rangle + |0,2\rangle) + \frac{1}{2}(1-e^{2i\phi})|1,1\rangle \end{aligned} \tag{3.9}$$

Now, inside the interferometer, we obtain a state in the form of Eq.3.2 with $N = 2$, thus a 2-photon NOON state. The effect of the phase shift is notably different, showing a doubled dependence, which can be interpreted by associating to the NOON state an effective de Broglie wavelength of λ/N [252]. This enhanced phase dependence can be experimentally accessed, but not through the same observable as the one of Eq.3.6, which would give a value of zero. A common choice is to perform an intensity correlation measurement on the two outputs of the interferometer, identified by the operator:

$$\hat{O} = \hat{a}_0^\dagger \hat{a}_1^\dagger \hat{a}_0 \hat{a}_1 \tag{3.10}$$

Its expectation value on the final state of Eq.3.9 can be calculated to give $\langle\hat{O}\rangle = \frac{1}{2}(1-\cos(2\phi))$, and is plotted in Fig.3.1.b (blue line). It shows a phase dependence oscillating twice as fast as for the classical case, with unit visibility. This time the variance results $(\Delta O)^2 = (\cos(\phi)\sin(\phi))^2$ and $|\partial\langle\hat{O}\rangle/\partial\phi| = |2\cos(\phi)\sin(\phi)|$, so that applying again Eq.3.7, we can retrieve a minimum uncertainty of $\Delta\phi = 1/2$. Such a value corresponds to the Heisenberg Limit, and indeed we obtain an improvement of $1/\sqrt{2}$ compared to the classical case for the same average number of photons $|\alpha|^2 = 2$.

Unfortunately we cannot scale up this simple scheme to increasing photon number. But, as shown in [238], we can idealize the Mach-Zender as a quantum logic circuit, where the first beam splitter is a state preparation device, creating a NOON state on the two arms, and the last beam splitter is a device performing a collective measurement. Inside our interferometric circuit we have a state which will evolve under the action of a phase shift operation as $|N,0\rangle + e^{iN\phi}|0,N\rangle$. A generalized measurement operator for this situation [248, 7], allowing to exploit the entangled nature of the NOON state, is $\hat{O} = |N,0\rangle\langle 0,N| + |0,N\rangle\langle N,0|$, for which $\langle\psi_{\text{NOON}}|\hat{O}|\psi_{\text{NOON}}\rangle = \cos(N\phi)$. This is the effect commonly referred to as phase super-resolution, leading to an N-fold enhancement over the resolution dictated by the photon wavelength. By using again Eq.3.7, we can also retrieve that the phase error scales as $1/N$, showing a Heisenberg limited phase sensitivity.

While the advantages given by a NOON states with high photon number N are clear and can find many applications, it is also clear that it is very complicated to generate, manipulate and measure a high dimensional entangled state, not to mention that any losses (which adversely scales with N) quickly spoils its quantum properties. In the following section, we review some of the recent results towards this goal.

3.2 Generating and measuring entangled photons: state of the art

Following the previous discussion, there is a great interest in the production of path entangled NOON state with high photon number N. Different theoretical proposals, based on linear optical elements and postselection, have been put forward to achieve this objective [253, 254, 255]. All these proposals rely on probabilistic generation techniques and complex experimental implementations.

Indeed, experimental demonstration of genuine NOON states of light, entangled only in the spatial degrees of freedom, are still limited to 2 photons, obtained through the HOM interference [256, 223, 257]. Higher path-entangled photon number states has been obtained only through postselection. A quantum-enhanced phase measurement with 4 spatially entangled photons was demonstrated using postselection on NOON-like states in the form $\sqrt{3/4}(|4,0\rangle + |0,4\rangle)/\sqrt{2} + 1/\sqrt{4}\,|2,2\rangle$ [258].

On the contrary, the use of polarization equivalents to the Mach-Zender scheme, or combination of polarization and spatial degrees of freedom, allowed to achieve higher dimensionality for maximally entangled states, owing to an easier experimental manipulation. The current state of the art consists of 10 photon entanglement in a GHZ state [12], showing a 10-fold enhancement in phase resolution using a 10-modes correlation measurements. Polarization NOON states have been realized with 3 [259] and 4 photons [260]. The higher dimensional NOON state achieved to date is with 5 photons [261], exploiting the interference between coherent and single photon light on a beam splitter. This technique could in principle be used to obtain a path entangled state showing high overlap with a NOON states for arbitrary value of N [262, 263]. Experimentally though, it has been realized with polarization entangled photons.

All these experiments have revealed the presence of a NOON state by observing the expected N-fold enhancement of interference oscillations in correlation measurement. However, super-resolution is not an ubiquitous feature of quantum states. As it was demonstrated in the work of Resch et al. [264], enhanced phase resolution can be obtained also without entangled states, by postselection on the measured coincidence rates. On the contrary, it is not possible to beat the Standard Quantum Limit of precision measurement. Later on, a bound on the achievable visibility of super-resolved oscillations using only classical states of light in a Mach-Zender interferometer has been derived [265]. Thus, a complete certification of a NOON state should include the observation of both super-resolution and super-precision. However, phase sensitivity beyond the Standard Quantum Limit is even more difficult to achieve with photon number entangled states, since losses affect them exponentially stronger than coherent states [238]. Any loss in the manipulation or detection of the photons rapidly washes out the quantum advantage by decreasing the interference fringes resolution. Using squeezed states of light the possibility of beating the SQL has been established since many years [266, 267], while for photon number state is was always based on postselection [258]. Only very recently phase sensitivity below the SQL without postselection has been shown using a 2-photon NOON state [268], encoded in polarization.

The above discussion highlights the difficulties not only in the generation, but also in the measurements of highly entangled states. The unambiguous identification of a quantum state can be obtained with Quantum State Tomography (QST), a well known method to experimentally reconstruct a density matrix [269]. Even if hardly scalable, this allows to collect all the physical information about the measured degrees of freedom of a quantum state. For photonic states, this technique is very well mastered for the characterization of single and entangled polarization qubits, and indeed it has been used to measure the density matrix of a polarization NOON state of 2, 3 and 4 photons [270]. However, the tomography of spatially entangled photons is still in its infancy, as it requires the precise control of multiple optical phases, increasing rapidly with the number of particles.

The development of integrated photonics architectures recently allowed the generation and manipulation of path entanglement on chip, owing to a robust reconfigurability and phase control [217, 271, 272, 273]. This approach can also boost more complex metrology applications using multi-modes interferometers and higher dimensional photonic states [274]. The full tomography of 2 path-entangled photonic qubit, encoded over 4 modes, has been demonstrated on chip [271, 272], but not for NOON states. In both cases, it was done for individually addressable qubit each occupying different spatial modes, thus two distinguishable photons. The tomography of a spatially entangled two-photon NOON state has been shown only using an homodyne detection technique [275], which requires a local oscillator phase stabilized with respect to the signal.

We are interested here in performing a full QST of a 2 photon path-entangled NOON state, thus two indistinguishable photons occupying two spatial modes, using only coincidence detection and a simple Mach-Zender layout. The technique for the generation of such state and the characterization of its density matrix is devised in the next section.

3.3 Tomography of a 2 photon NOON state

3.3.1 NOON generation with HOM interference

The most natural way to obtain a two-photon path entangled NOON state is to perform the Hong-Ou-Mandel experiment with single photons, as shown by Eq.3.9. When perfectly indistinguishable photons impinge on a 50 : 50 beam splitter, they interfere and exit in the maximally entangled state

$$|\psi_{2002}\rangle = \frac{1}{\sqrt{2}}\left(|2,0\rangle_{\mathrm{A,B}} - |0,2\rangle_{\mathrm{A,B}}\right) \tag{3.11}$$

where A and B represent the two output spatial modes of the beam splitter.

Considering the case of non-perfect interference, there will be also the possibility for the two photons to leave the beam splitter from different output ports, in the state $|1,1\rangle_{\mathrm{A,B}}$. This happens when the two impinging photons do not contribute equally to the probability amplitudes at the two outputs. Such a reduced interference can be due both to a limited indistinguishability of the photons and to an unbalanced beam splitter. We will neglect for the moment the physical origin of such an effect, that in both cases produces a $|1,1\rangle_{\mathrm{A,B}}$ state, limiting the fidelity to an ideal NOON state.

In the most general case then, the output state of the HOM interference, given two input single photons, is a mixed state which can be described by a 3 level system, whose basis is constituted by the 3 possible distributions of the two photons on the two output spatial modes: $|2,0\rangle_{\mathrm{A,B}}$,$|0,2\rangle_{\mathrm{A,B}}$,$|1,1\rangle_{\mathrm{A,B}}$. The resulting density matrix of the output state ρ_{HOM} is identified by:

$$\rho_{\mathrm{HOM}} = \begin{array}{c|ccc} & \langle 2,0|_{\mathrm{A,B}} & \langle 1,1|_{\mathrm{A,B}} & \langle 0,2|_{\mathrm{A,B}} \\ \hline |2,0\rangle_{\mathrm{A,B}} & \rho_{1,1} & \rho_{1,2} & \rho_{1,3} \\ |1,1\rangle_{\mathrm{A,B}} & \rho_{2,1} & \rho_{2,2} & \rho_{2,3} \\ |0,2\rangle_{\mathrm{A,B}} & \rho_{3,1} & \rho_{3,2} & \rho_{3,3} \end{array} \tag{3.12}$$

The diagonal terms $\rho_{1,1}$, $\rho_{3,3}$ and $\rho_{2,2}$ respectively describe the probability of observing both photons on the mode A, both on the mode B or one photon on each mode. The off-diagonal terms instead describe the coherences between two basis kets among $|2,0\rangle_{\mathrm{A,B}}$, $|1,1\rangle_{\mathrm{A,B}}$ and $|0,2\rangle_{\mathrm{A,B}}$. The case of the ideal state $|\psi_{2002}\rangle$ of Eq.3.11 is shown in Fig.3.2, where we can see that the population is equally distributed between the $|2,0\rangle_{\mathrm{A,B}}$ and $|0,2\rangle_{\mathrm{A,B}}$ components, with maximum coherences demonstrating the maximal entanglement. To fully characterize the output state of the HOM interference we need to reconstruct its density matrix, which can be done using a Quantum State Tomography technique.

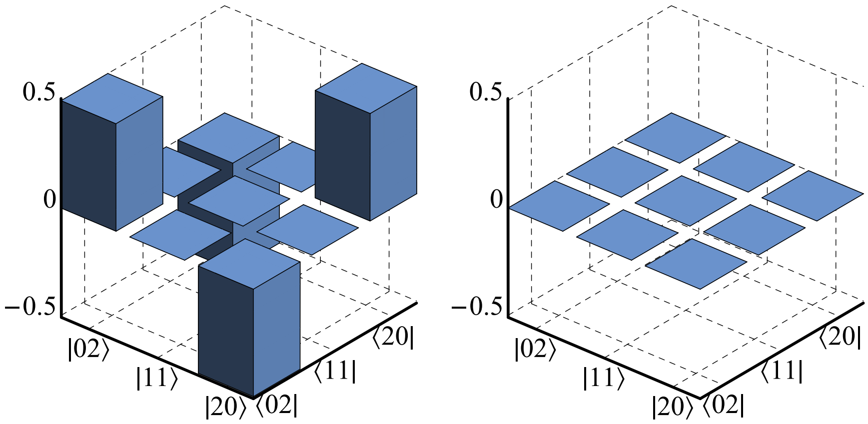

Figure 3.2 – Real part (left) and imaginary part (right) of the density matrix of the ideal 2-photon NOON state $|\psi_{2002}\rangle$.

3.3.2 Quantum tomography of spatially entangled photons

The general idea behind Quantum State Tomography is that, by performing a set of measurements over an ensemble of identical copies of a quantum system, it is possible to reconstruct its physical state. A physical state is identified by a complex density matrix ρ, satisfying three properties: it is Hermitian ($\rho_{i,j} = \rho^*_{j,i}$), normalized to unit trace ($\mathrm{Tr}[\rho] = \sum_i \rho_{i,i} = 1$) and positive semidefinite (thus it has non-negative eigenvalues). We can see that an $n \times n$ density matrix is completely described by $n^2 - 1$ real parameters, due to the hermiticity and normalization conditions [251]. Experimentally however the normalization of the state has to be tested, thus we need a total of n^2 independent measurements to fully reconstruct the density matrix. The link between a specific set of measurements and the elements of the density matrix is found by decomposing the latter into a linear combination of hermitian matrices. Since each matrix represents a projective measurement operator, we can use them to reconstruct the density matrix of the state.

We follow here the work of James et al. [269] to explain the simplest case of a single qubit. Considering the identity operator ($\hat{\sigma}_0$) and the Pauli spin matrices ($\hat{\sigma}_1$, $\hat{\sigma}_2$ and $\hat{\sigma}_3$), which are given by:

$$\hat{\sigma}_0 = \begin{pmatrix} 1 & 0 \\ 0 & 1 \end{pmatrix} \quad \hat{\sigma}_1 = \begin{pmatrix} 0 & 1 \\ 1 & 0 \end{pmatrix} \quad \hat{\sigma}_2 = \begin{pmatrix} 0 & -i \\ i & 0 \end{pmatrix} \quad \hat{\sigma}_3 = \begin{pmatrix} 1 & 0 \\ 0 & -1 \end{pmatrix} \tag{3.13}$$

the 2×2 density matrix of a two-level system can always be expressed in terms of the $\hat{\sigma}_i$ as:

$$\hat{\rho}_{2\times 2} = \frac{1}{2}\left(\frac{S_0}{S_0}\hat{\sigma}_0 + \frac{S_1}{S_0}\hat{\sigma}_1 + \frac{S_2}{S_0}\hat{\sigma}_2 + \frac{S_3}{S_0}\hat{\sigma}_3\right) = \frac{1}{2S_0}\begin{pmatrix} S_0 + S_3 & S_1 - iS_2 \\ S_1 + iS_2 & S_0 - S_3 \end{pmatrix} \tag{3.14}$$

where $S_i = \mathrm{Tr}[\hat{\rho}_{2\times 2}\hat{\sigma}_i]$. Performing the four measurements identified by $\hat{\sigma}_i$ on $\hat{\rho}_{2\times 2}$ allows to fully reconstruct the state of interest using the measurements outcomes S_i. We can see that S_0 is used to normalize all experimental results. This is simple to understand with respect to the polarization degree of freedom. If the qubit represents the polarization state of a photon, the tomography is analogous to the measurement of the Stokes parameters [276]. In this case the $\hat{\sigma}_i$ operators corresponds to a measurement of the total intensity, the intensity difference along the two linear, the two diagonal and the two circular polarizations.

To reconstruct the state of two polarization qubits, such as two different photons, a measurement of all combinations of the Stokes parameter for the two is required [269]. In the case of the path entangled NOON state we cannot individually manipulate the photons, being indistinguishable, leading to the representation of the state by a 3 × 3 density matrix.

The tomography procedure can be used for a higher dimensional state such as a qutrit, a three level system, as the one represented by the density matrix $\hat{\rho}_{\mathrm{HOM}}$ of Eq.3.12. In this case we need a minimum set of 9 measurements to reconstruct the state: 8 real parameters define a physical 3×3 density matrix, plus a single real parameter to normalize the experimentally obtained values [269]. To find a suitable set of measurements, we can start by writing the density matrix $\hat{\rho}_{\mathrm{HOM}}$ to be reconstructed as:

$$\hat{\rho}_{\mathrm{HOM}} = \frac{1}{3}\sum_{j=0}^{j=8} r_j \hat{\lambda}_j \tag{3.15}$$

where the $\hat{\lambda}_j$ are the eight SU(3) generator plus the identity operator, and the $r_j = \mathrm{Tr}[\hat{\rho}_{\mathrm{HOM}}\hat{\lambda}_j]$ are the expectation values of the operators $\hat{\lambda}_j$.

Even if it is not possible to directly measure the expectation values of the $\hat{\lambda}_j$ operators, they can be expressed as a linear combination of an arbitrary set, if complete, of physical measurements operators $\hat{\mu}_i$ [277]. Using a 9×9 invertible matrix A we can thus write the 9 measurements as $\hat{\mu}_i = \sum_j A_{ij}\hat{\lambda}_j$. The experimental results of these operators are given by:

$$n_i = \mathcal{N}\ \mathrm{Tr}[\hat{\rho}_{\mathrm{HOM}}\hat{\mu}_i] = \mathcal{N}\ \sum_{j=0}^{j=8} A_{ij}\mathrm{Tr}[\hat{\rho}_{\mathrm{HOM}}\hat{\lambda}_j] = \mathcal{N}\ \sum_{j=0}^{j=8} A_{ij} r_j \tag{3.16}$$

where $\mathcal{N} \in \mathbb{R}$ is a scaling factor depending on the experimental conditions.

Casting the density matrix $\hat{\rho}_{\mathrm{HOM}}$ and the expectation values r_j in form of column vectors having 9 elements (called ρ_k for the former and r_j for the latter), we can invert Eq.3.15 to express the r_j as a function of the density matrix elements ρ_k. We obtain $r_j = \sum_k B_{jk}\rho_k$, where the elements of the 9×9 invertible matrix B are given $B_{jk} = \langle\psi_j|\,\hat{\lambda}_k\,|\psi_j\rangle$, where ψ_j are the basis kets of the density matrix $\hat{\rho}_{\mathrm{HOM}}$. Inserting this relation into Eq.3.16 we obtain:

$$n_i = \mathcal{N}\ \sum_{j,k} A_{ij} B_{jk} \rho_k \tag{3.17}$$

Since we are not interested in the exact form of A and B, we can define a 9×9 matrix $M = \mathcal{N}(A \cdot B)$, in order to rewrite Eq.3.17 as:

$$n_i = \sum_{j=0}^{j=8} M_{ij} \rho_j \tag{3.18}$$

We obtain a linear relation between the measurements results and the density matrix elements through the matrix M. Inverting Eq.3.18 allows to fully reconstruct ρ_{HOM} using the measurement set $\hat{\mu}_i$:

$$\rho_i = \sum_{j=0}^{j=8} M_{ij}^{-1} n_j \tag{3.19}$$

For Eq.3.19 to be valid, a complete set of measurements for which the matrix M is invertible needs to be identified. In the following we exhibit a set of 9 different correlation measurements, giving access to a set of 9 equations in the form of Eq.3.18, from which we can retrieve the matrix M and its inverse.

We can understands the use of correlation measurements by considering the density matrix of the two-photon state of Eq.3.12, where the elements of ρ_{HOM} corresponds to all possible second order coherences of the field of the two photons on the two spatial modes, expressed as $\rho_{ij} = \langle \hat{a}_A^{\dagger n} \hat{a}_B^{\dagger 2-n} \hat{a}_A^{m} \hat{a}_B^{2-m} \rangle$ where $n, m = 0, 1, 2$ [270]. We can thus expect to be able to access them using two-photon correlation measurements, which can be expressed in the same form (when $n = m$). Indeed, it has been demonstrated explicitly for two orthogonal polarization modes of a single spatial mode that is possible to measure all N^{th} order coherences using only SU(2) transformations and N-fold coincidences [278]. This is the technique which was applied to reconstruct the density matrix of polarization NOON states [270], where the SU(2) transformations were implemented using phase retarders and waveplates and the photons were detected using cascaded SPADs. This scheme can in principle be transposed to path encoding, to analyse two orthogonal spatial modes of a single polarization mode. For instance, we can see that the same transformation applied by a half waveplate to the H and V polarizations, when oriented at 22.5° with respect to H, is applied by a beam splitter on its two input paths: in both cases balanced superposition of the two input modes is obtained at the output.

The most general transformation of SU(2) can be written as:

$$\begin{pmatrix} e^{i\phi} \sin\theta & e^{i\phi} \cos\theta \\ \cos\theta & -\sin\theta \end{pmatrix} \tag{3.20}$$

and can be obtained using a lossless beam splitter with variable reflectivity $\sqrt{R} = \sin\theta$ followed by a phase shifter of ϕ [279]. Experimentally, a variable beam splitter can be realized by a Mach-Zender interferometer, allowing to implement the same transformation. Still, this would imply the introduction of a second optical phase, which must be thoroughly controlled. Such a dual optical phase control in free space or in fibre optics is experimentally demanding. For this reason, we have developed an alternative approach based on the introduction of an ancillary spatial mode, which allows for the use of a single phase to perform the full tomography for an arbitrary N photon number. The experimental implementation of the setup is described in the next Section.

3.4 The tomography setup

The experimental setup to generate the two-photon state and complete the QST protocol can be divided into 3 parts:

- a state generation part, where identical copies of the quantum state ρ_{HOM} to be measured are generated using a single-photon source and an HOM interferometer;
- a state transformation part, where the required unitary transformations are applied to the state in order to access all the elements of its density matrix;
- a state detection part, where projective measurements are performed using SPADs.

For the state preparation, we use the single photons emitted by a QD-micropillar device under resonant excitation, as presented in Chapter 2. The experimental configuration in shown in Fig.3.3. Using a cross polarization configuration, we collect highly indistinguishable single photons, which are transferred to a fibre based HOM interferometer, where successively emitted photons are temporally overlapped using a delay line (see Fig.3.3). This is analogous to what was already explained in Section 2.2.3, with the difference that here the laser pulses are not doubled, but we use the photons generated by subsequent excitations. The HOM interferometer is implemented using a polarizing beam splitter (PBS), to split the single free space input beam, and a fibre beam splitter ($\mathrm{BS}_{\mathrm{HOM}}$), to recombine the two arms of the interferometer. One of the two arms contain a fibre delay line of 12.2 ns, adjusted to the repetition rate of the excitation laser. The input photons polarization is fixed using a polariser (Pol) and an half wave plate (HWP) oriented at 45° with respect to the optical axis of the polarizing beam splitter. Each photon has then 50% probability of going through either the short arm (the one without delay) or the long arm (the one with delay) of the interferometer. The polarization of the two photons is restored to be equal using polarization controllers (PC) composed of a quarter wave plate and a half wave plate. When a photon takes the long arm and the subsequent one takes the short arm, the two photons arrive at the same time at $\mathrm{BS}_{\mathrm{HOM}}$, where they interfere. Due to the probabilistic routing of the photons, we expect to create a NOON state with a probability of $\frac{1}{4}$, while with a probability of $\frac{3}{4}$ the two

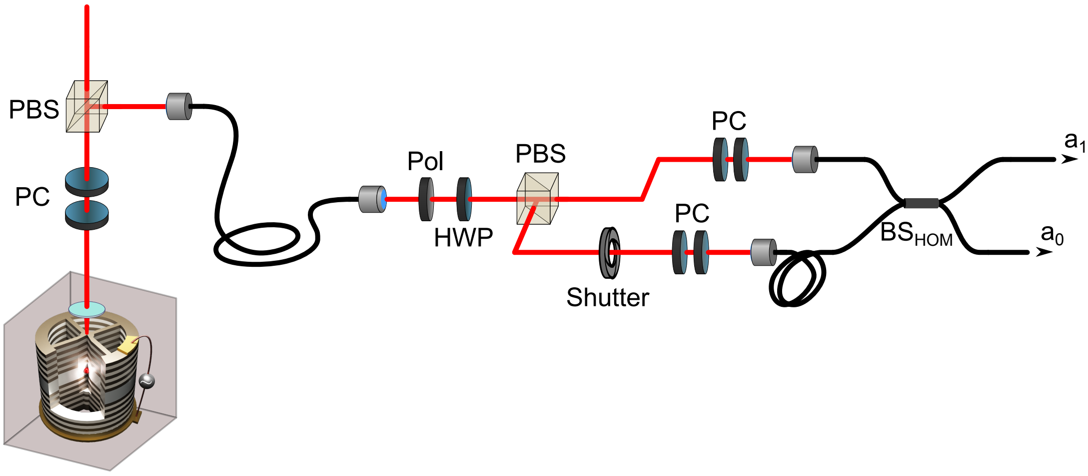

Figure 3.3 – Experimental setup for the generation of the NOON state. The single photons emitted by the QD-micropillar device are sent to a HOM interferometer, to probabilistically prepare the state ρ_{HOM} on the two modes $\hat{a}_0$ and $\hat{a}_1$ at the outputs of the fiber beam splitter $\mathrm{BS}_{\mathrm{HOM}}$.

photons will not temporally overlap, so only one photon will propagate through the tomography setup. Considering only the 2 photon subspace of the outcome of the HOM interference, the resulting state is described by the 3×3 density matrix ρ_{HOM} of Eq.3.12, which we want to reconstruct. Such a state is encoded over the two spatial modes $\hat{a}_0$ and $\hat{a}_1$, which are the two output ports of the fibre beam splitter $\mathrm{BS}_{\mathrm{HOM}}$ in Fig.3.3. To collect all tomographic measurements we employ 2 different experimental configurations that are explained in the following.

3.4.1 Measurement of the populations of the state

A first experimental configuration, shown in Fig.3.4, is used to retrieve the three populations of ρ_{HOM}. Here no transformation is applied to the state, and coincidence detection is directly performed on ρ_{HOM}. A correlation measurement between the two modes $\hat{a}_0$ and $\hat{a}_1$ is represented by the operator $\hat{R}_{0,1} = \hat{a}_0^\dagger \hat{a}_1^\dagger \hat{a}_0 \hat{a}_1$. Such two-photon measurement effectively implements the projector $|1,1\rangle\langle 1,1|$, as the state measured is not build on more than two photons. This gives access to the density matrix element $\rho_{2,2}$, the population of the $|1,1\rangle$ state. Similarly, an autocorrelation measurement on one optical mode $\hat{a}_0$ or $\hat{a}_1$ is given by $\hat{R}_{0,0} = \hat{a}_0^\dagger \hat{a}_0^\dagger \hat{a}_0 \hat{a}_0$ or $\hat{R}_{1,1} = \hat{a}_1^\dagger \hat{a}_1^\dagger \hat{a}_1 \hat{a}_1$ and implement the projectors $2\,|2,0\rangle\langle 2,0|$ or $2\,|0,2\rangle\langle 0,2|$. These two measurements provides the remaining populations $\rho_{1,1}$ and $\rho_{3,3}$ of the $|2,0\rangle$ and $|0,2\rangle$ states.

Experimentally, the population of the $|1,1\rangle$ state can be easily obtained by directing the outputs of the HOM interferometer to two SPADs and measuring the detected coincidence rate $R_{0,1}$, which corresponds to the standard experimental configuration used to measure the indistinguishability of two photons.

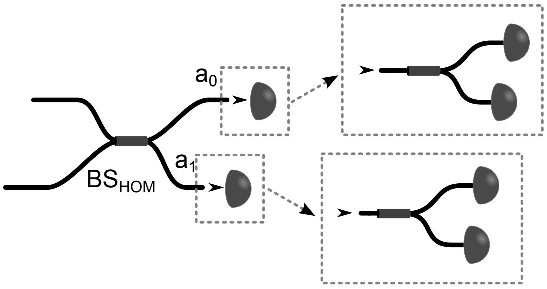

Figure 3.4 – Experimental configuration for the measurement of the population terms of ρ_{HOM}. Coincidence detection is performed on the two modes $\hat{a}_0$ and $\hat{a}_1$. Photon number resolution is achieved by demultiplexing each mode into two SPADs.

Retrieving the populations of the states $|2, 0\rangle$ and $|0, 2\rangle$ is less straightforward, since they corresponds to the probability of observing a two-photon state respectively on the mode $\hat{a}_0$ and on the mode $\hat{a}_1$. Using a photon number resolving detector would give the possibility to get direct access to these probabilities. On the contrary, single-photon avalanche diodes (SPADs) cannot discriminate the number of incident photons, as they always produce a single output pulse. Still, it has been demonstrated that is possible to resolve the photon number of a multi-photon state by spatially or temporally demultiplexing the state on two or more SPADs [280, 281, 282]. Following this idea, we use here a beam splitter to divide an incident pulse containing up to 2 photons onto two SPADs, and measure the detected coincidences. We can easily verify that, doing this, we can retrieve the result of an autocorrelation measurement on the incident pulse. For the general case of a balanced beam splitter with two input modes $\hat{b}_0$ and $\hat{b}_1$, and two output modes $\hat{b}_3$ and $\hat{b}_4$, the beam splitter input-output relations for the fields operators are given by:

$$\begin{pmatrix} \hat{b}_3 \\ \hat{b}_4 \end{pmatrix} = \frac{1}{\sqrt{2}} \begin{pmatrix} 1 & 1 \\ 1 & -1 \end{pmatrix} \begin{pmatrix} \hat{b}_0 \\ \hat{b}_1 \end{pmatrix} \tag{3.21}$$

Thus, the operator for the correlation measurement performed on the output modes ($\hat{b}_3$ and $\hat{b}_4$) using the input mode basis ($\hat{b}_0$ and $\hat{b}_1$) is:

$$\hat{R} = \hat{b}_3^\dagger \hat{b}_4^\dagger \hat{b}_3 \hat{b}_4 = \frac{1}{4} \left(\hat{b}_0^\dagger \hat{b}_0^\dagger \hat{b}_0 \hat{b}_0 - \hat{b}_0^\dagger \hat{b}_0^\dagger \hat{b}_1 \hat{b}_1 - \hat{b}_1^\dagger \hat{b}_1^\dagger \hat{b}_0 \hat{b}_0 + \hat{b}_1^\dagger \hat{b}_1^\dagger \hat{b}_1 \hat{b}_1 \right) \tag{3.22}$$

where we have used the commutation relations for the creation and annihilation operators ($[\hat{b}_i^\dagger, \hat{b}_j^\dagger] = [\hat{b}_i, \hat{b}_j] = 0$). If the state at the inputs of the beam splitter has vacuum on mode $\hat{b}_1$, only the first term of Eq.3.22 will give a non-zero contribution to the expectation value of such operator. As we see, up to a proportionality factor, the result corresponds to the intended autocorrelation

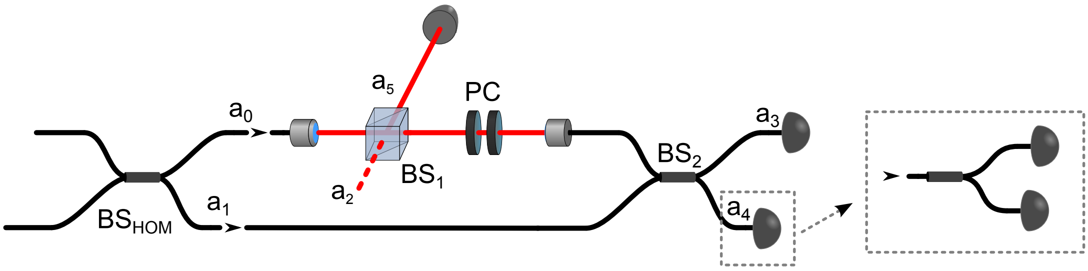

Figure 3.5 – Experimental setup to retrieve the coherence terms of ρ_{HOM}. A transformation is applied to the state using a split Mach-Zender interferometer, and coincidence detections are performed on the output modes $\hat{a}_3$, $\hat{a}_4$ and $\hat{a}_5$.

measurement on the input mode $\hat{b}_0$. Applying this procedure to the two modes $\hat{a}_0$ and $\hat{a}_1$, as represented in the dashed boxes of Fig.3.4, we can access the values of $\hat{R}_{0,0}$ and $\hat{R}_{1,1}$.

3.4.2 Measurement of the coherences of the state

In order to retrieve also the coherence terms of the density matrix ρ_{HOM} of Eq.3.12, a second experimental configuration is used, shown in Fig.3.5. Here we employ a split Mach-Zender layout, where the two output modes $\hat{a}_0$ and $\hat{a}_1$ of the HOM beam splitter ($\mathrm{BS}_{\mathrm{HOM}}$) are recombined on a second fibre beam splitter (BS_2). An ancillary mode $\hat{a}_2$ is introduced and entangled to the mode $\hat{a}_1$ using a free space beam splitter (BS_1), placed inside one arm of the interferometric setup. The free space path inside the interferometer is not optically stabilized, generating an optical phase difference (ϕ) between the two arms which vary slowly with time. This free space path contains also a polarization control stage (PC), needed to correct for any changes in the light polarization which happens during the propagation inside the fibres. By doing so we can be sure that the interference happening on the last beam splitter BS_2 is not limited by any polarization mismatch in the light coming from the two different input ports. A total of three output spatial modes are monitored using SPADs, by collecting time-tagged photon detection events: the two output ports $\hat{a}_3$ and $\hat{a}_4$ of the Mach-Zender interferometer, plus the second output $\hat{a}_5$ of the cube BS_1 placed inside one of its arms. This allows us to perform correlation measurements between any of the possible combinations of those modes, thus any $\hat{R}_{i,j} = \hat{a}_i^\dagger \hat{a}_j^\dagger \hat{a}_i \hat{a}_j$ with $i, j = 3, 4, 5$. Adding a beam splitter on any of the three output modes, we can also retrieve the result of an autocorrelation measurements where $i = j$, employing the same technique presented before for $\hat{R}_{0,0}$ and $\hat{R}_{1,1}$ (see Eq.3.21 and 3.22).

Each correlation measurements, for a specific value of ϕ, gives access to a different linear combination of the elements of the density matrix ρ_{HOM}. In order to retrieve the remaining 6 coherence terms ($\rho_{1,2}$, $\rho_{1,3}$, $\rho_{2,1}$ $\rho_{2,3}$, $\rho_{3,1}$, $\rho_{3,2}$) we need to perform 6 independent measurements, in addition to the 3 used to retrieve the populations terms. There are different possible sets of correlations that we can use to fully reconstruct the density matrix. Our set of choice for this second experimental configuration is given by $\hat{R}_{3,3}(\phi)$, $\hat{R}_{3,4}(\phi)$ and $\hat{R}_{3,5}(\phi)$, each performed for two different values of the phase ϕ.

We can qualitatively understand how such a measurements scheme works with an analogy to the tomography of polarization-entangled photons. The reconstruction of the density matrix of the polarization state of two entangled photons, requires to perform correlation measurements between non-orthogonal polarizations, where the two photons are detected along any combination of linear, diagonal and circular polarization. Mapping the spatial modes $\hat{a}_0$ and $\hat{a}_1$ to the polarization modes H and V, the above experimental configuration essentially mimics such correlation measurements. Detection on the output paths $\hat{a}_3$ and $\hat{a}_4$ accounts for the projection onto the $(H \pm e^{-i\phi}V)/\sqrt{2}$ polarizations. Thus while correlations like $R_{0,1}$ or $R_{0,0}$ would corresponds to detection on linear polarization basis, $R_{3,3}$ or $R_{3,4}$ would represents detection on diagonal or circular basis, depending on the value of ϕ. Correlations such as $R_{3,4}$ – without the additional cube BS_1 – evidencing a $\cos 2\phi$ dependence have already been demonstrated to confirm the NOON nature of a two-photon state [283]. Yet a complete polarization tomography must also include correlations such as $R_{i,5}$ with $i = 3, 4$, between modes before and after the transformations applied by the last beam splitter BS_2. These would correspond in the polarization analogy to correlations between linearly polarized photon V and diagonal or circular polarizations.

In the next section the mathematical derivation of the density matrix is presented in more details.

3.5 Theoretical description of the tomography

3.5.1 Description of the setup

In order to complete the quantum state tomography protocol, we model the experimental setup, presented in the previous section, in terms of unitary transformations. In such a way, we can determine the expected results as a function of the input state, hence use Eq.3.19 to retrieve the density matrix elements. As a first step, we consider pure input states to derive the relation between the measurements and the density matrix elements. The relations we obtain are then valid for any mixed state, whose density matrix is a linear superposition of pure-state density matrices weighted by the corresponding state probabilities.

A general pure input state can be expressed in terms of photon creator operators acting on the vacuum state [284] as:

$$|\psi_{in}\rangle = f(\hat{a}_i^\dagger)\,|0\rangle \tag{3.23}$$

using a polynomial function in the form $f(\hat{a}_i^\dagger) = \sum_n \prod_i (\hat{a}_i^\dagger)^n$. Given the unitary operation $\hat{U}$ implemented by the optical setup, the output state is:

$$|\psi_{out}\rangle = \hat{U} f(\hat{a}_i^\dagger)\,|0\rangle = \hat{U} f(\hat{a}_i^\dagger)\hat{U}^\dagger U\,|0\rangle = f(\hat{U}\hat{a}_i^\dagger\hat{U}^\dagger)\,|0\rangle = f(\hat{b}_i^\dagger)\,|0\rangle \tag{3.24}$$

where we have used the fact that an input vacuum state $\hat{U}\,|0\rangle$ will results in an output vacuum state $|0\rangle$. The explicit form of $|\psi_{out}\rangle$ in terms of the photon creation operators $\hat{b}_i = U^\dagger \hat{a}_i U$ acting on the output modes can be obtained using the following linear transformation:

$$\hat{b}_i = \sum_{j=1}^{n} S_{i,j}\hat{a}_j \tag{3.25}$$

where S, also called scattering matrix, is the matrix representation of the setup transformation $\hat{U}$ on the optical mode basis, relating the input to the output operators. By combining the local transformations acting on subsets of the optical modes, here implemented by beam splitters and phase shifters as shown in Eq.3.3, we can obtain the full form of the matrix S [285]. Thus using Eq.3.25 we can obtain $|\psi_{out}\rangle$ from any $|\psi_{in}\rangle$. Finally, applying the measurements operators on the output state we can retrieve both the expected single photon count rates R_i on the i^{th} detector and the expected coincidence rates $R_{i,j}$ between the i^{th} and the j^{th} detector:

$$R_i = \mathcal{N}_i \langle\psi_{out}|\,\hat{a}_i^\dagger\hat{a}_i\,|\psi_{out}\rangle \tag{3.26a}$$

$$R_{i,j} = \mathcal{N}_{ij} \langle\psi_{out}|\,\hat{a}_i^\dagger\hat{a}_j^\dagger\hat{a}_i\hat{a}_j\,|\psi_{out}\rangle \tag{3.26b}$$

The constants $\mathcal{N}_i = \mathcal{N}\xi_i$ and $\mathcal{N}_{ij} = \mathcal{N}\xi_i\xi_j$ are experimental scaling factors that include the production rate $\mathcal{N}$ of the input state and the efficiency ξ_i of the detectors (while the losses of the setup are already accounted for in the transformation U as detailed later).

As explained in the next section presenting the experimental results, to correct for fluctuations of the signal during the measurement, the coincidences will be normalized by the uncorrelated detection events. These uncorrelated events corresponds to single photon detections triggered by different excitation pulses, i.e. coincidences detected at delays $\tau \neq 0$. We thus calculate the ratio of the coincidences detected at zero time delay, due to the NOON state probabilistically generated $\frac{1}{4}$ of the times, to the ones coming from single photons entering for different delays in either one of the two input of the HOM beam splitter. The zero-time delay coincidences due to the NOON state can be calculated by considering an input state in the form

$$|\psi_{in}^{\mathrm{NOON}}\rangle = \alpha\,|2,0\rangle + \beta\,|1,1\rangle + \gamma\,|0,2\rangle = \left(\alpha\frac{(\hat{a}_0^\dagger)^2}{\sqrt{2}} + \beta\hat{a}_0^\dagger\hat{a}_1^\dagger + \gamma\frac{(\hat{a}_1^\dagger)^2}{\sqrt{2}}\right)|0\rangle \tag{3.27}$$

and using the measurement of Eq.3.26b on the resulting output state we obtain a coincidence rate of $R_{i,j}^{\text{NOON}} = \mathcal{N}_{ij} \langle\psi_{out}^{\text{NOON}}| \hat{a}_i^\dagger \hat{a}_j^\dagger \hat{a}_i \hat{a}_j |\psi_{out}^{\text{NOON}}\rangle$. For the uncorrelated detections instead we should consider that a single photon is entering in either one of the two input of the HOM beam splitter with the same probability. The input state we consider for the tomography is then an equal mixture of the two possibilities:

$$|\psi_{in}^{\pm}\rangle = \frac{|1,0\rangle \pm |0,1\rangle}{\sqrt{2}} = \frac{1}{\sqrt{2}}\left(\hat{a}_0^\dagger \pm \hat{a}_1^\dagger\right)|0\rangle \tag{3.28}$$

and using Eq.3.26a we obtain the resulting count rate on a detector as $R_i^{\pm} = \frac{1}{2}(R_i^+ + R_i^-)$ where $R_i^+ = \mathcal{N}_i \langle\psi_{out}^+| \hat{a}_i^\dagger \hat{a}_i |\psi_{out}^+\rangle$ and $R_i^- = \mathcal{N}_i \langle\psi_{out}^-| \hat{a}_i^\dagger \hat{a}_i |\psi_{out}^-\rangle$. The uncorrelated coincidence rate between two detectors will be given by $R_i^{\pm} \times R_j^{\pm}$. The normalized correlation measurements are thus described by:

$$R_{i,j} = \frac{R_{i,j}^{\text{NOON}}}{R_i^{\pm} \times R_j^{\pm}} \tag{3.29}$$

We use this relation now to obtain the expression of the correlation measurements presented in the previous section ($R_{0,0}$, $R_{0,1}$, $R_{1,1}$, $R_{3,3}(\phi)$, $R_{3,4}(\phi)$, $R_{3,5}(\phi)$, $R_{4,5}(\phi)$) as a function of the density matrix elements. Here, we consider pure states for clarity. The density matrix of Eq.3.12 can then be rewritten, considering a pure input state in the form of Eq.3.27, as:

$$\rho_{\text{HOM}} = \begin{array}{c} \\ |2,0\rangle \\ |1,1\rangle \\ |0,2\rangle \end{array} \begin{array}{c} \begin{array}{ccc} \langle 2,0| & \langle 1,1| & \langle 0,2| \end{array} \\ \begin{pmatrix} |\alpha|^2 & \alpha\beta^* & \alpha\gamma^* \\ \beta\alpha^* & |\beta|^2 & \beta\gamma^* \\ \gamma\alpha^* & \gamma\beta^* & |\gamma|^2 \end{pmatrix} \end{array} \tag{3.30}$$

where the link between the different matrix elements and the basis kets of the state appears: the three real elements on the diagonal identify the populations, while the non-diagonal terms identify the coherences between different components of the state.

In the case of the three measurements performed to retrieve the populations of ρ_{HOM} (see Section 3.4.1), no transformation is applied to the state, thus the matrix S is the identity matrix. As expected, the results are:

$$R_{0,0} = 2|\alpha|^2 \qquad R_{1,1} = 2|\gamma|^2 \qquad R_{0,1} = |\beta|^2 \tag{3.31}$$

For the measurement of the coherences of ρ_{HOM} (see Section 3.4.2), we need to model the transformation applied by the experimental setup of Fig.3.5. It can be done using the schematic representation shown in Fig.3.6. In this mode diagram, each spatial mode is represented by a solid line, which undergoes either a beam splitter transformation or a phase shift. Equivalently, it can be seen as a quantum logic circuit composed of only Hadamard gates and a phase gate. The blocks labelled η_i with $i = 1, 2, 3$ represent additional beam splitters used to

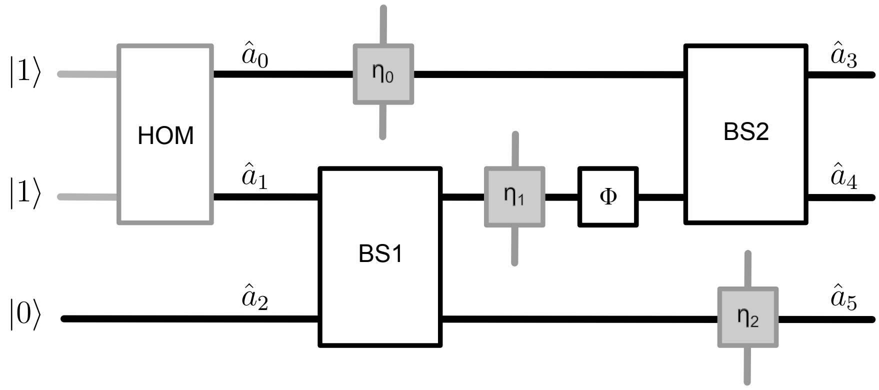

Figure 3.6 – Mode diagram corresponding to the split Mach-Zender setup of Fig.3.5. The input state in encoded over the modes $\hat{a}_0$ and $\hat{a}_1$, while the ancillary mode $\hat{a}_2$ is fed with vacuum. Correlations are performed on the output modes $\hat{a}_3$, $\hat{a}_4$ and $\hat{a}_5$. The HOM beam splitter is shown for completeness but not part of the transformation matrix S. The greyed elements represents losses, introduced as beam splitter transformations having reflectivity η_0, η_1 and η_2.

describe the optical losses of the experiment, related to fibre to fibre or free space to fibre coupling. Using this approach we can keep the global transformation of the setup unitary, at the cost of including more optical modes. While needed to account for the observations and to retrieve the tomography results shown in the next section, the losses η_i are neglected in the following in order to simplify the equations. Here we consider three input modes: two over which the state is encoded $(\hat{a}_0, \hat{a}_1)$ plus an ancillary one $\hat{a}_2$. Combining the one and two modes transformations (with specific form given in Eq.3.3), respectively given by a phase shift ϕ and two beam splitters BS_1 and BS_2 having reflectivities R_1 and R_2, we can express the inputs in terms of the output modes $(\hat{a}_3, \hat{a}_4, \hat{a}_5)$ using:

$$\begin{pmatrix} \hat{a}_0 \\ \hat{a}_1 \\ \hat{a}_2 \end{pmatrix} = S^{-1} \begin{pmatrix} \hat{a}_3 \\ \hat{a}_4 \\ \hat{a}_5 \end{pmatrix} \tag{3.32}$$

where, for the specific setup of Fig.3.6 the transformation matrix is:

$$S^{-1} = \begin{pmatrix} \sqrt{1-\mathrm{R}_2} & e^{i\phi}\sqrt{1-\mathrm{R}_1}\sqrt{\mathrm{R}_2} & e^{i\phi}\sqrt{\mathrm{R}_1}\sqrt{\mathrm{R}_2} \\ \sqrt{\mathrm{R}_2} & -e^{i\phi}\sqrt{1-\mathrm{R}_1}\sqrt{1-\mathrm{R}_2} & -e^{i\phi}\sqrt{\mathrm{R}_1}\sqrt{1-\mathrm{R}_2} \\ 0 & \sqrt{\mathrm{R}_1} & -\sqrt{1-\mathrm{R}_1} \end{pmatrix} \tag{3.33}$$

which using $\mathrm{R}_1 = 0.4$ and $\mathrm{R}_2 = 0.5$, as measured from the experimental setup, becomes:

$$S^{-1} = \begin{pmatrix} \frac{1}{\sqrt{2}} & \sqrt{\frac{3}{10}}e^{i\phi} & \frac{e^{i\phi}}{\sqrt{5}} \\ \frac{1}{\sqrt{2}} & -\sqrt{\frac{3}{10}}e^{i\phi} & -\frac{e^{i\phi}}{\sqrt{5}} \\ 0 & \sqrt{\frac{2}{5}} & -\sqrt{\frac{3}{5}} \end{pmatrix} \tag{3.34}$$

Using this transformation, we retrieve the explicit form of the output states $|\psi_{\text{out}}\rangle$ for any $|\psi_{\text{in}}\rangle$, and from 3.29 we find the results of the phase-dependent measurements $R_{i,j}(\phi)$ performed on the output modes as a function of the elements of Eq.3.30:

$$R_{3,4} = \frac{8}{25}|\alpha|^2 - \frac{24}{125}e^{-2i\phi}\alpha\gamma^* - \frac{24}{125}e^{2i\phi}\gamma\alpha^* + \frac{72}{625}|\gamma|^2 \tag{3.35}$$

$$R_{3,5} = \frac{8}{125}|\beta|^2 + \frac{8}{125}\sqrt{\frac{6}{5}}e^{-i\phi}\beta\gamma^* + \frac{8}{125}\sqrt{\frac{6}{5}}e^{i\phi}\gamma\beta^* + \frac{48}{625}|\gamma|^2 \tag{3.36}$$

$$R_{4,5} = \frac{8}{125}|\beta|^2 - \frac{8}{125}\sqrt{\frac{6}{5}}e^{-i\phi}\beta\gamma^* - \frac{8}{125}\sqrt{\frac{6}{5}}e^{i\phi}\gamma\beta^* + \frac{48}{625}|\gamma|^2 \tag{3.37}$$

$$\begin{aligned} R_{3,3} = {} & \frac{1}{50}|\alpha|^2 + \frac{1}{25}\sqrt{\frac{3}{10}}e^{-i\phi}\alpha\beta^* + \frac{3}{250}e^{-2i\phi}\alpha\gamma^* + \\ & \frac{1}{25}\sqrt{\frac{3}{10}}e^{i\phi}\beta\alpha^* + \frac{3}{125}|\beta|^2 + \frac{3}{125}\sqrt{\frac{3}{10}}e^{-i\phi}\beta\gamma^* + \\ & \frac{3}{250}e^{2i\phi}\gamma\alpha^* + \frac{3}{125}\sqrt{\frac{3}{10}}e^{i\phi}\gamma\beta^* + \frac{9}{1250}|\gamma|^2 \end{aligned} \tag{3.38}$$

Up to now we have used a pure state for a clearer observation of which terms of the density matrix contribute to the expected results. The same relations however are valid for a mixed input state. Is is sufficient to make a simple correspondence between the elements of Eq.3.30 and Eq.3.12 to obtain the expressions for the general case.

A complete set of correlation measurements for the reconstruction of ρ_{HOM} is obtained for:

$$\begin{aligned} R_{\text{set}}(\phi_1, \phi_2) = \big(& R_{0,0},\ R_{0,1},\ R_{1,1} \\ & R_{3,3}(\phi_1), R_{3,4}(\phi_1), R_{3,5}(\phi_1) \\ & R_{3,3}(\phi_2), R_{3,4}(\phi_2), R_{3,5}(\phi_2)\big) \end{aligned} \tag{3.39}$$

As later shown in Section 3.7.1, for $|\phi_1 - \phi_2| \neq 0, \frac{\pi}{2}, \pi$, the linear transformation matrix M relating the measurements vector $R_{\text{set}}(\phi_1, \phi_2)$ to the vectorial form of the density matrix elements $\rho_{\text{vec}} = (\rho_{1,1},\ \rho_{1,2},\ \rho_{1,3},\ \rho_{2,1},\ \rho_{2,2},\ \rho_{2,3},\ \rho_{3,1},\ \rho_{3,2},\ \rho_{3,3})$ is invertible, so that:

$$\rho_{\text{vec}} = M^{-1}\overline{R}_{\text{set}}(\phi_1, \phi_2) \tag{3.40}$$

where $\overline{R}_{\text{set}}(\phi_1, \phi_2)$ are the experimentally measured values of the set $R_{\text{set}}(\phi_1,\ \phi_2)$. This linear tomography procedure allows a simple reconstruction of the density matrix from the experimentally measured correlations.

Before showing the experimental results, we discuss in the next sections the expected coincidence rates from the above calculations.

3.5.2 Expected results

Using the formulas derived in the previous section, we can now plot the expected values of the following measurements:

$$R_{0,0},\ R_{1,1},\ R_{0,1},\ R_{3,3}(\phi),\ R_{3,4}(\phi),\ R_{3,5}(\phi),\ R_{4,5}(\phi) \tag{3.41}$$

for any input density matrix ρ_{HOM}. For the following simulations we use the complete model of the experimental setup, represented in Fig.3.6, including the losses, which have been experimentally measured to be $\eta_0 = 0.02$, $\eta_2 = 0.7$ while $\eta_2 \approx 0$ is negligible. Note that $R_{4,5}(\phi)$ is not necessary to obtain a complete measurement set for the linear tomography but included here for clarity. This allows to better understand how the different measurements are sensitive to the different elements of the density matrix. The first three measurements $(R_{0,0},\ R_{0,1},\ R_{1,1})$ of course do not depend on the value of the phase ϕ, as they are performed before the Mach-Zender interferometer. Still, they are also represented altogether as a function of ϕ for convenience.

The ideal case of a maximally entangled state $|\psi_{2002}\rangle = \frac{1}{\sqrt{2}}(|2,0\rangle - |0,2\rangle)$ corresponds to the real density matrix ρ_{HOM} of Fig.3.7.b, and the simulated experimental results are shown in Fig.3.7.a with solid lines. As expected $R_{0,1}$ is 0 and both $R_{0,0}$ and $R_{1,1}$ are equal to 1, since the population is equally distributed between $|2,0\rangle$ and $|0,2\rangle$ states. The coincidences $R_{3,3}(\phi)$ and $R_{3,4}(\phi)$ correspond to coincidences at the outputs of the split Mach-Zender where the 2-photon NOON state is interfering. Their phase dependence shows a π oscillation period, revealing the attended super-resolution, with a phase inversion between the two. This situation is equivalent to the one described in Eq.3.9: the output of the Mach-Zender oscillate between a separable $|1,1\rangle$ state and a 2-photon NOON state. Thus the maximum probability of observing a photon on each exits (measured by $R_{3,4}(\phi)$) corresponds to the minimum probability of observing both photons on the same exit (measured by $R_{3,3}(\phi)$), and the situation is inverted with a phase shift of $\pi/2$. The contrast between the maximum and minimum of such an interference depends on the intensity of the coherences between the $|2,0\rangle$ and $|0,2\rangle$ terms of ρ_{HOM}. If all the coherence terms are zero, no ϕ dependence is observed. This situation corresponds to the real density matrix of Fig.3.7.c,

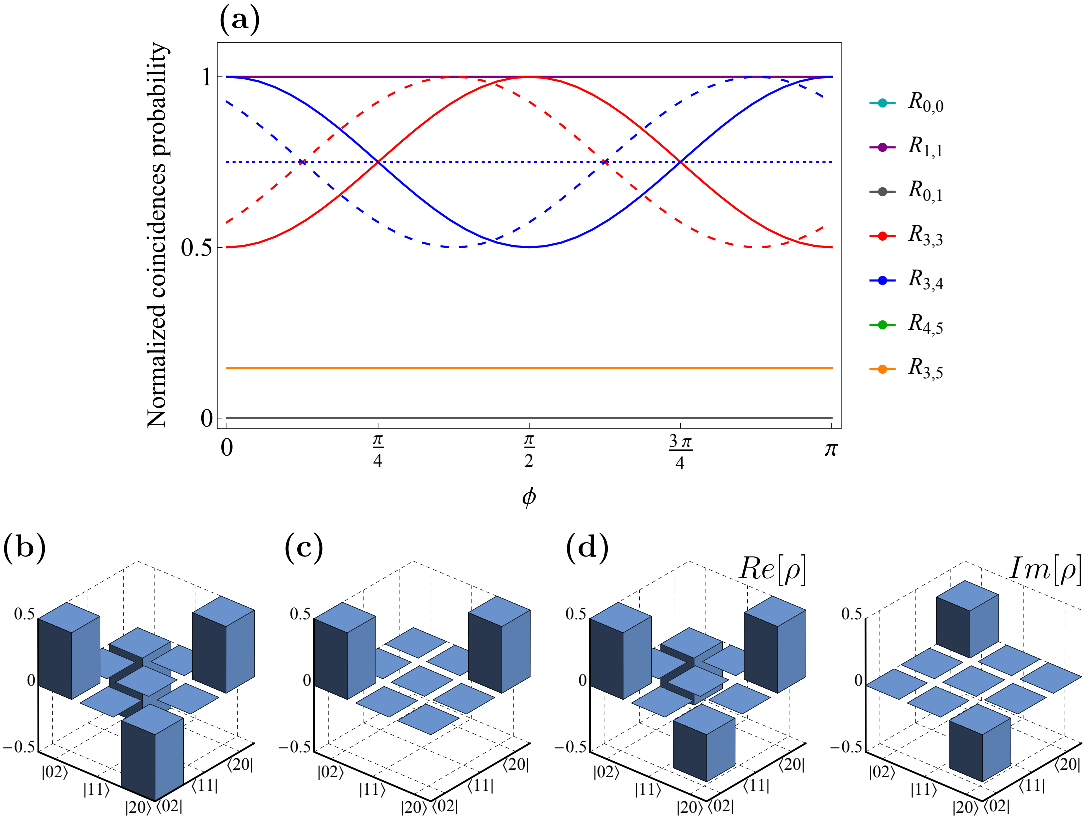

Figure 3.7 – (a) Phase dependence of the expected correlation rates for different form of the state ρ_{HOM}. Solid lines are for the ideal 2-photon NOON state $|\psi_{2002}\rangle$ shown in (b). Dotted lines are for the mixture of $|2,0\rangle$ and $|0,2\rangle$ states shown in (c). Dashed lines are for the pure state shown in (d), where the kets $|2,0\rangle$ and $|0,2\rangle$ have a relative phase shift of $\pi/4$ with respect to (b).

representing the state $\rho_{2002} = \frac{1}{2}(|2,0\rangle\langle 2,0| + |0,2\rangle\langle 0,2|)$ and the expected results are shown by the dotted lines in Fig.3.7.a. Now the values of $R_{3,3}$ and $R_{3,4}$ (overlapping red and blue dotted lines) are averaging the previous oscillatory behaviour (solid red and blue lines), while no difference is observed on the other measurements. We can notice that the maximum visibility is not 100% even in the case of the ideal state of Fig.3.7.b, which is due to the presence in our experimental configuration of optical losses and an additional beam splitter cube BS_1. These limitations are already accounted for, leading the maximum visibility of almost 50%.

To show the phase sensitivity of the setup, we now introduce a $\frac{\pi}{4}$ phase shift between the two kets of the maximally entangled state $|\psi_{2002}\rangle$, leading to the state $\frac{1}{\sqrt{2}}\left(|2,0\rangle - e^{-i\pi/4}\,|0,2\rangle\right)$. The corresponding density matrix is shown in Fig.3.7.d, where the coherence terms are shared among the real (left) and

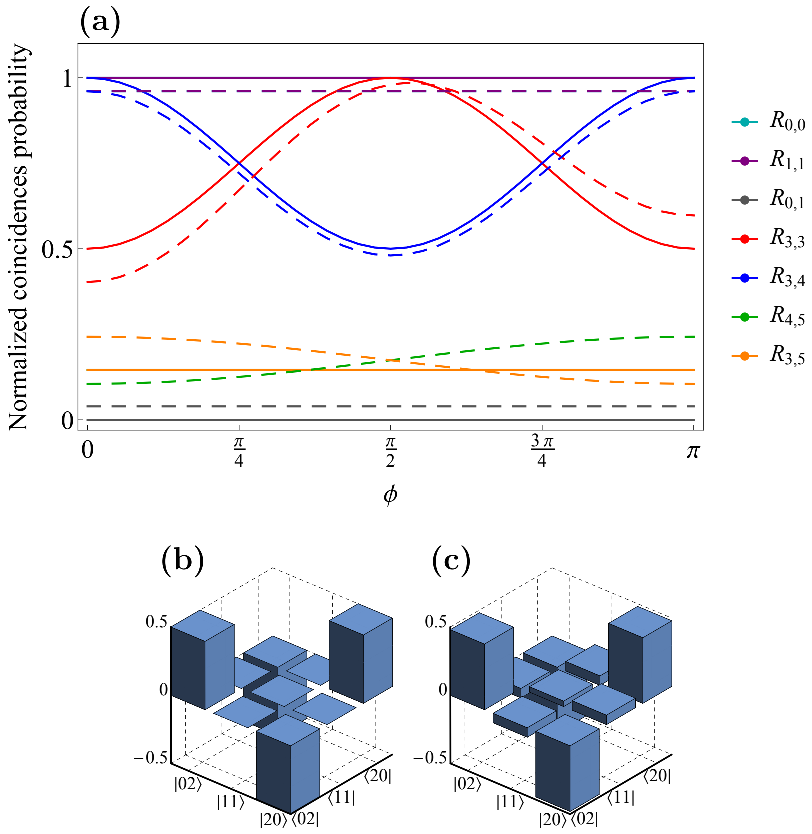

Figure 3.8 – (a) Comparison of the correlation rates expected from the ideal 2-photon NOON state $|\psi_{2002}\rangle$ (solid lines) of panel (b) and the imperfect NOON state $|\psi_{11}\rangle$ (dashed lines) of panel (c).

imaginary (right) part of the matrix. The expected results from this state are shown in Fig.3.7.a using dashed lines. Again, no difference is observed except for the values of $R_{3,3}$ and $R_{3,4}$, which both experience an horizontal shift of $\frac{\pi}{8}$ in units of optical phase difference ϕ. This highlights how the horizontal position gives access to the imaginary part of the coherence terms of the density matrix (i.e., the inner phase of the 2-photon NOON state). Moreover, we can observe again that an optical phase shift of ϕ in the interferometer corresponds to a 2ϕ phase shift between the $|2,0\rangle$ and $|0,2\rangle$ basis kets, giving the twofold improvement in phase resolution.

To complete the analysis, we now consider the case of a non-maximally entangled state, by including a non-zero population of the $|1,1\rangle$ component in the density matrix. Starting from the ideal NOON state $|\psi_{2002}\rangle$ (shown again in Fig.3.8.b) and moving 4% of the population to the $|1,1\rangle$ ket, we can obtain the pure state $|\psi_{11}\rangle = \frac{\cos(0.2)}{\sqrt{2}}\left(|2,0\rangle - |0,2\rangle\right) - \sin(0.2)\,|1,1\rangle$ whose density matrix is shown in Fig.3.8.c. The simulated results are plotted in Fig.3.8.a (dashed lines) along with the results from the ideal NOON state already shown before (solid

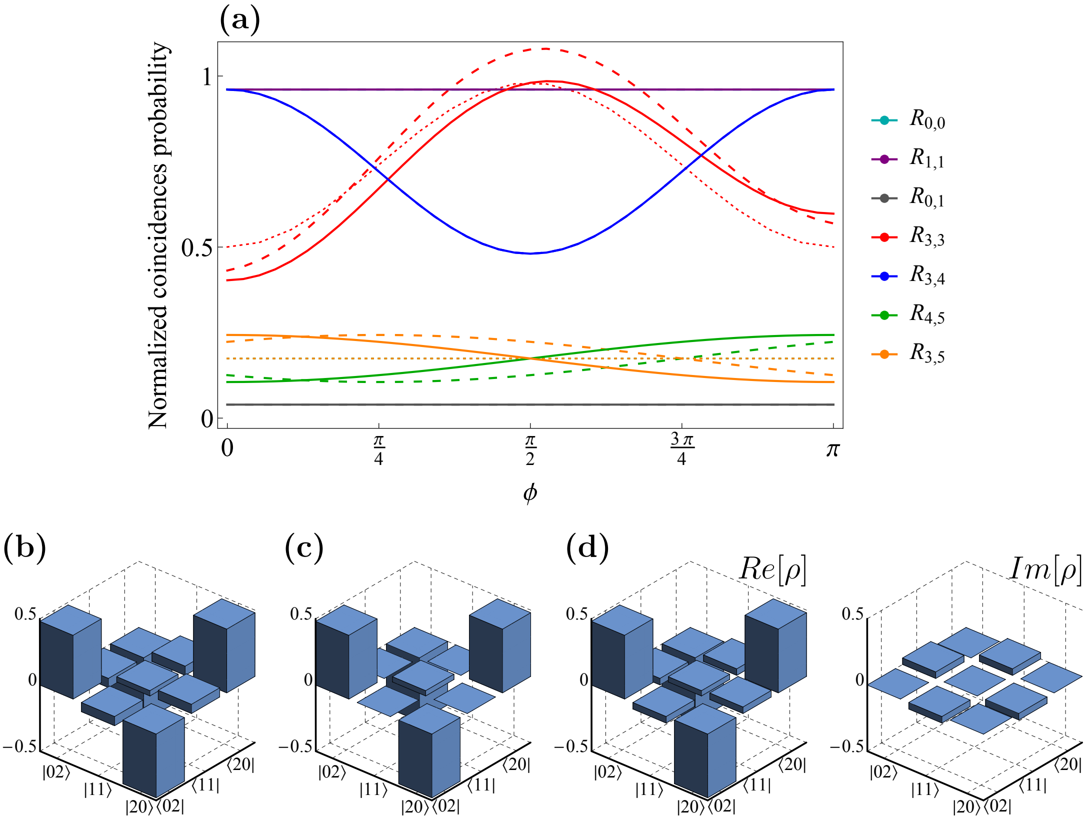

Figure 3.9 – (a) Expected correlation rates for different forms of non-ideal NOON states. Solid lines are for the pure state $|\psi_{11}\rangle$, shown in panel (b). Dotted lines are for the mixed state ρ_{11}, shown in panel (c). Dashed lines are for the pure state shown in panel (d), analogous to the state in (b) but with a phase shift of $\pi/4$ on the ket $|1,1\rangle$.

lines), for a comparison. Now the value of $R_{0,1}$ is increased by the population of the $|1,1\rangle$ component, while $R_{0,0}$ and $R_{1,1}$ are decreased by the same amount. The dependence on ϕ of $R_{3,4}$ is affected through the decreased populations of the $|2,0\rangle$ and $|0,2\rangle$ components. $R_{3,4}$ shows the same $\cos(2\phi)$ dependence as $R_{3,3}$, but slightly altered by a $\cos(\phi)$ modulation. The most interesting feature is in $R_{3,5}$ and $R_{4,5}$, which now show a $\cos(\phi)$ dependence reflecting the interference of the one photon component. Analogously to what observed in the previous case, the visibility of such an interference effect depends on the intensity of the coherence terms relating the $|1,1\rangle$ ket with the other components of the density matrix.

This can be verified in Fig.3.9.a, where we plot again the results from the pure state $|\psi_{11}\rangle$ of Fig.3.8.c (whose density matrix is shown also in Fig.3.9.b) using solid lines, this time together with the mixed state $\rho_{11} = 0.96\,|\psi_{2002}\rangle\,\langle\psi_{2002}| + 0.04\,|1,1\rangle\,\langle 1,1|$ (dotted lines) whose density matrix is shown in Fig.3.9.c. With a same population for the $|1,1\rangle$ ket, but no coherence relating it to the other states, the $\cos(\phi)$ dependence of $R_{3,5}$ and $R_{4,5}$ is averaged out in the dotted lines. An effect is observed also on $R_{3,3}$, where the $\cos(\phi)$ modulation is suppressed.

Finally, the dashed lines of the Fig.3.9.a show the results from the pure state $\frac{\cos(0.2)}{\sqrt{2}}(|2,0\rangle - |0,2\rangle) - \sin(0.2)e^{-\pi/4}|1,1\rangle$ (density matrix of Fig.3.9.d). The difference of this last state with the one of Fig.3.9.c is again a phase shift of $\pi/4$ of the $|1,1\rangle$ component. Such a shift is reflected in an horizontal translation of $R_{3,5}$ and $R_{4,5}$, this time of $\pi/4$ in units of optical phase shift ϕ. We can thus say that these last two measurements allows to access the coherences of the $|1,1\rangle$ ket with respect to the other two states $|2,0\rangle$ and $|0,2\rangle$. We see that they do not provide any enhanced phase resolution, as opposite to the coherences between the kets $|2,0\rangle$ and $|0,2\rangle$.

To summarize, the above examples gave a practical understanding of how the different measurements are linked to the different elements of the density matrix: $R_{0,0}$, $R_{1,1}$ and $R_{0,1}$ to the population terms, $R_{3,3}$ and $R_{3,4}$ to the coherence terms between $|2,0\rangle$ and $|0,2\rangle$, $R_{3,5}$ and $R_{4,5}$ to the coherence terms of $|1,1\rangle$. To reconstruct the density matrix we combine the above measurements, using different tomography reconstruction techniques, as shown in the following sections.

3.6 Experimental results

We now presents the experimental implementation of the tomography approach. The QD-micropillar source of single photon is excited resonantly and the emitted photons are collected under resonant excitation, in order to obtain highly indistinguishable photons as explained in Chapter 2. By careful alignment of the experimental setup we can repeatedly obtain a value of $g^{(2)}(0) = 0.03 \pm 0.01$ in the emission from the device QD3, used to perform the measurements presented here.

3.6.1 Populations

As presented in Section 3.4, to retrieve the population terms we use the experimental setup shown in Fig.3.4. To access the $|1,1\rangle$ component we perform the cross correlation measurement $\hat{R}_{0,1} = \hat{a}_0^\dagger \hat{a}_1^\dagger \hat{a}_0 \hat{a}_1$ between the two outputs of the HOM beam splitter. The result of this measurement is shown in Fig.3.10.a, where the number of detected coincidences is plotted as a function of the time delay between the two detected photons. Each peak represents the coincidences arising from different laser pulses, except for the zero time delay ones, which are triggered by a same excitation pulse. The limited number of coincidences at zero time delay reflects a high degree of indistiguishability, meaning a small value of the population term $\rho_{2,2}$. The first sidepeaks, at delays ±12.2ns, shows

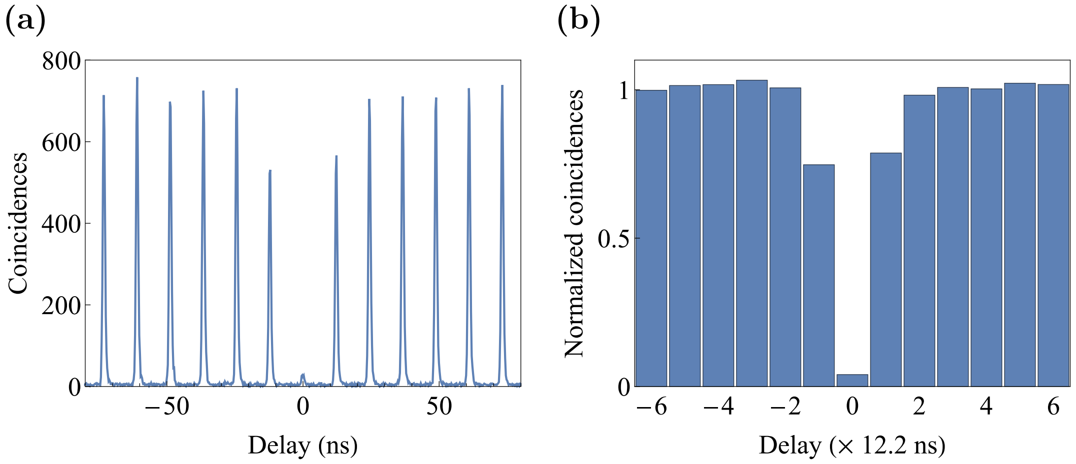

Figure 3.10 – Measured correlation histogram for $\hat{R}_{0,1}$. (a) Raw measurement, showing the detected coincidences as a function of the delay. (b) Integrated coincidences counts arising from each laser excitation pulse, normalized to the average area of uncorrelated peaks (at delays $\geq 2 \times 12.2ns$).

a reduced height due to the probabilistic routing in the HOM of photons emitted with a temporal separation of 12.2 ns. This reduced height can be theoretically predicted [215], however those peaks are not used in the following analysis. In order to remove errors due to signal fluctuation during the measurement, which are expected from mechanical instabilities changing the laser spot-source overlap, the number of coincidences is normalized. After background subtraction (typically 5 counts in the measurements of Fig.3.10 and Fig.3.11), the detected counts are integrated in a temporal area of 1 ns around each peak, and the normalization is performed with respect to the average area of peaks at delays $\tau \geq 2 \times 12.2$ ns, representing uncorrelated detection events triggered by different excitation pulses. This normalization results in the plot of Fig.3.10.b. The total number of counts in the peak at zero time delay corresponds to the normalized coincidence rate $R_{0,1}$ that we use for the tomography.

To access $|2,0\rangle$ and $|0,2\rangle$ components we perform the two autocorrelation measurements $\hat{R}_{0,0} = \hat{a}_0^\dagger \hat{a}_0^\dagger \hat{a}_0 \hat{a}_0$ and $\hat{R}_{1,1} = \hat{a}_1^\dagger \hat{a}_1^\dagger \hat{a}_1 \hat{a}_1$ by demultiplexing each output of the HOM beam splitter into two SPADs, as represented in Fig.3.4. The results of these two measurements are shown in Fig.3.11.a and 3.11.b. We see that this time we have a high number of coincidences at zero time delay, implying a big population for the $|2,0\rangle$ and $|0,2\rangle$ components. The same normalization as for the previous measurement is applied, where the counts are integrated into a 1 ns area and normalized with respect to the uncorrelated peaks areas. The results are shown in Fig.3.11.c and 3.11.d, from which we can retrieve the values of the coincidences rates $R_{0,0}$ and $R_{1,1}$.

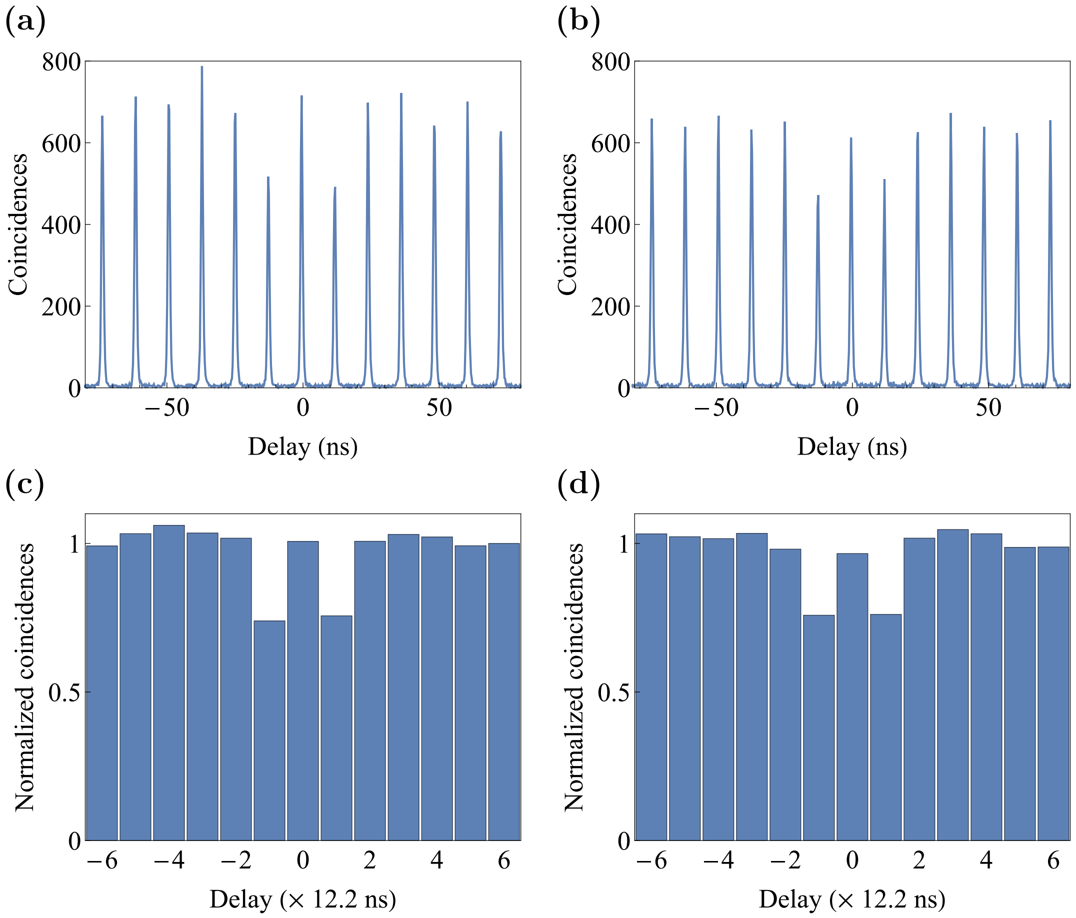

Figure 3.11 – Measured correlation histogram for $\hat{R}_{0,0}$ and $\hat{R}_{1,1}$. (a) and (b) shows raw measurements respectively for $\hat{R}_{0,0}$ and $\hat{R}_{1,1}$. (c) and (d) shows the same histograms normalized to uncorrelated detection events, as explained in the text.

3.6.2 Coherences

To access the coherences we employ the setup shown in Fig.3.5, which allows us to perform the phase dependent correlation measurements $\hat{R}_{i,j} = \hat{a}_i^\dagger \hat{a}_j^\dagger \hat{a}_i \hat{a}_j$ for $i, j = 3, 4, 5$.

The unitary transformation implemented by this part of the setup (and therefore the results of the correlation measurements $\hat{R}_{i,j}$ performed on the output modes) depends also on the value of the phase difference (ϕ) between the two arm of the interferometer. Here, this phase shift is not stabilized, but we periodically determine its value. To this end, an electronically controlled shutter (indicated as Shutter in Fig.3.3) is placed in front of one entrance of the HOM beam splitter ($\mathrm{BS_{HOM}}$). By closing this shutter, we can have a single photon propagating through the split Mach-Zender setup of Fig.3.5. This corresponds to the situation described by Eq.3.8, and the probability amplitudes of the photon through the two arms will interfere on the final beam splitter BS_2 according to the value of the phase shift ϕ. The difference in the count rate detected at the two outputs $\hat{a}_3$ and $\hat{a}_4$ of the interferometer will oscillate as $\cos(\phi)$, with a maximum visibility limited by the experimental losses and the presence of BS_1. Such signal is detected every 10 s, with 100 ms integration time, and the time trace of the results, normalized between 1 and -1, is shown in Fig.3.12.a. The acquisition performed between two subsequent phase estimation is then assigned a specific value of ϕ between 0 and π, in steps of $\pi/19$, according to the measured intensity difference. A total of 4164 acquisitions of 10 seconds each are performed and their distribution depending on the assigned phase is shown in the histogram of Fig.3.12.b, revealing a reasonably uniform dispersion.

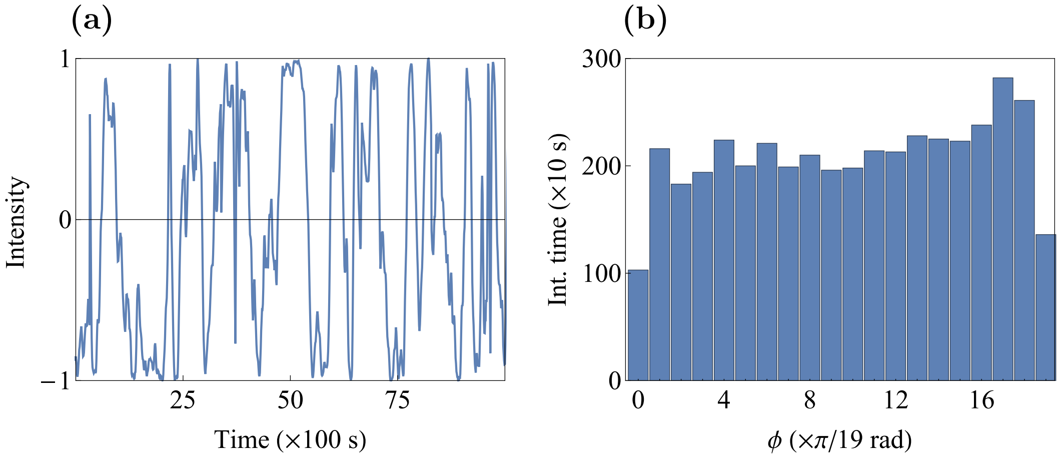

Figure 3.12 – (a) Sample of the measured intensity difference between the outputs $\hat{a}_3$ and $\hat{a}_4$ due to single photon interference, used for the estimation of the interferometer phase. (b) Histogram of the total acquisition time for each phase value.

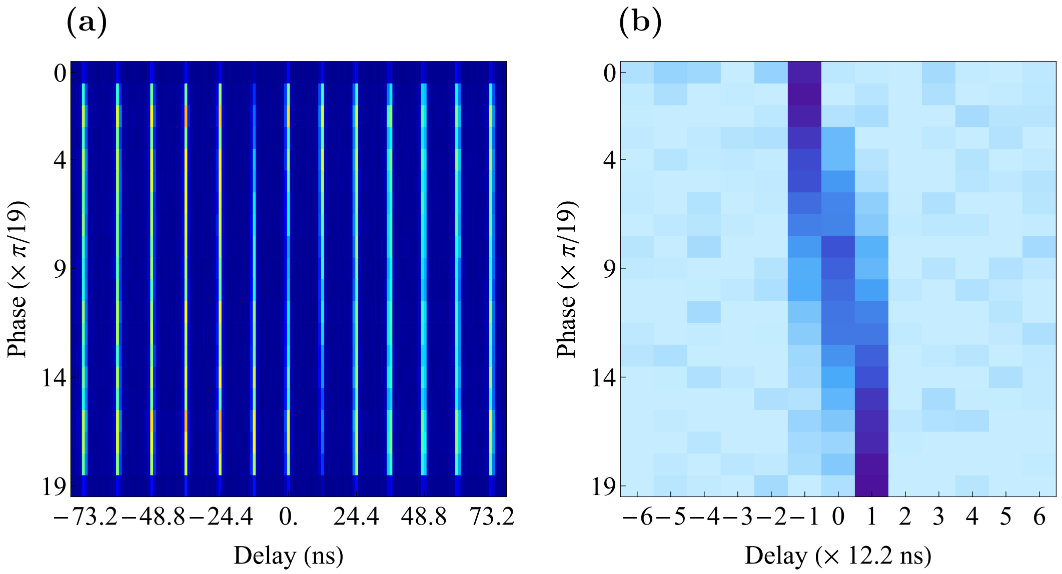

Figure 3.13 – (a) Experimental results for $\hat{R}_{3,4}(\phi)$ as a function of the delay between detections and interferometer phase. (b) $\hat{R}_{3,4}(\phi)$ normalized to uncorrelated detection peaks.

As an example of the phase-dependent correlations measured with this technique, we present the result of $\hat{R}_{3,4}(\phi)$, shown in the 2D plots of Fig.3.13.a (raw) and b (normalized). The detected coincidences are plotted as a function of the time delay (horizontal axis) and the interferometer phase (vertical axis). Each horizontal line corresponds then to a correlation histogram for a specific value of the phase ϕ. By normalizing the measurements to the uncorrelated peaks, we obtain the plot of Fig.3.13.b. Here the phase dependence of the detected coincidences at zero time delay is well visible, and shows a full 2π oscillation in a range of a π optical phase shift. The first sidepeaks, at ±12.2 ns delays, also shows a phase dependence, but in this case it doesn't have the twofold resolution of the zero-delay peaks. They reflect instead the interference of single photons propagating individually in the Mach-Zender setup, as also reported elsewhere [286]. However, we are interested here only in the phase dependence of the zero time delay peak, which is reflecting the NOON state interference. The normalized values of these zero-delay coincidences are plotted in Fig.3.14 as a function of ϕ, for all the phase-dependent measurements performed, with error bars calculated considering a Poissonian noise on the detected count rates. The correlations $R_{3,3}$ and $R_{3,4}$ shows a clear harmonic oscillation over a phase range of π. This is exactly what is expected from the enhanced phase sensitivity of the 2-photon NOON state, here detected by measuring one or two outputs of the split Mach-Zender setup. The correlations $R_{3,5}$ and $R_{4,5}$ instead are performed between one of these two outputs and the additional beam splitter inside one of the Mach-Zender arms. They share an almost constant value, but we can still observe that $R_{4,5}$ is statistically higher that $R_{3,5}$ for values of ϕ close to 0, a situation which is reversed towards π.

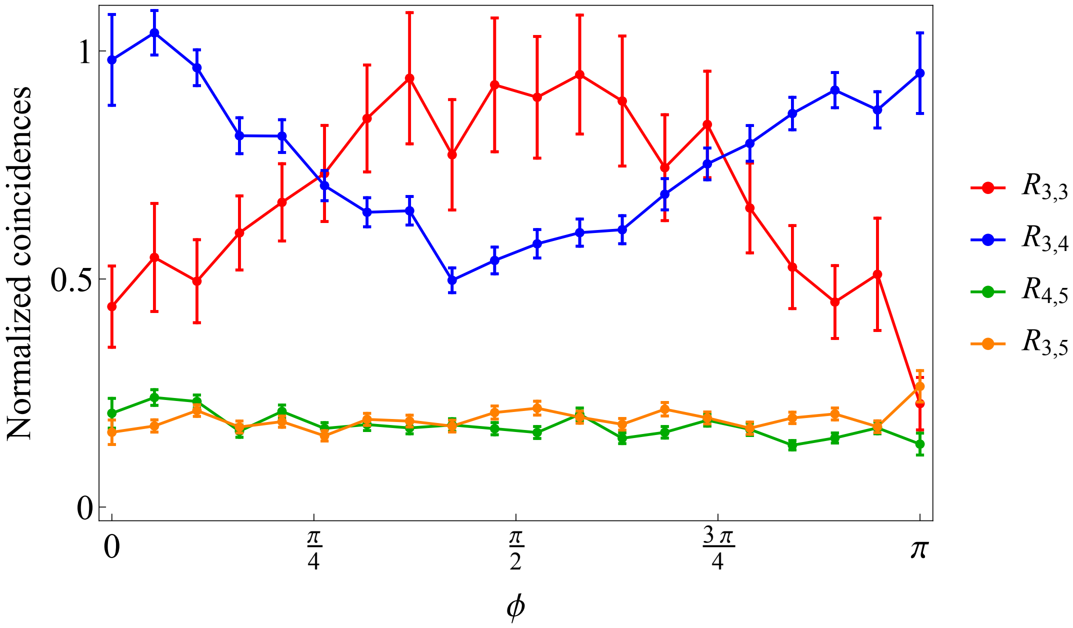

Figure 3.14 – Experimental values of the normalized zero-delay coincidences for the correlations $\hat{R}_{3,3}(\phi)$, $\hat{R}_{3,4}(\phi)$, $\hat{R}_{3,5}(\phi)$ and $\hat{R}_{4,5}(\phi)$ as a function of the interferometer phase ϕ. Error bars calculated from Poissonian noise on the detected coincidences counts.

3.7 Tomographic reconstruction

3.7.1 Linear tomography

We show here that a complete measurement set is given by the following choice of nine measurements:

$$\begin{aligned} R_{\text{set}}(\phi_1,\phi_2) = \big(&R_{0,0},\ R_{0,1},\ R_{1,1} \\ &R_{3,3}(\phi_1), R_{3,4}(\phi_1), R_{3,5}(\phi_1) \\ &R_{3,3}(\phi_2), R_{3,4}(\phi_2), R_{3,5}(\phi_2)\big) \end{aligned} \tag{3.42}$$

for $|\phi_1 - \phi_2| \neq 0, \frac{\pi}{2}, \pi$, allowing the linear reconstruction of the density matrix as shown by Eq.3.40. We immediately see that the experimental procedure is yielding more measurements than required: the distribution of the acquisitions in 20 different phase bins leads to 20 possible choices for the values of ϕ_1 and ϕ_2, from 0 to π in steps of $\frac{\pi}{19}$. Each possible couple (ϕ_1, ϕ_2) thus defines a different measurement set that can be considered for the tomography. Looking at the plot of Fig.3.7.a some possible choices already appear unsuitable. Given the π periodicity of the measurements, we cannot use the couple $\phi_1 = 0$ and $\phi_2 = \pi$, as they both contains the same information. Also, looking at the couple of points $\phi_1 = \frac{\pi}{4}$ and $\phi_2 = \frac{3\pi}{4}$, the $R_{3,3}$ and $R_{3,4}$ measurements shows no difference for a pure (solid line) or mixed (dotted line) state, and effectively they turn out to be only sensitive to the imaginary part of the coherences.

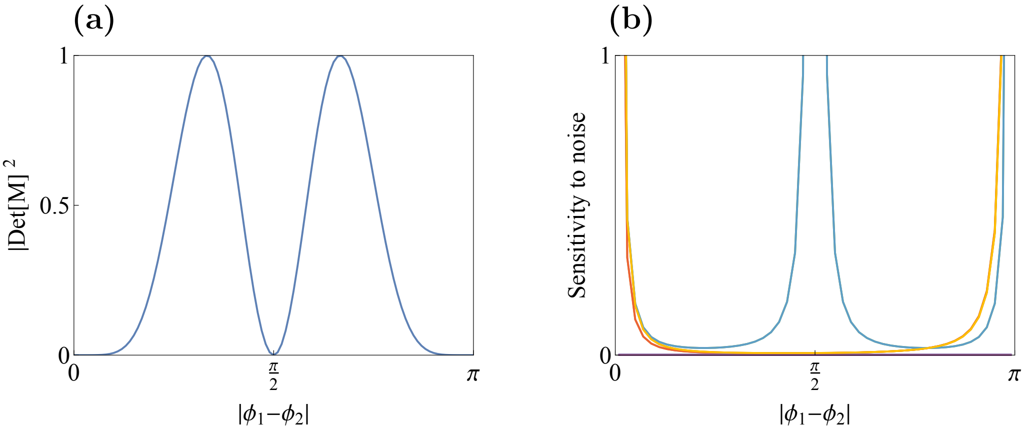

Figure 3.15 – (a) Determinant of the matrix M normalized to 1, as a function of $|\phi_1 - \phi_2|$, showing zeros for integer multiples of $\pi/2$. (b) Estimated noise sensitivity of the calculated density matrix elements, showing singular points for the zeros of the determinant of M.

To address more analytically the choice of phases, we make a simple study of the matrix M (defined in Eq.3.40). The only requirement for the completeness of the measurement set is to have an invertible matrix [269], thus we can look for the zeros of its determinant. This is shown in Fig.3.15.a, where the value of the determinant of M is traced as a function of $|\phi_1 - \phi_2|$. It reveals that the matrix cannot be inverted when the difference between the angles is a multiple of $\frac{\pi}{2}$, as previously mentioned. Additionally we can make a basic estimation of the sensitivity to noise as a guide in the choice of phases. Each density matrix element is given by a linear combination of the measurements in $R_{\text{set}}(\phi_1, \phi_2)$, defined by the corresponding row of M^{-1}. We empirically take as an estimator for their noise sensitivity the square root of the sum of the modulus of each elements in the defining row, corresponding to the assumption of a Poisson noise. The results are shown in Fig.3.15.b as a function of $|\phi_1 - \phi_2|$. In agreement with the plot of Fig.3.15.a, the noise sensitivity of the reconstructed density matrix elements diverges at either 0 and π or at $\frac{\pi}{2}$. The optimal choice providing the lowest uncertainty would be then $|\phi_1 - \phi_2| = \frac{\pi}{4}$ or $\frac{3\pi}{4}$.

Following the above discussion we proceed with the linear tomographic reconstruction of ρ_{lin} for $\phi_1 = 0$ and $\phi_2 = \frac{5\pi}{19}$ (the closest to $\frac{\pi}{4}$ among the measured values). The real and imaginary part of the resulting matrix are shown in Fig.3.16, both in numeric and graphical form. This density matrix shows strong overlap with what could be expected for the output state of an HOM interference of highly indistinguishable photons, having large coherences between the $|2,0\rangle$ and $|0,2\rangle$ kets and small population for the $|1,1\rangle$ component. We note however that it shows small deviations from a physical density matrix. More specifically, it is not exactly normalized (the trace is $\text{Tr}[\rho_{\text{lin}}] = 1.034$) and one of its eigenvalues $(0.917, 0.121$ and $-0.004)$ is negative. To assess the overlap of the reconstructed state with the ideal NOON state $|\psi_{2002}\rangle$ we can normalize the unphysical state by its trace, so as to derive a meaningful value of fidelity of $F = 0.85$.

The fact that the linear tomography procedure is very sensitive to experimental noise, and can produce unphysical properties in the resulting matrix, is well know [269]. To overcome these limitations a Maximum Likelihood Estimation is normally employed.

3.7.2 Maximum likelihood tomography

In order to avoid any violation of the physical properties of the density matrix obtained from the linear tomography, we now apply a Maximum Likelihood Estimation (MLE) method, following the work of James et al. [269]. This allows to find the most probable physical matrix accounting for the observed measurements. First, we define a 3×3 density matrix ρ_{phys} having the 3 mathematical properties of a physical state: normalization, positivity and Hermiticity. Such a matrix can be written as:

$$\rho_{\text{phys}} = \frac{T^\dagger T}{\text{Tr}(T^\dagger T)} \tag{3.43}$$

$$\begin{pmatrix} +0.501 & -0.034 & -0.388 \\ -0.034 & +0.055 & -0.038 \\ -0.388 & -0.038 & +0.478 \end{pmatrix}$$

$$\begin{pmatrix} +0.000 & +0.005 & +0.178 \\ -0.005 & +0.000 & +0.043 \\ -0.178 & -0.043 & +0.000 \end{pmatrix}$$

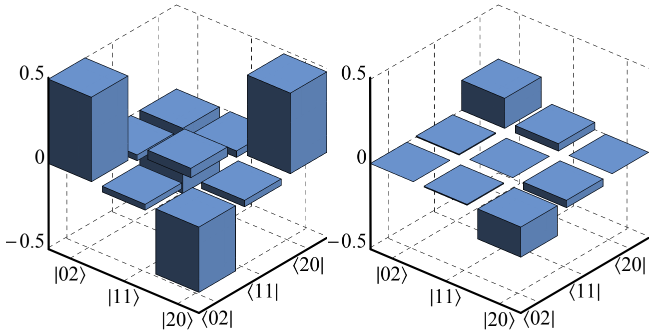

Figure 3.16 – Numerical and graphical representations of the density matrix ρ_{lin} reconstructed from the linear tomography procedure for $(\phi_1, \phi_2) = (0, \frac{5\pi}{19})$.

where the matrix T is defined as function of 9 real parameters:

$$T = \begin{pmatrix} t_1 & 0 & 0 \\ t_4 + i\, t_5 & t_2 & 0 \\ t_6 + i\, t_7 & t_8 + i\, t_9 & t_3 \end{pmatrix} \tag{3.44}$$

We now proceed to find the best estimate for the 9 parameters t_i. To do so we maximize a likelihood function describing the probability of obtaining the observed measurements as a function of the elements of ρ_{phys}, expressed in terms of t_i. Assuming a statistical noise with Poissonian distribution for the measurements, the joint probability of obtaining the set of 9 measurements of Eq.3.42 is:

$$P(t_1, ..., t_9) = \prod_{\nu=1}^{9} \exp\left(-\frac{(R_\nu - \overline{R}_\nu)^2}{\sigma_\nu^2}\right) \tag{3.45}$$

where R_ν are the elements of $R_{\text{set}}(\phi_1, \phi_2)$, calculated for ρ_{phys}, and $\overline{R}_\nu$ the corresponding experimental values, having $\sigma_\nu = \sqrt{\overline{R}_\nu}$. Using the `minimize` function of the Mathematica software, we can find the global minimum of $-\log(P)$, allowing us to maximize the likelihood function of Eq.3.45.

Applying the MLE procedure to the same set of measurements as for the linear tomography, with $\phi_1 = 0$ and $\phi_2 = \frac{5\pi}{19}$, we obtain the density matrix shown in Fig.3.17.a and b. This matrix has a trace of 1 and non-negative eigenvalues (0.891, 0.109, 0) and the imaginary part is almost negligible. We now have a valid physical state, showing a fidelity to the ideal NOON state $|\psi_{2002}\rangle$ of $F = 0.89$. The phase dependence of the expected results for the reconstructed state ρ_{phys} is plotted in Fig.3.17.c (solid lines), for a comparison with the experimental values (points). The left part of the plot is well accounted for by ρ_{phys}, which can be understood since ϕ_1, $\phi_2 \in [0, \frac{\pi}{2}]$. On the contrary, the right part of the plot is slightly deviating from the measured behaviour.

From the discussion at the beginning of the section, it appears interesting to study in more details the effect of the choice of the measurement set on the

(a)

$$\begin{pmatrix} +0.492 & -0.044 & -0.409 \\ -0.044 & +0.038 & -0.027 \\ -0.409 & -0.027 & +0.470 \end{pmatrix}$$

$$\begin{pmatrix} +0.000 & +0.006 & +0.027 \\ -0.006 & +0.000 & +0.021 \\ -0.027 & -0.021 & +0.000 \end{pmatrix}$$

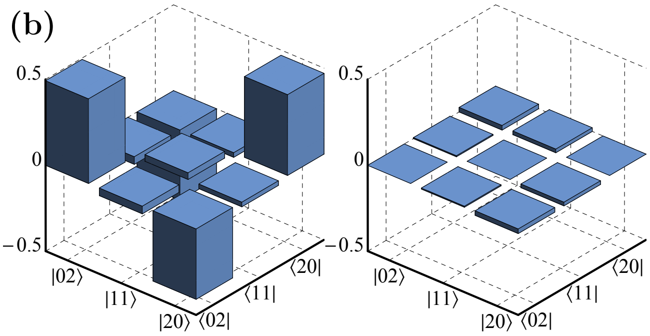

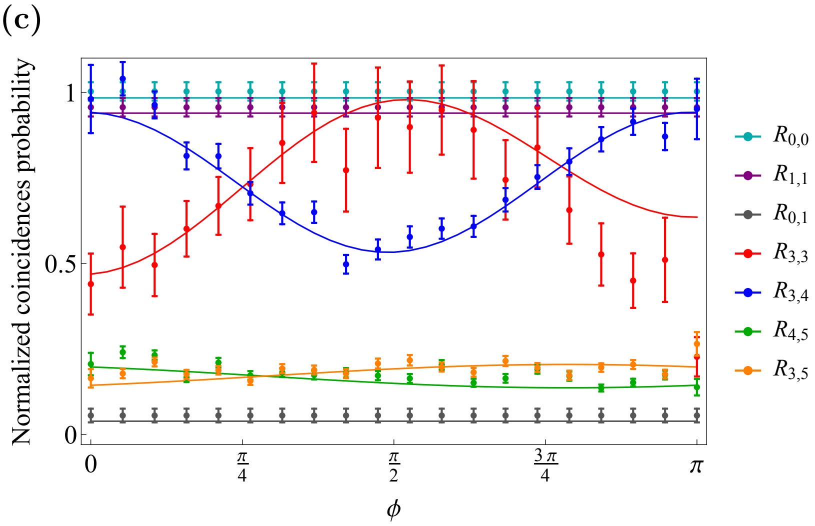

Figure 3.17 – Numerical (a) and graphical (b) representation of the density matrix ρ_{phys} obtained using MLE tomography with the standard set of 9 measurements for $(\phi_1, \phi_2) = (0, \frac{5\pi}{19})$. (c) Expected correlation rates from the density matrix ρ_{phys} (solid lines) along with experimental values (points).

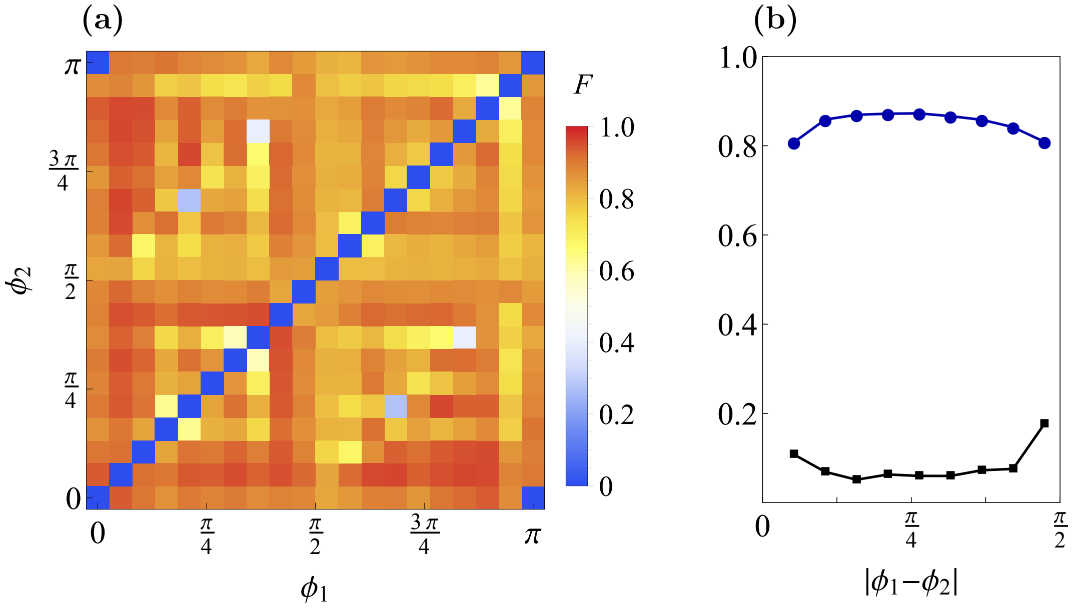

Figure 3.18 – (a) Fidelity to the ideal 2-photon N00N state $|\psi_{2002}\rangle$ of the matrix ρ_{phys} deduced from MLE tomography as a function of the chosen values of ϕ_1 and ϕ_2. (b) Average value of the fidelity (blue dots) and its standard deviation (black squares) as a function of $|\phi_2 - \phi_1|$, extracted from panel (a).

resulting matrix. We have thus calculated the density matrix for any possible couple of phases (ϕ_1, ϕ_2), and its fidelity to the ideal state $|\psi_{2002}\rangle$ is shown in Fig.3.18.a, as a function of ϕ_1 and ϕ_2. The plot is symmetric with respect to the diagonal $\phi_1 = \phi_2$, where the matrix cannot be computed. Noticeable fluctuations appears in the fidelity value and can be attributed to experimental noise or limited statistics, which can affects the outcome of the MLE procedure differently depending on the specific phase values (ϕ_1, ϕ_2) chosen. It is also possible to observe a drop of the fidelity in the vicinity of $(\phi_1, \phi_2) = (\frac{\pi}{4}, \frac{3\pi}{4})$ as expected from what was predicted from Fig.3.15. Starting from this plot, we have calculated the average value of the fidelity $\overline{F}$ and its standard deviation σ_F, as a function of $|\phi_2 - \phi_1|$ (see Fig.3.18.b). No dependence is evidenced on both as long as $|\phi_2 - \phi_1| \neq 0$ and $|\phi_2 - \phi_1| \neq \pi/2$, where the noise produce a threefold increase of the standard deviation σ_F. Away from these two points we have $\overline{F} = 0.87$ and $\sigma_F = 0.06$.

3.7.3 Overcomplete tomography

Both tomography techniques making use of a complete set of 9 measurements, presented up to now, are naturally affected by the choice of the measurement set and experimental noise. Having much more than 9 measurements available

$$\begin{pmatrix} +0.488 & +0.046 & -0.432 \\ +0.046 & +0.046 & -0.014 \\ -0.432 & -0.014 & +0.466 \end{pmatrix}$$

$$\begin{pmatrix} +0.000 & -0.043 & +0.006 \\ +0.043 & +0.000 & +0.010 \\ -0.006 & -0.010 & +0.000 \end{pmatrix}$$

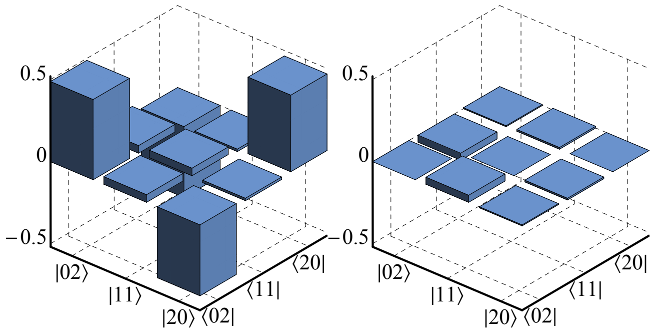

Figure 3.19 – Numerical and graphical representation of the density matrix ρ_{over} obtained using the overcomplete set of 79 measurements.

owing to our experimental procedure, it is natural to extend the MLE technique to use the overcomplete set of 79 measurements. These 79 measurements are composed by the three phase independent correlations $R_{0,0}$, $R_{1,1}$ and $R_{0,1}$, plus the four correlations $R_{3,3}(\phi)$, $R_{3,4}(\phi)$, $R_{3,5}(\phi)$ and $R_{4,5}(\phi)$ each performed for 19 different values of ϕ, from 0 to $18\pi/19$ Note that such an overcomplete set could in principle be extended by repeating the correlations for additional values of ϕ with an active control of the phase.

The likelihood function of Eq.3.45 can be straightforwardly extended, to include the 79 terms defining the probability of observing the whole overcomplete set of measurements. The density matrix ρ_{over} resulting from the maximization the new likelihood function is shown in Fig.3.19. We obtain a fidelity to the NOON state $|\psi_{2002}\rangle$ of 0.91, which is also compatible with the average fidelities of Fig.3.18.b, within their standard deviation. The matrix is indeed dominated by the $|2,0\rangle$ and $|0,2\rangle$ components, which are highly coherent, revealing the spatial entanglement created through the HOM interference. A small population of the $|1,1\rangle$ component is presents, as expected from the non-perfect indistinguishability measured on the two interfering single photons, limiting the fidelity to the ideal state. The coincidence rates expected from the newly reconstructed state ρ_{over} are plotted in Fig.3.20, along with the experimentally measured values. There is a very good agreement between the two on the full ϕ scale. Noticeably, the very small phase dependence of $R_{3,5}$ and $R_{4,5}$ is well reproduced, reflecting the non zero coherences between the $|1,1\rangle$ and $|2,0\rangle$ or $|0,2\rangle$ components.

The data we retrieve by the overcomplete tomography appears very reliable. Being able to observe the full ϕ dependence, we can mitigate the effect of the noise, which significantly depends on the choice of the measurement set. Although we have not mathematically proved it, this result suggests that it would be favourable to distribute a limited statistics over an overcomplete set, instead of increasing the statistics of a standard tomographic set of measurements.

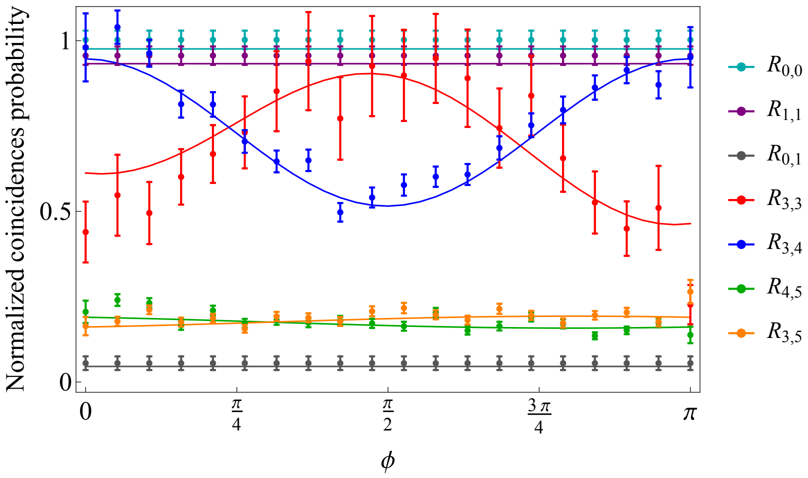

Figure 3.20 – Expected correlation rates from the density matrix ρ_{over} (solid lines) along with experimental values (points).

3.7.4 Hidden differences method

We have seen that the state measured at the output of the HOM interference, while showing genuine spatial entanglement, has a finite fidelity of $F = 0.91$ to an ideal 2 photon NOON state. This can be mainly ascribed to the presence of a population of the $|1,1\rangle$ component. It is of practical interest to identify the source of such a limitation, which could be either due to the setup or the single-photon source, allowing to characterize the performances of both. In particular, we can identify the two main causes which affect the creation of a maximally entangled 2 photon state: an unbalanced reflection and transmission coefficients of the HOM beam splitter, or a partial distinguishability of the two impinging photons.

On one hand, two perfectly indistinguishable photons interfering on a beam splitter where $|R| \neq |T|$, will result in a $|1,1\rangle$ population:

$$|1,1\rangle \xrightarrow{\text{HOM}} \sqrt{2RT}\,(|2,0\rangle - |0,2\rangle) + (R-T)\,|1,1\rangle \tag{3.46}$$

On the other hand, with a perfect beam splitter, where $|R| = |T|$, two distinguishable photons will create a $|1,1\rangle$ population as they will propagate independently:

$$|1_a, 1_b\rangle \xrightarrow{\text{HOM}} \frac{1}{\sqrt{2}}\,(|2_{ab},0\rangle - |0,2_{ab}\rangle) + |1_a,1_b\rangle - |1_b,1_a\rangle \tag{3.47}$$

Interestingly enough, none of these mechanism could create an unbalance between the $|2,0\rangle$ and $|0,2\rangle$ populations, neither can reduce the coherences of the state.

In the present experiment, the single-photon source is operated under resonant excitation without any spectral filtering of the zero phonon line, in order to increase the brightness in the rather lossy setup. Under these conditions, we can expect two different origins for the distinguishability of the photons. First, the phonon sideband emission, which contribute to the emission spectrum in the absence of spectral filtering as presented in Chapter 2, is being collected. This slightly reduce the indistinguishability of the single photon emitted by the QD [100]. Second, by employing a cross polarization scheme for the resonant excitation, there is a small fraction of residual laser light that is not completely filtered and is effectively distinguishable from the single photons.

The most interesting difference between Eq.3.46 and Eq.3.47 is in the last terms of the equations, describing the situation in which the two photons exits from two different output ports of the HOM beam splitter. In the first case, the two photons are indistinguishable, while in the second case they are distinguishable in some degrees of freedom, like spectral profile or polarization, here represented by the indices a and b. However our setup cannot access any degrees of freedom other than the spatial modes over which the detection measurements are performed. Thus seems that the two situations described by Eq.3.46 and by Eq.3.47 cannot be told apart, as we cannot access the information carried by the modes a and b.

This is not the case: as demonstrated by Adamson and coworkers [287, 288], in such situations the presence of distinguishing information in hidden degrees of freedom can be detected using a more refined analysis. To understand how such information can be extracted, we briefly outline their demonstration. We begin by considering a state of two photons, which must be symmetric under particle exchange, where they are distinguishable only in some hidden degrees of freedom, experimentally not accessible. Separating the state into two part, one for the visible and one for the hidden degrees of freedom, they can be both either symmetric or antisymmetric, so that the whole state respect the bosonic symmetrization of the wave function. The visible degrees of freedom of the state, with which we operate, will be described by the reduced density matrix ρ_{vis} obtained from the global state ρ by tracing over the hidden degrees of freedom:

$$\rho_{\text{vis}} = \text{Tr}_{\text{hid}}[\rho] \tag{3.48}$$

Now, separating the symmetric (S) and antisymmetric (A) subspaces of ρ_{vis}, it can be demonstrated that there are no coherences between the two, thus ρ_{vis} can be written as:

$$\rho_{\text{vis}} = \begin{pmatrix} \rho^S_{\text{vis}} & 0 \\ 0 & \rho^A_{\text{vis}} \end{pmatrix} \tag{3.49}$$

We see that the visible degrees of freedom gives access to ρ^S_{vis} and ρ^A_{vis}, but not to the coherences between them. Measuring a population in the antisymmetric space ρ^A_{vis}, where the two photons are assumed to be indistinguishable, imply the presence of an hidden degree of freedom where the two particles are distinguishable, in order not to violate the global symmetry of the state.

In our case the visible degrees of freedom are the spatial modes, for which we introduce the 4-state basis $\{|2,0\rangle\,,\ |0,2\rangle\,,\ |\psi^+\rangle\,,\ |\psi^-\rangle\}$, where $|\psi^{\pm}\rangle = \frac{|1_a,1_b\rangle \pm |1_b,1_a\rangle}{\sqrt{2}}$ are the symmetric and antisymmetric state of two possibly distinguishable photons, a and b, on each path. Now the symmetric subspace of ρ_{vis} is spanned by $\{|2,0\rangle\,,\ |0,2\rangle\,,\ |\psi^+\rangle\}$, while the antisymmetric one by $|\psi^-\rangle$, and the 4×4 density matrix ρ_{vis} reads in this basis:

$$\rho_{\text{vis}} = \begin{pmatrix} \rho_{20,20} & \rho_{20,\psi^+} & \rho_{20,02} & 0 \\ \rho_{\psi^+,02} & \rho_{\psi^+,\psi^+} & \rho_{02,\psi^+} & 0 \\ \rho_{02,20} & \rho_{\psi^+,02} & \rho_{02,02} & 0 \\ 0 & 0 & 0 & \rho_{\psi^-,\psi^-} \end{pmatrix} \tag{3.50}$$

The tomography method presented before is repeated to reconstruct a matrix in the form of ρ_{vis} from the experimental data. The mathematical model developed in section 3.5 is extended to a pure input state of the form

$$|\psi_{in}\rangle = \left(\alpha \hat{a}^{\dagger}_{0,a}\hat{a}^{\dagger}_{0,b} + \beta \hat{a}^{\dagger}_{0,a}\hat{a}^{\dagger}_{1,b} + \gamma \hat{a}^{\dagger}_{0,b}\hat{a}^{\dagger}_{1,a} + \delta \hat{a}^{\dagger}_{1,a}\hat{a}^{\dagger}_{1,b}\right)|0\rangle \tag{3.51}$$

and calculating the results of correlations measurements given by

$$R_{i,j} = \langle\psi_{out}|\, \hat{a}^{\dagger}_{i,a}\hat{a}^{\dagger}_{j,b}\hat{a}_{j,b}\hat{a}_{i,a} + \hat{a}^{\dagger}_{i,b}\hat{a}^{\dagger}_{j,a}\hat{a}_{j,a}\hat{a}_{i,b}\, |\psi_{out}\rangle \tag{3.52}$$

we determine the new relations between the density matrix elements of ρ_{vis} and the experimental results $R_{i,j}$. We also formally verify that, as expected, no measurement is sensitive to the coherence terms between the symmetric and antisymmetric part of ρ_{vis}, even when considered non-zero. We then apply the MLE method to find the best estimate for a physical density matrix ρ_{vis}, accounting for the overcomplete set of measurements.

To understand how it is experimentally possible to discriminate the presence of population in the symmetric or antisymmetric subspaces, we can observe the simulations shown in Fig.3.21. In the left plot (Fig.3.21.a), solid lines shows the expected results from the state $|\psi_{11}\rangle$ previously presented in Fig.3.9.b. In the basis of the visible degrees of freedom introduced above, such state can be written as $|\psi^+_{11}\rangle = \frac{\cos(0.2)}{\sqrt{2}}\left(|2,0\rangle - |0,2\rangle\right) - \sin(0.2)\,|\psi^+\rangle$ where we have a population of the $|1,1\rangle$ component in the symmetric subspace. Moving this population to the antisymmetric subspace, thus considering a state $|\psi^-_{11}\rangle = \frac{\cos(0.2)}{\sqrt{2}}\left(|2,0\rangle - |0,2\rangle\right) - \sin(0.2)\,|\psi^-\rangle$, we obtain the result shown by the dashed lines. No phase dependence is observed anymore on the measurements $R_{3,5}$ and $R_{4,5}$. As can be expected, in this condition no interference is happening between the two photons, being distinguishable, when they recombine on the last beam splitter. A small effect is also observed on $R_{3,3}$ and $R_{3,4}$, which can be clarified by looking at Fig.3.21.b. Here we show with solid lines the expected results from the mixed state ρ_{11} of Fig.3.9.c, which in the new basis reads $\rho^+_{11} = 0.96\,|\psi_{2002}\rangle\langle\psi_{2002}| + 0.04\,|\psi^+\rangle\langle\psi^+|$, where the $|1,1\rangle$ component has no coherence

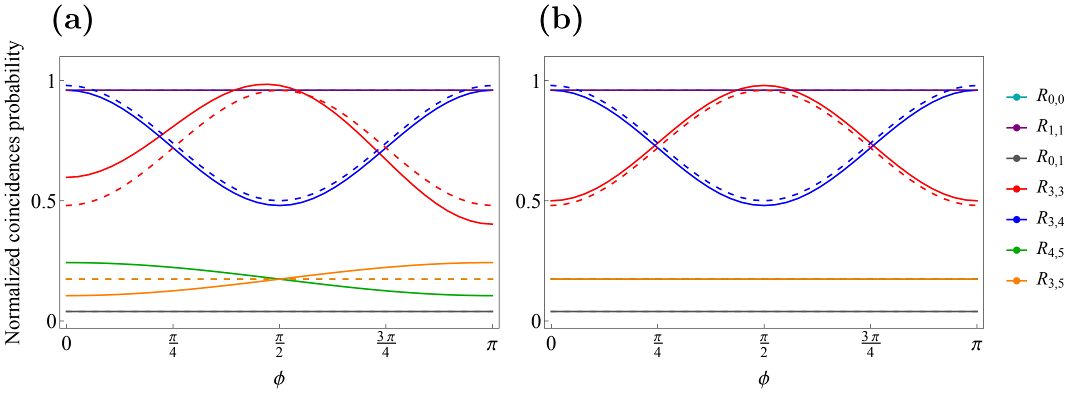

Figure 3.21 – (a) Expected correlation rates for the state of Fig.3.9.c (solid lines), where the $|1,1\rangle$ population is in the symmetric subspace, and same state but with the $|1,1\rangle$ population in the antisymmetric subspace. (b) Expected correlation rates for Fig.3.9.d, with $|1,1\rangle$ population in the symmetric (solid lines) and antisymmetric (dashed lines) subspaces.

with the rest of the state. Moving this population to the antisymmetric subspace, thus considering the state $\rho^-_{11} = 0.96\,|\psi_{2002}\rangle\langle\psi_{2002}| + 0.04\,|\psi^-\rangle\langle\psi^-|$, we see from the dashed lines that $R_{3,3}$ is lowered and $R_{3,4}$ is raised. Since now the two photon are distinguishable, they will no more show an HOM-like bunching, due to which they previously exited from the same ports.

The matrix ρ_{vis} deduced from the 79 experimental measurements following this analysis is shown in Fig.3.22. By comparing it with the 3×3 matrix ρ_{over} of Fig.3.19, we see that the two are equivalent, if we consider $|1,1\rangle$ to be given by the sum of ρ_{ψ^+,ψ^+} and ρ_{ψ^-,ψ^-}. Thus the method of the hidden differences allows effectively to discriminate the $|1,1\rangle$ population of the state into a symmetric and an antisymmetric part. Now, looking at Fig.3.22, in ρ_{vis} most of the population of the $|1,1\rangle$ component appears in the antisymmetric part ρ_{ψ^-,ψ^-}, with a negligible contribution to the symmetric part ρ_{ψ^+,ψ^+}. Following the previous discussion, we can ascribe most of the NOON state imperfection to a partial distinguishability of the single photons coming from the source, and not to imperfections in the HOM beam splitter.

Furthermore, we have shown that the second order correlation function on the signal from the source, $g^{(2)}(0) = 0.03$, gives a lower bound on the measured population of $|1,1\rangle$. Having obtained $\rho_{\psi^+,\psi^+} + \rho_{\psi^-,\psi^-} = 0.047$, means that most of the inferred photon distinguishability is due to contribution from residual background laser.

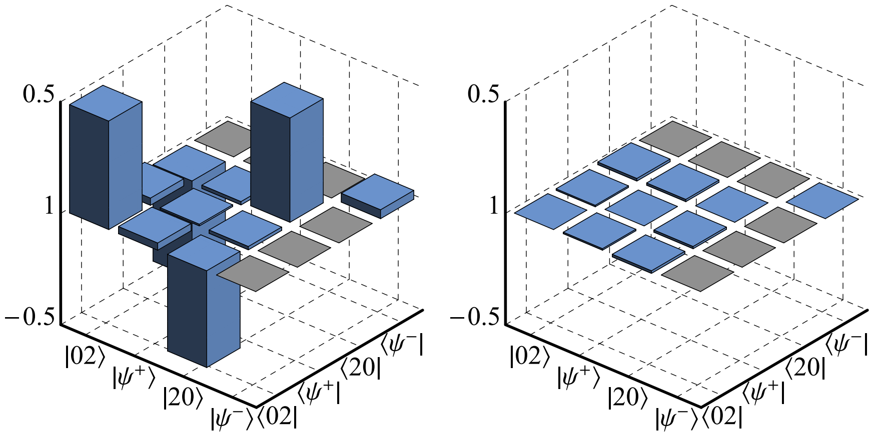

$$\begin{pmatrix} +0.486+0.000i & +0.032-0.007i & -0.434+0.011i & 0 \\ +0.032+0.007i & +0.007+0.000i & -0.015+0.010i & 0 \\ -0.434-0.011i & -0.015-0.010i & +0.467+0.000i & 0 \\ 0 & 0 & 0 & +0.040+0.000i \end{pmatrix}$$

Figure 3.22 – Density matrix ρ_{vis} showing the distinguishable and indistinguishable parts of the two-photon state. Grey elements are not accessible from our visible degrees of freedom.

3.8 Conclusions and perspectives

In this chapter we have shown that using a simple Mach-Zender setup and coincidence detection measurements we can perform a full Quantum State Tomography of a two-photon path-encoded NOON state. We can thus certify the presence of a NOON state even in the absence of a precision beyond the standard quantum limit. Moreover this coincidence-based scheme is simpler than an homodyne detection, since it does not require a local oscillator matched to the single photon fields. We have explored different types of tomography reconstructions, observing that an overcomplete approach allows a more robust and precise reconstruction of the state. The results highlights the spatial entanglement between the two photons at the output of the HOM interference, and we achieve a high fidelity to an ideal 2-photon NOON state owing to the high indistinguishability of the photons emitted by the QD-micropillar device. Using the method of hidden differences is also possible to identify the sources of imperfections lowering the fidelity, distinguishing between limitations due to the source or the experimental setup. This can be an important diagnostic tool for many applications in the field of quantum information.

It is interesting to extend the tomography method presented here to NOON states for any photon number N. Is has been shown that using Photon Number

Resolving detectors is possible to access all N^{th} order coherence of the field [278, 270], thus we can expect that our scheme can be simply extended by employing PNR detectors, to implement N^{th} order photon correlations.

We analyse explicitly the case of a $N = 3$ photon NOON state. The density matrix $\hat{\rho}_{3003}$ of the 3 indistinguishable photons distributed over the 2 modes $\hat{a}_0$ and $\hat{a}_1$ has 16 elements to be accessed, and its Fock state basis is given by $\{|3,0\rangle\,,\ |2,1\rangle\,,\ |1,2\rangle\,,\ |0,3\rangle\}$. We can use an ideal PNR detector to perform a correlation measurement $\hat{C}^{n,m}_{i,j} = |n\rangle\langle n| \otimes |m\rangle\langle m|$ between n photons on the mode i and m photons on the mode j. Direct detection of the state using the PNR detectors allows to retrieve the four populations from:

$$\hat{C}^{3,0}_{0,1},\ \hat{C}^{2,1}_{0,1},\ \hat{C}^{1,2}_{0,1}\ \hat{C}^{0,3}_{0,1} \tag{3.53}$$

Following the same procedure as for the two-photon NOON state, we can now collect phase-dependent correlation measurements by placing PNR detectors at the three outputs of the split Mach-Zender setup. Performing each measurement for two different values (ϕ_1 and ϕ_2) of the interferometer phase ϕ, 6 additional correlations are sufficient for the reconstruction of the density matrix $\hat{\rho}_{3003}$. We find that the measurement set:

$$\hat{C}^{3,0}_{3,4}(\phi),\ \hat{C}^{0,3}_{3,4}(\phi),\ \hat{C}^{2,1}_{3,4}(\phi),\ \hat{C}^{2,1}_{3,5}(\phi),\ \hat{C}^{1,2}_{4,5}(\phi),\ \hat{C}^{2,1}_{4,5}(\phi) \tag{3.54}$$

for $|\phi_1 - \phi_2| \neq k\frac{\pi}{2}, k\frac{\pi}{3}$, together with the four population measurements, allows the linear reconstruction of the density matrix.

In general, the density matrix of an N photon 2-path state has $(N+1)^2$ elements, given that we have $N+1$ possible distributions of N indistinguishable photons over 2 modes. Introducing an ancillary mode, we obtain 3 accessible output modes over which the photons can be distributed. The distribution of N photons over 3 modes gives us $(N+2)(N+1)/2$ possible configurations. Detecting each of these possible photon output distribution for two different values of the interferometer phase already gives more measurements than the $(N+1)^2$ density matrix elements. The tomographic problem is then reduced to the identification of two possible values of phases giving a complete set of measurements.

The generation of path entangled NOON states for high photon number has not been experimentally demonstrated yet. To this end, the interference between a single photon state and a coherent state on a beam splitter could allows to obtain a path entangled state showing high overlap with a NOON states for arbitrary value of N [262, 263]. Combining this generation technique with the tomography protocol presented in this chapter is a viable method for the demonstration of path entangled NOON state for arbitrary photon number N, using a simple experimental setup.

Chapter 4

Giant optical nonlinearity and Fock state filtering

A strong limitation for many optical quantum information processing schemes is the use of linear optical gates, which are intrinsically probabilistic. Deterministic operations could be achieved using the nonlinear interaction between a single photon and a single atom. With this objective, we study in this chapter the nonlinear optical response of the QD-micropillar device and measure how it affects the photon statistics of the incident optical field. We shows that our device act as a very efficient receiver of single photons, providing an almost ideal light-matter interface which could be directly exploited to realize photon-photon gates.

In Section 4.1, we describe how the nonlinear behaviour of a CQED device can be used to realize a quantum gate and in Section 4.2, we review the current state of the field. In Section 4.3, the experimental setup is presented and in Section 4.4, it is used to study the optical nonlinear response of the device and the photon blockade effect. In Section 4.5, we highlight the behaviour of the device as a single photon Fock state filter and in Section 4.6, we perform additional measurements to quantify the suppression of multi-photon states. Conclusions and perspectives for this work are given in Section 4.7.

4.1 Towards deterministic quantum gates

Single photons are ideal information carriers due to the fact that they are hardly disturbed by the environment. For the same reason though, it is also difficult to engineer effective photon-photon interactions, a fundamental requirement to process the quantum information. A long-standing goal for different areas of physics is the implementation of nonlinear optical effects at the level of single light quanta, where a single photon can affect the propagation of another one [289].

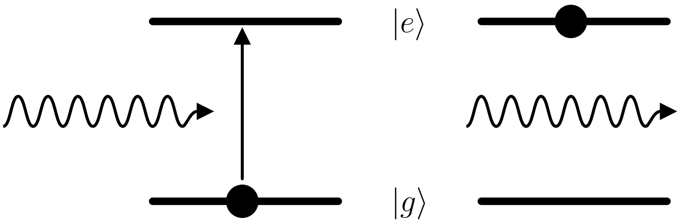

Figure 4.1 – Nonlinearity of a two-level system: the absorption of a single photon saturates the transition. Being in the excited state, the two-level system does not interact with additional photons

In the field of quantum information processing the manipulation of single photon is of fundamental importance. As both single and two qubit gates are required, an effective interaction between photons is necessary. In linear optical quantum computing schemes, this is achieved by postselection on the quantum interference effect between photons on beam splitters. The resulting effective interactions are probabilistic, making it difficult to scale up the number of qubits and operations in the presence of losses. Efficient gates could otherwise be realized with strong nonlinear optical effects in matters [290, 291], mediating the photon-photon interaction. Achieving an effective nonlinear interaction between single photons could leads to the realization of deterministic gates. The interest is however not limited to the quantum domain, as also classical photonic transistor could be used for fast and energy efficient optical signal processing [292].

A two-level system, such as the optical transition of an atomic system, shows an ideal nonlinear response: it can only absorbs or emits a single photon at one time. If the atom-photon interaction is strong enough, a single atom can then be used as a nonlinear medium: a first photon fully saturates the transition, so that the response to a second photon will be drastically different, as represented in Fig. 4.1. This scheme can be applied either to a natural atom or to an artificial one such as a QD, owing to the anharmonicity of its energy spectrum, which allows to isolate a specific transition. A device based on this principle, to provide a deterministic photon-photon interaction needs to implement a perfect atom-photon interface. Moreover, it must be operated with photonic wave packets and without postselection. Cavity QED (CQED) appears then as an ideal platform to achieve this objective. It allows both to strongly enhance the interaction between the cavity photons and the atom and also to engineer an efficient interface with the propagating light outside the cavity.

4.1.1 Single photon nonlinear optics with CQED

To understand the optical response of the atom-cavity device to the incident light, we can study its reflectivity spectrum. The general description of a CQED device has been presented in Chapter 1, where we have introduced the master equation and the input output formalism used to simulate the experimental results presented in this work. With a semiclassical approach, where the quantum fluctuations are neglected, it is possible to analytically calculate the complex reflection coefficient $r(\omega)$ as a function of the excitation energy ω. In a stationary regime, thus continuous wave excitation, and for low incident power, far from the atom saturation threshold, it can be shown that [117, 293]:

$$r(\omega) = 1 - \frac{\kappa_{\rm top}}{\frac{\kappa}{2} - i\left(\omega - \omega_{\rm c} - \frac{g^2}{(\omega - \omega_{\rm a} + i\gamma)}\right)} \tag{4.1}$$

where ω is the energy of the excitation laser while ω_c and ω_a are the energy of the cavity and the atom resonance. As presented in section 1.2.4, g is the coupling strength between the cavity and the transition, $\gamma = \frac{\gamma_{\rm sp}}{2} + \gamma^*$ is the total dephasing rate of the atom and $\kappa = \kappa_{\rm top} + \kappa_{\rm bottom} + \kappa_{\rm loss}$ is the cavity damping rate. Using Eq. 4.1, we can calculate the reflectivity $R = |r(\omega)|^2$ of the atom-cavity system to understand how the coupling between the two introduce a nonlinear behaviour.

The bare cavity reflectivity spectrum, which is a Lorentzian dip centred on the cavity resonance, is strongly modified by the presence of a two-level atom. This can be seen Fig. 4.2, showing the reflectivity spectrum of an ideal CQED device in the strong (a) and weak (b) coupling regime. The calculations are shown for a symmetric cavity, with $\kappa_{\rm top} = \kappa_{\rm bottom} = \kappa/2$, in absence of pure dephasing, thus $\gamma^* = 0$, and with the atomic transition in exact resonance with the cavity mode $\omega_a = \omega_c$. In both situations, the response at zero detuning changes from highly transmissive ($R \approx 0$, dashed line) for an empty cavity to highly reflective ($R \approx 1$, solid line) when the cavity field is coupled to an atomic transition. The light-atom coupling is regulated by the intensity of the light: when the transition is saturated, it gets effectively decoupled from the light field, drastically changing the optical response of the device [117]. The underlying mechanism for the two situation of Fig.4.2 is slightly different, as in the strong coupling regime the nonlinear response is determined by the Jaynes-Cummings ladder, while in the weak coupling regime is determined by the anharmonic spectrum of the atom [294]. The case of the strong coupling regime can be understood by looking at the energy level diagram of Fig.1.6. If the incident field cause a transition between the ground state and one of the dresses state of the first manifold of the Jaynes-Cummings hamiltonian, no additional photons can be absorbed because a different energy is required for any transition to the second manifold. In the weak coupling regime instead the cavity does not significantly alter the energy level spacings of the atom. Once the two-level atom has been excited, no other absorption can take place. In both cases however, the two-level system can only absorbs or emits a single photon, thus it can deterministically prevent the propagation of multi-photon states. The transport

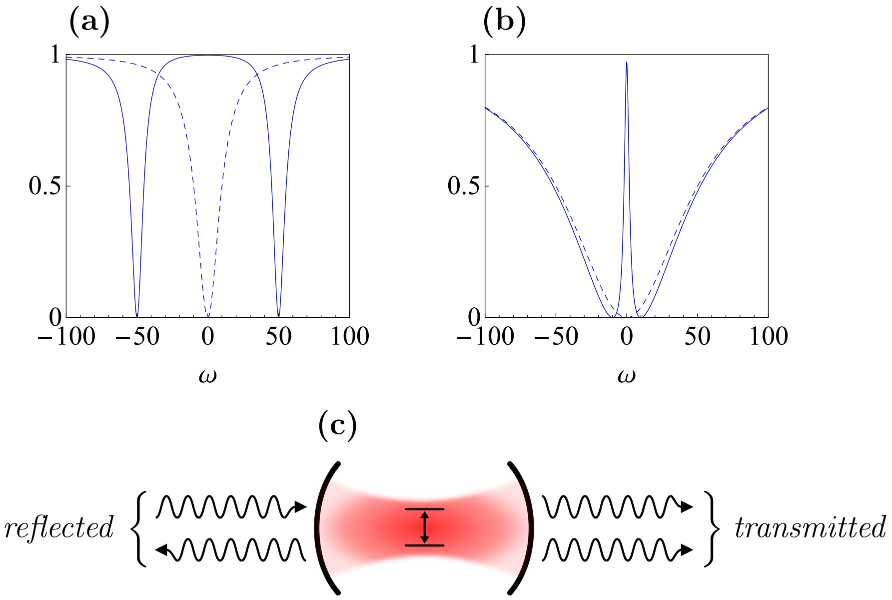

Figure 4.2 – Calculated reflectivity spectrum of a CQED device (with a symmetric cavity, where $\kappa_{\mathrm{top}} = \kappa_{\mathrm{bottom}}$) in the strong coupling regime (a) and weak coupling regime (b). Panel (c) shows the 1D atom situation, where the destructive interference between the laser and atom fields destructively interfere in the forward direction, leading to a deterministic reflection of a photon.

of light through the cavity then happens on a single photon basis, a phenomenon called photon blockade [295].

In the weak coupling regime, the presence of the emitter changes the response of the cavity by introducing a strongly reflective peak in an otherwise transmittive cavity (see Fig.4.2.b). This can be understood as the destructive interference in the forward direction between the incident field and the field radiated by the atom (see Fig.4.2.c). The incident photons then can only be reflected in the backwards direction, if the transition is not saturated. Moreover, as a two-level system can only radiate a single photon field, its contribution to the reflected light will be strongly antibunched. Such effect is the essence of the 1D atom situation [296]. As shown in the works of Hofmann et al. [297] and Auffèves et al. [117], it is possible to achieve a regime where the saturation of the atomic transition occurs at the intensity level of a single incident photon per lifetime, realizing a giant optical nonlinearity.

This effect can be used to realize photon-photon gates using different protocols [298]. For example, in a two pulse scheme, a first control photon can be used to switch the reflectivity of the device by saturating the transition, so that a second signal photon is deterministically transmitted. Such a strong nonlinearity can also be used to generate nonclassical state of light from an incident Poissonian pulse: only the single photon part of the incident light gets reflected back. However, the efficiency of photon-photon gates based on the photon blockade effect operated by a two-level system shows limitations. In particular, the achievable effective interaction time and bandwidth between the two photons is constrained by the lifetime of the transition [294], as we also observe in more details in Section 4.4.3. To overcome these limitations a lambda system is required, giving a viable way for the realization of deterministic photon-photon gates.

In the following section, we review recent works for the realization of effective photon-photon interactions with CQED.

4.2 State of the art

The experimental study of the nonlinear response of an atom-cavity system has been pioneered by the observation of the phase shift induced by a single natural atom on cavity photons [299]. The photon blockade effect has then been demonstrated both in the strong [300] and in the weak [301] coupling regimes. The development of the manipulation of atomic states and the realization of high quality atom-cavity interfaces, allowed recently to demonstrate different quantum functionalities using CQED with natural atoms. Photon filters have been reported [159, 160], where the nonlinear response of the atom is used to reflect only a single photon from an incident pulse, in a situation analogous to the one-dimensional atom regime, transforming the classical statistics of the laser into a highly nonclassical one. In the strong coupling regime, the deterministic operation of quantum gates has been demonstrated, realizing controlled phase flip and CNOT gates [23, 302, 22]. Recently these operations have reached the few-photon level. In the work of Shomroni et al. [22] a gate pulse containing 3 photon on average is used to switch an atom-cavity device from 64% reflective to 90% transmissive for a second target photon, demonstrating an optical routing of single photons.

Obtaining the same results in solid-state devices would give the potential for a scalable and integrated fabrication of deterministic quantum gates. The photon blockade effect in the solid-state has first been observed through the generation of nonclassical states of light using a QD strongly coupled to a photonic crystal cavity [303, 304, 305]. By directly exciting the first manifold of the Jaynes–Cummings ladder or the second one through a two-photon resonance, it is possible to observe either photon antibunching or photon bunching in the photoluminescence signal, with $g^{(2)}(0)$ values ranging from 0.75 to 1.5. This reveals the individual or pairwise absorption and emissions of the photons. The same devices have also been used to demonstrate proof-of-principle optical gates. The use of two laser excitations allowed to show ultrafast and energy-efficienct optical transistors [306, 307, 308], where a weak control signal (as low as few hundred photons) can switch the reflection or transmission of an intense target signal. A CNOT gate between a photon and a neutral exciton [309] and a quantum phase switch [158] between a photon and a spin have also been reported. Here, the polarization state of an incident photon is coherently rotated depending on the QD state. These works employed a cross-polarization configuration, which allows to postselect on the photons that effectively entered the cavity, to eventually show that the photon statistics of laser pulses injected in the cavity is strongly modified by the nonlinear response of the device.

Recently the study of the nonlinear optical response of a QD has been extended to the weak coupling regime, under CW excitation [310, 311]. Javadi et al. [310] demonstrated the saturation of a QD neutral exciton transition coupled to a photonic-crystal waveguide for a critical photon number of 0.81 photons per lifetime, inside the waveguide. They observe an 8% change in the transmission of the waveguide (30% after correction for spectral diffusion and blinking) and a transition from a bunched to a Poisson statistics for the transmitted light. Bennett et al. [311] reported the modification of the photon statistics of a light beam reflected from a QD-micropillar device. They show the transition between sub-Poissonian ($g^{(2)}(0) \approx 0.75$) to super-Poissonian ($g^{(2)}(0) \approx 1.75$) by tuning the QD transition in a slightly off resonant condition. Snijders et al. [312] instead studied the transmission from a polarization-degenerate micropillar cavity coupled to a QD. They shows that appropriate polarization postselection allows to completely cancels the light which has not interacted with the QD, in order to collect only the field modified by the exciton transition. They can observe strong photon bunching, with $g^{(2)}(0)$ values up to 40.

All the works here mentioned however employed either a CW excitation regime or a strong postselection, due to the limited input and output coupling with the optical modes of the photonic crystals used. While a CW excitation allows to overcome bandwidth limitations of the devices, it is not compatible with quantum information protocols where single photons must be individually processed. In a pulsed regime on the contrary, a polarization postselection scheme is useful to suppress the uncoupled scattered light in the detection, but it is not compatible with the realization of a deterministic gate.

The strongest nonlinearity previously observed without postselection in solid-state emitters has been demonstrated in our group in 2012 by Loo et al. [155], using a QD strongly coupled to a micropillar cavity. Such work was based on micropillars not electrically contacted, where a pulsed excitation regime allowed to achieve a nonlinear threshold of 8 incident photons per pulse, and an absolute reflectivity variation of 10%, as represented in Fig.4.3.a. While showing a very high input coupling efficiency, the system was still limited by a small output coupling efficiency $\eta_{\text{out}} = 0.16$ and a dephasing rate $\gamma = 10\mu\text{eV}$ of the QD transition, responsible for a higher nonlinearity threshold and limited switching in the reflectivity value. Fig.4.3.b describe the attainable performances with

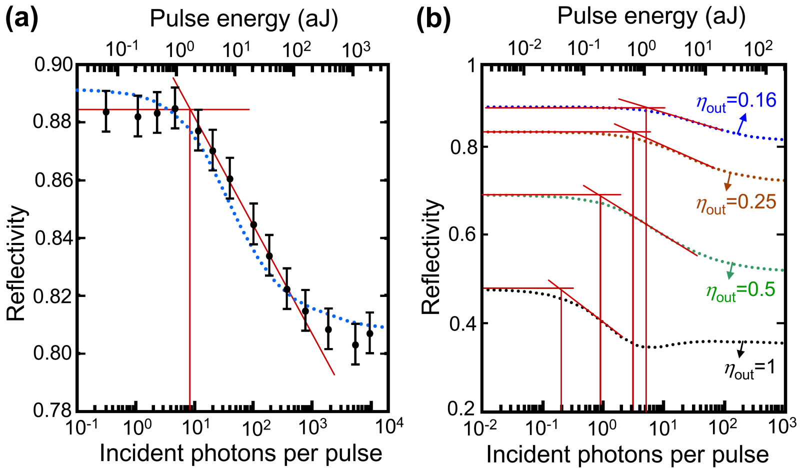

Figure 4.3 – Non-linearity of a QD-micropillar device in the strong coupling regime, figure reproduced from [155]. (a) Pulsed reflectivity measurement showing a nonlinearity threshold for 8 average incident photon per pulse. (b) Calculated power-dependence of the reflectivity for different values of the output coupling efficiency η_{out}.

such system. While a very high output coupling efficiency allows to minimize the incident photon number required to saturate the QD, the contrast in reflectivity between the unsaturated and saturated conditions is still fundamentally limited by the presence of dephasing.

Using the electrically contacted QD-micropillar devices presented in Section 1.3, it is possible to achieve a very high cooperativity, which ensures a high atom-photon interaction strength, and very high input and output coupling efficiencies, which optimally interface the propagating photons with the device. Owing to the near-ideal 1D atom situation, we expect to be able to observe an optical nonlinear response at the very few photon level and the effect of the photon blockade in the reflected field.

4.3 Reflectivity measurements

4.3.1 Experimental setup

We want to study here the effect of the QD-micropillar device on the optical field that is interacting with it, without applying any kind of postselection. The experimental setup, shown in Fig.4.4.a, is the same as the one used in Section 2.6 to study the resonant fluorescence from the QD, with the notable difference that this time we do not collect the signal emitted in cross polarization, but the light which is directly reflected along the same polarization as the incident

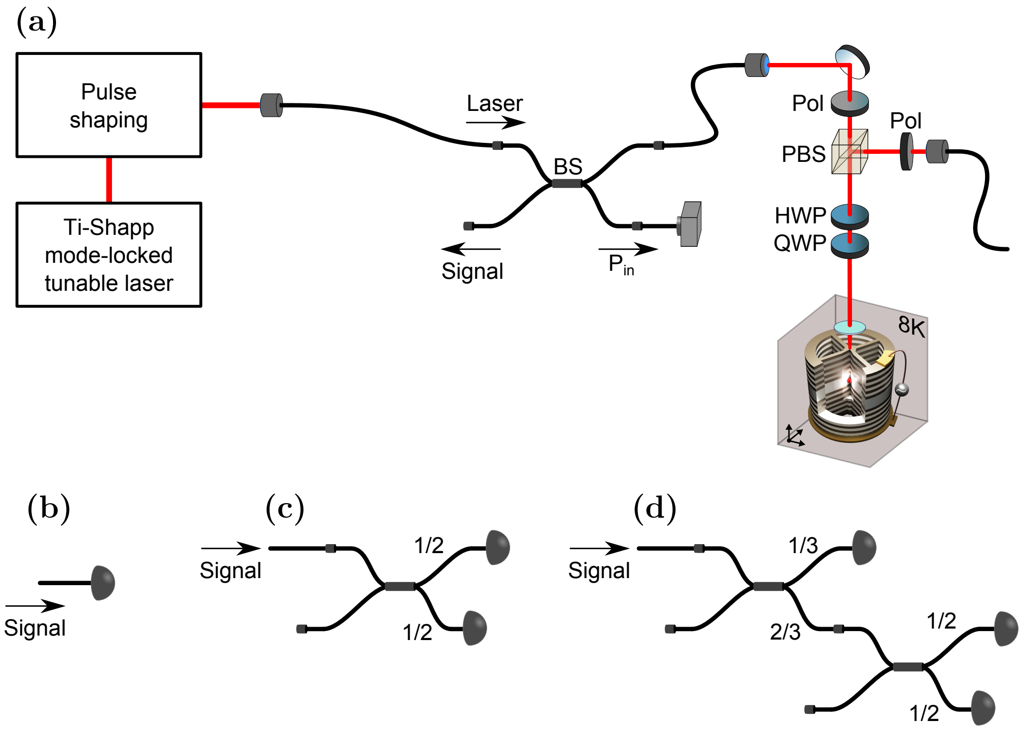

Figure 4.4 – (a) Experimental setup for the measurements of the reflected field. (b) The signal is detected with a single SPAD to retrieve the average reflected photon number $\langle n_{\text{out}} \rangle$. In (c) and (d) the signal is divided on two or three SPADs to retrieve the values of the the second and third order intensity correlation functions $g^{(2)}(0)$ and $g^{(3)}(0,0)$.

one. Introducing a fibre beam splitter (BS) before the excitation/collection fibre allows using such a simple configuration to perform polarized reflectivity measurements. The excitation laser (Laser), either CW or pulsed, is injected in one input of the beam splitter. One of the two outputs is coupled to a calibrated photodiode, to monitor the input power (P_{in}), while the second output is coupled to the fibre going towards the sample. Once collimated in free space, the laser is first going through a polarizing beam splitter (PBS) and a polarization control stage (PC) composed of a quarter and a half wave plate, in order to be able to select a well defined polarization. Then, the free space beam is focused with an objective onto the micropillar cavity, to a diffraction limited spot size closely matching the pillar diameter. The signal coming from the optical mode of the micropillar is collected using the same fibre as for the excitation. This means that the PBS define a single polarization mode, and the fibre defines a single spatial mode, being used both for the incident and for the reflected field. Finally, the reflected signal (Signal) can be read from the unused input port of the fibre beam splitter BS.

As already explained in the previous chapters, the fundamental mode of the micropillar can be decomposed into two linearly polarized modes, H and V, slightly split in energy. To avoid any polarization rotation induced by the cavity modes splitting, we align the polarization of the excitation (same as the collection) along one of the two modes, in the following considered to be H polarized mode.

Depending on the analysis to be performed, the signal coming from the source can be directed towards different detectors configurations. To measure the total reflected intensity, the signal is directed towards a single fibre-coupled SPAD (Fig.4.4.b). To measure higher order correlation of the field, we can demultiplex the signal to multiple SPADs as explained before. Here we employ a balanced fiber beam splitter and two SPADs to measure the second order correlation function (Fig.4.4.c), or two cascaded 33:66 and 50:50 beam splitters and 3 SPADs to measure the third order correlation function (Fig.4.4.d).

4.3.2 Extraction of the device parameters

A complete characterization of the device parameters defining its physical properties, as anticipated in Section 1.3.2, can be performed by measuring the reflectivity spectrum of the device.

To experimentally obtain a reflectivity spectrum, a narrowband frequency-tunable continuous wave laser, having 1MHz linewidth, is used to excite the device along the linear polarization H. The laser wavelength is slowly swept across the optical mode of the micropillar, and the total reflected intensity is collected using the configuration shown in Fig.4.4.b. The absolute reflectivity R is then calculated by normalizing the reflected intensity to the incident power. By monitoring the time evolution of the laser energy, we can convert the time dependence of the reflected intensity to the energy dependence of the absolute reflectivity. The result is shown in Fig.4.5 for the device QD3.

The electrical control allows to spectrally tune the QD transition. When the QD is far detuned from the cavity mode, we can measure the reflectivity spectra of the empty micropillar cavity. The result is shown in Fig.4.5.a, along with the fit of the empty cavity reflectivity. The total width of the cavity corresponds to the value of the total cavity damping rate of $\kappa = 90\mu \pm 10eV$, corresponding to a quality factor of about $Q = \frac{\omega_c}{\kappa} \approx 14,000$. From the minimum value of reflectivity at the resonance energy of the cavity ω_c around 5%, we can also extract the top mirror output coupling efficiency $\eta_{\text{top}} = \frac{\kappa_{\text{top}}}{\kappa}$. From Eq.4.1 we see that for an empty cavity, thus $g = 0$, we obtain:

$$R_{\min}(\omega_c) = \left|1 - 2\frac{\kappa_{\text{top}}}{\kappa}\right|^2 \tag{4.2}$$

which leads to $\eta_{\text{out}} = 0.64$. This formula actually gives two possible values for η_{out}, but we can discard the lower one given the high brightness experimentally observed in the same device operated as a single-photon source. As we have a

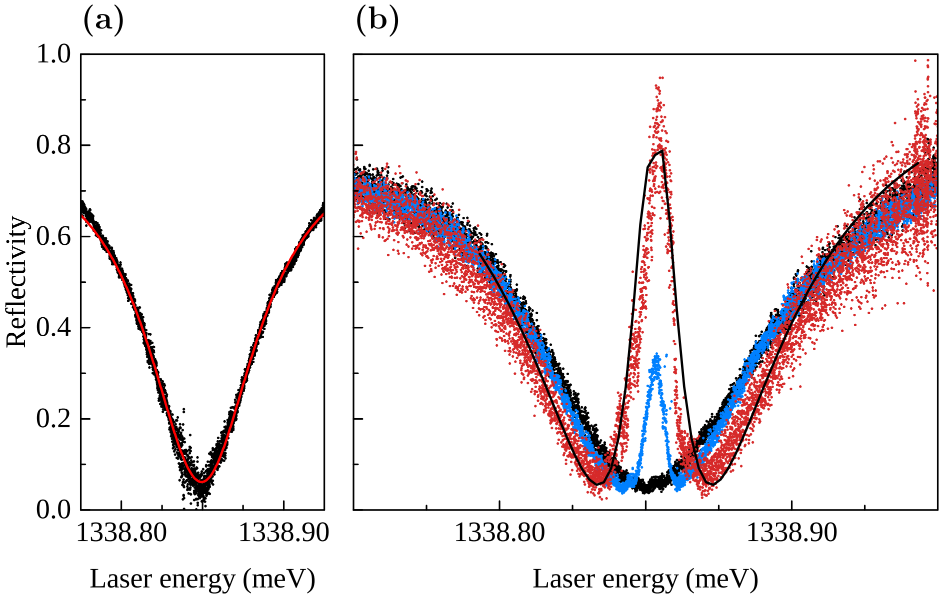

Figure 4.5 – Experimental (symbols) and simulated (lines) reflectivity of the device QD3 as a function of the incident laser energy. (a) Reflectivity spectrum of the empty cavity when the exciton is spectrally detuned through bias application. (b) Reflectivity spectrum with the exciton resonance at the cavity mode energy, for an incident power of $P_{\text{in}} = 14\text{pW}$ (red points), $P_{\text{in}} = 0.84\text{nW}$ (red points) and $P_{\text{in}} = 2\text{nW}$ (black points). The black line shows the simulation for the lowest power.

much higher reflective bottom mirror in the micropillar, the fact that we have an output coupling efficiency lower that 1 is due to the presence of sidewall losses, which effectively acts as a transmission port for the cavity. A very high input coupling efficiency $\eta_{\text{in}} \geq 95\%$ has been determined by measuring the diameters of the input and output modes, assuming both to have a Gaussian profile.

By tuning the QD transition in exact resonance with the cavity mode, we observe the appearance of a very intense peak due the light resonantly scattered by the QD, as shown in Fig.4.5.b. At very low excitation power (red points), when the transition is not saturated, the signal at the cavity resonance energy ω_c reaches a reflectivity value of almost 90% of the maximum cavity reflectivity, demonstrating a highly coherent response of the QD. By increasing the power, the contribution from the light scattered by the QD decreases, due to the saturation of the exciton transition (blue points). Eventually, at very high power (black points), when the transition is fully saturated we reach again the empty cavity condition, where the reflectivity value at the cavity energy ω_c is minimum.

With a theoretical adjustment of the reflectivity spectrum of the combined QD-cavity device given by Eq.4.1, at the minimum excitation power where the transition is not saturated, we can extract the remaining parameters of the device. The theoretical model as well as the fits shown by the solid lines in

Fig.4.5 have been developed and performed by Bogdan Reznychenko and Alexia Auffeves. The coupling strength between the exciton and the cavity, of $g = 19 \pm 0.2\mu eV$, is mainly determined by the peak width, and the total exciton dephasing rate $\gamma = \frac{\gamma_{\text{sp}}}{2} + \gamma^* = 0.35 \pm 0.1\mu eV$ is mainly determined by the peak height. Considering that for a QD in bulk GaAs medium the exciton spontaneous emission rate γ_{sp} is in the range of $0.5 - 0.6\mu eV$ (corresponding to a lifetime between 1 and 1.3ns), from the deduced value of total dephasing rate we can assume an almost negligible pure dephasing γ^*. The same theoretical adjustment also provides the exciton fine structure splitting $\Delta_{\text{FSS}} = 3 \pm 1\mu eV$ and the relative orientation between the QD dipoles and the cavity axis $\theta = 15 \pm 5^{\circ}$.

The device operates in the weak coupling regime, having $g < |\kappa - \gamma|/4$, with a state of the art value of cooperativity $C = \frac{g^2}{\kappa\gamma} = 14 \pm 7$, corresponding to a Purcell Factor $F_{\text{P}} = 2C = 28 \pm 14$. From such a high cooperativity we can also calculate a mode coupling $\beta = 2C/(2C + 1)$ in the range $0.93 - 0.98$. The high values of β, η_{in} and η_{out} shows that the device is very close to the ideal one-dimensional atom situation. An incident photon will couple 95% of the times to the optical mode of the cavity, and will interact with the QD with 98% probability before being lost. Symmetrically, the QD will emit a photon with $93 - 98\%$ probability in the cavity mode, and such photon will be collected from the top 64% of the times.

The quality of this light-matter interface is reflected in the fast saturation and high contrast observed on the exciton transition when increasing the excitation power, as shown in Fig.4.5. An important figure of merit in this situation is the critical intracavity photon number $n_c = \frac{\gamma\gamma_{sp}}{4g^2}$, which is a measure of the number of photons per lifetime inside the cavity at which the saturation of the QD begins to affect the response of the device [155, 120]. We obtain here a record critical intracavity photon number of only $n_c \approx 10^{-4}$ for the onset of the nonlinearity in a CW measurement, with a switching in the absolute reflectivity value as high as 85% when the transition is fully saturated.

4.4 Interaction with coherent wavepackets

4.4.1 Optical nonlinearity at the single photon level

In the previous section, we have experimentally characterized the device parameters, describing its physical properties under low power CW operation. Nevertheless, to be operated as a quantum gate, the device needs to interact with spatially localized photons, thus we are interested in characterizing its response to light wave packets, for which we can define an average number of photons. As we will see, the achievable performances in this case are also affected by the properties of the incident wave packets. In the following, we probe the cavity with coherent light pulses of controlled temporal profile and power, coming from

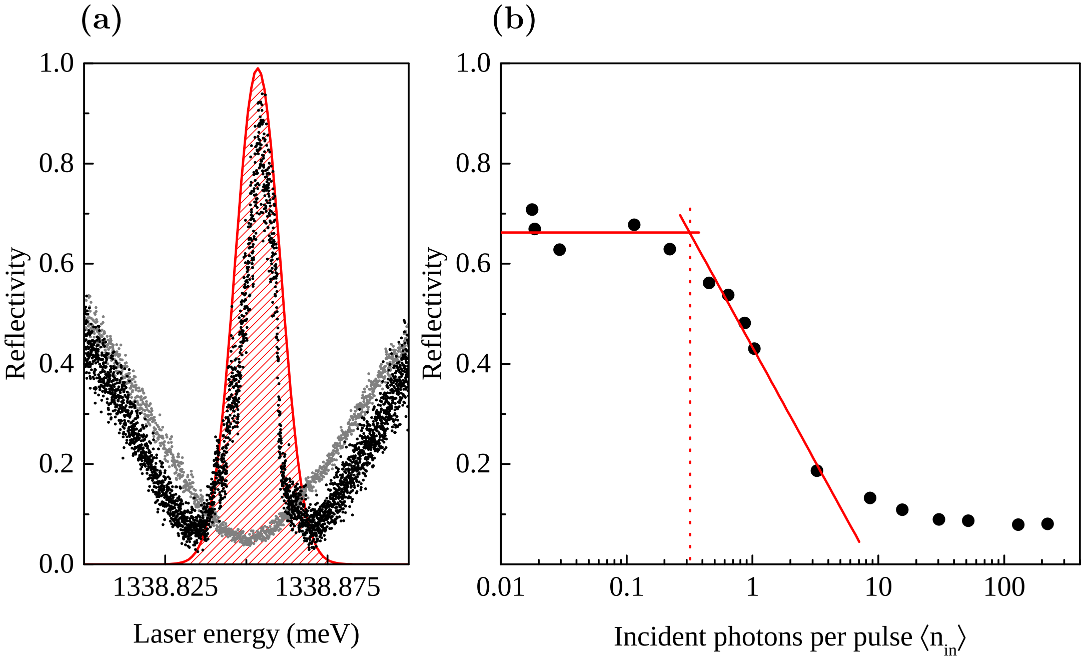

Figure 4.6 – (a) Measured continuous-wave reflectivity spectrum for the unsaturated (black points) and saturated (grey points) QD transition, superimposed to a Gaussian pulse of 125 ps FWHM (red line) representing the excitation pulse. (b) Reflectivity under pulsed excitation, as a function of the incident power. The red lines shows linear fits to the first five and following five experimental points. Their intersection gives the estimation for the onset of the nonlinearity effect.

a tunable pulsed titanium-sapphire laser.

Using the external bias, the QD transition is kept in resonance with the cavity mode at the energy ω_c. The laser frequency ω_{laser} is fixed at the value of ω_c, and the 3 ps pulses of the laser are spectrally shaped using a monochromator to closely match the exciton radiative lifetime of 125 ps (see Fig.4.6.a). This excitation scheme allows to probe the central region of the reflectivity spectra as shown in Fig.4.6.a, where the nonlinear behaviour is determined by the saturation of the exciton transition. As before, the total reflected intensity is detected with a single fiber coupled SPAD, using the configuration of Fig.4.4.b. As explained in Section 2.2.1, in the limit of low detection efficiency, from the measured count rate R_{photons} we can retrieve the output average photon number per pulse as

$$\langle n_{\text{out}} \rangle = \sum_n nP(n) = \frac{R_{\text{photons}}}{\Gamma_{\text{laser}}\eta_{\text{setup}}} \tag{4.3}$$

where Γ_{laser} is the repetition rate of the laser, and η_{setup} the total efficiency of the setup. From the incident power P_{in} instead, we can retrieve the average photon number per pulse sent on the device as $\langle n_{\text{in}} \rangle = \frac{P_{\text{in}}}{\Gamma_{\text{laser}}\hbar\omega_{\text{laser}}}$. The reflectivity is calculated by normalizing the total reflected intensity to the incident one, thus from $R = \frac{\langle n_{\rm out}\rangle}{\langle n_{\rm in}\rangle}$, and is shown in Fig.4.6.b as a function of the average photon per excitation pulse $\langle n_{\rm in}\rangle$.

In the low photon number regime the strong coherent response of the exciton is dominating the reflected signal, resulting in a very high reflectivity of $R_{\rm max} = 68 \pm 2\%$. This value is lower than the one obtained in the CW case due to the finite spectral width of the incident laser pulses. The measured value of reflectivity gradually decrease by increasing the excitation power, and for high photon number it saturates at $R_{\rm min} = 8\pm1\%$, which corresponds to the minimum reflectivity obtained from the empty cavity using the 125 ps laser pulses. This 60% change in the absolute value of reflectivity corresponds to a contrast of $(R_{\rm max} - R_{\rm min})/R_{\rm min} \approx 7.5$, an strong improvement over previous solid-state implementations, where the best contrasts were limited around 1.1 [155, 310]. To extract the threshold for the onset of the nonlinearity effect, we consider the intersection of two linear fits to the values in the low and intermediate $\langle n_{\rm in}\rangle$ regions (first five and following five data points), shown by the red lines in Fig.4.6.b. The threshold defined in this way is observed for an average incident photon number of only $\langle n_{\rm in}\rangle = 0.3 \pm 0.1$, a value $25 - 40$ times smaller than the previous state of the art [155]. We stress that, contrary to many work evaluating the photon number inside the device, this value of the reported photon number is the one outside the cavity, sent onto the device.

Under pulsed excitation, the optical nonlinearity of the exciton transition shows an extremely low threshold at the single photon limit and a very high contrast, demonstrating that the device is acting as a very efficient interface between the propagating wave packets and the QD inside the cavity. The fact that each incident photon have a high probability of interacting with the transition is a central feature for the realization of deterministic photon gates and filters, where we want an efficient reflection of the single photon component.

4.4.2 Antibunching of the reflected field

The observation of such a strong nonlinearity is a consequence of the system being close to the one dimensional atom situation. This means not only that each incident photon interacts with the transition, but also that the fluorescence is coherently reflected. Being the field radiated by a two-level system, which can only scatter single photons, we expect to observe antibunching in such reflection. We thus study now the photon statistics of the reflected field.

The excitation scheme is exactly the same as the one used in the previous section, but this time we measure the second order correlation function $g^{(2)}(\tau)$ of the reflectivity, using the configuration shown in Fig.4.4.c. The collected signal is split with a 50:50 fibre beam splitter into two fibre-coupled SPADs, and a correlation measurement is performed on the detection events. As explained in section 2.2.2, we can access the second order correlation function from the

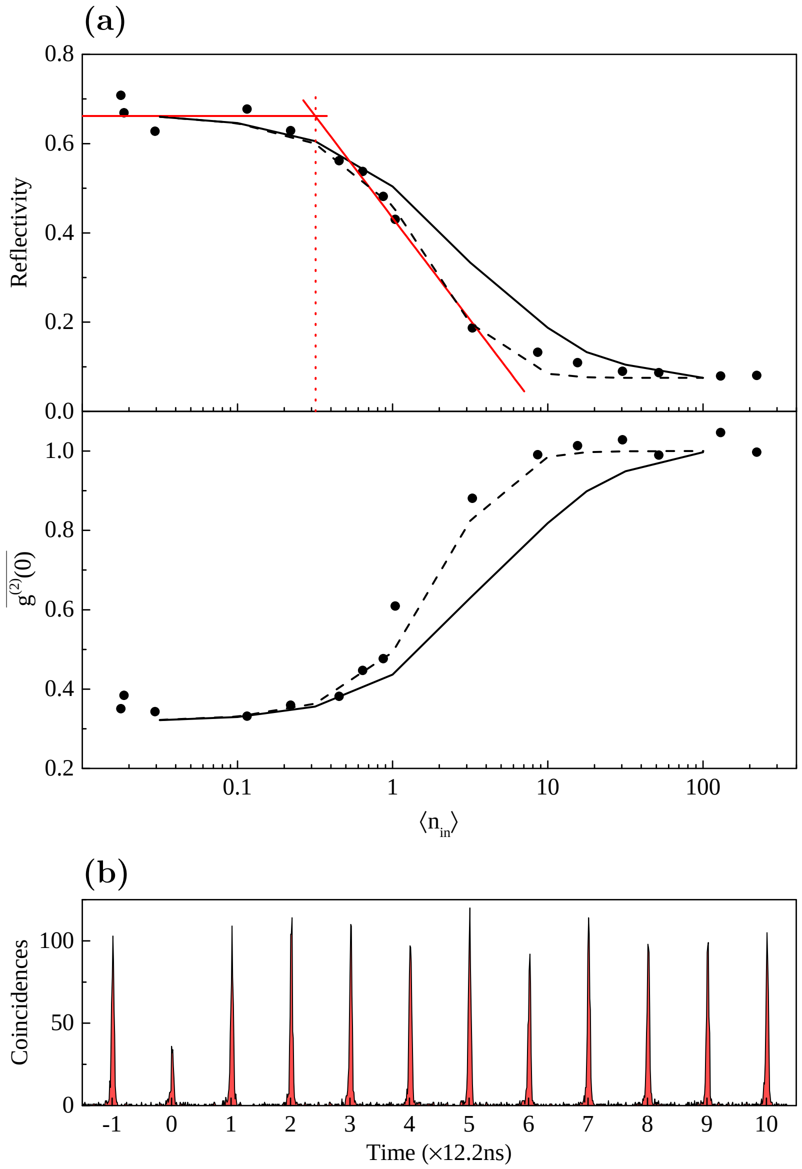

Figure 4.7 – Nonlinear response and photon blockade from the QD-micropillar device QD3. (a) Top panel shows the nonlinearity curve as in Fig.4.6, while the bottom panel shows the measured $\overline{g^{(2)}(0)}$ as a function of the excitation power. For an unsaturated transition a strong antibunching is observed. Solid lines shows simulations using the parameters extracted from the CW measurement of Fig.4.5. Dashed lines shows simulations including the effect of a power-dependent electron tunneling out of the QD (see main text). (b) Measurement of the second order correlation function for an incident photon number of about 0.1.

normalized value of the detected coincidences at zero time delay $\overline{g^{(2)}(0)}$, which for low detection efficiency is given by:

$$\overline{g^{(2)}(0)} = \frac{2P(2) + 6P(3) + ...}{\langle n_{\text{out}} \rangle^2} \tag{4.4}$$

At very low excitation power we observe a clear antibunching (see Fig.4.7.b, obtained for $\langle n_{\text{in}} \rangle \approx 0.02$), which is not present at high power. A detailed study of the measured value of the $\overline{g^{(2)}(0)}$ as a function of the average incident photon per excitation pulse $\langle n_{\text{in}} \rangle$ is shown in Fig.4.7.a (bottom panel), along with the nonlinearity curve (top panel), which was presented the previous section. The behaviour of the two curves closely matches. In the low photon number regime, the strong response from the QD introduces a large fraction of antibunched light, and indeed for $\langle n_{\text{in}} \rangle \leq 0.1$, we measure a value of $\overline{g^{(2)}(0)} \approx 0.35$, meaning that the reflected light intensity is dominated by single photons. The measurement of antibunched light in the reflection demonstrate the photon blockade effect induced by the transition. The absorption of a first photon from the incident pulse by the QD, prevents the absorption of any other photons from the pulse as long as the QD is in the excited state, thus for a time determined by the exciton radiative lifetime. The emission from the exciton is then efficiently collected from the top mirror, while the part of the pulse which has not interacted with the QD is transmitted according to the spectrum of the empty cavity. This result, obtained without any postselection, contrasts with previous studies of the photon blockade effect in solid-state devices, where limited antibunching of $g^{(2)}(0) \approx 0.6 - 0.9$ was reported even after removing the laser light which had not entered the cavity [310, 158, 313].

When increasing the incident photon number the value of the $\overline{g^{(2)}(0)}$ increases up to 1, meaning that the beam statistics evolves from sub-Poissonian to Poissonian. At high power indeed, the QD is fully saturated, and most of the incident pulse does not interact with the transition. The reflected laser is dominating the measured signal, and we are effectively observing an empty cavity.

The black lines in Fig.4.7 shows the calculated reflectivity and $\overline{g^{(2)}(0)}$, resulting from the parameters determined with the CW reflectivity measurements of Fig.4.5. The simulations are performed by A. Auffeves and B. Reznychenko using the model presented in section 1.3.2, using a Gaussian temporal profile for the incident pulses. There is a good overall agreement with the measured values, especially for the nonlinearity threshold and contrast. However, we can experimentally observe a slightly sharper transition in the experimental data for $\langle n_{\text{in}} \rangle \geq 1$. There are various phenomena which can account for this difference: a deviation in the incident pulse from a Gaussian profile used in the simulations, a mechanical instability of the experimental setup resulting in effective fluctuation of the input coupling efficiency with the micropillar, or finally a power-dependent electron tunnelling out of the QD. These three hypothesis have been explored, but the effect of the first two, while can reasonably be present, is not strong enough to explain the observed deviation. On the contrary a power-dependent electron tunnelling out of the QD allows to reproduce well the experimental data. This implies that if an electron has successfully escaped, upon excitation the QD will be in a charged state at a detuned frequency from the cavity, thus there will be no atomic transition at the neutral exciton energy. This is taken into account as a reduction of the occupation probability of the exciton state with increasing power, and the results are shown with dashed lines in Fig.4.7. The new expected values for the reflectivity and the second order correlation function (R' and $\overline{g^{(2)}(0)}'$) have been determined from the previously calculated ones (R and $\overline{g^{(2)}(0)}$) using the following equations:

$$R' = Rp_X + R_c(1 - p_X) \tag{4.5a}$$

$$\overline{g^{(2)}(0)}' = \overline{g^{(2)}(0)}p_X + g_c^{(2)}(0)(1 - p_X) \tag{4.5b}$$

where p_X is the probability for the QD to be in the neutral exciton state and R_c and $g_c^{(2)}(0) = 1$ are respectively the reflectivity and the second order correlation function expected from the empty cavity. With a phenomenological dependence of $p_X = \frac{1}{1+(\langle n_{\mathrm{in}}\rangle/N_0)^2}$ where $N_0 = 3$, it is possible to faithfully reproduce the experimental observation for the whole power range explored in Fig.4.7. The threshold of $N_0 = 3$ photons additionally tells us that this reduction of the occupation probability for the exciton state does not affect the low incident photon number regime, which is the one to which we are mainly interested in the following.

4.4.3 Influence of the excitation pulse duration

The nonlinearity contrast and threshold, as well as the maximum antibunching observable, depend not only on the device characteristics but also on the wavepacket used to probe it. To understand how it is affected, we study here the optical nonlinearity of the QD-micropillar device for different temporal width of the excitation pulses. This study is performed on a different device, named QD4, presenting the following parameters: $\eta_{\mathrm{top}} = 0.64$, $g = 19\mu eV$, $\kappa = 100\mu eV$, $\gamma = 0.5\mu eV$. The exciton fine structure splitting is $\Delta_{\mathrm{FSS}} = 10\mu eV$ and relative orientation of QD and cavity axis is $\theta = 20^{\circ}$. The resulting cooperativity is $C \approx 7$, meaning a mode coupling $\beta \approx 0.93$.

The results for reflectivity and $\overline{g^{(2)}(0)}$ are shown in Fig.4.8, obtained with excitation pulses of $55ps$ (panel a), $95ps$ (panel b) and $125ps$ (panel c). In the bottom row, the black circles shows the value of the $\overline{g^{(2)}(0)}$ measured on the reflected field having H polarization, as was done for Fig.4.7.a. The red diamonds instead, shows the value of the $\overline{g^{(2)}(0)}$ measured on the field emitted along the orthogonal V polarization, obtained using the cross polarization configuration described in section 2.6.

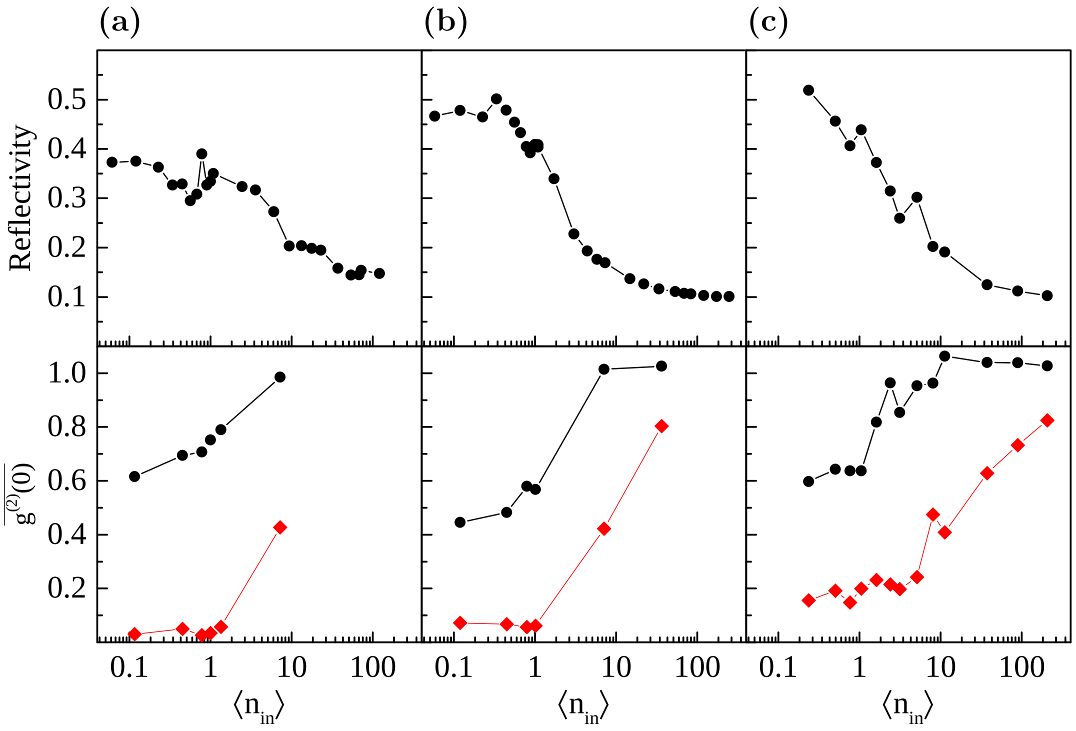

Figure 4.8 – Power dependence of the reflectivity (top row) and $\overline{g^{(2)}(0)}$ (bottom row) for different duration of the excitation pulses: 55ps (a), 95ps (b) and 125ps (c). The $\overline{g^{(2)}(0)}$ is measured both on the directly reflected field (black circles) and in a cross polarization configuration (red). Measurements performed on device QD4.

The measured reflectivity shows that the nonlinearity contrast (reflectivity difference between the saturated and unsaturated conditions) increases and the nonlinearity threshold (value of $\langle n_{\text{in}} \rangle$ for which the reflectivity begins to decrease) decreases when using longer pulses. In the low photon number regime, we have a higher value of the reflectivity, in the central region a steeper decrease, and in the high photon number regime we have a lower value of the reflectivity. This can be simply understood as a longer pulse will have a narrower spectrum.

By reducing the spectral width of the excitation pulse we observe a twofold improvement: first, a smaller amount of light will be reflected back by the cavity, independently the QD response, and second, there will be a more efficient interaction of the light which entered the cavity with the exciton transition. This is shown in Fig.4.9, where the spectrum of the measured reflected signal is plotted for three different excitation pulse lengths of 25 ps, 35 ps and 55 ps at a same excitation power, with (red line) and without (black line) the QD transition tuned at the cavity mode energy. In each case the laser central wavelength is tuned to the cavity resonance. The longer the pulse, the narrower the spectrum, thus the higher is the contribution of the QD to the total reflected intensity. In the limit of a CW excitation, we achieve the best contrast possible determined by the physical parameters of the QD-micropillar device, as we have seen in the measurement of Fig.4.5.

A better contrast could also imply a higher antibunching, as there will be a bigger fraction of single photons, coming from the QD, with respect to the Poisson light, coming from the laser reflected by the cavity. This effect can be studied by observing the measured $\overline{g^{(2)}(0)}$ on the reflected field (black circles in Fig.4.8) in the low incident photon number regime, where the QD transition is not saturated. Indeed, going from Fig.4.8.a to Fig.4.8.b, we observe a strong decrease in the minimum value for the $\overline{g^{(2)}(0)}$, going from 0.62 to 0.45. However, going from Fig.4.8.b to Fig.4.8.c, the minimum value of the $\overline{g^{(2)}(0)}$ increases again to 0.60. Here the stronger response of the QD is compensated for longer pulses by the excitation dynamics of the QD leading to the degradation of the $\overline{g^{(2)}(0)}$. The longer the pulse, the higher the probability of multiple single-photon emissions during the same excitation, because the transition has a higher chance of emitting a photon and being reexcited before the end of the incident pulse. This effect can indeed be verified by measuring the $\overline{g^{(2)}(0)}$ in a cross polarization configuration, which is shown by the red diamonds in Fig.4.8. The polarization filtering allows suppressing the reflected laser in order to analyse the emission of the exciton transition only. The $\overline{g^{(2)}(0)}$ shows a different behaviour now: the minimum value, measured in the low incident photon number regime, is monotonically increasing with the excitation pulses duration. Here we measure respectively 0.03, 0.07 and 0.16. This reflects the higher chance of multiple single photon emission during a single excitation cycle for longer pulses. At higher excitation power all values of the $\overline{g^{(2)}(0)}$ increase up to one. This is explained by two effects. First, the $\overline{g^{(2)}(0)}$ is expected to increase when going beyond π pulse excitation, as it reflects the oscillatory behaviour of the Rabi oscillations under pulsed excitation as recently reported [314]. Additionally, an imperfect polarization filtering leads to the leak of scattered laser light into the detectors, becoming significant for high excitation powers.

An optimal trade-off between nonlinearity contrast and $\overline{g^{(2)}(0)}$, giving the strongest antibunching in the reflected field, has been obtained for an excitation pulse length close the QD lifetime, leading also to the experimental results of Fig.4.7 in the case of device QD3.

These considerations can be ultimately traced back to the time-energy uncertainty relation. As we study a two-level system, there is a single timescale given by the radiative lifetime of the exciton transition which defines the properties of our device. If the excitation pulse is shorter than this lifetime, its spectrum will not show a good overlap with the transition. On the contrary, if the pulse is narrower than the transition bandwidth, it will be long enough to trigger multiple excitations. This effect, as theoretically demonstrated by the work of Rosenblum et al. [294], puts a limit of 64% in the efficiency of a photon routing device based on the photon blockade effect using a two-level system. To overcome such

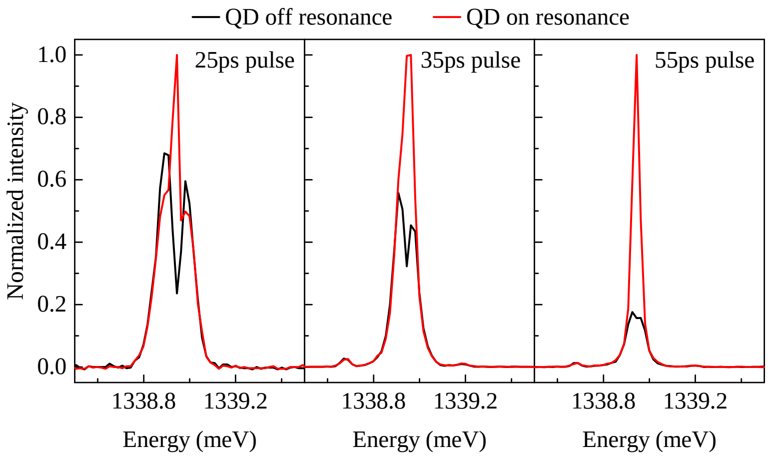

Figure 4.9 – Reflected intensity from the device QD4 as a function of the energy under pulsed excitation, for different temporal durations of the laser pulses. The black lines shows the empty cavity response, while the red lines the case with the exciton at the cavity mode energy. The longer the pulse, the higher the contribution from the QD to the total reflected intensity.

a limitation, a lambda system or a 4 level system would be needed, where the photon to be routed are not required to interact with the system within the lifetime of a single transition.

4.5 Filtering single photon Fock states

In this section we analyse in more detail the reflected intensity from the device and its second order correlation function. In the low photon number regime, where the QD transition is not saturated and a strong antibunching is observed, we interpret the behaviour of the device as a single photon Fock state filter.

4.5.1 Temporal evolution of the reflected wavepackets

An interesting insight on the processes leading to the reflection of light from the QD-micropillar device is given by the temporal evolution of the reflected wavepackets. In order to measure this time dependence, we send the collected signal to a single SPAD having time resolution of $\approx 30ps$, and record the detected counts as a function of the delay with respect to the excitation pulse. The result relative to device QD4 is shown in Fig.4.10.a, for the two cases of the empty cavity (black dashed line), and when the QD transition is brought in resonance with the cavity (red solid line) through proper bias application. Here we use excitation pulses of about 55 ps.

If the exciton transition is far detuned from the cavity mode, we expect to measure the time dependence of the laser pulses being reflected back by the cavity, which is what is shown by the dashed line in Fig.4.10.a. This peak is in reality composed of two contributions, which cannot be distinguished due to the finite temporal resolution of our detectors. The reflectivity profile of the cavity is resulting from the destructive interference of the light directly reflected from the top mirror and the light reflected from the bottom mirror after being entered the cavity. Having an extended spectral width in the incident pulse, we can expect that this destructive interference is not equally effective for all the spectral components of the pulse. In the time domain this result in the temporal separation between two contributions. It can be seen in the simulation of Fig.4.10.b, performed by our collaborator Bogdan Reznychenko, where it is considered a short Gaussian incident pulse having a duration of 20 ps, shorter than the cavity lifetime of 42 ps. The first reflected peak (A_1) corresponds to the light directly reflected from the top mirror before any destructive interference with the light which entered the cavity can take place. The second peak (A_2) is due to the light exiting the cavity after the end of the excitation pulse, when no more interference is possible and shows a decay time corresponding to the lifetime of the cavity photons.

If we bring the exciton transition in resonance with the cavity mode, we observe for low excitation power the appearance of an additional signal delayed in time, coming from the light which is now resonantly scattered by the QD. The experimental results is plotted in Fig.4.10.a with a red solid line, revealing a two peak shape, and is also accounted theoretically, as shown in Fig.4.10.b where it is represented by the peak A_3. The pulse arising from the QD shows a delay due to the light-matter interaction, called the Wigner time delay, which is maximum at resonance. Such a delay, previously measured with a single natural atom [315], is a consequence of the dispersive behaviour of the two-level system in the linear response regime. In striking contrast to the other two peaks, which maintains the Poisson statistics of the incident laser pulses, the light in the peak A_3 is antibunched, being due to the QD exciton emission.

The simulations of Fig.4.10.b, also show that by bringing the QD transition in spectral resonance with the cavity, the appearance of the peak A_3 is linked to a decrease of the intensity of the peak A_2. The intensity difference in the peak A_2 corresponds to the light that has interacted with the QD and has been converted into the peak A_3. In this simulation, a moderate change is observed because we consider an incident laser pulse of 20 ps, which has a limited spectral overlap with the transition. On the contrary, by reducing the spectral width of the excitation pulse we observe a twofold improvement, as explained in the previous section: first, a smaller amount of light reflected back by the cavity means a smaller contribution from A_1, and second, a more efficient interaction of the light which entered the cavity with the exciton transition means a higher contribution from A_3, at the expense of A_2. The resulting value of $\overline{g^{(2)}(0)}$ that

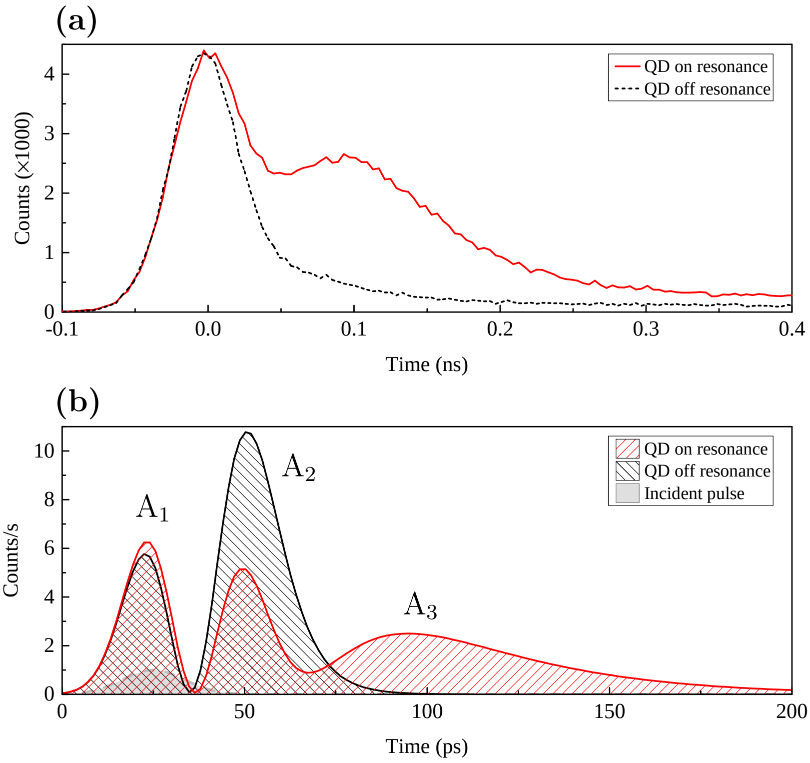

Figure 4.10 – Measured (a) and simulated (b) temporal dependence of the reflected wave packets from the QD-cavity device QD4. The measurement is performed with laser pulses of 55 ps, while the simulation with a 20 ps pulse. Black lines shows the case of the empty cavity, red lines the case with the exciton at the resonance energy.

we measure on the reflectivity signal (black symbols of Fig.4.8) thus depend on the ratio of the intensity of the peak A_3 to the intensities of the peaks A_1 and A_2, which both show a Poisson statistics.

As a last remark, we can use again Fig.4.10.b to understand what happens when the QD transition gets saturated. When the incident number of photons per pulse is high enough, the contribution from the peak A_3 will saturate to a maximum value, whose intensity is determined by the interaction efficiency between the excitation and the transition, as explained in the previous paragraphs. On the contrary the signals from the peaks A_1 and A_2, which are determined by the reflectivity spectrum of the cavity, grows linearly with the incident power. Eventually the fraction of light coming from the QD becomes negligible with respect to these two contributions, and the signal reflected by the empty cavity is recovered.

4.5.2 Mode reconstruction

In the previous section, we have seen that we can attribute different temporally separated component of the reflected intensity to different sources, namely the laser light reflected by the cavity, and the light scattered by the QD transition. From the CW reflectivity spectrum we have extracted an almost negligible pure dephasing for our exciton transition, meaning that the QD is mainly acting as a coherent scatterer. The field reflected by the device is thus the result of the coherent interference between the laser field and the field re-emitted by the QD. The interference term is limited by the temporal overlap between these two contributions. This overlap depends on the pulse length used for the experiment: the longer the pulse, the larger the overlap. In this section, to analyse the performances of our device as a single photon filter, we neglect this temporal overlap and consider the reflected field as a mixture of coherent light reflected by the cavity, having a Poisson statistics, and single photon light scattered by the QD, composed of vacuum and single photons. Based on this assumption, we can use the measured reflectivity and $\overline{g^{(2)}(0)}$ to quantify the contribution of the two components and determine an average photon number for each.

In order to do so, we use the formalism of the probability generating functions, following the approach of Goldschmidt et al. [316]. A probability generating function $G_X(s)$ is a power series representation of the probability distribution of a discrete random variable X, and can be written as:

$$G_X(s) = \sum_{k=0}^{k=\infty} s^k P(X = k) \tag{4.6}$$

where the coefficient of each polynomial term is the probability for the random variable X to assume the value k. It can be shown that the probability generating function $G_{X+Y}(s)$ of the distribution of two independent random variables is given by the product of the two functions $G_{X+Y}(s) = G_X(s)G_Y(s)$.

In our case, the discrete variable is the photon number of the reflected field. The total average photon number observed is given by $\langle n_{out} \rangle = \mu_{QD} + \mu_\alpha$, where the first contribution, μ_{QD}, is the average photon number coming from the QD, and the second one, μ_α, is the average photon number from the laser. The field coming from the QD is composed of only vacuum and single photons, thus is described by the generating function:

$$G_{QD}(s) = (1 - \mu_{QD}) + s\mu_{QD} \tag{4.7}$$

while the field of the laser, a coherent state, is described by a Poisson distribution:

$$G_\alpha(s) = e^{-\mu_\alpha(1-s)} \tag{4.8}$$

The generating function for the total reflected mixture is then:

$$G_{total}(s) = G_{QD}(s)G_\alpha(s) = (1 - \mu_{QD}(1 - s))\, e^{-\mu_\alpha(1-s)} \tag{4.9}$$

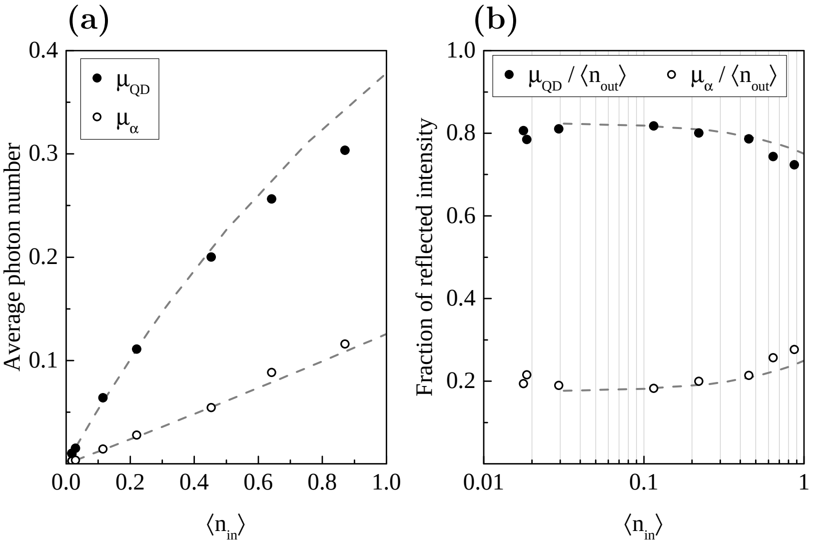

Figure 4.11 – Reconstruction of the reflected field as a mixture of coherent and single photon light, as a function of the incident power. (a) Average photon number for the two components in the reflected field, as calculated from the measured reflectivity and $\overline{g^{(2)}(0)}$. (b) Fraction of reflected intensity due to the single photons and to the laser pulse.

This function can be expressed in terms of the measured values of the intensity correlations, as the k^{th} order derivative of $G_{total}(s)$, calculated in $s = 1$, gives the k^{th} order correlation function at zero time delay [316]:

$$g^{(k)}(0) = \frac{G^{(k)}_{total}(s=1)}{\langle n_{out}\rangle^k} \tag{4.10}$$

Calculating Eq.4.10 for $k = 1$ and $k = 2$ we obtain respectively:

$$\langle n_{out}\rangle = \mu_{QD} + \mu_\alpha \tag{4.11}$$

$$g^{(2)}(0) = 2\mu_{QD}\mu_\alpha + \mu_\alpha^2 \tag{4.12}$$

which can be used to retrieve the values of μ_{QD} and μ_α in the reflected field, from the experimentally measured values of reflectivity $\overline{R} = \langle n_{\text{out}}\rangle/\langle n_{\text{in}}\rangle$ and second order correlation function $\overline{g^{(2)}(0)}$, previously shown in Fig.4.7.

The assumption to have only single photons being emitted from the QD is reasonable in the low photon number regime, where we can neglect the possibility of multiple excitations. We thus limit this analysis to the region where $\langle n_{out}\rangle \leq 1$, and the resulting values for μ_{QD} and μ_α are shown in Fig.4.11.a, respectively with filled and empty circles. As expected, the coherent light reflected by the cavity linearly increase with the excitation power. On the contrary, the average photon number coming from the QD saturates when approaching $\langle n_{out}\rangle \approx 1$. Still, it is clear that in this range the reflected field is dominated by the QD field. To quantify how much of the detected intensity radiated back is composed of single photons, we plot in Fig.4.11.b the ratios $\mu_{QD}/\langle n_{out}\rangle$ and $\mu_\alpha/\langle n_{out}\rangle$ as a function of $\langle n_{in}\rangle$ in logarithmic scale. We see that, when the transition is not saturated and when sending coherent state on the device, 80% of the reflected intensity is composed of single photons.

The above observations has been performed on the light directly reflected from the device, without any kind of postselection, and demonstrate that the QD-micropillar device efficiently acts as a single-photon Fock-state filter.

4.6 Suppression of multi-photon components

To complete the analysis of the previous section, and have a better insight of the composition of the reflected field, we experimentally measure the third order correlation function, as presented in this section.

4.6.1 Performing three-photon correlation measurements

We perfomed a generalized HBT experiment by coupling the collected signal to a fiber beam splitter having a splitting ratio of $R : T \approx 33 : 66$, and the transmission port of this to a second beam splitter having a splitting ratio of $R : T \approx 50 : 50$. In this way we can equally split the signal onto 3 fiber-coupled SPADs, as depicted in Fig.4.4.d, and perform a three-photon coincidence detection.

The degree of third order coherence of the field emitted by the source is given by:

$$g^{(3)}(\tau_1, \tau_2) = \frac{\langle \hat{a}^\dagger(t)\hat{a}^\dagger(t+\tau_1)\hat{a}^\dagger(t+\tau_2)\hat{a}(t)\hat{a}(t+\tau_1)\hat{a}(t+\tau_2)\rangle}{\langle \hat{a}^\dagger(t)\hat{a}(t)\rangle\langle \hat{a}^\dagger(t+\tau_1)\hat{a}(t+\tau_1)\rangle\langle \hat{a}^\dagger(t+\tau_2)\hat{a}(t+\tau_2)\rangle} \tag{4.13}$$

We consider here for simplicity a single mode field. As already shown in Section 2.2.2 for the second order correlation function, this equation can be conveniently discretized for our pulsed excitation scheme, considering each operator $\hat{a}^\dagger(k)$ as being integrated over the k^{th} pulse. At zero time delay, when all operators are acting on the same light pulse, the above equation can be written as:

$$g^{(3)}(0,0) = \frac{\langle (\hat{a}^\dagger)^3(\hat{a})^3\rangle}{\langle \hat{a}^\dagger\hat{a}\rangle^3} = \frac{\langle \hat{n}(\hat{n}-1)(\hat{n}-2)\rangle}{\langle \hat{n}\rangle^3} \tag{4.14}$$

By calculating the expectation values for a generic wavepacket described by a state ρ, we obtain [169]:

$$g^{(3)}(0,0) = \frac{\mathrm{Tr}[\rho\hat{n}(\hat{n}-1)(\hat{n}-2)]}{\mathrm{Tr}[\rho\hat{n}]^3} = \frac{\sum_{n=0}^{\infty} n(n-1)(n-2)P(n)}{\left(\sum_{n=0}^{\infty} nP(n)\right)^3} \tag{4.15}$$

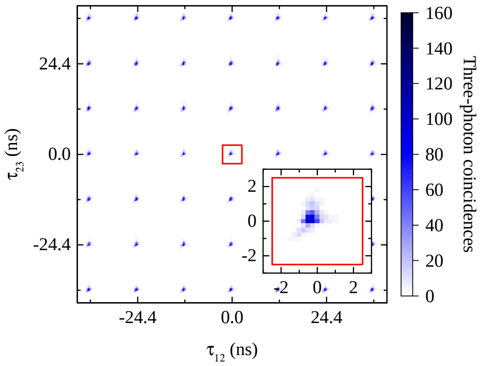

Figure 4.12 – Histogram of the three-photon coincidence detection measurement performed on device QD3. The events on the detectors are plotted as a function of the time delay between two different couples of detectors. The peak at zero-time delay, normalized to the average height of the uncorrelated peaks at non-zero delays, allows to retrieve the value of $g^{(3)}(0,0)$.

where $P(n)$ is the probability of observing n photons. Recalling that the average photon number of the reflected field is given by $\langle n_{\text{out}}\rangle = \sum_{n=0}^{\infty} nP(n)$, we have for our case:

$$g^{(3)}(0,0) = \frac{6P(3) + 24P(4) + \ldots}{\langle n_{\text{out}}\rangle^3} \tag{4.16}$$

From this equation, we see that the third-order correlation function is related to the probability of having more than two photon in the pulse, providing additional information to the already measured second order correlation function.

Experimentally, we collect all the time-tagged photon detection events on each of the three detectors, with 256ps resolution. From the data, we then reconstruct a two dimensional correlation histogram as the one shown in Fig.4.12, by plotting the number of coincidences detected on the three detectors as a function of the time delays τ_{12} and τ_{23} between two different couples of detectors. The experimental value of the third order correlation function at zero time delay $g^{(3)}(0,0)$ is extracted by normalizing the central peak, giving the number of coincidences detected from a same light pulse, with respect to the peaks at delays $\tau_{12} \neq 0$, $\tau_{23} \neq 0$ and $\tau_{12} \neq \tau_{23}$, giving the number of uncorrelated coincidences triggered by different pulses.

The outcome of such measurement is given by the ratio of the conditional probability of having all detectors to click divided by the product of the individual detection probabilities. Following the work of Stevens et al. [169], we can show that the result is given by:

$$\overline{g^{(3)}(0,0)} = \frac{P_{123}(\text{click},\text{click},\text{click})}{P_1(\text{click})P_2(\text{click})P_3(\text{click})} = \\ \frac{6P(3)+24P(4)\left(1-\frac{1}{6}\eta_0-\frac{1}{6}\eta_1-\frac{1}{6}\eta_2\right)+...}{\prod_{i=1}^{3}\left(P(1)+2P(2)\left(1-\frac{1}{6}\eta_i\right)+...\right)} \tag{4.17}$$

where η_1, η_2 and η_3 are the efficiencies of the three detectors. In the limit of low detection efficiency, Eq. 4.17 reduces to the same form of Eq.4.16: $\lim_{\eta_0,\eta_1,\eta_2\to 0} \overline{g^{(3)}(0,0)} = g^{(3)}(0,0)$. The three detectors used here have a detection efficiency of about 28% while the overall setup transmission is limited to few percent, so that the low detection efficiency limit is valid. Moreover, it is to be associated with the fact that most of the field that we want to analyse is coming from the QD, emitting single photons, thus the probability of multiphoton events is very low. Considering that $P(n+1) \ll P(n)$, to the leading terms Eq.4.17 gives the same result as Eq.4.16, thus $\overline{g^{(3)}(0,0)}$ is a faithful estimation of $g^{(3)}(0,0)$.

To extract the experimental value of $\overline{g^{(3)}(0,0)}$, the detected coincidences of the histogram of Fig.4.12 are integrated in an area of $5\times 5ns$ around each peak, and normalized to the average area of the uncorrelated peaks, as explained before, resulting in the correlation map shown in Fig.4.13. The dashed lines at $\tau_{12}=0$, $\tau_{23}=0$ and $\tau_{12}=\tau_{23}$ highlight the peaks for which we have a zero delay between at least two detectors, and the height of the central peak, where the three lines cross, gives us the value of $\overline{g^{(3)}(0,0)}$. Performing the three photon correlation measurement on the incident pulse, we obtain the uniform map of Fig.4.13.d. This corresponds to a value of $\overline{g^{(3)}(0,0)}=1$, confirming the Poisson statistics of the incident field. By performing the same measurement on the reflected field, for an incident average photon number of $\langle n_{\text{in}}\rangle = 0.5$, we obtain the correlation map shown in Fig.4.13.a. Here, we clearly see presence of an antibunching on the lines corresponding to $\tau_{12}=0$, $\tau_{23}=0$ and $\tau_{12}=\tau_{23}$, where $\overline{g^{(3)}(\tau_{12},\tau_{23})}=0.55$. These peaks correspond to a zero time delay between only two detectors, thus is equivalent to a direct measurement of the second order correlation function [305], giving $\overline{g^{(2)}(0)}=0.55$. At the centre of the map instead, we have a zero time delay between all the three detectors, where we measure a value of $\overline{g^{(3)}(0,0)}=0.18$. The much lower value of $\overline{g^{(3)}(0,0)}$ reveals that the three photon events are indeed much more suppressed that the two photon events.

Increasing the power, the antibunching pattern gradually disappear, as shown in the measurements of Fig.4.13.b and Fig.4.13.c. The former is obtained for an incident average photon number $\langle n_{in}\rangle = 1$, and gives $\overline{g^{(2)}(0)}=0.65$ and $\overline{g^{(3)}(0,0)}=0.36$. The latter instead is obtained for $\langle n_{in}\rangle = 2.4$, and gives $\overline{g^{(2)}(0)}=0.9$ and $\overline{g^{(3)}(0,0)}=0.8$. Looking at the sequence of panels of Fig.4.13,

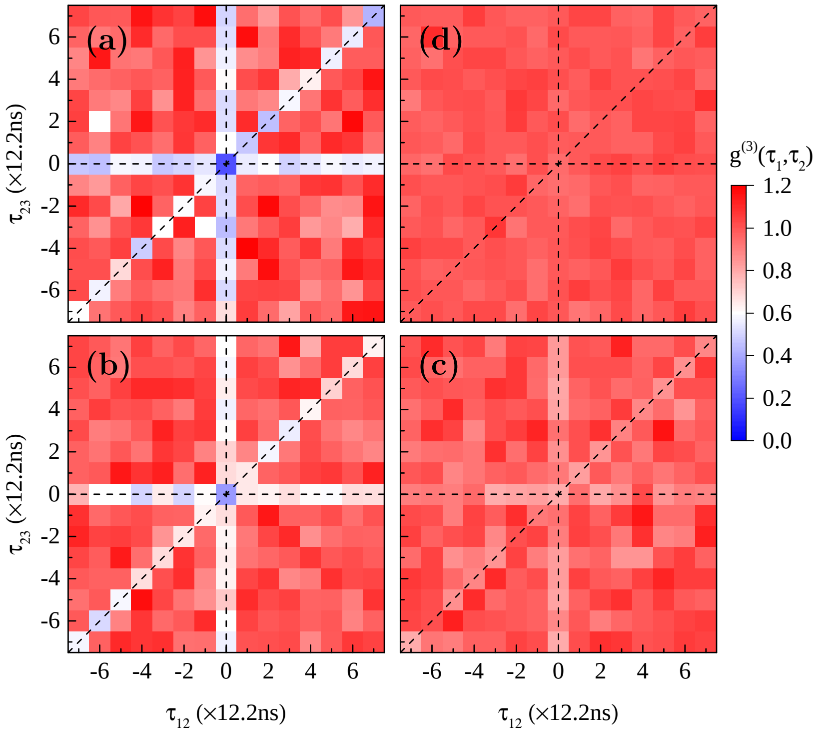

Figure 4.13 – Plots of the $\overline{g^{(3)}(\tau_{12},\tau_{23})}$, retrieved by integrating a 5×5ns area around each peak of the raw histograms as the one of Fig.4.12. Panels (a), (b) and (c) show the measurements performed on the reflected field respectively for an average incident photon number of 0.55, 1 and 2.4. Panel (d) instead shows the same measurement performed on the incident field. The set of measurements highlights the transition from an antibunched to a Poisson photon distribution in the reflected signal.

from a to d, the transition from a sub-Poisson to a Poisson statistics in the reflected field, as the QD gets saturated, is clearly visible.

4.6.2 Reconstruction of the photon-number distribution

Having measured the correlation functions up to the third order, we have enough information to reconstruct the photon number distribution for the field, up to three photons. We can assume that the probability of observing more than three photons in the reflected field is negligible, thus $P(n \geq 4) \ll P(n < 4)$, which allows to greatly simplify the relations we have derived up to now. This assumption is valid throughout most of the analysed range shown in Fig.4.7.a, since in the low incident photon number regime the reflected field is dominated by the single photon emission of the QD, while in the high incident photon number regime the reflectivity is very low, implying a small average photon number reflected. Anyhow, we are interested in the region before the saturation of the QD.

The three experimental configurations of Fig.4.4.b, Fig.4.4.c and Fig.4.4.d have been used to measure respectively the average photon number $\overline{\langle n_{\text{out}}\rangle}$, the second order correlation $\overline{g^{(2)}(0)}$ and the third order correlation $\overline{g^{(3)}(0,0)}$ of the field. Neglecting the possibility of having more than three photons, we can set $P(n \geq 4) = 0$ in Eq.4.3, Eq.4.4 and Eq.4.17, leading to the following set of relations:

$$\overline{\langle n_{\text{out}}\rangle} = \sum_{n=0}^{3} nP(n) = P(1) + 2P(2) + 3P(3) \tag{4.18a}$$

$$\overline{g^{(2)}(0)} = \frac{2P(2) + 6P(3)}{\langle n_{\text{out}}\rangle^2} \tag{4.18b}$$

$$\overline{g^{(3)}(0,0)} = \frac{6P(3)}{\langle n_{\text{out}}\rangle^3} \tag{4.18c}$$

Including the normalization of probabilities:

$$1 = \sum_{n=0}^{3} P(n) = P(0) + P(1) + P(2) + P(3) \tag{4.18d}$$

we obtain a system of four equations which can be solved to obtain the values of $P(n)$ for $n = 0, 1, 2, 3$, starting from the experimental values of $\overline{\langle n_{\text{out}}\rangle}$, $\overline{g^{(2)}(0)}$ and $\overline{g^{(3)}(0,0)}$.

This analysis has been performed for the three experimental measurements shown in Fig.4.13.a-c. The corresponding photon number distributions are plotted in Fig.4.14.a-c, respectively for $\langle n_{in}\rangle = 0.5$, 1 and 2.4. Each plot shows the photon number distribution for the incident field, calculated from a Poisson distribution having average photon number $\langle n_{in}\rangle$, with red bars. The photon number distribution for the reflected field, calculated using the set of equations 4.18, is shown with blue bars. For each measurement, the output photon number distribution determine the output average photon number $\langle n_{out}\rangle$, which are calculated to be 0.2, 0.5 and 0.7. Having the values of $\langle n_{out}\rangle$, we also calculated a corresponding Poisson distribution of photon, plotted with black circles.

For the lowest excitation power, Fig.4.14.a, the measured output photon distribution (blue bars) strongly deviates from a Poisson distribution (black circles), showing that the QD-cavity device is efficiently modifying the light statistics. Compared to the input field, we observe a slight increase of the vacuum component, $P_{\text{out}}(0)/P_{\text{in}}(0) \approx 1.2$, and a decrease of the one photon component, $P_{\text{out}}(1)/P_{\text{in}}(1) \approx 0.7$ compatible with the measured $\eta_{\text{out}} = 0.64$. On the contrary, we have a strong suppression of the two and three photons components, respectively of $P_{\text{out}}(2)/P_{\text{in}}(2) \approx 0.2$ and $P_{\text{out}}(3)/P_{\text{in}}(3) \approx 0.04$. Going towards higher excitation powers, as shown in Fig.4.14.b and Fig.4.14.c, the vacuum component increases and the output photon distribution is approaching a Poisson statistics, due to the progressive saturation of the exciton transition.

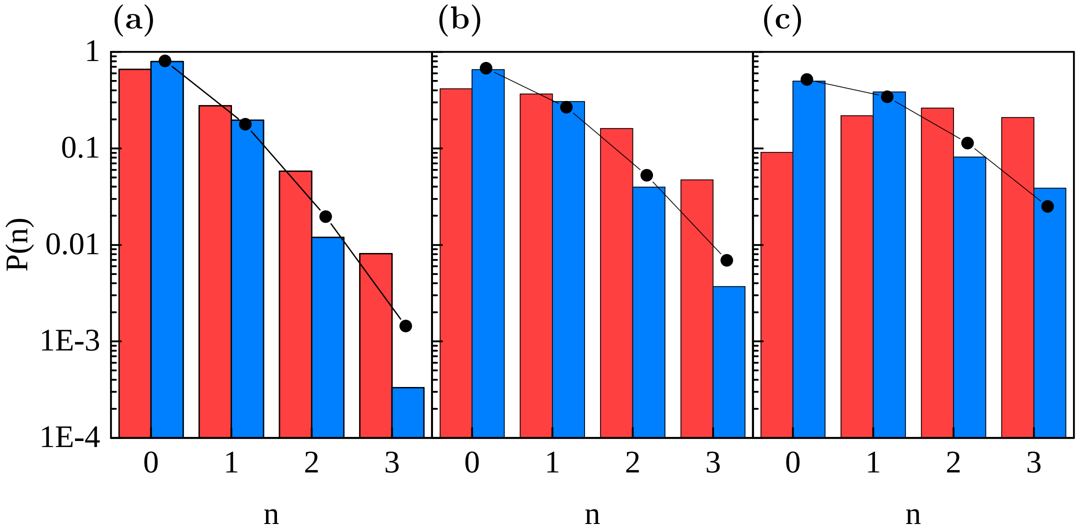

Figure 4.14 – Photon number distribution of the incident field (red bars) and reflected field (blue bars) for an average incident photon number of 0.55 (a), 1 (b) and 2.4 (c). Black dots shows the equivalent Poisson distribution for the reflected field.

These results demonstrate that, when the QD is not saturated, the device is performing as an excellent multi-photon state suppressor, preferentially filtering single photons and transforming the incident coherent light into a pulse showing a highly non-classical statistics.

4.7 Conclusions and perspectives

In this chapter, we have demonstrated that the QD-micropillar device shows a state of the art nonlinear threshold of only 0.3 average incident photon per excitation pulse. In addition to this, we have observed a dominant single photon contribution to the directly reflected intensity, showing that the device implements an efficient single photon Fock state filter, represented in Fig.4.15.a. The two-level system inside the cavity, here excited by laser pulses, only scatters the single photon part of the incident coherent state. We observe in the directly reflected intensity mainly single photons, while the higher Fock components are transmitted though the lateral waveguides [46].

The light-matter interface provided by the QD-micropillar device is ideally suited to realize efficient two-photon gates, which can be done with different approaches. A path encoding gate can be implemented with the neutral exciton state of the QD, as it is the case for this work. In a two pulse scheme, the presence of a first photon is used to switch the response of the cavity such that the second one is reflected. This implementation requires a modification of the current device geometry, in order to collect both the reflected and the transmitted part

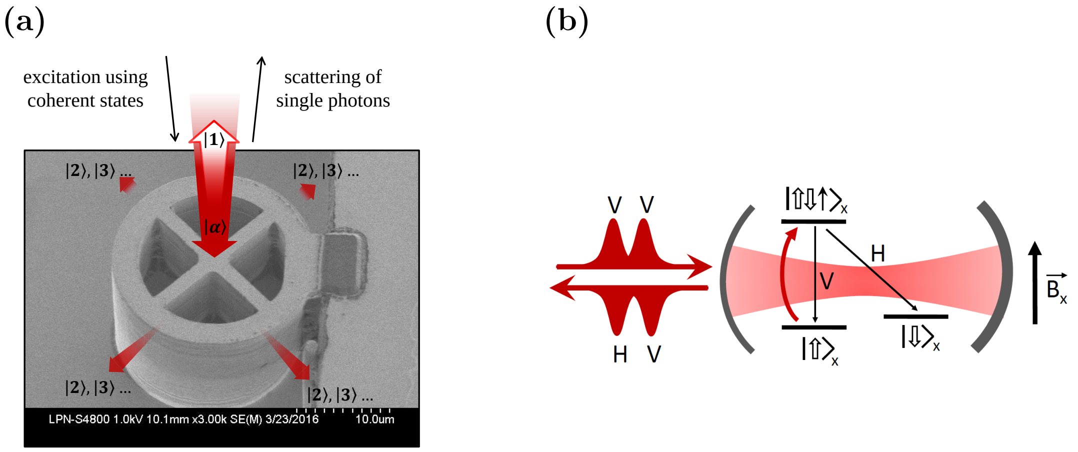

Figure 4.15 – (a) Schematic of the filtering of single photon Fock states with a QD-micropillar device. (b) Figure reproduced from [298]. Schematics for the realization of a polarization encoded quantum gate using a charge exciton state coupled to a micropillar cavity.

of the field. Right now, the analysis of the cavity losses shows dominant losses though the 4 lateral waveguides. As a result, the four ridges can be replaced by a single one coupled to the cavity, where most of the light that is not reflected will be directed. It can be done with the same fabrication technology currently used, and no major roadblock is expected. However, such path encoding gate based on the photon blockade of a two-level system is inherently limited to a 64% efficiency [294], as we have explained in Section.4.4.3, due to the fact that the effective interaction between photon is restricted within the radiative lifetime of the QD exciton state.

A deterministic gate can be obtained instead by using the spin of an additional charge carrier trapped into the QD, to realize a polarization encoding two-photon gate [294, 317, 318]. This does not require a change of geometry, but the spin-selective transitions of the four level system provided by a charged exciton state. By applying a transverse magnetic field, is possible to slightly lift the degeneracy of the CX states, in order to obtain a Λ configuration showing an H and a V polarized transitions. This is represented in Fig.4.15.b, where we also consider the two transitions to be equally accelerated by the cavity, and an output coupling efficiency $\eta_{\text{out}} = 1$, such that every emitted photon is exiting from the top port. By sending a V polarized photon, having the QD initially in the $|\Uparrow\rangle$ state, will lead to the reflection of an H polarized photon, leaving the QD in the $|\Downarrow\rangle$ state. This mechanism, called single-photon Raman interaction, swaps the ground state of the QD and the polarization state of the photon [319, 320, 321]. Once the QD is in the $|\Downarrow\rangle$ state, an incident V polarized photon will be directly reflected, as it cannot interact with the QD.

This mechanism can be used to realize deterministic spin-photon and photon-

photon gates. The deterministic insertion of a resident spin in the QD can be realized by engineering the doping profile in the structure [322]. The QD-micropillar device provides the required efficient light-matter interface to achieve a high input and output coupling efficiency, as well as a state of the art cooperativity. Efficient photon-photon gates can be realized by combining these techniques in micron-sized device, a fundamental step towards the realization of deterministic gates.

Chapter 5

Conclusions and perspectives

Single photons are a central resource for many applications in quantum computation, communication and metrology. Advances in these fields rely on the improvement of the techniques for the generation, manipulation and detection of single photons. Additionally, the interfacing of single photons with material quantum systems is a fundamental step for the distribution of the quantum information across a network. A promising strategy is the use of cavity quantum electrodynamics effects to control the interaction between a single atom and a single photon, in order to realize efficient sources and gates. This has been largely studied also in the solid state, to interface an artificial atom with the propagating photons in a scalable platforms, benefiting for instance from semiconductor technology.

In this work, we have shown that an optimal light-matter interface can be provided by an electrically controlled QD-micropillar device. We have seen that such device allows to obtain a state of the art cooperativity, as high as $C = 14$, corresponding to a mode coupling $\beta \approx 0.93 - 0.98$, as well as very high input and output coupling efficiencies respectively in the range of $\eta_{\text{in}} \approx 0.90 - 0.95$ and $\eta_{\text{out}} \approx 0.65 - 0.70$. We have reached a regime very close to the 1-dimensional atom situation, which allows the QD-micropillar device to optimally perform both as an emitter and as a receiver of single photons. Its efficiency as an emitter has been presented in Chapter 2, with the demonstration of a bright source of fully indistinguishable single photons. The efficiency of the device as a receiver has been presented in Chapter 4, where we have demonstrated a nonlinear optical response at the level of a single incident photon. Additionally, we used the single photons emitted by the source to generate a path entangled NOON state and we have proposed a novel technique to reconstruct its full density matrix, as shown in Chapter 3.

The availability of bright sources of single photons can find immediate applications for quantum computation and communication [48]. In 2017, intermediate computation protocols such as boson sampling have been shown to benefit from orders of magnitude efficiency improvement using QD-based sources [221, 222]. High efficiency sources can also be used to boost QKD protocols [323], and are required to produce multi-photon entangled states. For instance, the generation of large cluster states could allow to implement measurement-based quantum computing protocols [324], and with a large improvement in the source efficiency, even all-optical quantum repeaters [325]. A technical limitation for the transfer of photons is given by the relatively high losses of standard telecom fibres at wavelengths around 900 nm, corresponding to the emission typically observed from InGaAs QDs. Recently however, the efficient quantum frequency conversion to telecom wavelength (1.3 and 1.5 μm) has been demonstrated [326, 327], an important achievement towards the use of the available optical fiber infrastructures for long distance quantum communications.

Beside computation and communication, multi-photon entangled states are interesting resources also for metrology. Notably, path entangled NOON states can be used in interferometric protocols to perform Heisenberg-limited sensing. High NOON states could be realized using the interference of coherent states and Fock states on a beam splitter [263]. An important aspect in this case, is the certification of the generation of a maximally entangled state, up to now limited to the observation of super-resolved fringes. As shown in Chapter 3, the tomography technique reported in this work could be extended to higher photon numbers using PNR detectors. This can gives a viable way to perform the tomography of two-path NOON states for high photon numbers.

The QD-micropillar system represents also a promising building block to realize a quantum network. While an efficient light-matter interface has been demonstrated here, additional requirements are needed to implemented a scalable network [14]. A first step towards this objective is the fabrication of multiple devices showing their optical transitions at a same energy. This gives the possibility of interfacing different devices as well as combining multiple solid-state single-photon sources in a same multi-photon experiment, which could boost its performances beyond what can be obtained by demultiplexing the photons emitted by a single source. The fabrication of identical devices is mostly limited by the inhomogeneous broadening of the QDs resulting from the self-assembly fabrication method. The in-situ lithography currently employed already allows the deterministic coupling of a single micropillar cavity to a specific QD, both spatially and also spectrally with a precision of $\Delta\lambda = 0.5$ nm. The electrical control is further used to finely adjust the transition energy of the QD, allowing the exact spectral matching between the emitter and the cavity. However, no active control of the optical mode of the cavity is possible after its fabrication, and the resulting devices shows different transition energies, depending on the specific QD targeted during the fabrication phase. To interface multiple devices, a first strategy is to fabricate all the micropillars with the same diameter. The QD energies can then be tuned with the electrical control so to match the cavity

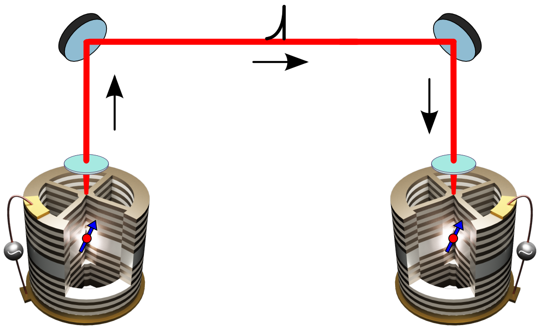

Figure 5.1 – Realization of a simple network using the QD-micropillar device both as an emitter and as a receiver.

modes. Alternatively, piezoelectric actuators can be used to apply strain to the micropillars, so to controllably modify both the QD and the cavity mode energy. This, together with the electrical contacts, allows the independent tuning of the cavity and of the QD energy. Multiple devices can then be connected using the single photon Fock state emitted by a QD to excite another one. This allows to realize cascaded quantum systems and study the interaction of a two-level system with a quantum light state [328, 329, 35]. Additionally, it can be used to test the feasibility of a larger scale network of QD-micropillar devices.

A second fundamental step is the control of the charge state of the QD. Using a trion state instead of a neutral exciton state allows to increase the efficiency of the device. On one side, this will improve the brightness of the device as a single photon source, since it overcomes the limitations due to the polarization rotation process, as described in Section 2.6.3. On the other side, it would allow to overcome the limitations of a quantum gate based on a two-level system, as explained in Section 4.4.3. The four level system provided by the spin-selective transitions of the trion state can be used to implement a polarization encoded gate, which can be fully deterministic [294]. To place an additional charge carrier in the QD, the doping profile can be engineered to define a potential barrier for the holes, in such a way that the application of a bias will favour the tunneling out of the QD of the electrons only [322]. This can be used to create a positively charged trion and benefit from the relatively long coherence time of the hole spin [71]. To complete the in-situ fabrication however, the bias must be applied during the lithography step, in order to correctly identify the spectral position of the charged exciton state at a non zero applied bias. This requires a modification of the fabrication process, where the gates will be defined after the growth of the planar cavity. Once the charge state of the QD can be controlled, the spin of the additional charge can be used as a stationary qubit, which can be optimally interfaced to the propagating photons thanks to the micropillar cavity. Such device can be used to realize efficient spin-photon entangling gates [33, 32], generate cluster states through the repeated interactions of independent photons with a single spin [317]. Finally, by connecting different devices, it is also possible to distribute the entanglement between distant spins [35]. Note that it has been recently shown that it is possible to improve the coherence time of the electron or hole spin in the QD by manipulating the underlying nuclear spin bath [330, 331, 332]. Such extended coherence time of the stationary qubit is an important step towards the implementation of memory-based quantum repeaters [333].

Overall, the QD-micropillar devices show great potential to implement key functionalities for the development of a scalable quantum network in the solid-state.

List of publications

- **Overcomplete quantum tomography of a path-entangled two-photon state**
  L. De Santis, G. Coppola, C. Antón, N. Somaschi, C. Gómez, A. Lemaître, I. Sagnes, L. Lanco, J. Loredo, O. Krebs and P. Senellart.
  ArXiv:1707.07837 (2017)

- **Reducing phonon-induced decoherence in solid-state single-photon sources with cavity quantum electrodynamics**
  T. Grange, N. Somaschi, C. Antón, L. De Santis, G. Coppola, V. Giesz, A. Lemaître, I. Sagnes, A. Auffèves, P. Senellart.
  Physical Review Letters **118**, 253602 (2017)

- **A solid-state single-photon filter**
  L. De Santis, C. Antón, B. Reznychenko, N. Somaschi, G. Coppola, J. Senellart, C. Gómez, A. Lemaître, I. Sagnes, A. G. White, L. Lanco, A. Auffèves and P. Senellart.
  Nature Nanotechnology **12**, 663–667 (2017)

- **Scalable performance in solid-state single-photon source**
  J. C. Loredo, N. A. Zakaria, N. Somaschi, C. Antón, L. De Santis, V. Giesz, T. Grange, M. A. Broome, O. Gazzano, G. Coppola, I. Sagnes, A. Lemaître, A. Auffèves, P. Senellart, M. P. Almeida, and A. G. White.
  Optica **3**, 433-440 (2016)

- **Coherent manipulation of a solid-state artificial atom with few photons**
  V. Giesz, N. Somaschi, G. Hornecker, T. Grange, B. Reznychenko, L. De Santis, J. Demory, C. Gómez, I. Sagnes, A. Lemaître, O. Krebs, N. D. Lanzillotti-Kimura, L. Lanco, A. Auffèves and P. Senellart.
  Nature Communications **7**, 11986 (2016)

- **Near-optimal single-photon sources in the solid state**
  N. Somaschi*, V. Giesz*, L. De Santis*, J. C. Loredo, M. P. Almeida, G. Hornecker, S. L. Portalupi, T. Grange, C. Antón, J. Demory, C. Gómez, I. Sagnes, N. D. Lanzillotti-Kimura, A. Lemaître, A. Auffèves, A. G. White, L. Lanco and P. Senellart. *Equally contributing authors.
  Nature Photonics **10**, 340–345 (2016)

- **Cavity-enhanced two-photon interference using remote quantum dot sources**
  V. Giesz, S. L. Portalupi, T. Grange, C. Antón, L. De Santis, J. Demory, N. Somaschi, I. Sagnes, A. Lemaître, L. Lanco, A. Auffèves and P. Senellart.
  Phys. Rev. B **92**, 161302(R) (2015)

Bibliography

[1] J. P. Dowling and G. J. Milburn. Quantum technology: the second quantum revolution. *Philosophical Transactions of the Royal Society A: Mathematical, Physical and Engineering Sciences*, 361(1809):1655–1674, 2003.

[2] Richard P. Feynman. Simulating physics with computers. *International Journal of Theoretical Physics*, 21(6-7):467–488, 1982.

[3] Seth Lloyd. Universal Quantum Simulators. *Science*, 273(5278):1073–1078, aug 1996.

[4] Thaddeus D. Ladd, Fedor Jelezko, Raymond Laflamme, Yasunobu Nakamura, Christopher Monroe, and J. L. O'Brien. Quantum computers. *Nature*, 464(7285):45–53, mar 2010.

[5] Michael a. Nielsen, Isaac L. Chuang, and Daniel F. V. James. Quantum Computation and Quantum Information. In *Physics Today*, volume 54, page 60. 2001.

[6] I. M. Georgescu, S. Ashhab, and Franco Nori. Quantum simulation. *Reviews of Modern Physics*, 86(1):153–185, 2014.

[7] Vittorio Giovannetti, Seth Lloyd, and Lorenzo Maccone. Quantum Metrology. *Physical Review Letters*, 96(1):010401, jan 2006.

[8] Nicolas Gisin and Rob Thew. Quantum communication. *Nat Photon*, 1(3):165–171, 2007.

[9] Eleni Diamanti, Hoi-Kwong Lo, Bing Qi, and Zhiliang Yuan. Practical challenges in quantum key distribution. *Nature Publishing Group*, (May):1–12, 2016.

[10] P. Schindler, M. Müller, D. Nigg, J. T. Barreiro, E. A. Martinez, M. Hennrich, T. Monz, S. Diehl, P. Zoller, and R. Blatt. Quantum simulation of dynamical maps with trapped ions. *Nature Physics*, 9(6):361–367, 2013.

[11] R. Barends, L. Lamata, J. Kelly, L. García-Álvarez, A. G. Fowler, A. Megrant, E. Jeffrey, T. C. White, D. Sank, J. Y. Mutus, B. Campbell, Yu Chen, Z. Chen, B. Chiaro, A. Dunsworth, I.-C. Hoi, C. Neill, P. J. J. O'Malley, C. Quintana, P. Roushan, A. Vainsencher, J. Wenner, E. Solano, and John M. Martinis. Digital quantum simulation of fermionic models with a superconducting circuit. *Nature Communications*, 6:7654, jul 2015.

[12] Xi-Lin Wang, Luo-Kan Chen, W. Li, H.-L. Huang, C. Liu, C. Chen, Y.-H. Luo, Z.-E. Su, D. Wu, Z.-D. Li, H. Lu, Y. Hu, X. Jiang, C.-Z. Peng, L. Li, N.-L. Liu, Yu-Ao Chen, Chao-Yang Lu, and Jian-Wei Pan. Experimental Ten-Photon Entanglement. *Physical Review Letters*, 117(21):210502, nov 2016.

[13] Gershon Kurizki, Patrice Bertet, Yuimaru Kubo, Klaus Mølmer, David Petrosyan, Peter Rabl, and Jörg Schmiedmayer. Quantum technologies with hybrid systems. *Proceedings of the National Academy of Sciences*, 112(13):3866–3873, mar 2015.

[14] H. J. Kimble. The quantum internet. *Nature*, 453(7198):1023–1030, jun 2008.

[15] Chandra M Natarajan, Michael G Tanner, and Robert H Hadfield. Superconducting nanowire single-photon detectors: physics and applications. *Superconductor Science and Technology*, 25(6):063001, jun 2012.

[16] J. L. O'Brien, G. J. Pryde, A. G. White, T. C. Ralph, and D. Branning. Demonstration of an all-optical quantum controlled-NOT gate. *Nature*, 426(6964):264–7, nov 2003.

[17] Jeremy L. O'Brien, Akira Furusawa, and Jelena Vučković. Photonic quantum technologies. *Nature Photonics*, 3(12):687–695, dec 2009.

[18] D. Valente, Y. Li, J. P. Poizat, J. M. Gérard, L. C. Kwek, M. F. Santos, and A. Auffèves. Universal optimal broadband photon cloning and entanglement creation in one-dimensional atoms. *Physical Review A*, 86(2):022333, aug 2012.

[19] Stephan Ritter, Christian Nölleke, Carolin Hahn, Andreas Reiserer, Andreas Neuzner, Manuel Uphoff, Martin Mücke, Eden Figueroa, Joerg Bochmann, and Gerhard Rempe. An elementary quantum network of single atoms in optical cavities. *Nature*, 484(7393):195–200, apr 2012.

[20] V. Giesz, N. Somaschi, G. Hornecker, T. Grange, B. Reznychenko, L. De Santis, J. Demory, C. Gomez, I. Sagnes, A. Lemaître, O. Krebs, N. D. Lanzillotti-Kimura, L. Lanco, A. Auffeves, and P. Senellart. Coherent

manipulation of a solid-state artificial atom with few photons. *Nature Communications*, 7(May):11986, jun 2016.

[21] Peter Lodahl, Sahand Mahmoodian, and Søren Stobbe. Interfacing single photons and single quantum dots with photonic nanostructures. *Reviews of Modern Physics*, 87(2):347–400, may 2015.

[22] I. Shomroni, S. Rosenblum, Y. Lovsky, O. Bechler, G. Guendelman, and B. Dayan. All-optical routing of single photons by a one-atom switch controlled by a single photon. *Science*, 345(6199):903–906, aug 2014.

[23] Andreas Reiserer, Norbert Kalb, Gerhard Rempe, and Stephan Ritter. A quantum gate between a flying optical photon and a single trapped atom. *Nature*, 508(7495):237–240, apr 2014.

[24] T E Northup and R Blatt. Quantum information transfer using photons. 8(5):356–363, 2014.

[25] Julien Claudon, Joël Bleuse, Nitin Singh Malik, Maela Bazin, Périne Jaffrennou, Niels Gregersen, Christophe Sauvan, Philippe Lalanne, and Jean Michel Gérard. A highly efficient single-photon source based on a quantum dot in a photonic nanowire. *Nature Photonics*, 4(3):174–177, 2010.

[26] Thomas M. Babinec, Birgit J. M. Hausmann, Mughees Khan, Yinan Zhang, Jeronimo R. Maze, Philip R. Hemmer, and Marko Lončar. A diamond nanowire single-photon source. *Nature Nanotechnology*, 5(3):195–199, 2010.

[27] J. Y. Y. Marzin, J. M. M. Gérard, A. Izraël, D. Barrier, and G. Bastard. Photoluminescence of single InAs quantum dots obtained by self-organized growth on GaAs. *Physical Review Letters*, 73(5):716–719, aug 1994.

[28] G. S. Solomon, M. Pelton, and Y. Yamamoto. Single-mode Spontaneous Emission from a Single Quantum Dot in a Three-Dimensional Microcavity. *Physical Review Letters*, 86(17):3903–3906, apr 2001.

[29] P Michler, A Kiraz, C Becher, W V Schoenfeld, P M Petroff, L Zhang, E Hu, and A Imamoglu. A quantum dot single-photon turnstile device. *Science (New York, N.Y.)*, 290(5500):2282–5, dec 2000.

[30] Kartik Srinivasan and Oskar Painter. Linear and nonlinear optical spectroscopy of a strongly coupled microdisk-quantum dot system. *Nature*, 450(7171):862–865, 2007.

[31] David Press, Thaddeus D. Ladd, Bingyang Zhang, and Yoshihisa Yamamoto. Complete quantum control of a single quantum dot spin using ultrafast optical pulses. *Nature*, 456(7219):218–221, 2008.

[32] Kristiaan De Greve, Leo Yu, Peter L. McMahon, Jason S. Pelc, Chandra M. Natarajan, Na Young Kim, Eisuke Abe, Sebastian Maier, Christian Schneider, Martin Kamp, Sven Höfling, Robert H. Hadfield, Alfred Forchel, M. M. Fejer, and Yoshihisa Yamamoto. Quantum-dot spin-photon entanglement via frequency downconversion to telecom wavelength. *Nature*, 491(7424):421–425, 2012.

[33] W B Gao, P Fallahi, E Togan, J Miguel-Sanchez, and a Imamoglu. Observation of entanglement between a quantum dot spin and a single photon. *Nature*, 491(7424):426–30, 2012.

[34] J. R. Schaibley, A. P. Burgers, G. A. McCracken, L. M. Duan, P. R. Berman, D. G. Steel, A. S. Bracker, D. Gammon, and L. J. Sham. Demonstration of quantum entanglement between a single electron spin confined to an InAs quantum dot and a photon. *Physical Review Letters*, 110(16), 2013.

[35] Aymeric Delteil, Zhe Sun, Wei-bo Gao, Emre Togan, Stefan Faelt, and Atac Imamoglu. Generation of heralded entanglement between distant hole spins. *Nature Physics*, 12(3):218–223, mar 2016.

[36] O. Gazzano, S. Michaelis De Vasconcellos, K. Gauthron, C. Symonds, J. Bloch, P. Voisin, J. Bellessa, A. Lemaître, and P. Senellart. Evidence for confined Tamm plasmon modes under metallic microdisks and application to the control of spontaneous optical emission. *Physical Review Letters*, 107(24), 2011.

[37] M. Gschrey, A. Thoma, P. Schnauber, M. Seifried, R. Schmidt, B. Wohlfeil, L. Krüger, J. H. H. Schulze, T. Heindel, S. Burger, F. Schmidt, A. Strittmatter, S. Rodt, and S. Reitzenstein. Highly indistinguishable photons from deterministic quantum-dot microlenses utilizing three-dimensional in situ electron-beam lithography. *Nature Communications*, 6(May):7662, jul 2015.

[38] A. Dousse, L. Lanco, J. Suffczyński, E. Semenova, A. Miard, A. Lemaître, I. Sagnes, C. Roblin, J. Bloch, and P. Senellart. Controlled Light-Matter Coupling for a Single Quantum Dot Embedded in a Pillar Microcavity Using Far-Field Optical Lithography. *Physical Review Letters*, 101(26):267404, dec 2008.

[39] A. Dousse, J. Suffczyński, R. Braive, A. Miard, A. Lemàtre, I. Sagnes, L. Lanco, J. Bloch, P. Voisin, and P. Senellart. Scalable implementation

of strongly coupled cavity-quantum dot devices. *Applied Physics Letters*, 94(12), 2009.

[40] Adrien Dousse, Jan Suffczyński, Alexios Beveratos, Olivier Krebs, Aristide Lemaître, Isabelle Sagnes, Jacqueline Bloch, Paul Voisin, and Pascale Senellart. Ultrabright source of entangled photon pairs. *Nature*, 466(7303):217–220, 2010.

[41] O. Gazzano, S. Michaelis de Vasconcellos, C. Arnold, A. Nowak, E. Galopin, I. Sagnes, L. Lanco, A. Lemaître, and P. Senellart. Bright solid-state sources of indistinguishable single photons. *Nature communications*, 4:1425, jan 2013.

[42] O. Gazzano, M. P. Almeida, A. K. Nowak, S. L. Portalupi, A. Lemaître, I. Sagnes, A. G. White, and P. Senellart. Entangling Quantum-Logic Gate Operated with an Ultrabright Semiconductor Single-Photon Source. *Physical Review Letters*, 110(25):250501, jun 2013.

[43] V. Giesz, S. L. Portalupi, T. Grange, C. Antón, L. De Santis, J. Demory, N. Somaschi, I. Sagnes, A. Lemaître, L. Lanco, A. Auffèves, and P. Senellart. Cavity-enhanced two-photon interference using remote quantum dot sources. *Physical Review B*, 92(16):161302, oct 2015.

[44] N Somaschi, V Giesz, L. De Santis, J C Loredo, M P Almeida, G Hornecker, S. L. Portalupi, T. Grange, C. Antón, J. Demory, C. Gómez, I. Sagnes, N. D. Lanzillotti-Kimura, A. Lemaítre, A. Auffeves, A. G. White, L. Lanco, and P. Senellart. Near-optimal single-photon sources in the solid state. *Nature Photonics*, 10(5):340–345, mar 2016.

[45] L. De Santis, G. Coppola, C. Antón, N. Somaschi, C. Gómez, A. Lemaître, I. Sagnes, L. Lanco, J. C. Loredo, O. Krebs, and P. Senellart. Overcomplete quantum tomography of a path-entangled two-photon state. *arXiv preprint*, 1707.07837, jul 2017.

[46] Lorenzo De Santis, Carlos Antón, Bogdan Reznychenko, Niccolo Somaschi, Guillaume Coppola, Jean Senellart, Carmen Gómez, Aristide Lemaître, Isabelle Sagnes, Andrew G. White, Loïc Lanco, Alexia Auffèves, and Pascale Senellart. A solid-state single-photon filter. *Nature Nanotechnology*, 12(7):663–667, may 2017.

[47] R. C. Ashoori. Electrons in artificial atoms. *Nature*, 379(6564):413–419, feb 1996.

[48] Igor Aharonovich, Dirk Englund, and Milos Toth. Solid-state single-photon emitters. *Nature Photonics*, 10(10):631–641, sep 2016.

[49] A Imamoglu, Dd Awschalom, G Burkard, D P DiVincenzo, D Loss, M Sherwin, and A Small. Quantum information processing using quantum dot spins and cavity QED. *Physical Review Letters*, 83(20):4204–4207, 1999.

[50] Ernst Bauer. Phänomenologische Theorie der Kristallabscheidung an Oberflächen. I. *Zeitschrift für Kristallographie*, 110(1-6):372–394, jan 1958.

[51] V. A. Shchukin, N. N. Ledentsov, P. S. Kop'ev, and D Bimberg. Spontaneous Ordering of Arrays of Coherent Strained Islands. *Physical Review Letters*, 75(16):2968–2971, oct 1995.

[52] L Goldstein, F Glas, J Y Marzin, M N Charasse, and G Le Roux. Growth by mo ˜ ecu ! ar beam epijtaxy and characterizatuon oflnAs / GaAs strained-layer superlattices. *Applied Physics Letters*, 47(November):1099–1101, 1985.

[53] D Leonard, M Krishnamurthy, C M Reaves, S P Denbaars, and P M Petroff. Direct formation of quantum-sized dots from uniform coherent islands of InGaAs on GaAs surfaces. *Applied Physics Letters*, 63(23):3203–3205, dec 1993.

[54] S Fafard, D Leonard, J L Merz, and P M Petroff. Selective excitation of the photoluminescence and the energy levels of ultrasmall InGaAs/GaAs quantum dots. *Applied Physics Letters*, 65(11):1388–1390, sep 1994.

[55] G. S. Solomon, J. A. Trezza, and J. S. Harris. Effects of monolayer coverage, flux ratio, and growth rate on the island density of InAs islands on GaAs. *Applied Physics Letters*, 66(23):3161–3163, jun 1995.

[56] D. Bimberg, M. Grundmann, and NN Ledentsov. *Quantum dot Heterostructures,*. John Wiley & Sons, 1999.

[57] M.I. Dyakonov. *Spin Physics in Semiconductors*, volume 157 of *Springer Series in Solid-State Sciences*. Springer Berlin Heidelberg, Berlin, Heidelberg, 2008.

[58] Fb Pedersen and Yc Chang. Energy levels of one and two holes in parabolic quantum dots. *Physical review. B*, 53(3):1507, 1996.

[59] Eliana Biolatti, Irene D'Amico, Paolo Zanardi, and Fausto Rossi. Electro-optical properties of semiconductor quantum dots: Application to quantum information processing. *Physical Review B*, 65(7):075306, jan 2002.

[60] Alberto Franceschetti and Alex Zunger. Direct Pseudopotential Calculation of Exciton Coulomb and Exchange Energies in Semiconductor Quantum Dots. *Physical Review Letters*, 78(5):915–918, 1997.

[61] T. Takagahara. Theory of exciton doublet structures and polarization relaxation in single quantum dots. *Physical Review B*, 62(24):16840–16855, dec 2000.

[62] P. Michler. *Single Quantum Dots: Fundamentals, Applications, and New Concepts*, volume 90 of *Topics in Applied Physics*. Springer Berlin Heidelberg, Berlin, Heidelberg, 2003.

[63] a. J. Bennett, M. a. Pooley, R. M. Stevenson, M. B. Ward, R. B. Patel, A. Boyer de la Giroday, N. Sköld, I. Farrer, C. A. Nicoll, D. a. Ritchie, and a. J. Shields. Electric-field-induced coherent coupling of the exciton states in a single quantum dot. *Nature Physics*, 6(12):947–950, dec 2010.

[64] R. Trotta, E. Zallo, C. Ortix, P. Atkinson, J. D. Plumhof, J. Van Den Brink, A. Rastelli, and O. G. Schmidt. Universal recovery of the energy-level degeneracy of bright excitons in ingaas quantum dots without a structure symmetry. *Physical Review Letters*, 109(14):1–5, 2012.

[65] Oliver Benson, Charles Santori, Matthew Pelton, and Yoshihisa Yamamoto. Regulated and Entangled Photons from a Single Quantum Dot. *Physical Review Letters*, 84(11):2513–2516, 2000.

[66] N. Akopian, N. H. Lindner, E. Poem, Y. Berlatzky, J. Avron, D. Gershoni, B. D. Gerardot, and P. M. Petroff. Entangled photon pairs from semiconductor quantum dots. *Physical Review Letters*, 96(13):7–10, 2006.

[67] Robert J. Young, R. Mark Stevenson, Paola Atkinson, Ken Cooper, David A. Ritchie, and Andrew J. Shields. Improved fidelity of triggered entangled photons from single quantum dots. *New Journal of Physics*, 8, 2006.

[68] Takashi Kuroda, Takaaki Mano, Neul Ha, Hideaki Nakajima, Hidekazu Kumano, Bernhard Urbaszek, Masafumi Jo, Marco Abbarchi, Yoshiki Sakuma, Kazuaki Sakoda, Ikuo Suemune, Xavier Marie, and Thierry Amand. Symmetric quantum dots as efficient sources of highly entangled photons: Violation of Bell's inequality without spectral and temporal filtering. *Physical Review B - Condensed Matter and Materials Physics*, 88(4):3–7, 2013.

[69] Jiaxiang Zhang, Johannes S. Wildmann, Fei Ding, Rinaldo Trotta, Yongheng Huo, Eugenio Zallo, Daniel Huber, Armando Rastelli, and Oliver G. Schmidt. High yield and ultrafast sources of electrically triggered entangled-photon pairs based on strain-tunable quantum dots. *Nature Communications*, 6:1–7, 2015.

[70] Xiaodong Xu, Yanwen Wu, Bo Sun, Qiong Huang, Jun Cheng, D. G. Steel, A. S. Bracker, D. Gammon, C. Emary, and L. J. Sham. Fast spin state initialization in a singly charged InAs-GaAs quantum dot by optical cooling. *Physical Review Letters*, 99(9):1–4, 2007.

[71] Brian D. Gerardot, Daniel Brunner, Paul A. Dalgarno, Patrik Öhberg, Stefan Seidl, Martin Kroner, Khaled Karrai, Nick G. Stoltz, Pierre M. Petroff, and Richard J. Warburton. Optical pumping of a single hole spin in a quantum dot. *Nature*, 451(7177):441–444, 2008.

[72] Susan M. Clark, Kai Mei C. Fu, Thaddeus D. Ladd, and Yoshihisa Yamamoto. Quantum computers based on electron spins controlled by ultrafast off-resonant single optical pulses. *Physical Review Letters*, 99(4):2–5, 2007.

[73] Richard J. Warburton. Single spins in self-assembled quantum dots. *Nature Materials*, 12(6):483–493, 2013.

[74] Ren-Bao Liu, Wang Yao, and L.J. Sham. Quantum computing by optical control of electron spins. *Advances in Physics*, 59(5):703–802, 2010.

[75] E. Moreau, I. Robert, L. Manin, V. Thierry-Mieg, J. M. Gérard, and I. Abram. Quantum Cascade of Photons in Semiconductor Quantum Dots. *Physical Review Letters*, 87(18):183601, 2001.

[76] Charles Santori, Matthew Pelton, Glenn Solomon, Yseulte Dale, and Yoshihisa Yamamoto. Triggered Single Photons from a Quantum Dot. *Physical Review Letters*, 86(8):1502–1505, feb 2001.

[77] A. Kiraz, S. Fälth, C. Becher, B. Gayral, W. V. Schoenfeld, P. M. Petroff, Lidong Zhang, E. Hu, and A. Imamoğlu. Photon correlation spectroscopy of a single quantum dot. *Physical Review B*, 65(16):161303, 2002.

[78] C. Schulhauser, A. Högele, R. J. Warburton, A. O. Govorov, W. Schoenfeld, J. M. Garcia, P. M. Petroff, and K. Karrai. Magnetic properties of charged excitons in self-assembled quantum dots. *Physica Status Solidi (B) Basic Research*, 238(2):293–296, 2003.

[79] Adam Babinski, S. Awirothananon, J. Lapointe, Z. Wasilewski, S. Raymond, and M. Potemski. Single-dot spectroscopy in high magnetic fields. *Physica E: Low-dimensional Systems and Nanostructures*, 26(1-4):190–193, feb 2005.

[80] V. Weisskopf and E. Wigner. Berechnung der naturlichen Linienbreite auf Grund der Diracschen Lichttheorie. *Zeitschrift fur Physik*, 63(1-2):54–73, jan 1930.

[81] L A Khalfin. Contribution to the decay theory of a quasi-stationary state. *Soviet Phys. JETP*, 6(33):1053, 1958.

[82] L. Fonda, G. C. Ghirardi, and A. Rimini. Decay theory of unstable quantum systems. *Reports on Progress in Physics*, 41(4):587–631, apr 1978.

[83] Daniel Adam Steck. *Quantum and Atom Optics.* 2007.

[84] Gilbert Grynberg, Alain Aspect, and Claude Fabre. *Introduction to Quantum Optics: From the Semi-classical Approach to Quantized Light.* Cambridge University Press, 2010.

[85] X. Brokmann, L. Coolen, M. Dahan, and J. P. Hermier. Measurement of the radiative and nonradiative decay rates of single CdSe nanocrystals through a controlled modification of their spontaneous emission. *Physical Review Letters*, 93(10):1–4, 2004.

[86] Jeppe Johansen, Søren Stobbe, Ivan S. Nikolaev, Toke Lund-Hansen, Philip T. Kristensen, Jørn M. Hvam, Willem L. Vos, and Peter Lodahl. Size dependence of the wavefunction of self-assembled InAs quantum dots from time-resolved optical measurements. *Physical Review B - Condensed Matter and Materials Physics*, 77(7):1–4, 2008.

[87] A. Kiraz, M. Atatüre, and A. Imamoğlu. Quantum-dot single-photon sources: Prospects for applications in linear optics quantum-information processing. *Physical Review A*, 69(3):032305, mar 2004.

[88] L Allen and J. H. Eberly. *Optical Resonance and Two-Level Atoms*, volume 14. 1978.

[89] D. Gammon, E. S. Snow, B. V. Shanabrook, D. S. Katzer, and D. Park. Homogeneous Linewidths in the Optical Spectrum of a Single Gallium Arsenide Quantum Dot. *Science*, 273(5271):87–90, 1996.

[90] B. Krummheuer, V. M. Axt, and T. Kuhn. Theory of pure dephasing and the resulting absorption line shape in semiconductor quantum dots. *Physical Review B*, 65(19):195313, 2002.

[91] A. J. Ramsay, Achanta Venu Gopal, E. M. Gauger, A. Nazir, B. W. Lovett, A. M. Fox, and M. S. Skolnick. Damping of exciton rabi rotations by acoustic phonons in optically excited InGaAs/GaAs quantum dots. *Physical Review Letters*, 104(1):20–23, 2010.

[92] T. Takaghara and H. Wang. Theory of exciton dephasing in single quantum dots. *Technical Digest. Summaries of Papers Presented at the International Quantum Electronics Conference. Conference Edition. 1998 Technical Digest Series, Vol.7 (IEEE Cat. No.98CH36236)*, 60(4):58–59, 1998.

[93] E. A. Muljarov and R. Zimmermann. Dephasing in quantum dots: Quadratic coupling to acoustic phonons. *Physical Review Letters*, 93(23):1–4, 2004.

[94] L. Besombes, K. Kheng, L. Marsal, and H. Mariette. Acoustic phonon broadening mechanism in single quantum dot emission. *Physical Review B*, 63(15):155307, mar 2001.

[95] I. Favero, G. Cassabois, R. Ferreira, D. Darson, C. Voisin, J. Tignon, C. Delalande, G. Bastard, Ph. Roussignol, and J. M. Gérard. Acoustic phonon sidebands in the emission line of single InAs/GaAs quantum dots. *Physical Review B*, 68(23):233301, 2003.

[96] E. Peter, J. Hours, P. Senellart, A. Vasanelli, A. Cavanna, J. Bloch, and J. M. Gérard. Phonon sidebands in exciton and biexciton emission from single GaAs quantum dots. *Physical Review B*, 69(4):041307, 2004.

[97] N. H. Bonadeo, Gang Chen, D. Gammon, D. S. Katzer, D. Park, and D. G. Steel. Nonlinear Nano-Optics: Probing One Exciton at a Time. *Physical Review Letters*, 81(13):2759–2762, 1998.

[98] P. Borri, W. Langbein, S. Schneider, U. Woggon, R. Sellin, D. Ouyang, and D. Bimberg. Ultralong Dephasing Time in InGaAs Quantum Dots. *Physical Review Letters*, 87(15):157401, sep 2001.

[99] A. J. Ramsay, T. M. Godden, S. J. Boyle, E. M. Gauger, A. Nazir, B. W. Lovett, A. M. Fox, and M. S. Skolnick. Phonon-induced Rabi-frequency renormalization of optically driven single InGaAs/GaAs quantum dots. *Physical Review Letters*, 105(17):1–4, 2010.

[100] T. Grange, N. Somaschi, C. Antón, L. De Santis, G. Coppola, V. Giesz, A. Lemaître, I. Sagnes, A. Auffèves, and P. Senellart. Reducing Phonon-Induced Decoherence in Solid-State Single-Photon Sources with Cavity Quantum Electrodynamics. *Physical Review Letters*, 118(25):253602, jun 2017.

[101] Jake Iles-Smith, Dara P. S. McCutcheon, Ahsan Nazir, and Jesper Mørk. Phonon scattering inhibits simultaneous near-unity efficiency and indistinguishability in semiconductor single-photon sources. *Nature Photonics*, 11(8):521–526, jul 2017.

[102] Tomasz Jakubczyk, Valentin Delmonte, Sarah Fischbach, Daniel Wigger, Doris E. Reiter, Quentin Mermillod, Peter Schnauber, Arsenty Kaganskiy, Jan Hindrik Schulze, André Strittmatter, Sven Rodt, Wolfgang Langbein, Tilmann Kuhn, Stephan Reitzenstein, and Jacek Kasprzak. Impact of Phonons on Dephasing of Individual Excitons in Deterministic Quantum Dot Microlenses. *ACS Photonics*, 3(12):2461–2466, 2016.

[103] K. Kowalik, O. Krebs, P. Senellart, A. Lemaître, B. Eble, A. Kudelski, J. Gaj, and P. Voisin. Stark spectroscopy of Coulomb interactions in individual InAs/GaAs self-assembled quantum dots. *Physica Status Solidi (C) Current Topics in Solid State Physics*, 3(11):3890–3894, 2006.

[104] M. M. Vogel, S. M. Ulrich, R. Hafenbrak, P. Michler, L. Wang, A. Rastelli, and O. G. Schmidt. Influence of lateral electric fields on multiexcitonic transitions and fine structure of single quantum dots. *Applied Physics Letters*, 91(5):051904, jul 2007.

[105] Andreas V. Kuhlmann, Julien Houel, Arne Ludwig, Lukas Greuter, Dirk Reuter, Andreas D. Wieck, Martino Poggio, and Richard J. Warburton. Charge noise and spin noise in a semiconductor quantum device. *Nature Physics*, 9(9):570–575, jul 2013.

[106] Alexander Högele, Stefan Seidl, Martin Kroner, Khaled Karrai, Richard J. Warburton, Brian D. Gerardot, and Pierre M. Petroff. Voltage-controlled optics of a quantum dot. *Physical Review Letters*, 93(21):19–22, 2004.

[107] J. Houel, A. V. Kuhlmann, L. Greuter, F. Xue, M. Poggio, R. J. Warburton, B. D. Gerardot, P. A. Dalgarno, A. Badolato, P. M. Petroff, A. Ludwig, D. Reuter, and A. D. Wieck. Probing single-charge fluctuations at a GaAs/AlAs interface using laser spectroscopy on a nearby InGaAs quantum dot. *Physical Review Letters*, 108(10):1–5, 2012.

[108] Pascale Senellart, Glenn Solomon, and Andrew White. High-performance semiconductor quantum-dot single-photon sources. *Nature Nanotechnology*, 12(11):1026–1039, nov 2017.

[109] E. M. Purcell. Spontaneous emission probabilities at radio frequencies. *Physical Review*, 69(11-12):674–674, jun 1946.

[110] P. Goy, J. M. Raimond, M. Gross, and S. Haroche. Observation of cavity-enhanced single-atom spontaneous emission. *Physical Review Letters*, 50(24):1903–1906, 1983.

[111] Daniel Kleppner. Inhibited Spontaneous Emission. *Physical Review Letters*, 47(4):233–236, jul 1981.

[112] Randall G. Hulet, Eric S. Hilfer, and Daniel Kleppner. Inhibited spontaneous emission by a Rydberg atom. *Physical Review Letters*, 55(20):2137–2140, 1985.

[113] Serge Haroche. Controlling photons in a box and exploring the quantum to classical boundary. *Annalen der Physik*, 525(10-11):753–776, nov 2013.

[114] Herbert Walther, Benjamin T H Varcoe, Berthold-Georg Englert, and Thomas Becker. Cavity quantum electrodynamics. *Reports on Progress in Physics*, 69(5):1325–1382, 2006.

[115] Howard J. Carmichael. *Statistical Methods in Quantum Optics 2*. Theoretical and Mathematical Physics. Springer Berlin Heidelberg, Berlin, Heidelberg, 2008.

[116] A. Auffèves, D. Gerace, J.-M. Gérard, M. França Santos, L. C. Andreani, and J.-P. Poizat. Controlling the dynamics of a coupled atom-cavity system by pure dephasing. *Physical Review B*, 81(24):245419, jun 2010.

[117] Alexia Auffèves-Garnier, Christoph Simon, Jean-Michel Gérard, and Jean-Philippe Poizat. Giant optical nonlinearity induced by a single two-level system interacting with a cavity in the Purcell regime. *Physical Review A*, 75(5):053823, may 2007.

[118] H. J. Carmichael, R. J. Brecha, M. G. Raizen, H. J. Kimble, and P. R. Rice. Subnatural linewidth averaging for coupled atomic and cavity-mode oscillators. *Physical Review A*, 40(10):5516–5519, 1989.

[119] Lucio Claudio Andreani, Giovanna Panzarini, and Jean-Michel Gérard. Strong-coupling regime for quantum boxes in pillar microcavities: Theory. *Physical Review B*, 60(19):13276–13279, 1999.

[120] M. A. Armen and H. Mabuchi. Low-lying bifurcations in cavity quantum electrodynamics. *Physical Review A*, 73(6):063801, jun 2006.

[121] A. Dousse. *Deterministic cavity-quantum dot coupling and fabrication of an ultrabright source of entangled photon pairs*. PhD thesis, 2010.

[122] U. Fano. Effects of Configuration Interaction on Intensities and Phase Shifts. *Physical Review*, 124(6):1866–1878, dec 1961.

[123] S M Barnett and P. M. Radmore. Quantum theory of cavity quasimodes. *Optics Communications*, 68(5):364–368, 1988.

[124] B. J. Dalton, Stephen M. Barnett, and P. L. Knight. Quasi mode theory of macroscopic canonical quantization in quantum optics and cavity quantum electrodynamics. *Journal of Modern Optics*, 46(9):1315–1341, jul 1999.

[125] J. M. Gerard and B. Gayral. Strong Purcell effect for InAs quantum boxes in three-dimensional solid-state microcavities. *Lightwave Technology, Journal of*, 17(11):2089–2095, 1999.

[126] J. Gérard, B. Sermage, B. Gayral, B. Legrand, E. Costard, and V. Thierry-Mieg. Enhanced Spontaneous Emission by Quantum Boxes in a Monolithic Optical Microcavity. *Physical Review Letters*, 81(5):1110–1113, 1998.

[127] Mathieu Munsch, Nitin S. Malik, Emmanuel Dupuy, Adrien Delga, Joël Bleuse, Jean Michel Gérard, Julien Claudon, Niels Gregersen, and Jesper Mørk. Dielectric GaAs antenna ensuring an efficient broadband coupling between an inas quantum dot and a gaussian optical beam. *Physical Review Letters*, 110(17):1–5, 2013.

[128] T. Lund-Hansen, S. Stobbe, B. Julsgaard, H. Thyrrestrup, T. Sünner, M. Kamp, A. Forchel, and P. Lodahl. Experimental realization of highly efficient broadband coupling of single quantum dots to a photonic crystal waveguide. *Physical Review Letters*, 101(11):1–4, 2008.

[129] M. Arcari, I. Söllner, A. Javadi, S. Lindskov Hansen, S. Mahmoodian, J. Liu, H. Thyrrestrup, E. H. Lee, J. D. Song, S. Stobbe, and P. Lodahl. Near-Unity Coupling Efficiency of a Quantum Emitter to a Photonic Crystal Waveguide. *Physical Review Letters*, 113(9):1–5, 2014.

[130] K. J. Vahala. Optical microcavities. *Nature*, 424(6950):839–46, aug 2003.

[131] Susumu Noda, Masayuki Fujita, and Takashi Asano. Spontaneous-emission control by photonic crystals and nanocavities. *Nature Photonics*, 1(8):449–458, 2007.

[132] A. Kiraz, P. Michler, C. Becher, B. Gayral, A. Imamoğlu, Lidong Zhang, E. Hu, W. V. Schoenfeld, and P. M. Petroff. Cavity-quantum electrodynamics using a single InAs quantum dot in a microdisk structure. *Applied Physics Letters*, 78(25):3932–3934, jun 2001.

[133] F. Liu, A. J. Brash, J. O'Hara, L. M. P. P. Martins, C. L. Phillips, R. J. Coles, B. Royall, E. Clarke, C. Bentham, N. Prtljaga, I. E. Itskevich, L. R. Wilson, M. S. Skolnick, and A. M. Fox. High Purcell factor generation of coherent on-chip single photons. jun 2017.

[134] Dirk Englund, David Fattal, Edo Waks, Glenn Solomon, Bingyang Zhang, Toshihiro Nakaoka, Yasuhiko Arakawa, Yoshihisa Yamamoto, and Jelena Vučkovićc. Controlling the spontaneous emission rate of single quantum dots in a two-dimensional photonic crystal. *Physical Review Letters*, 95(1):2–5, 2005.

[135] T Yoshie, A Scherer, J Hendrickson, G Khitrova, H M Gibbs, G Rupper, C Ell, O B Shchekin, and D G Deppe. Vacuum Rabi splitting with a single quantum dot in a photonic crystal nanocavity. *Nature*, 432(7014):200–203, nov 2004.

[136] S. Laurent, B. Eble, O. Krebs, A. Lemaître, B. Urbaszek, X. Marie, T. Amand, and P. Voisin. Electrical control of hole spin relaxation in charge tunable InAs/GaAs quantum dots. *Physical Review Letters*, 94(14):1–4, 2005.

[137] K. H. Madsen, S. Ates, J. Liu, A. Javadi, S. M. Albrecht, I. Yeo, S. Stobbe, and P. Lodahl. Efficient out-coupling of high-purity single photons from a coherent quantum dot in a photonic-crystal cavity. *Physical Review B - Condensed Matter and Materials Physics*, 90(15):1–11, 2014.

[138] Christophe Arnold, Vivien Loo, Aristide Lematre, Isabelle Sagnes, Olivier Krebs, Paul Voisin, Pascale Senellart, and Loïc Lanco. Optical bistability in a quantum dots/micropillar device with a quality factor exceeding 200 000. *Applied Physics Letters*, 100:0–3, 2012.

[139] Simone Luca Portalupi, Gaston Hornecker, Valérian Giesz, Thomas Grange, Aristide Lemaître, Justin Demory, Isabelle Sagnes, Norberto D. Lanzillotti-Kimura, Loïc Lanco, Alexia Auffèves, and Pascale Senellart. Bright Phonon-Tuned Single-Photon Source. *Nano Letters*, 15(10):6290–6294, oct 2015.

[140] Xing Ding, Yu He, Z.-C. Duan, Niels Gregersen, M.-C. Chen, S. Unsleber, S. Maier, Christian Schneider, Martin Kamp, Sven Höfling, Chao-Yang Lu, and Jian-Wei Pan. On-Demand Single Photons with High Extraction Efficiency and Near-Unity Indistinguishability from a Resonantly Driven Quantum Dot in a Micropillar. *Physical Review Letters*, 116(2):020401, jan 2016.

[141] Sebastian Unsleber, Yu-Ming He, Stefan Gerhardt, Sebastian Maier, Chao-Yang Lu, Jian-Wei Pan, Niels Gregersen, Martin Kamp, Christian Schneider, and Sven Höfling. Highly indistinguishable on-demand resonance fluorescence photons from a deterministic quantum dot micropillar device with 74% extraction efficiency. *Optics Express*, 24(8):8539, apr 2016.

[142] F. Findeis, A. Zrenner, G. Böhm, and G. Abstreiter. Phonon-assisted biexciton generation in a single quantum dot. *Physical Review B*, 61(16):R10579–R10582, 2000.

[143] K. Kowalik, O. Krebs, A. Lemaître, S. Laurent, P. Senellart, P. Voisin, and J. A. Gaj. Influence of an in-plane electric field on exciton fine structure in InAs-GaAs self-assembled quantum dots. *Applied Physics Letters*, 86(4), 2005.

[144] Stefan Strauf, Nick G. Stoltz, Matthew T. Rakher, Larry A. Coldren, Pierre M. Petroff, and Dirk Bouwmeester. High-frequency single-photon source with polarization control. *Nature Photonics*, 1(12):704–708, 2007.

[145] C. Böckler, S. Reitzenstein, C. Kistner, R. Debusmann, A. Löffler, T. Kida, S. Höfling, A. Forchel, L. Grenouillet, J. Claudon, and J. M. Grard. Electrically driven high- Q quantum dot-micropillar cavities. *Applied Physics Letters*, 92(9):2006–2009, 2008.

[146] T. Heindel, C. Schneider, M. Lermer, S. H. Kwon, T. Braun, S. Reitzenstein, S. Höfling, M. Kamp, and A. Forchel. Electrically driven quantum dot-micropillar single photon source with 34% overall efficiency. *Applied Physics Letters*, 96(1):10–13, 2010.

[147] C Schneider, T Heindel, A Huggenberger, T A Niederstrasser, S Reitzenstein, A. Forchel, S. Höfling, and M. Kamp. Microcavity enhanced single photon emission from an electrically driven site-controlled quantum dot. *Applied Physics Letters*, 100(9):091108, feb 2012.

[148] A. K. Nowak, S. L. Portalupi, V. Giesz, O. Gazzano, C. Dal Savio, P.-F. Braun, K. Karrai, C. Arnold, L. Lanco, I. Sagnes, A. Lemaître, and P. Senellart. Deterministic and electrically tunable bright single-photon source. *Nature communications*, 5:3240, feb 2014.

[149] Michael E. Reimer, Gabriele Bulgarini, Nika Akopian, Moïra Hocevar, Maaike Bouwes Bavinck, Marcel A. Verheijen, Erik P A M Bakkers, Leo P. Kouwenhoven, and Val Zwiller. Bright single-photon sources in bottom-up tailored nanowires. *Nature Communications*, 3, 2012.

[150] C. Schneider, A. Huggenberger, T. Sünner, T. Heindel, M. Strau, S. Göpfert, P. Weinmann, S. Reitzenstein, L. Worschech, M. Kamp, S. Höfling, and A. Forchel. Single site-controlled In(Ga)As/GaAs quantum dots: Growth, properties and device integration. *Nanotechnology*, 20(43), 2009.

[151] Antonio Badolato. Deterministic Coupling of Single Quantum Dots to Single Nanocavity Modes. *Science*, 308(5725):1158–1161, may 2005.

[152] K. Hennessy, A. Badolato, M. Winger, D. Gerace, M. Atatüre, S. Gulde, S. Fält, E. L. Hu, and A. Imamoglu. Quantum nature of a strongly coupled single quantum dot-cavity system. *Nature*, 445(7130):896–899, 2007.

[153] Andreas Muller, Edward B. Flagg, Michael Metcalfe, John Lawall, and Glenn S. Solomon. Coupling an epitaxial quantum dot to a fiber-based external-mirror microcavity. *Applied Physics Letters*, 95(17):1–4, 2009.

[154] Lukas Greuter, Daniel Najer, Andreas V Kuhlmann, Sascha R Valentin, Arne Ludwig, Andreas D Wieck, Sebastian Starosielec, Richard J Warburton, Lukas Greuter, Daniel Najer, Andreas V Kuhlmann, Sascha R Valentin, Arne Ludwig, Andreas D Wieck, Sebastian Starosielec, and Richard J Warburton. Epitaxial lift-off for solid-state cavity quantum electrodynamics Epitaxial lift-off for solid-state cavity quantum electrodynamics. 075705(2015), 2017.

[155] V. Loo, C. Arnold, O. Gazzano, A. Lemaître, I. Sagnes, O. Krebs, P. Voisin, P. Senellart, and L. Lanco. Optical Nonlinearity for Few-Photon Pulses on a Quantum Dot-Pillar Cavity Device. *Physical Review Letters*, 109(16):166806, oct 2012.

[156] M. T. Rakher, N. G. Stoltz, L. A. Coldren, P. M. Petroff, and D. Bouwmeester. Externally mode-matched cavity quantum electrodynamics with charge-tunable quantum dots. *Physical Review Letters*, 102(9):6–9, 2009.

[157] A. B. Young, R. Oulton, C. Y. Hu, A. C T Thijssen, C. Schneider, S. Reitzenstein, M. Kamp, S. Höfling, L. Worschech, A. Forchel, and J. G. Rarity. Quantum-dot-induced phase shift in a pillar microcavity. *Physical Review A - Atomic, Molecular, and Optical Physics*, 84(1):2–5, 2011.

[158] Shuo Sun, Hyochul Kim, Glenn S. Solomon, and Edo Waks. A quantum phase switch between a single solid-state spin and a photon. *Nature Nanotechnology*, 11(6):539–544, feb 2016.

[159] J D Thompson, T G Tiecke, N P de Leon, J Feist, A V Akimov, M Gullans, A S Zibrov, V. Vuletic, and M D Lukin. Coupling a Single Trapped Atom to a Nanoscale Optical Cavity. *Science*, 340(6137):1202–1205, jun 2013.

[160] Serge Rosenblum, Orel Bechler, Itay Shomroni, Yulia Lovsky, Gabriel Guendelman, and Barak Dayan. Extraction of a single photon from an optical pulse. *Nature Photonics*, 10(1):19–22, nov 2015.

[161] Jacques Carolan, Chris Harrold, Chris Sparrow, E. Martin-Lopez, Nicholas J. Russell, Joshua W. Silverstone, Peter J. Shadbolt, Nobuyuki Matsuda, Manabu Oguma, Mikitaka Itoh, Graham D. Marshall, Mark G. Thompson, Jonathan C. F. Matthews, Toshikazu Hashimoto, Jeremy L. O'Brien, and Anthony Laing. Universal linear optics. *Science*, 349(6249):711–716, aug 2015.

[162] Robert H. Hadfield. Single-photon detectors for optical quantum information applications. *Nature Photonics*, 3(12):696–705, dec 2009.

[163] A. Migdall, S.V. Polyakov, J. Fan, and J.C. Bienfang. *Single-Photon Generation and Detection.* 2013.

[164] Roy Glauber. The Quantum Theory of Optical Coherence. *Physical Review*, 130(6):2529–2539, jun 1963.

[165] Rodney Loudon. The Quantum Theory of Light, 1983.

[166] C C Gerry and P L Knight. *Introductory Quantum Optics*, volume 22. Cambridge University Press, jul 2006.

[167] Edo Waks, Charles Santori, and Yoshihisa Yamamoto. Security aspects of quantum key distribution with sub-Poisson light. *Physical Review A*, 66(4):042315, oct 2002.

[168] R. Hanbury Brown and R.Q. Twiss. LXXIV. A new type of interferometer for use in radio astronomy. *The London, Edinburgh, and Dublin Philosophical Magazine and Journal of Science*, 45(366):663–682, jul 1954.

[169] M J Stevens, S Glancy, S W Nam, and R P Mirin. Third-order antibunching from an imperfect single-photon source. *Opt Express*, 22(3):3244–3260, feb 2014.

[170] CK Hong, ZY Ou, and L Mandel. Measurement of subpicosecond time intervals between two photons by interference. *Physical Review Letters*, 59(18):2044–2046, 1987.

[171] François Hénault. Quantum physics and the beam splitter mystery. In Chandrasekhar Roychoudhuri, Al F. Kracklauer, and Hans De Raedt, editors, *Proc. SPIE*, volume 9570, page 95700Q, sep 2015.

[172] Peter J. Mosley, Jeff S. Lundeen, Brian J. Smith, Piotr Wasylczyk, Alfred B. U'Ren, Christine Silberhorn, and Ian A. Walmsley. Heralded Generation of Ultrafast Single Photons in Pure Quantum States. *Physical Review Letters*, 100(13):133601, apr 2008.

[173] C. Santori, D. Fattal, J. Vucković, G. S. Solomon, and Y. Yamamoto. Indistinguishable photons from a single-photon device. *Nature*, 419(6907):594–7, oct 2002.

[174] Valerian Giesz. *Cavity-enhanced Photon-Photon Interactions With Bright Quantum Dot Sources*. PhD thesis, 2016.

[175] Andreas Christ and Christine Silberhorn. Limits on the deterministic creation of pure single-photon states using parametric down-conversion. *Physical Review A*, 85(2):023829, feb 2012.

[176] Samuel L. Braunstein and P van Loock. Quantum information with continuous variables. *Reviews of Modern Physics*, 77(2):513, 2005.

[177] Pieter Kok, W. J. Munro, Kae Nemoto, T. C. Ralph, Jonathan P. Dowling, and G. J. Milburn. Linear optical quantum computing with photonic qubits. *Reviews of Modern Physics*, 79(1):135–174, jan 2007.

[178] Allen L. and J. H. Eberly. *Optical resonance and two-level atoms*. 1975.

[179] W. Lange, G. Agarwal, and H. Walther. Observation of Two-Photon Decay of Rydberg Atoms in a Driven Cavity. *Physical Review Letters*, 76(18):3293–3296, 1996.

[180] Alex Hayat, Pavel Ginzburg, and Meir Orenstein. Observation of two-photon emission from semiconductors. *Nature Photonics*, 2(4):238–241, mar 2008.

[181] Yasutomo Ota, Satoshi Iwamoto, Naoto Kumagai, and Yasuhiko Arakawa. Spontaneous Two-Photon Emission from a Single Quantum Dot. *Physical Review Letters*, 107(23):233602, nov 2011.

[182] Axel Kuhn, Markus Hennrich, and Gerhard Rempe. Deterministic Single-Photon Source for Distributed Quantum Networking. pages 4–7, 2002.

[183] H. G. Barros, A. Stute, T. E. Northup, C. Russo, P. O. Schmidt, and R. Blatt. Deterministic single-photon source from a single ion. *New Journal of Physics*, 11, 2009.

[184] W. E. Moerner. Single-photon sources based on single molecules in solids. *New Journal of Physics*, 6:1–21, 2004.

[185] J Beugnon, M P a Jones, J Dingjan, B Darquié, G Messin, a Browaeys, and P Grangier. Quantum interference between two single photons emitted by independently trapped atoms. *Nature*, 440(7085):779–82, apr 2006.

[186] Tim Schröder, Matthew E. Trusheim, Michael Walsh, Luozhou Li, Jiabao Zheng, Marco Schukraft, Alp Sipahigil, Ruffin E. Evans, Denis D. Sukachev, Christian T. Nguyen, Jose L. Pacheco, Ryan M. Camacho, Edward S. Bielejec, Mikhail D. Lukin, and Dirk Englund. Scalable focused ion beam creation of nearly lifetime-limited single quantum emitters in diamond nanostructures. *Nature Communications*, 8(May):15376, may 2017.

[187] Alexander Hoegele, Christophe Galland, Martin Winger, and Atac Imamoglu. Photon antibunching in the photoluminescence spectra of a single carbon nanotube. *Physical Review Letters*, 100(21):5–8, 2008.

[188] Jörg Wrachtrup. 2D materials: Single photons at room temperature. *Nature Nanotechnology*, 11(1):7–8, 2016.

[189] Kartik Srinivasan, Andreas Stintz, Sanjay Krishna, and Oskar Painter. Photoluminescence measurements of quantum-dot-containing semiconductor microdisk resonators using optical fiber taper waveguides. *Physical Review B - Condensed Matter and Materials Physics*, 72(20):1–9, 2005.

[190] Raphaël S. Daveau, Krishna C. Balram, Tommaso Pregnolato, Jin Liu, Eun H. Lee, Jin D. Song, Varun Verma, Richard Mirin, Sae Woo Nam, Leonardo Midolo, Søren Stobbe, Kartik Srinivasan, and Peter Lodahl. Efficient fiber-coupled single-photon source based on quantum dots in a photonic-crystal waveguide. 4(2), 2016.

[191] I. Friedler, C. Sauvan, J. P. Hugonin, P. Lalanne, J. Claudon, and J. M. Gérard. Solid-state single photon sources: the nanowire antenna. *Optics Express*, 17(4):2095, 2009.

[192] T. Sosnowski, T. Norris, H. Jiang, J. Singh, K. Kamath, and P. Bhattacharya. Rapid carrier relaxation in In0.4Ga0.6As/GaAs quantum dots characterized by differential transmission spectroscopy. *Physical Review B*, 57(16):R9423–R9426, 1998.

[193] R. Heitz, M. Grundmann, N. N. Ledentsov, L. Eckey, M. Veit, D. Bimberg, V. M. Ustinov, A. Yu Egorov, A. E. Zhukov, P. S. Kop'ev, and Zh I. Alferov. Multiphonon relaxation processes in self organized InAs/GaAs quantum dots. *Applied Physics Letters*, 68(3):361–363, jan 1996.

[194] F. Adler, M. Geiger, A. Bauknecht, F. Scholz, H. Schweizer, M. H. Pilkuhn, B. Ohnesorge, and A. Forchel. Optical transitions and carrier relaxation in self assembled InAs/GaAs quantum dots. *Journal of Applied Physics*, 80(7):4019–4026, oct 1996.

[195] Y. Toda, O. Moriwaki, M. Nishioka, and Y. Arakawa. Efficient Carrier Relaxation Mechanism in InGaAs/GaAs Self-Assembled Quantum Dots Based on the Existence of Continuum States. *Physical Review Letters*, 82(20):4114–4117, may 1999.

[196] E. Peter, S. Laurent, J. Bloch, J. Hours, S. Varoutsis, I. Robert-Philip, A. Beveratos, A. Lemaître, A. Cavanna, G. Patriarche, P. Senellart, and D. Martrou. Fast radiative quantum dots: From single to multiple photon emission. *Applied Physics Letters*, 90(22):223118, may 2007.

[197] Charles Santori, David Fattal, Jelena Vuckovic, Glenn S. Solomon, and Yoshihisa Yamamoto. Single-photon generation with InAs quantum dots. *New Journal of Physics*, 6:89–89, jul 2004.

[198] Charles Santori, David Fattal, Jelena Vučković, Glenn S. Solomon, Edo Waks, and Yoshihisa Yamamoto. Submicrosecond correlations in photoluminescence from InAs quantum dots. *Physical Review B*, 69(20):205324, may 2004.

[199] Kh Schmidt, G Medeiros-Ribeiro, M Oestreich, Pm Petroff, and Gh Döhler. Carrier relaxation and electronic structure in InAs self-assembled quantum dots. *Physical review B*, 54(16):11346–11353, 1996.

[200] M. Steer, D. Mowbray, W. Tribe, M. Skolnick, M. Sturge, M. Hopkinson, a. Cullis, C. Whitehouse, and R. Murray. Electronic energy levels and energy relaxation mechanisms in self-organized InAs/GaAs quantum dots. *Physical Review B*, 54(24):17738–17744, 1996.

[201] H Kamada, H Gotoh, J Temmyo, T Takagahara, and H Ando. Exciton Rabi Oscillation in a Single Quantum Dot. *Physical Review Letters*, 87(24):246401, nov 2001.

[202] H Htoon, T Takagahara, D Kulik, O Baklenov, a L Holmes, and C K Shih. Interplay of Rabi Oscillations and Quantum Interference in Semiconductor Quantum Dots. *Physical Review Letters*, 88(8):087401, feb 2002.

[203] R. Heitz, I. Mukhametzhanov, O. Stier, A. Madhukar, and D. Bimberg. Enhanced Polar Exciton-LO-Phonon Interaction in Quantum Dots. *Physical Review Letters*, 83(22):4654–4657, nov 1999.

[204] Yanwen Wu, I. M. Piper, M. Ediger, P. Brereton, E. R. Schmidgall, P. R. Eastham, M. Hugues, M. Hopkinson, and R. T. Phillips. Population Inversion in a Single InGaAs Quantum Dot Using the Method of Adiabatic Rapid Passage. *Physical Review Letters*, 106(6):067401, feb 2011.

[205] T. H. Stievater, Xiaoqin Li, D. G. Steel, D. Gammon, D. S. Katzer, D. Park, C. Piermarocchi, and L. J. Sham. Rabi Oscillations of Excitons in Single Quantum Dots. *Physical Review Letters*, 87(13):133603, sep 2001.

[206] J R Schaibley, a P Burgers, G a McCracken, D. G. Steel, a S Bracker, D Gammon, and L. J. Sham. Direct detection of time-resolved Rabi oscillations in a single quantum dot via resonance fluorescence. *Physical Review B*, 87(11):115311, mar 2013.

[207] S. Ates, S. Ulrich, S. Reitzenstein, a. Löffler, a. Forchel, and P. Michler. Post-Selected Indistinguishable Photons from the Resonance Fluorescence of a Single Quantum Dot in a Microcavity. *Physical Review Letters*, 103(16):167402, oct 2009.

[208] Yu-Ming He, Yu He, Yu-Jia Wei, Dian Wu, Mete Atatüre, Christian Schneider, Sven Höfling, Martin Kamp, Chao-Yang Lu, and Jian-Wei Pan. On-demand semiconductor single-photon source with near-unity indistinguishability. *Nature nanotechnology*, 8(3):213–7, mar 2013.

[209] J A Barker and E. P. O'Reilly. Theoretical analysis of electron-hole alignment in InAs-GaAs quantum dots. *Physical Review B*, 61(20):13840–13851, may 2000.

[210] J. J. Finley, M. Sabathil, P. Vogl, G. Abstreiter, R. Oulton, A. I. Tartakovskii, D. J. Mowbray, M. S. Skolnick, S. L. Liew, A. G. Cullis, and M. Hopkinson. Quantum-confined Stark shifts of charged exciton complexes in quantum dots. *Physical Review B*, 70(20):201308, nov 2004.

[211] R. J. Young, R. M. Stevenson, A. J. Shields, P. Atkinson, K. Cooper, D. A. Ritchie, K. M. Groom, A. I. Tartakovskii, and M. S. Skolnick. Inversion of exciton level splitting in quantum dots. *Physical Review B*, 72(11):113305, sep 2005.

[212] Andreas V. Kuhlmann, Jonathan H. Prechtel, Julien Houel, Arne Ludwig, Dirk Reuter, Andreas D. Wieck, and Richard J. Warburton. Transform-limited single photons from a single quantum dot. *Nature Communications*, 6:8204, sep 2015.

[213] A. Muller, E. B. Flagg, P. Bianucci, X. Y. Wang, D. G. Deppe, W. Ma, J. Zhang, G. J. Salamo, M. Xiao, and C. K. Shih. Resonance fluorescence from a coherently driven semiconductor quantum dot in a cavity. *Physical Review Letters*, 99(18):2–5, 2007.

[214] K. Kuroda, T. Kuroda, K. Watanabe, T. Mano, K. Sakoda, G. Kido, and N. Koguchi. Final-state readout of exciton qubits by observing resonantly excited photoluminescence in quantum dots. *Applied Physics Letters*, 90(5):1–4, 2007.

[215] Juan C. Loredo, Nor A. Zakaria, Niccolo Somaschi, Carlos Anton, Lorenzo de Santis, Valerian Giesz, Thomas Grange, Matthew A. Broome, Olivier Gazzano, Guillaume Coppola, Isabelle Sagnes, Aristide Lemaitre, Alexia Auffeves, Pascale Senellart, Marcelo P. Almeida, and Andrew G. White. Scalable performance in solid-state single-photon sources. *Optica*, 3(4):433, apr 2016.

[216] Scott Aaronson and Alex Arkhipov. The computational complexity of linear optics. In *Proceedings of the 43rd annual ACM symposium on Theory of computing - STOC '11*, page 333, New York, New York, USA, 2011. ACM Press.

[217] Andrea Crespi, Roberto Osellame, Roberta Ramponi, Daniel J. Brod, Ernesto F. Galvão, Nicolò Spagnolo, Chiara Vitelli, Enrico Maiorino, Paolo Mataloni, and Fabio Sciarrino. Integrated multimode interferometers with arbitrary designs for photonic boson sampling. *Nature Photonics*, 7(7):545–549, may 2013.

[218] Matthew A. Broome, Alessandro Fedrizzi, Saleh Rahimi-Keshari, Justin Dove, Scott Aaronson, Timothy C. Ralph, and Andrew G. White. Photonic Boson Sampling in a Tunable Circuit. *Science*, 339(6121):794–798, feb 2013.

[219] Max Tillmann, Borivoje Dakić, René Heilmann, Stefan Nolte, Alexander Szameit, and Philip Walther. Experimental boson sampling. *Nature Photonics*, 7(July):540–544, 2013.

[220] Justin B. Spring, Benjamin J. Metcalf, Peter C. Humphreys, W. Steven Kolthammer, X.-M. Jin, Marco Barbieri, Animesh Datta, Nicholas Thomas-Peter, Nathan K. Langford, Dmytro Kundys, James C. Gates, B. J. Smith, P. G. R. Smith, and Ian A. Walmsley. Boson Sampling on a Photonic Chip. *Science*, 339(6121):798–801, feb 2013.

[221] J. C. Loredo, M. A. Broome, P. Hilaire, O. Gazzano, I. Sagnes, A. Lemaitre, M. P. Almeida, P. Senellart, and A. G. White. Boson Sampling with Single-Photon Fock States from a Bright Solid-State Source. *Physical Review Letters*, 118(13):1–7, 2017.

[222] Hui Wang, Yu He, Yu-Huai Li, Zu-En Su, Bo Li, He-Liang Huang, Xing Ding, Ming-Cheng Chen, Chang Liu, Jian Qin, Jin-Peng Li, Yu-Ming He, Christian Schneider, Martin Kamp, Cheng-Zhi Peng, Sven Höfling, Chao-Yang Lu, and Jian-Wei Pan. High-efficiency multiphoton boson sampling. *Nature Photonics*, 11(6):361–365, 2017.

[223] E J S Fonseca, C H Monken, and S Pádua. Measurement of the de Broglie Wavelength of a Multiphoton Wave Packet. *Physical Review Letters*, 82(14):2868–2871, apr 1999.

[224] Yonatan Israel, Shamir Rosen, and Yaron Silberberg. Supersensitive Polarization Microscopy Using NOON States of Light. *Physical Review Letters*, 112(10):103604, mar 2014.

[225] Peter A. Morris, Reuben S. Aspden, Jessica E. C. Bell, Robert W. Boyd, and Miles J. Padgett. Imaging with a small number of photons. *Nature Communications*, 6:5913, jan 2015.

[226] Agedi N. Boto, Pieter Kok, Daniel S. Abrams, Samuel L. Braunstein, Colin P. Williams, and Jonathan P. Dowling. Quantum Interferometric Optical Lithography: Exploiting Entanglement to Beat the Diffraction Limit. *Physical Review Letters*, 85(13):2733–2736, sep 2000.

[227] Milena D'Angelo, Maria V. Chekhova, and Yanhua Shih. Two-Photon Diffraction and Quantum Lithography. *Physical Review Letters*, 87(1):013602, jun 2001.

[228] Michael A. Taylor, Jiri Janousek, Vincent Daria, Joachim Knittel, Boris Hage, Hans-A. Bachor, and Warwick P. Bowen. Biological measurement beyond the quantum limit. *Nature Photonics*, 7(3):229–233, feb 2013.

[229] Florian Wolfgramm, Chiara Vitelli, Federica A. Beduini, Nicolas Godbout, and Morgan W. Mitchell. Entanglement-enhanced probing of a delicate material system. *Nature Photonics*, 7(1):28–32, dec 2012.

[230] The LIGO Scientific Collaboration. A gravitational wave observatory operating beyond the quantum shot-noise limit. *Nature Physics*, 7(12):962–965, sep 2011.

[231] The LIGO Scientific Collaboration. Enhanced sensitivity of the LIGO gravitational wave detector by using squeezed states of light. *Nature Photonics*, 7(8):613–619, jul 2013.

[232] Vittorio Giovannetti, Seth Lloyd, and Lorenzo Maccone. Quantum-enhanced measurements: beating the standard quantum limit. *Science (New York, N.Y.)*, 306(5700):1330–1336, 2004.

[233] V. Meyer, M. A. Rowe, D. Kielpinski, C. A. Sackett, W. M. Itano, C. Monroe, and D. J. Wineland. Experimental Demonstration of Entanglement-Enhanced Rotation Angle Estimation Using Trapped Ions. *Physical Review Letters*, 86(26):5870–5873, jun 2001.

[234] C. F. Roos, M. Chwalla, K. Kim, M. Riebe, and R. Blatt. 'Designer atoms' for quantum metrology. *Nature*, 443(7109):316–319, sep 2006.

[235] Artur Widera, Olaf Mandel, Markus Greiner, Susanne Kreim, Theodor W. Hänsch, and Immanuel Bloch. Entanglement Interferometry for Precision Measurement of Atomic Scattering Properties. *Physical Review Letters*, 92(16):160406, apr 2004.

[236] J. Geremia. Real-Time Quantum Feedback Control of Atomic Spin-Squeezing. *Science*, 304(5668):270–273, apr 2004.

[237] V Giovannetti, S Lloyd, and L Maccone. Advances in quantum metrology. *Nature Photonics*, 5(4):222–229, 2011.

[238] Jonathan P. Dowling. Quantum Optical Metrology – The Lowdown on High-N00N States. (April 2015):38, 2009.

[239] Pieter Kok, SL Braunstein, and JP Dowling. Quantum lithography, entanglement and Heisenberg-limited parameter estimation. *Journal of Optics B: Quantum ...*, 6(8):S811–S815, aug 2004.

[240] Samuel L. Braunstein. Quantum limits on precision measurements of phase. *Physical Review Letters*, 69(25):3598–3601, dec 1992.

[241] Konrad Banaszek, Rafal Demkowicz-Dobrzanski, and Ian A. Walmsley. Quantum states made to measure. *Nature Photonics*, 3(12):673–676, 2009.

[242] P. A. M. Dirac. The Quantum Theory of the Emission and Absorption of Radiation. *Proceedings of the Royal Society A: Mathematical, Physical and Engineering Sciences*, 114(767):243–265, mar 1927.

[243] Z. Y. Ou. Fundamental quantum limit in precision phase measurement. *Physical Review A*, 55(4):2598–2609, apr 1997.

[244] J. J . Bollinger, Wayne M. Itano, D. J. Wineland, and D. J. Heinzen. Optimal frequency measurements with maximally correlated states. *Physical Review A*, 54(6):R4649–R4652, 1996.

[245] Michael Martin Nieto. Quantum phase and quantum phase operators: some physics and some history. *Physica Scripta*, 1993(T48):1–19, 1993.

[246] P. Carruthers and Michael Martin Nieto. Phase and Angle Variables in Quantum Mechanics. *Reviews of Modern Physics*, 40(2):411–440, apr 1968.

[247] Carlton M. Caves. Quantum-mechanical noise in an interferometer. *Physical Review D*, 23(8):1693–1708, apr 1981.

[248] Hwang Lee, Pieter Kok, and Jonathan P. Dowling. A quantum Rosetta stone for interferometry. *Journal of Modern Optics*, 49(14-15):2325–2338, nov 2002.

[249] Barry C. Sanders. Quantum dynamics of the nonlinear rotator and the effects of continual spin measurement. *Physical Review A*, 40(5):2417–2427, sep 1989.

[250] Gabriel A. Durkin and Jonathan P. Dowling. Local and Global Distinguishability in Quantum Interferometry. *Physical Review Letters*, 99(7):070801, aug 2007.

[251] Karl Blum. *Density Matrix Theory and Applications*, volume 64 of *Springer Series on Atomic, Optical, and Plasma Physics*. Springer Berlin Heidelberg, Berlin, Heidelberg, 2012.

[252] Joseph Jacobson, Gunnar Björk, Isaac Chuang, and Yoshihisa Yamamoto. Photonic de Broglie Waves. *Physical Review Letters*, 74(24):4835–4838, jun 1995.

[253] G. J. Pryde and A. G. White. Creation of maximally entangled photon-number states using optical fiber multiports. *Physical Review A*, 68(5):052315, nov 2003.

[254] Pieter Kok, Hwang Lee, and Jonathan P. Dowling. Creation of large-photon-number path entanglement conditioned on photodetection. *Physical Review A*, 65(5):052104, apr 2002.

[255] Hugo Cable and Jonathan P. Dowling. Efficient Generation of Large Number-Path Entanglement Using Only Linear Optics and Feed-Forward. *Physical Review Letters*, 99(16):163604, oct 2007.

[256] Z. Y. Ou, X. Y. Zou, L. J. Wang, and L. Mandel. Experiment on nonclassical fourth-order interference. *Physical Review A*, 42(5):2957–2965, sep 1990.

[257] J. Rarity, P. Tapster, E. Jakeman, T. Larchuk, R. Campos, M. Teich, and B. Saleh. Two-photon interference in a Mach-Zehnder interferometer. *Physical Review Letters*, 65(11):1348–1351, sep 1990.

[258] Tomohisa Nagata, Ryo Okamoto, Jeremy L. O'Brien, Keiji Sasaki, and Shigeki Takeuchi. Beating the Standard Quantum Limit with Four Entangled Photons. 726(2007), 2007.

[259] M W Mitchell, J S Lundeen, and A M Steinberg. Super-resolving phase measurements with a multiphoton entangled state. *Nature*, 429(6988):161–164, may 2004.

[260] Philip Walther, Jian-Wei Pan, Markus Aspelmeyer, Rupert Ursin, Sara Gasparoni, and Anton Zeilinger. De Broglie wavelength of a non-local four-photon state. *Nature*, 429(6988):158–61, may 2004.

[261] Itai Afek, Oron Ambar, and Yaron Silberberg. High-NOON States by Mixing Quantum and Classical Light. *Science*, 328(5980):879–881, may 2010.

[262] Luca Pezzé and Augusto Smerzi. Mach-Zehnder Interferometry at the Heisenberg Limit with Coherent and Squeezed-Vacuum Light. *Physical Review Letters*, 100(7):073601, feb 2008.

[263] Holger F. Hofmann and Takafumi Ono. High-photon-number path entanglement in the interference of spontaneously down-converted photon pairs with coherent laser light. *Physical Review A - Atomic, Molecular, and Optical Physics*, 76(3):1–4, 2007.

[264] K. J. Resch, K. L. Pregnell, R. Prevedel, A. Gilchrist, G. J. Pryde, J. L. O'Brien, and A. G. White. Time-Reversal and Super-Resolving Phase Measurements. *Physical Review Letters*, 98(22):223601, may 2007.

[265] I. Afek, O. Ambar, and Y. Silberberg. Classical Bound for Mach-Zehnder Superresolution. *Physical Review Letters*, 104(12):123602, mar 2010.

[266] K. Goda, O. Miyakawa, E. E. Mikhailov, S. Saraf, R. Adhikari, K. McKenzie, R. Ward, S. Vass, A. J. Weinstein, and N. Mavalvala. A quantum-enhanced prototype gravitational-wave detector. *Nature Physics*, 4(6):472–476, jun 2008.

[267] H. Yonezawa, D. Nakane, T. A. Wheatley, K. Iwasawa, S. Takeda, H. Arao, K. Ohki, K. Tsumura, D. W. Berry, T. C. Ralph, H. M. Wiseman, E. H. Huntington, and A. Furusawa. Quantum-Enhanced Optical-Phase Tracking. *Science*, 337(6101):1514–1517, sep 2012.

[268] Sergei Slussarenko, Morgan M. Weston, Helen M. Chrzanowski, Lynden K. Shalm, Varun B. Verma, Sae Woo Nam, and Geoff J. Pryde. Unconditional violation of the shot noise limit in photonic quantum metrology. pages 1–5, jul 2017.

[269] Daniel F. V. James, Paul G. Kwiat, William J. Munro, and Andrew G. White. Measurement of qubits. *Physical Review A*, 64(5):052312, oct 2001.

[270] Y. Israel, I. Afek, S. Rosen, O. Ambar, and Y. Silberberg. Experimental tomography of NOON states with large photon numbers. *Physical Review A*, 85(2):022115, feb 2012.

[271] P. J. Shadbolt, M. R. Verde, A. Peruzzo, A. Politi, A. Laing, M. Lobino, J. C. F. Matthews, M. Thompson, and J. L. O'Brien. Generating, manipulating and measuring entanglement and mixture with a reconfigurable photonic circuit. *Nature Photonics*, 6(1):45–49, 2011.

[272] J W Silverstone, R Santagati, D Bonneau, M J Strain, M Sorel, J. L. O'Brien, and M G Thompson. Qubit entanglement between ring-resonator photon-pair sources on a silicon chip. *Nature Communications*, 6:7948, aug 2015.

[273] Max Tillmann, Si Hui Tan, Sarah E. Stoeckl, Barry C. Sanders, Hubert De Guise, René Heilmann, Stefan Nolte, Alexander Szameit, and Philip Walther. Generalized multiphoton quantum interference. *Physical Review X*, 5(4):1–23, 2015.

[274] Mario A. Ciampini, Nicolò Spagnolo, Chiara Vitelli, Luca Pezzè, Augusto Smerzi, and Fabio Sciarrino. Quantum-enhanced multiparameter estimation in multiarm interferometers. *Scientific Reports*, 6:1–8, 2016.

[275] Alexander E. Ulanov, Ilya A. Fedorov, Demid Sychev, Philippe Grangier, and A. I. Lvovsky. Loss-tolerant state engineering for quantum-enhanced metrology via the reverse Hong–Ou–Mandel effect. *Nature Communications*, 7(May):11925, jun 2016.

[276] George Gabriel Stokes. On the Composition and Resolution of Streams of Polarized Light from different Sources. In *Mathematical and Physical Papers*, volume 9, pages 233–258. Cambridge University Press, Cambridge, 1852.

[277] R. T. Thew, K. Nemoto, a. G. White, and W. J. Munro. Qudit quantum-state tomography. *Physical Review A*, 66(1):012303, jul 2002.

[278] U. Schilling, J. Von Zanthier, and G. S. Agarwal. Measuring arbitrary-order coherences: Tomography of single-mode multiphoton polarization-entangled states. *Physical Review A - Atomic, Molecular, and Optical Physics*, 81(1):1–5, 2010.

[279] Bernard Yurke, Samuel L. McCall, and John R. Klauder. SU(2) and SU(1,1) interferometers. *Physical Review A*, 33(6):4033–4054, jun 1986.

[280] M J Fitch, B C Jacobs, T B Pittman, and J D Franson. Photon-number resolution using time-multiplexed single-photon detectors. *Physical Review A*, 68(4):043814, oct 2003.

[281] Pieter Kok and Samuel L. Braunstein. Detection devices in entanglement-based optical state preparation. *Physical Review A*, 63(3):033812, feb 2001.

[282] H. Paul, P. Törmä, T. Kiss, and I. Jex. Photon Chopping: New Way to Measure the Quantum State of Light. *Physical Review Letters*, 76(14):2464–2467, 1996.

[283] Anthony J Bennett, James P Lee, David J P Ellis, Thomas Meany, Eoin Murray, Frederik F Floether, Jonathan P Griffths, Ian Farrer, David A Ritchie, and Andrew J Shields. Cavity-enhanced coherent light scattering from a quantum dot. *Science Advances*, 2(4):e1501256–e1501256, apr 2016.

[284] X Wang, T Hiroshima, A Tomita, and M Hayashi. Quantum information with Gaussian states. *Physics Reports*, 448(1-4):1–111, 2007.

[285] Michael Reck, Anton Zeilinger, Herbert J. Bernstein, and Philip Bertani. Experimental realization of any discrete unitary operator. *Physical Review Letters*, 73(1):58–61, jul 1994.

[286] M. Müller, H. Vural, C. Schneider, A. Rastelli, O. G. Schmidt, S. Höfling, and P. Michler. Quantum-Dot Single-Photon Sources for Entanglement Enhanced Interferometry. *Physical Review Letters*, 118(25):257402, jun 2017.

[287] R. Adamson, L. Shalm, M. Mitchell, and A. Steinberg. Multiparticle State Tomography: Hidden Differences. *Physical Review Letters*, 98(4):043601, jan 2007.

[288] R. B A Adamson, P. S. Turner, M. W. Mitchell, and A. M. Steinberg. Detecting hidden differences via permutation symmetries. *Physical Review A*, 78(3):033832, sep 2008.

[289] Darrick E. Chang, Vladan Vuletić, and Mikhail D. Lukin. Quantum nonlinear optics — photon by photon. *Nature Photonics*, 8(9):685–694, aug 2014.

[290] J. D. Franson, B. C. Jacobs, and T. B. Pittman. Quantum computing using single photons and the Zeno effect. *Physical Review A*, 70(6):062302, dec 2004.

[291] Kae Nemoto and W. J. Munro. Nearly Deterministic Linear Optical Controlled-NOT Gate. *Physical Review Letters*, 93(25):250502, dec 2004.

[292] David A B Miller. Are optical transistors the logical next step? *Nature Photonics*, 4(1):3–5, jan 2010.

[293] Vivien Loo. *Excitation résonante et non-linéarité à faible nombre de photons d'une boîte quantique en microcavité.* PhD thesis, 2012.

[294] Serge Rosenblum, Scott Parkins, and Barak Dayan. Photon routing in cavity QED: Beyond the fundamental limit of photon blockade. *Physical Review A*, 84(3):033854, sep 2011.

[295] A. Imamoglu, H. Schmidt, G. Woods, and M. Deutsch. Strongly Interacting Photons in a Nonlinear Cavity. *Physical Review Letters*, 79(8):1467–1470, aug 1997.

[296] Q. A. Turchette, R. J. Thompson, and H. J. Kimble. One-dimensional atoms. *Applied Physics B: Lasers and Optics*, 60, 1995.

[297] Holger F Hofmann, Kunihiro Kojima, Shigeki Takeuchi, and Keiji Sasaki. Optimized phase switching using a single-atom nonlinearity. *Journal of Optics B: Quantum and Semiclassical Optics*, 5(3):218–221, jun 2003.

[298] Loic Lanco. Enhancing photon-photon and spin-photon interactions with quantum-dot based light-matter interfaces.

[299] Q. A. Turchette, C. J. Hood, W. Lange, H. Mabuchi, and H. J. Kimble. Measurement of Conditional Phase Shifts for Quantum Logic. *Physical Review Letters*, 75(25):4710–4713, dec 1995.

[300] K. M. Birnbaum, A. Boca, R. Miller, a. D. Boozer, T. E. Northup, and H. J. Kimble. Photon blockade in an optical cavity with one trapped atom. *Nature*, 436(7047):87–90, jul 2005.

[301] B. Dayan, A. S. Parkins, T. Aoki, E. P. Ostby, K. J. Vahala, and H. J. Kimble. A Photon Turnstile Dynamically Regulated by One Atom. *Science*, 319(5866):1062–1065, 2008.

[302] Bastian Hacker, Stephan Welte, Gerhard Rempe, and Stephan Ritter. A photon–photon quantum gate based on a single atom in an optical resonator. *Nature*, 536(7615):193–196, jul 2016.

[303] Andrei Faraon, Ilya Fushman, Dirk Englund, Nick Stoltz, Pierre Petroff, and Jelena Vučković. Coherent generation of non-classical light on a chip via photon-induced tunnelling and blockade. *Nature Physics*, 4(11):859–863, nov 2008.

[304] Andreas Reinhard, Thomas Volz, Martin Winger, Antonio Badolato, Kevin J. Hennessy, Evelyn L. Hu, and Ataç Imamoğlu. Strongly correlated photons on a chip. *Nature Photonics*, 6(2):93–96, dec 2011.

[305] Armand Rundquist, Michal Bajcsy, Arka Majumdar, Tomas Sarmiento, Kevin Fischer, Konstantinos G Lagoudakis, Sonia Buckley, Alexander Y Piggott, and Jelena Vučković. Nonclassical higher-order photon correlations with a quantum dot strongly coupled to a photonic-crystal nanocavity. *Physical Review A*, 90(2):023846, aug 2014.

[306] Thomas Volz, Andreas Reinhard, Martin Winger, Antonio Badolato, Kevin J Hennessy, Evelyn L Hu, and Ataç Imamoğlu. Ultrafast all-optical switching by single photons. *Nature Photonics*, 6(9):607–611, aug 2012.

[307] Ranojoy Bose, Deepak Sridharan, Hyochul Kim, Glenn S. Solomon, and Edo Waks. Low-photon-number optical switching with a single quantum dot coupled to a photonic crystal cavity. *Physical Review Letters*, 108(22):1–5, 2012.

[308] Dirk Englund, Arka Majumdar, Michal Bajcsy, Andrei Faraon, Pierre Petroff, and Jelena Vučković. Ultrafast photon-photon interaction in a strongly coupled quantum dot-cavity system. *Physical Review Letters*, 108(9):2–5, 2012.

[309] Hyochul Kim, Ranojoy Bose, Thomas C. Shen, Glenn S. Solomon, and Edo Waks. A quantum logic gate between a solid-state quantum bit and a photon. *Nature Photonics*, 7(5):373–377, 2013.

[310] A. Javadi, I. Söllner, M. Arcari, S. Lindskov Hansen, L. Midolo, S. Mahmoodian, G Kiršanske, T. Pregnolato, E. H. Lee, J. D. Song, S. Stobbe, and P. Lodahl. Single-photon non-linear optics with a quantum dot in a waveguide. *Nature Communications*, 6:8655, oct 2015.

[311] A. J. Bennett, J. P. Lee, D. J. P. Ellis, I. Farrer, D. A. Ritchie, and A. J. Shields. A semiconductor photon-sorter. *Nature Nanotechnology*, 11(10):857–860, jul 2016.

[312] H. Snijders, J. A. Frey, J. Norman, M. P. Bakker, E. C. Langman, A. Gossard, J. E. Bowers, M. P. van Exter, D. Bouwmeester, and W. Löffler. Purification of a single-photon nonlinearity. *Nature Communications*, 7:12578, aug 2016.

[313] Kai Müller, Armand Rundquist, Kevin a Fischer, Tomas Sarmiento, Konstantinos G Lagoudakis, Yousif a Kelaita, Carlos Sánchez Muñoz, Elena del Valle, Fabrice P Laussy, and Jelena Vučković. Coherent Generation of Nonclassical Light on Chip via Detuned Photon Blockade. *Physical Review Letters*, 114(23):233601, jun 2015.

[314] Kevin A. Fischer, Lukas Hanschke, Jakob Wierzbowski, Tobias Simmet, Constantin Dory, Jonathan J. Finley, Jelena Vuckovic, and Kai Müller. Signatures of two-photon pulses from a quantum two-level system. *Nature Physics*, (February), 2017.

[315] R Bourgain, J Pellegrino, S Jennewein, Y R P Sortais, and A Browaeys. Direct measurement of the Wigner time delay for the scattering of light by a single atom. *Optics Letters*, 38(11):1963, jun 2013.

[316] Elizabeth A. Goldschmidt, Fabrizio Piacentini, Ivano Ruo Berchera, Sergey V. Polyakov, Silke Peters, Stefan Kück, Giorgio Brida, Ivo P. Degiovanni, Alan Migdall, and Marco Genovese. Mode reconstruction of a light field by multiphoton statistics. *Physical Review A*, 88(1):013822, jul 2013.

[317] C. Y. Hu, W. J. Munro, and J. G. Rarity. Deterministic photon entangler using a charged quantum dot inside a microcavity. *Physical Review B*, 78(12):125318, sep 2008.

[318] Cristian Bonato, Florian Haupt, Sumant S. R. Oemrawsingh, Jan Gudat, Dapeng Ding, Martin P. van Exter, and Dirk Bouwmeester. CNOT and Bell-state analysis in the weak-coupling cavity QED regime. *Physical Review Letters*, 104(16):160503, apr 2010.

[319] D. Pinotsi and A. Imamoglu. Single photon absorption by a single quantum emitter. *Physical Review Letters*, 100(9):1–4, 2008.

[320] Kazuki Koshino, Satoshi Ishizaka, and Yasunobu Nakamura. Deterministic photon-photon $\sqrt{\mathrm{SWAP}}$ gate using a Λ system. *Physical Review A - Atomic, Molecular, and Optical Physics*, 82(1):1–4, 2010.

[321] Serge Rosenblum, Adrien Borne, and Barak Dayan. Analysis of deterministic swapping of photonic and atomic states through single-photon Raman interaction. *Physical Review A*, 95(3):1–11, 2017.

[322] Jonathan H. Prechtel, Andreas V. Kuhlmann, Julien Houel, Arne Ludwig, Sascha R. Valentin, Andreas D. Wieck, and Richard J. Warburton. Decoupling a hole spin qubit from the nuclear spins. *Nature Materials*, 15(9):981–986, 2016.

[323] Kazuya Takemoto, Yoshihiro Nambu, Toshiyuki Miyazawa, Yoshiki Sakuma, Tsuyoshi Yamamoto, Shinichi Yorozu, and Yasuhiko Arakawa. Quantum key distribution over 120km using ultrahigh purity single-photon source and superconducting single-photon detectors. *Scientific Reports*, 5(September):4–6, 2015.

[324] Robert Raussendorf, Daniel E. Browne, and Hans J. Briegel. Measurement-based quantum computation on cluster states. *Physical Review A*, 68(2):022312, aug 2003.

[325] Koji Azuma, Kiyoshi Tamaki, and Hoi Kwong Lo. All-photonic quantum repeaters. *Nature Communications*, 6:1–7, 2015.

[326] Sebastian Zaske, Andreas Lenhard, Christian A. Keßler, Jan Kettler, Christian Hepp, Carsten Arend, Roland Albrecht, Wolfgang-Michael Schulz, Michael Jetter, Peter Michler, and Christoph Becher. Visible-to-Telecom Quantum Frequency Conversion of Light from a Single Quantum Emitter. *Physical Review Letters*, 109(14):147404, oct 2012.

[327] Leo Yu, Chandra M. Natarajan, Tomoyuki Horikiri, Carsten Langrock, Jason S. Pelc, Michael G. Tanner, Eisuke Abe, Sebastian Maier, Christian Schneider, Sven Höfling, Martin Kamp, Robert H. Hadfield, Martin M. Fejer, and Yoshihisa Yamamoto. Two-photon interference at telecom wavelengths for time-bin-encoded single photons from quantum-dot spin qubits. *Nature Communications*, 6(May):1–10, 2015.

[328] J. C. López Carreño, C. Sánchez Muñoz, E. del Valle, and F. P. Laussy. Excitation with quantum light. II. Exciting a two-level system. *Physical Review A*, 94(6):063826, dec 2016.

[329] J. P. Lee, E. Murray, A. J. Bennett, D. J. P. Ellis, C. Dangel, I. Farrer, P. Spencer, D. A. Ritchie, and A. J. Shields. Electrically driven and electrically tunable quantum light sources. *Applied Physics Letters*, 110(7):071102, feb 2017.

[330] Xiaodong Xu, Wang Yao, Bo Sun, Duncan G. Steel, Allan S. Bracker, Daniel Gammon, and L. J. Sham. Optically controlled locking of the nuclear field via coherent dark-state sopctroscopy. *Nature*, 459(7250):1105–1109, 2009.

[331] E. A. Chekhovich, M. N. Makhonin, K. V. Kavokin, A. B. Krysa, M. S. Skolnick, and A. I. Tartakovskii. Pumping of nuclear spins by optical excitation of spin-forbidden transitions in a quantum dot. *Physical Review Letters*, 104(6):1–4, 2010.

[332] G. Éthier-Majcher, D. Gangloff, R. Stockill, E. Clarke, M. Hugues, C. Le Gall, and M. Atatüre. Improving a Solid-State Qubit through an Engineered Mesoscopic Environment. *Physical Review Letters*, 119(13):1–6, 2017.

[333] H.-J. Briegel, W. Dür, J. I. Cirac, and P. Zoller. Quantum Repeaters: The Role of Imperfect Local Operations in Quantum Communication. *Physical Review Letters*, 81(26):5932–5935, dec 1998.

université PARIS-SACLAY
ÉCOLE DOCTORALE
Ondes et Matière
(EDOM)

Title: Single photon generation and manipulation with semiconductor quantum dot devices

Keywords: Quantum dots, single photons, quantum optics, Cavity QED

Abstract: Quantum phenomena can nowadays be engineered to realize fundamentally new applications. This is the field of quantum technology, which holds the promise of revolutionizing computation, communication and metrology. By encoding the information in quantum mechanical systems, it appears to be possible to solve classically intractable problems, achieve absolute security in distant communications and beat the classical limits for precision measurements. Single photons as quantum information carriers play a central role in this field, as they can be easily manipulated and can be used to implement many quantum protocols. A key aspect is the interfacing between photons and matter quantum systems, a fundamental operation both for the generation and the readout of the photons. This has been driving a lot of research toward the realization of efficient atom-cavity systems, which allows the deterministic and reversible transfer of the information between the flying photons and the optical transition of a stationary atom. The realization of such systems in the solid-state gives the possibility of fabricating integrated and scalable quantum devices.

With this objective, in this thesis work, we study the light-matter interface provided by a single semiconductor quantum dot, acting as an artificial atom, deterministically coupled to a micropillar cavity. Such a device is shown to be an efficient emitter and receiver of single photons, and is used to implement basic quantum functionalities. First, under resonant optical excitation, the device is shown to act as a very bright source of single photons. The strong acceleration of the spontaneous emission in the cavity and the electrical control of the structure, allow generating highly indistinguishable photons with a record brightness. This new generation of single-photon sources can be used to generate path entangled NOON states. Such entangled states are important resources for sensing application, but their full characterization has been scarcely studied. We propose here a novel tomography method to fully characterize path entangled NOON state and experimentally demonstrate the method to derive the density matrix of a two-photon path entangled state. Finally, we study the effect of the quantum dot-cavity device as a non-linear filter. The optimal light matter interface achieved here leads to the observation of an optical nonlinear response at the level of a single incident photon. This effect is used to demonstrate the filtering of single photon Fock state from classical incident light pulses. This opens the way towards the realization of efficient photon-photon effective interactions in the solid-state, a fundamental step to overcome the limitations arising from the probabilistic operations of linear optical gates that are currently employed in quantum computation and communication.

université
PARIS-SACLAY

ÉCOLE DOCTORALE
Ondes et Matière
(EDOM)

Titre : Génération et manipulation de photons uniques avec boîtes quantiques semi-conductrices

Mot-clefs : Boîtes quantiques, photons uniques, optique quantique, Cavity QED

Résumé : Les phénomènes quantiques les plus fondamentaux comme la cohérence quantique et l'intrication sont aujourd'hui explorés pour réaliser de nouvelles technologies. C'est le domaine des technologies quantiques, qui promettent de révolutionner le calcul, la communication et la métrologie. En encodant l'information dans les systèmes quantiques, il serait possible de résoudre des problèmes inaccessibles aux ordinateurs classiques, de garantir une sécurité absolue dans les communications et de développer des capteurs dépassant les limites classiques de précision. Les photons uniques, en tant que vecteurs d'information quantique, ont acquis un rôle central dans ce domaine, car ils peuvent être manipulés facilement et être utilisés pour mettre en œuvre de nombreux protocoles quantiques. Pour cela, il est essentiel de développer des interfaces très efficaces entre les photons et les systèmes quantiques matériels, tels les atomes uniques, une fonctionnalité fondamentale à la fois pour la génération et la manipulation des photons. La réalisation de tels systèmes dans l'état solide permettrait de fabriquer des dispositifs quantiques intégrés et à large échelle.

Dans ce travail de thèse, nous étudions l'interface lumière-matière réalisée par une boîte quantique unique, utilisée comme un atome artificiel, couplée de façon déterministe à une cavité de type micropilier. Un tel dispositif s'avère être un émetteur et un récepteur efficace de photons uniques. Tout d'abord, sous une excitation optique résonante, nous montrons comment nos composants sont des sources très brillantes de photons uniques. L'accélération de l'émission spontanée de la boîte quantique dans la cavité et le contrôle électrique de la structure permettent de générer des photons très indiscernables avec une très haute brillance. Cette nouvelle génération de sources de photons uniques peut être utilisée pour générer des états de photons intriqués en chemin appelés états NOON. Ces états intriqués sont des ressources importantes pour la détection de phase optique, mais leur caractérisation optique a été peu étudiée jusqu'à présent. Nous présentons une nouvelle méthode de tomographie pour caractériser les états de NOON encodés en chemin et implémentons expérimentalement cette méthode dans le cas de deux photons. Enfin, nous étudions le comportement de nos composants comme filtres non-linéaires de lumière. L'interface optimale entre la lumière et la boîte quantique permet l'observation d'une réponse optique non-linéaire au niveau d'un seul photon incident. Cet effet est utilisé pour démontrer le filtrage des états Fock à un seul photon à partir d'impulsions classiques incidentes. Ceci ouvre la voie à la réalisation d'interactions effectives entre deux photons dans un système à l'état solide, une étape fondamentale pour surmonter les limitations dues au fonctionnement probabilistes des portes optiques linéaires.